

REPUBLIQUE DU CAMEROUN

Paix – Travail – Patrie

UNIVERSITE DE YAOUNDE I

FACULTE DES SCIENCES

DEPARTEMENT DE CHIMIE

INORGANIQUE



REPUBLIC OF CAMEROUN

Peace – Work – Fatherland

UNIVERSITY OF YAOUNDE I

FACULTY OF SCIENCE

DEPARTMENT OF INORGANIC

CHEMISTRY

Metal Complexes of Thioureas, Dithiocarbamates and Xanthates as Versatile Molecular Source Precursors for the Preparation of Metal Sulfide MS (M = Pb, Cu, Cd, In and Ga) Nanoparticles and Thin films.

Submitted in partial fulfilment of the requirements for the award of
the Doctorat/PhD in Chemistry

Par : **KETCHEMEN YOUSOU Idriss Kevin**
MSc in Chemistry (UYI)

Sous la direction de
NDIFON Peter Teke
Professor, University of Yaounde I
Neerish REVAPRASADU
Professor, University of Zululand, SA

Année Académique : 2020



ATTESTATION OF THESIS CORRECTION

We the undersigned NENWA Justin (Professor, examiner), NDIFON Peter TEKE (Professor, supervisor), TCHOUANKEU Jean Claude (Associate Professor, president) attest that this Ph.D thesis defended on the 20th February 2020 in the pedagogic block , hall S01 / 02 of the Faculty of Science, University of Yaounde I, by Mr KETCHEMEN YOUSOU Idriss Kevin on the theme "*Metal Complexes of Thioureas, Dithiocarbamates and Xanthates as Versatile Molecular Source Precursors for the Preparation of Metal Sulfide MS (M = Pb, Cu, Cd, In and Ga) Nanoparticles and Thin films*", for the award of a Ph.D in Inorganic Chemistry, has been corrected in conformity with the recommendations of the defense jury.

In this testimony whereof, this attestation is issued.

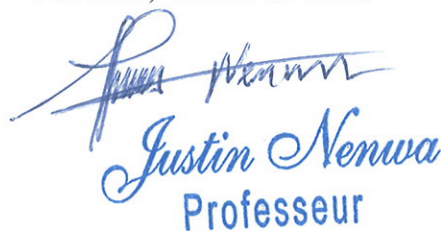
Yaounde, March 02 2020



Peter C. Ndifon, PhD
Supervisor Professeur

NDIFON Peter TEKE

Professor



Justin Nenuwa
Professeur

Examiner

NENWA Justin

Professor



President

TCHOUANKEU Jean Claude

Associate Professor

Dedication

This work is dedicated to the late “**Professor Paul O’Brien** and my **maternal grandmother**”.

Acknowledgements

I am immensely indebted to my home supervisor and Head of the department of Inorganic Chemistry Prof. Ndifon Peter Teke at the University of Yaounde I, for his immense guidance, encouragement, commitment and support throughout my PhD programme.

I wish to express my sincere thanks, respect and admiration to my host supervisor Prof. Neerish Revaprasadu at the University of Zululand (South Africa) for his continuous guidance, encouragement, commitment and paramount support during this project. I also acknowledge the love and hospitality of his wife Shaneera Revaprasadu and their kids Manav, Mahee and Aryana.

My profound and sincere gratitude to the Royal Society Department For International Development Africa Capacity Building Initiative (RS-DFID ACBI) and the NRF/DST South Africa through SARChI granted to Prof. Neerish Revaprasadu for their financial support, which enabled me to carry out this research work smoothly.

I am equally thankful to all the staff members of the chemistry department of the University of Zululand; Prof. Motaung, Dr. Segapelo, Sibusiso Buthelezi, Zibane Welcome and my colleagues of the laboratory; Dr. Sixberth Mlowe, Dr. Rekha Dunpall, Dr. Malik Dilshad, Dr. Siphamandla Masikane, Fr. Dr. Charles Gervas, Zimele Mzimela, Zikhona, former postdocs, students and research visitors for assistance, care and useful discussions during my stay in Zululand (South Africa).

My deepest gratitude to Dr Fon Fabian and his family for their love, warm hospitality and constant care during my stay in South Africa.

I wish to express my special thanks to all the research fellows and the PhD students of the O'Brien group at the School of Chemistry of the University of Manchester, and especially Dr. David Lewis, Dr. Paul McNaught, Dr. Masood Akhtar, Dr. Ghulam Murtaza, and Suliman Alderhami for their commendable help, whenever I required during my stay in Manchester.

My sincere gratitude to Mr Ngah Richard, his wife and kids Sherelle and Jay for their kind hospitality, love and constant care throughout my stay in the UK.

I thank Prof. Ketcha Joseph Mbadcam, former Head of Department of Inorganic Chemistry, University of Yaounde I for his assistance, encouragement and for facilitating this project.

I am thankful to all the lecturers of the Department of Inorganic Chemistry particularly to Prof. Michel M. Belombe, Prof. Daniel Njopwouo, Prof. Ghogomu Paul Mingo, Prof. Emmanuel Ngameni, Prof. Samuel Laminsi, Prof. Agwara Moise Ondoh, Prof. Justin Nenwa, Prof. Antoine Elimbi, Prof. Horace Ngomo, Prof. Emmanuel Djoufack, Dr. Linda Nyamen, Dr. Awawou Paboudam, Dr. Nchimi Katia, Dr. Neba and Prof. Julius Ndi for their encouragements and useful suggestions.

I wish also to express my special thanks and gratitude to the Coordination chemistry research team and the following PhD and Masters students of the Inorganic Chemistry Department, Dr. Sally Ntum, Dr. Walter Kun, Maurice Kuate, Gaelle Sado, Marley Kuimeke, Francis Ngounoue, Adrien Yepseu and Nadege Maptue for their moral support and constant care.

I thank my parents **Youssou Claude** and **Pagnia Rose** for their support, countless sacrifices and constant love throughout my education. I also thank Dr **Nana Merbel**, Mrs **Tchoumtang Alliance**, **Pourfilet Valerie**, **Njoya Armande**, my siblings and cousins for teaching me to be patient, honest, obliging, generous and hardworking.

My sincere gratitude to Prof. Kala and his family for their love, care, encouragements and support.

Special thanks to my friend, Jeannette Ngadjeu for her love, patience and support.

My sincere thanks to all people who made any contribution, however small, to the completion of this work.

TABLE OF CONTENTS

Dedication	i
Acknowledgements	ii
TABLE OF CONTENTS	iv
LIST OF ABBREVIATIONS AND SYMBOLS	vii
LIST OF SCHEMES	ix
LIST OF IMAGES	xii
LIST OF TABLES	ix
LIST OF FIGURES	xi
ABSTRACT	xv
RESUME	xvii
GENERAL INTRODUCTION	1
CHAPTER 1: LITERATURE REVIEW ON SEMICONDUCTOR NANOMATERIALS	7
1.1. Semiconductor nanomaterials	7
1.2. Properties of semiconductor nanomaterials	8
1.2.1. Optical properties	9
1.2.2. Magnetic properties	11
1.3. Surface passivation of nanomaterials	13
1.4. Synthesis of nanomaterials	16
1.4.1. Precipitation route.....	18
1.4.2. Solution phase thermal decomposition or the hot injection route	19
1.4.3. Heat up route	23
1.4.4. Deposition of thin films.....	23
1.4.5. Solventless route (Melt method).....	27
1.5. Single source precursors (SSPs)	28
1.5.1. Sulfur based single source precursors	28
1.5.2. Thiourea complexes as SSPs	29
1.5.3. Dithiocarbamate complexes as SSPs.....	30
1.5.4. Dithiocarbonato complexes (Xanthates) as SSPs.....	31
1.6. Critical parameters for growth and shape control of nanomaterials	34

1.7. Applications of semiconductor nanomaterials	37
1.7.1. Solar cells	37
1.7.2. Sensing.....	37
1.7.3. Health care delivery.....	38
1.7.4. Photocatalysis and environmental pollution control	39
1.8. Statement of the research problem	39
1.9. Objectives	40
1.9.1. Main objective	40
1.9.2. Specific objectives.....	40
CHAPTER 2: EXPERIMENTAL METHODS	42
2.1. Reagents	42
2.2. Syntheses of the ligands and complexes as SSPs	42
2.2.1. Syntheses of N-morpholine and N-pyrrolidine-N ² -benzoylthiourea ligands	42
2.2.2. Synthesis of sodium piperidine dithiocarbamate ligand.....	43
2.2.3. Syntheses of metal(II) N-morpholine and N-pyrrolidine [M(morph/pyrr-tu)].....	43
2.2.4. Syntheses of cadmium(II) dihexyl dithiocarbamate complex	44
2.2.5. Syntheses of cadmium(II) diethyl dithiocarbamate, piperidinyl	45
2.2.6. Syntheses of cadmium(II), indium(III) and gallium(III) ethyl xanthate complexes ...	47
2.3. Syntheses of organically capped metal sulfide nanoparticles using	49
2.3.1. Syntheses of lead sulfide (PbS) nanoparticles	49
2.3.2. Syntheses of copper sulfide (Cu _x S _y) nanoparticles.....	51
2.3.3. Syntheses of cadmium sulfide (CdS) nanoparticles	52
2.4. Syntheses of undoped CdS, In-doped and Ga-doped CdS	53
2.4.1. Syntheses of undoped CdS nanoparticles	54
2.4.2. Syntheses of In-doped and Ga-doped CdS nanoparticles.....	54
2.5. Syntheses of some metal sulfide thin films by the aerosol-assisted	55
2.6. Characterization of the ligands and the metal complexes	58
2.6.1. Elemental analyses	58
2.6.2. Melting point determination	58
2.6.3. Thermal analyses	59
2.6.4. Infra-red analyses	60
2.6.5. ¹ H Nuclear magnetic resonance (NMR) analyses	61

2.6.6. Single crystal X-ray crystallography	62
2.7. Characterization of the organically capped metal sulfide nanoparticles	63
2.7.1. Optical spectroscopies	63
2.7.2. Electron beam techniques	65
2.7.3. X-Ray diffraction technique	67
CHAPTER 3: RESULTS AND DISCUSSION	68
3.1. Syntheses and characterisation of precursors.....	68
3.1.1. Syntheses and characterization of heterocyclic thiourea ligands and lead.....	68
3.1.2. Syntheses and characterization of heterocyclic thiourea ligands and copper	76
3.1.3. Dithiocarbamates (dihexyl, diethyl, piperidine) and Cd(II) complexes	82
3.1.4. Ethyl xanthate metal complexes of (Cd(II), In(III) and Ga(III)).....	86
3.2. Organically-capped PbS nanoparticles	89
3.2.1. Preparation and characterization of PbS nanoparticles using.....	90
3.2.2. Preparation and characterization of PbS nanoparticles using.....	97
3.3. Organically-capped Cu_xS_y nanoparticles	104
3.3.1. Preparation and Characterization of Cu _x S _y nanoparticles using copper.....	105
3.3.2. Preparation and Characterization of Cu _x S _y nanoparticles using copper.....	112
3.4. Organically-capped CdS nanoparticles	120
3.4.1. Preparation and characterization of CdS nanoparticles using cadmium	121
3.4.2. Study the effect of precursor type and capping group on the morphology	130
3.5. Undoped CdS, In-doped and Ga-doped CdS nanoparticles	134
3.5.1. Syntheses and characterization of In-doped CdS nanoparticles.....	134
3.5.2. Syntheses and characterization of Ga-doped CdS nanoparticles.....	139
3.6. Deposition of lead sulfide, copper sulfide and cadmium sulfide thin films	144
3.6.1. Syntheses and characterization of lead sulfide thin films.....	145
3.6.2. Syntheses and characterization of copper sulfide thin films	154
3.6.3. Syntheses and characterization of cadmium sulfide thin films	158
GENERAL CONCLUSION AND PERSPECTIVES	173
REFERENCES	175
ANNEX 1: Publications.....	198
ANNEX 2. Spectroscopic infrared and ¹H NMR spectra of the ligands and metal complexes.....	227
ANNEX 3. Crystallographic data of the Pb(II) and Cu(II) crystal structures.	230

LIST OF ABBREVIATIONS AND SYMBOLS

AACVD	Aerosol assisted chemical vapour deposition
CO	Castor oil
CVD	Chemical vapour deposition
DOS	Density of energy states
DT	Dodecanethiol
Eg	Energy band gap
EDX	Energy dispersive X-ray spectroscopy
FTIR	Fourier transform infrared spectroscopy
$Cd_{1-x}Ga_xS$	Gallium doped cadmium sulfide
HDA	Hexadecylamine
HOMO	Highest occupied molecular orbital
HRTEM	High resolution transmission electron microscopy
$Cd_{1-x}In_xS$	Indium doped cadmium sulfide
LP-MOCVD	Low pressure-metal organic chemical vapour deposition
LUMO	Lowest unoccupied molecular orbital
MRI	Magnetic resonance imaging
MOCVD	Metal organic chemical vapour deposition
m	Multiplet (NMR spectra)
NIR	Near infrared
OLA	Oleylamine

PL Photoluminescence

P-XRD Powder X-ray diffraction

q Quartet (NMR spectra)

SEM Scanning electron microscopy

SSP Single source precursor

TEM Transmission electron microscopy

t Triplet (NMR spectra)

TOP Tri-octylphosphine

TOPO Tri-octylphosphine oxide

LIST OF SCHEMES

Scheme 1. Global syntheses of thiourea ligand (R'= alkyl, aryl and R= alkyl).	29
Scheme 2. Global syntheses of dithiocarbamate ligand.	30
Scheme 3. Global syntheses of xanthate ligand (R= alkyl).	32
Scheme 4. Chemical reaction scheme for the syntheses of the piperidine ligand.	43
Scheme 5. Chemical reaction scheme for the syntheses of the thiourea complexes.	44
Scheme 6. Chemical reaction scheme for the syntheses of the Cd(II) dihexyl dithiocarbamate.	45
Scheme 7. Chemical reaction for the syntheses of the Cd(II) diethyl, piperidine.	46
Scheme 8. Chemical reaction for the syntheses of the Cd(II), In(III) and Ga(III).	48

LIST OF IMAGES

Image 1. a) Some tubes of synthesized a) OLA-capped PbS and b) CO-capped.	50
Image 2. Some tubes of synthesized a) DT-capped Cu_xS_y and b) OLA-capped Cu_xS_y	51
Image 3. Some tubes of synthesized a) OLA-capped and b) HDA-capped CdS nanoparticles...	53
Image 4. Synthesized a) Undoped CdS, In-doped CdS and b) Undoped CdS, Ga-doped.	54
Image 5. Glass substrate of deposited a) Cu_xS_y , b) PbS and c) CdS thin films.	56
Image 6. Barloworld SMP10 melting point apparatus.....	59
Image 7. Melting point apparatus.....	59
Image 8. Perkin-Elmer pyris 6 thermogravimetric analyzer.	60
Image 9. Bruker FT-IR tensor 27 spectrophotometer.	61
Image 10. Nuclear Magnetic Resonance Bruker advance III 400 MHz spectrophotometer.....	62
Image 11. Perkin Elmer Lambda 1050 UV/Vis/NIR spectrophotometer	64
Image 12. Varian Cary 50 Conc UV-visible spectrophotometer	64
Image 13. Perkin-Elmer LS 55 spectrofluorimeter	65
Image 14. Scanning electron microscope.....	66
Image 15. Bruker AXS D8 diffractometer.	67

LIST OF TABLES

Table 1. Reaction parameters for the syntheses of PbS nanoparticles	50
Table 2. Reaction parameters for the syntheses of Cu _x S _y nanoparticles	52
Table 3. Reaction parameters for the syntheses of PbS nanoparticles	53
Table 4. Reaction parameters for the syntheses of undoped CdS, In-doped CdS and	55
Table 5. Reaction parameters for the deposition of PbS, Cu _x S _y and CdS thin films	57
Table 6. Elemental analyses data for the ligands and lead complexes	69
Table 7. Spectroscopic data for the ligands and lead complexes	70
Table 8. Crystal data and structure refinement details for Pb-morphu complex (1)	73
Table 9. Selected bond parameters describing complex (1)	74
Table 10. Elemental analyses data for the ligands and copper complexes	77
Table 11. Spectroscopic data for the ligands and copper complexes	78
Table 12. Crystal data and structure refinement details for Cu-morphu complex (3)	81
Table 13. Selected bond parameters describing Cu-morphu complex (3)	82
Table 14. Elemental analytical data for the ligand and cadmium complexes	83
Table 15. Spectroscopic data for the ligand and cadmium complexes	84
Table 16. Data from decomposition patterns	85
Table 17. Elemental analytical data for the complexes	86
Table 18. Spectroscopic data for the complexes	87
Table 19. Data from decomposition patterns	88
Table 20. EDX of In-doped CdS	138
Table 21. EDX of Ga-doped CdS nanoparticles	143
Table 22. Calculated lattice parameter/Å (calculated for all peaks below $2\theta = 60^{\circ}$)	147
Table 23. The values of the lattice parameter calculated twice for each temperature	149
Table 24. Elemental composition found by EDX spectroscopy of Pb and S in the thin	151
Table 25. Elemental composition found by EDX spectroscopy of Cu and S in the thin	155
Table 26. Phases and morphologies of copper sulfide thin films obtained	155
Table 27. Optical properties of the deposited CdS thin films.	161
Table 28. Elemental analyses by EDX (atomic %) of CdS thin films using each.	172

LIST OF FIGURES

Figure 1. Spatial electronic state diagram for (a) bulk material and (b) nanomaterial. ⁷⁵	9
Figure 2. Schematic illustration of Fermi level context in (a); metal and	10
Figure 3. Fluorescence emission of (a); (CdSe) ZnS quantum dots of different sizes. ⁷⁶	11
Figure 4. Magnetic moments rising from electron orbital motion (left). ⁸⁶	13
Figure 5. Scheme showing semiconductor nanoparticles capped with (a) TOPO. ⁸	15
Figure 6. TEM images of: (a) non-capped PbS nanoparticles and (b) OA-capped PbS. ⁹¹	16
Figure 7. Scheme showing the various synthetic methods of Top-down and Bottom-up.	17
Figure 8. Process of the crystal growth of colloidal nanoparticles (Ostwald ripening). ⁹³	19
Figure 9. Reaction scheme for the syntheses of molecular precursors. ¹⁰⁴	21
Figure 10. Schematic setup for hot injection route for nanocrystals. ¹⁰⁷	23
Figure 11. Schematic illustration of a deposited thin film material onto a substrate.....	24
Figure 12. Schematic illustration of the process involved during chemical vapour. ¹¹⁵	25
Figure 13. Setup of the AACVD technique. ¹¹⁵	27
Figure 14. Schematic representation of the mechanism during growth of nanoparticle. ⁹²	35
Figure 15. Schematic illustration of growth and stabilization of nanoparticles. ¹⁴⁰	36
Figure 16. Schematic illustration of the application of the contrast agent on the tumor. ⁷⁴	38
Figure 17. Schematic set up for the preparation of metal sulfide nanoparticles.....	49
Figure 18. Schematic set up for an AACVD reaction.....	57
Figure 19. Thermogravimetric analysis (TGA) plots of Pb(II) complexes (1) and (2) at.....	71
Figure 20. Thermal displacement plot (50% probability) of (1) showing the distorted.	72
Figure 21. Dimeric structure of Pb-morphtu (1) stabilized by Pb···S and weak.	75
Figure 22. One dimensional polymer of (1) comprising dimeric molecules cross-linked.....	76
Figure 23. Thermogravimetric analysis (TGA) plots of Cu(II) complexes (3) and (4) at a.	79
Figure 24. Single X-ray crystal structure of.....	80
Figure 25. Thermogravimetric analysis (TGA) plots of complexes from Cd(II) dihexyl (a).....	85
Figure 26. TGA curves for (a) Cd(eth-xan) ₂ , (b) In(eth-xan) ₃ and (c) Ga(eth-xan) ₃	88
Figure 27. Proposed decomposition of metal ethyl xanthate complexes by a modified.....	89
Figure 28. TEM images of PbS nanoparticles prepared from Pb-morphtu in OLA at.	91
Figure 29. Powder X-ray diffractograms of PbS nanoparticles prepared from Pb-morphtu.	92

Figure 30. NIR UV absorption spectra of PbS nanoparticles prepared from Pb-morphu in.	93
Figure 31. TEM images of PbS nanoparticles prepared from Pb-morphu in CO at.....	94
Figure 32. Powder X-ray diffractograms of PbS nanoparticles prepared from Pb-morphu.	95
Figure 33. NIR UV absorption spectra of PbS nanoparticles prepared from Pb-morphu.	96
Figure 34. TEM images of PbS nanoparticles prepared from Pb-pyrriu in OLA at.....	98
Figure 35. Powder X-ray diffractograms of PbS nanoparticles prepared from Pb-pyrriu.	99
Figure 36. NIR UV absorption spectra of PbS nanoparticles prepared from Pb-pyrriu.	100
Figure 37. TEM images of PbS nanoparticles prepared from Pb-pyrriu in CO at.....	101
Figure 38. Powder X-ray diffractograms of PbS nanoparticles prepared from Pb-pyrriu.	102
Figure 39. NIR UV absorption spectra of PbS nanoparticles prepared from Pb-pyrriu.	103
Figure 40. TEM images of copper sulfide nanoparticles prepared at (a) 150 °C.,	106
Figure 41. P-XRD of nanoparticles prepared from Cu-morphu complex in OLA at.	107
Figure 42. TEM images of nanoparticles prepared at (a) 150 °C, (b) 190 °C..	109
Figure 43. P-XRD of nanoparticles obtained from Cu-morphu complex at (a) 150 °C.	110
Figure 44. TEM images of nanoparticles prepared at (a) 150 °C, (b) 190 °C and.	111
Figure 45. P-XRD pattern of Cu _{1.75} S nanoparticles obtained from Cu-morphu complex	112
Figure 46. TEM images of copper sulfide nanoparticles synthesized at (e) 150 °C.....	114
Figure 47. P-XRD of nanoparticles prepared from Cu-pyrriu complex in OLA at.	115
Figure 48. TEM images of nanocrystals fabricated at (g) 150 °C, (h) 190 °C.	116
Figure 49. P-XRD of nanoparticles obtained from Cu-pyrriu complex at (a) 150 °C.....	117
Figure 50. TEM images of nanoparticles prepared at (d) 150 °C, (e) 190 °C and..	118
Figure 51. P-XRD pattern of Cu _{1.75} S nanoparticles obtained from Cu-pyrriu complex at.....	119
Figure 52. CdS nanoparticles prepared from a) Cd(II) dihexyl dtc, b) Cd(II) diethyl dtc.	122
Figure 53. Particle size distribution of the prepared CdS nanocrystallites synthesized.	123
Figure 54. P-XRD patterns of HDA capped CdS nanoparticles prepared from.	124
Figure 55. UV-visible absorption spectra of HDA capped CdS nanoparticles prepared.....	125
Figure 56. CdS nanoparticles synthesized from a) Cd(II) dihexyl dtc, b) Cd(II) diethyl.	127
Figure 57. Particle size distribution of the prepared CdS nanocrystallites prepared from	128
Figure 58. P-XRD patterns of OLA capped CdS nanoparticles prepared from.....	129
Figure 59. UV-visible absorption spectra of OLA capped CdS nanoparticles prepared	130
Figure 60. Plots of band gap energy and average particle sizes versus the precursor	132

Figure 61. Plots of band gap energy and average particle sizes versus the precursor	133
Figure 62. P-XRD patterns of In-doped CdS nanoparticles.....	135
Figure 63. Lattice constant as a function of [In]/[In]+[Cd] ratio.....	136
Figure 64. Secondary electron microscopy SEM images (20 kV) of Cd _{1-x} In _x S nanoparticles..	137
Figure 65. Elemental mapping distributions (20 kV) of Cd, In and S (colored images)	138
Figure 66. Raman spectra of In-doped CdS nanoparticles.....	139
Figure 67. P-XRD patterns of Ga-doped CdS nanoparticles.	140
Figure 68. Lattice constant as a function of [Ga]/[Ga]+[Cd] ratio.	141
Figure 69. Secondary electron microscopy SEM images (10 kV) of Cd _{1-x} Ga _x S.....	142
Figure 70. EDX spectrum mapping of the elemental distributions (20 kV) of Cd, Ga and S ...	143
Figure 71. Raman spectra of Ga-doped CdS nanoparticles.	144
Figure 72. P-XRD patterns of PbS thin films deposited from complex (1) at temperatures.	146
Figure 73. P-XRD patterns of PbS thin films deposited from complex (2) at temperatures.	147
Figure 74. Highly resolved p-XRD pattern. The lattice constant a value can be measured.	148
Figure 75. SEM images of PbS films deposited from complex (1) onto glass substrates..	150
Figure 76. UV–Vis absorption spectra of PbS films deposited on glass substrate using.	152
Figure 77. UV–Vis absorption spectra of PbS films deposited on glass substrate using.	153
Figure 78. a) P-XRD pattern of CuS deposited on glass substrate by AACVD from.	156
Figure 79. a) P-XRD pattern of CuS deposited on glass substrate by AACVD from	157
Figure 80. (Left UV-Vis absorption spectra of CdS films deposited on glass substrate	159
Figure 81. (Left UV-Vis absorption spectra of CdS films deposited on glass substrate	159
Figure 82. (Left UV-Vis absorption spectra of CdS films deposited on glass substrate	160
Figure 83. Photoluminescence emission spectra of CdS thin films deposited at.....	162
Figure 84. Photoluminescence emission spectra of CdS thin films deposited at.....	163
Figure 85. Photoluminescence emission spectra of CdS thin films deposited using mixed.....	164
Figure 86. Powder X-ray patterns of CdS films deposited at 400 °C using complexes.	165
Figure 87. Powder X-ray patterns of CdS films deposited at 450 °C using complexes.	166
Figure 88. Powder X-ray patterns of CdS films deposited using mixed.....	167
Figure 89. SEM images of CdS films deposited on glass substrate at 400 °C using	168
Figure 90. SEM images of CdS films deposited on glass substrate at 450 °C using.....	169
Figure 106. SEM images of CdS films deposited on glass substrate at 450 °C using mixed....	171

ABSTRACT

Morpholine and pyrrolidine heterocyclic thiourea, dihexyl, diethyl, heterocyclic piperidine dithiocarbamate and ethyl xanthate ligands as well as their respective lead(II), copper(II), cadmium(II), indium(III) and gallium(III) complexes were prepared and characterized using known analytical methods such as melting points, microanalysis, infrared spectroscopy (IR), nuclear magnetic resonance (NMR) and thermogravimetric analyses (TGA). These compounds were obtained in very good yields ranging from 73-88% for the ligands and 60-96% for the metal complexes. Infrared analyses showed that the ligands bonded in a bidentate mode using both S-donors for bonding in the case of dithiocarbamate and xanthate and S-donor and O-donor for bonding in the case of thiourea. Thermogravimetric analyses showed that the metal complexes decomposed in the temperature range from 136 to 600 °C.

The prepared Pb(II), Cu(II), Cd(II), In(III) and Ga(III) complexes were used as single source precursors, either for thermolysis in hot capping agents or in the melt method, to produce lead sulfide (PbS), copper sulfide (Cu_xS_y), cadmium sulfide (CdS), In-doped CdS and Ga-doped CdS nanoparticles respectively. Some reaction parameters such as the nature of the precursor, the capping group and the reaction temperature were varied in order to investigate their effects on the shape, size and the optical properties of the prepared nanoparticles. UV-visible and photoluminescence (PL) spectroscopies were used to elucidate the optical properties of the synthesized metal sulfides while transmission electron microscopy (TEM), high resolution transmission electron microscopy (HRTEM) and scanning electron microscopy (SEM) techniques were used to determine their shapes and sizes, and powder X-ray diffraction (p-XRD) technique used to determine their crystallinity. The PbS and CdS nanoparticles revealed quantum confinement in their absorption band edges. The variation of the capping agents (hexadecylamine, oleylamine, dodecanethiol and castor oil) slightly affected the shape at lower temperatures (150, 190, 200 °C) and considerably at higher temperatures (>200 °C). An increase of the band gap energy (shift to lower wavelengths) was observed when the capping group was varied from hexadecylamine to oleylamine for the CdS nanoparticles. The variation of the reaction temperature (150, 190, 200, 230 and 250 °C) showed a significant effect on the shape and size of the PbS, Cu_xS_y and CdS nanoparticles. Lead sulfide nanoparticles were produced in shapes ranging from

spherical to oval, rod and predominantly cubes. Copper sulfide nanoparticles were obtained as cubes, spherical, hexagonal nanodisks and rod shapes while spherical, cubic and rods shaped CdS were formed. In-doped and Ga-doped CdS nanoparticles have been synthesized by the solventless thermolysis of melted precursors. SEM images revealed that the shape of CdS changes with indium and gallium doping. The P-XRD analyses revealed the cubic rock salt phase for PbS nanoparticles, roxbyite phase for Cu_xS_y nanoparticles and wurtzite phase for CdS, In-doped CdS and Ga-doped CdS nanoparticles. P-XRD results demonstrated that both indium and gallium readily doped into the hexagonal cadmium sulfide structure causing the predicted reduction in the hexagonal unit cell.

The lead, copper and cadmium complexes were also used to deposit lead sulfide, copper sulfide and cadmium sulfide thin films on glass substrate at different temperatures ranging from 350 to 450 °C by the aerosol assisted chemical vapor deposition technique (AACVD). The thin films were characterised by SEM, energy dispersive X-ray spectroscopy (EDX) and X-ray diffraction (XRD) techniques. SEM images of the deposited lead sulfide (PbS) thin films from Pb-morphu complex revealed that the particle sizes were found be range between 83–85 nm and 71–105 nm for Pb-pyrriu complex. Copper sulfide thin films of diverse morphologies ranging from cubic to snowy or irregular crystallites depending on the deposition temperature were observed. The surface morphology and size of the CdS films determined using scanning electron microscopy, showed the formation of films of various morphologies depending on the precursor, the deposition temperature and solvent used. The optical properties of the PbS films were studied by near infra-red, UV–Vis spectroscopy and band gaps ranging from 1.46 – 1.55 eV were observed, suggesting a strong blue shift compared to the bulk PbS. The CdS films showed an overall blue shift in their absorption band edge (2.35 – 2.49 eV) compared to the bulk CdS. Elemental composition of all the thin films was confirmed by energy dispersive X-ray spectroscopy. Finally, the structures of lead and copper N-morpholine-N'-benzoylthiourea complexes and other precursors were also elucidated using single crystal X-ray techniques.

Keywords: Single source precursors, Heterocyclic thiourea, Dithiocarbamate, Xanthate complexes, Thermolysis, Aerosol assisted chemical vapour deposition, Melt method, Metal sulfide, Indium and Gallium doped CdS, Nanoparticles, Thin films, Optical properties.

RESUME

Les ligands hétérocycliques de morpholine et de pyrrolidine, des ligands dihexyl, diéthyl, pipéridine dithiocarbamates hétérocycliques et xanthate d'éthyle ainsi que leurs complexes respectifs de plomb(II), de cuivre(II), de cadmium(II), d'indium(III) et de gallium(III) ont été préparés et caractérisés en utilisant des méthodes analytiques connues telles que les points de fusion, la microanalyse, la spectroscopie infrarouge (IR), la résonance magnétique nucléaire (RMN) et l'analyse thermogravimétrique (ATG). Ces composés étaient obtenus avec de très bons rendements allant de 73 à 88% pour les ligands et de 60 à 96% pour les complexes métalliques. Les analyses infrarouges ont montré que les ligands se liaient de manière bidentée en utilisant les deux donneurs S pour se lier dans le cas du dithiocarbamate et du xanthate et les donneurs S et O pour la liaison dans le cas de la thiourée. Les analyses thermogravimétriques ont montré que les complexes métalliques se décomposaient dans la plage de température allant de 136 à 600 ° C.

Les complexes préparés de Pb(II), Cu(II), Cd(II), In(III) et Ga(III) ont été utilisés comme précurseurs à source unique pour la thermolyse dans des agents surfactants à chaud ou également pour le procédé de fusion permettant d'obtenir du sulfure de plomb (PbS), de sulfure de cuivre (Cu_xS_y), de sulfure de cadmium (CdS), de nanoparticules CdS dopées à l'indium et CdS dopées au gallium respectivement. Certains paramètres de réaction tels que la nature du précurseur, le groupe surfactant et la température de réaction ont été modifiés afin d'étudier leur effet sur la forme, la taille et les propriétés optiques des nanoparticules préparées. Les spectroscopies UV-visible et de photoluminescence (PL) ont été utilisées pour élucider les propriétés optiques des sulfures métalliques synthétisés, tandis que les techniques de microscopie électronique en transmission (MET), de microscopie électronique en transmission à haute résolution (METHR) et de microscopie électronique à balayage (MEB) ont été utilisées pour déterminer leur forme, leur taille et leur poudre de diffraction à rayons X (P-DRX) utilisée pour déterminer leur cristallinité. Les nanoparticules de PbS and CdS ont révélé un confinement quantique à partir de leur bande d'absorption. La variation des agents surfactants (hexadécylamine, oleylamine, dodecanethiol et castor oil) a légèrement affecté la forme à des températures plus basses (150, 190, 200 ° C) et considérablement à des températures plus élevées (>200 ° C). Une augmentation de l'énergie de la bande interdite (décalage vers les longueurs d'onde inférieures) a été observée lorsque l'agent stabilisant variait de l'hexadécylamine à l'oleylamine pour les nanoparticules de CdS.

La variation de la température de réaction (150, 190, 200, 230 et 250 ° C) a montré un effet significatif sur la forme et la taille des nanoparticules PbS, Cu_xS_y et CdS. Les nanoparticules de sulfure de plomb ont été produites sous des formes allant de sphériques à ovales, en bâtonnets et principalement en cubes. Des nanoparticules de sulfure de cuivre ont été obtenues sous forme de cubes, de nanodisques sphériques, hexagonaux et de barres, tandis que des formes sphériques, cubiques et en forme de barres étaient formées. Les nanoparticules de CdS dopées à In et dopées au Ga ont été synthétisées par thermolyse sans solvant de précurseurs fondus. Les images en microscopie électronique à balayage ont révélé que la forme du CdS change avec le dopage à l'indium et au gallium. Les analyses aux rayons X ont révélé la phase sel gemme cubique pour les nanoparticules de PbS, la phase roxbyite pour les nanoparticules de Cu_xS_y et la phase wurtzite pour les nanoparticules de CdS, CdS dopées à In et de CdS dopées au Ga. Les résultats de P-DRX ont montré que l'indium et le gallium étaient facilement dopés dans la structure hexagonale de sulfure de cadmium, ce qui entraînait la réduction prévue de la cellule unitaire hexagonale.

Les complexes de plomb, de cuivre et de cadmium ont également été utilisés pour déposer des couches minces de sulfure de plomb, de sulfure de cuivre et de sulfure de cadmium sur un substrat de verre à diverses températures allant de 350 à 450 °C grâce à la technique de dépôt en phase vapeur assisté par aérosol (DPVAA). Les couches minces ont été caractérisées par des techniques de microscopie électronique à balayage, de spectroscopie par rayons X à dispersion d'énergie (EDX) et de diffraction de rayons X (DRX). Les images au MEB des couches minces de sulfure de plomb (PbS) déposées du Pb-morphot complexé ont révélé que la taille des particules se situait entre 83 et 85 nm et entre 71 et 105 nm pour le Pb-pyrrtu complexé. Les couches minces de sulfure de cuivre de morphologies diverses, allant de cristallites cubiques à enneigés ou irrégulières, en fonction de la température de dépôt, ont été observées. La morphologie de surface et la taille des films de CdS, déterminées par microscopie électronique à balayage (MEB), ont montré la formation de films de différentes morphologies en fonction du précurseur, de la température de dépôt et du solvant utilisé. Les propriétés optiques des couches minces de PbS ont été étudiées par le proche infrarouge (PIR), spectroscopie UV – Vis et des bandes interdites allant de 1,46 à 1,55 eV ont été observées, suggérant un fort décalage bleu par rapport au PbS massif. Les couches minces de CdS ont montré un décalage bleu à partir de leur bande d'absorption (2,35 - 2,49 eV) par rapport au CdS massif. La composition élémentaire de toutes les couches minces a été confirmée par la spectroscopie de rayons X à dispersion d'énergie. Enfin, les structures des

complexes N-morpholine-N'-benzoylthiourée de plomb et de cuivre et d'autres précurseurs ont également été déterminées à l'aide de la technique des rayons X monocristallins.

Mots clés: Précurseurs à source unique, Complexes de Thiourée hétérocyclique, Dithiocarbamate, Xanthate, Thermolyse, Dépôt chimique en phase vapeur assisté par aérosol, Méthode de fusion, Sulfure métallique, CdS dopé à l'indium ou au gallium, Nanoparticules, Couches minces, Propriétés optiques.

GENERAL INTRODUCTION

The development of the nanotechnology, i.e. the techniques to control or manipulate matter on the nanoscale (atomic scale) to create new and unique materials and products (structures, devices and systems that have novel properties with enormous potentials), is such that this field is invading all the different branches of industry, including textile, cosmetic materials science, engineering and medicine. Nanotechnology is a wide and interdisciplinary area of research which has gained much worldwide interest over the past few years¹. It is as a result of this growing interest that researchers like Richard Smalley in 1999 said *“Just wait the 21st century is going to be incredible. We are about to be able to build things that work on the smallest possible length scales, atom by atom. These nanothings will revolutionize industries and our lives”*. Nanomaterials have the potential for modernization due to their small structures and this is because nanotechnology allows us to understand and create materials, devices and systems with fundamentally new properties and functions. This has significantly increased their commercial impact over the past few years and this is expected to revolutionize all industrial sectors in the future². This was predicted in 1999 by M. C. Roco, R. S. Williams, P. Alivisatos when they said that *“Nanoscience and technology will change the nature of almost every human-made object in the 21st century”*.

The word “nano” denotes one billionth of a meter or 10^{-9} m in size, and purely it is expressed as 1 nanometer (nm). Nanomaterials are therefore defined as materials having at least one dimension in the range of 1 – 100 nm. They can be in 0D (spheres, cubes and polyhedrons), 1D (rods and wires), 2D (thin films, prisms and plates) and 3D (nanoparticles)³. Nanostructured materials have significantly different properties due to their size and shape⁴⁻⁷. These properties are generated mainly by two main factors, both relating to the size of the material.⁸

The first factor is the surface to volume ratio and the key advantage of nanomaterials is their large surface to volume ratio. As a material becomes smaller, the ratio of the number of surface atoms compared to those in the interior increases. This characteristic can be exploited in various potential industrial applications such as catalytic processing because of the enhanced chemical reactivity^{9,10}. The second factor affecting the properties is the size of the materials. As the size of the solid decreases, the band gap gradually increases because of the quantum confinement effects, creating

a variation in the electronic properties of the crystal when using semiconductor nanomaterials. For instance, as the particle size decreases, its electronic band quantizes progressively, resulting in an increase of the energy band gap. In nanostructured materials, charge carriers are limited in three dimensions and, as the dimensions of the nanocrystal become analogous to the excitonic radius, quantum size effects take place¹¹. The quantum effect causes the continuous band of the material to split into distinct, quantized levels and the first excitonic transition “band gap” increases in energy with the decrease of the diameter of the crystal. This has been confirmed by several reports on nanomaterials as well as the fact that the optical absorptions of the semiconductor nanocrystallites show a blue shift in the absorption edge with decrease of the particle size.^{12,13} Additionally, the properties of the nanostructured materials are also determined by their morphology as it can influence the energy band gap. When the bulk materials are converted to ‘nanosize’ different changes of physical properties are observed in the density of energy states (DOS). The DOS essentially scales easily with size, but with a scaling rule that is different from that found from surface effects. It is defined to a first approximation by the ‘particle in a box’ model in which the size of the box is assumed by the particle size. The morphology of the semiconductor nanomaterial also affects the energy band gap (E_g) of nanomaterials through the excited-state dynamics. This is the case with nanorods of cadmium selenide (CdSe) of the same length (~ 30 nm) but different diameters, 2.5 and 8.0 nm, that exhibited 8 times faster intraband energy relaxation for thicker rods than thin rods.^{14,15}

Research on nanomaterials as semiconductors has attracted much attention due to their novel and potentially useful optoelectronic properties. Semiconductor nanomaterials can exhibit 3D quantum confinement and have potential technological applications. Amongst the various semiconductors, metal chalcogenides have been extensively studied by researchers and scientists, owing to their unique physical properties and potential for application in optical devices. Three types of metal chalcogenides exist, namely metal sulfide (MS), metal selenide (MSe) and metal telluride (MTe), and our focus in this work has been on metal sulfide nanostructured materials. Metal sulfides nanomaterials are abundant and cheap, due to the natural existence of numerous types on the planet earth. They have a very important and elaborate chemistry owing to the wide variety of recognized metal sulfide phases and their various properties. Bulk metal sulfide materials are employed technologically for diverse applications such as in pigments, luminescent materials for cathode ray

tubes etc¹⁶. Nanostructured metal sulfides find more applications as a result of their enhanced, sized dependant properties.

Major progress has been made on the preparation of nanomaterials resulting in the formation of nanomaterials of different morphologies, which are particularly important for applications in diverse fields of technology. The accurate controlled synthetic routes of the size, shape, chemical composition, crystal structure, and surface chemistry of nanocrystallites lead to their exceptional properties. Some predictions of the optical properties of semiconductor nanomaterials are known from theoretical models¹⁷. Different synthetic routes for the preparation of semiconductor nanomaterials have been reported^{12,18,19}. The best synthetic method should produce pure, crystalline, essentially monodispersed nanocrystallites having a surface that is independently derivatized²⁰. There are two general synthetic pathways for the preparation of nanostructured materials namely, the top-down (physical destruction of larger material) and the bottom-up (build up from molecular precursors, often colloidal) routes. Several synthetic methods have been reported for the synthesis of nanoparticles, which usually follow two routes; precipitation from solution, habitually at room temperature and frequently involving the reduction of a metal salt and the decomposition of molecular precursors at higher reaction temperature in either the solid, liquid (solution) or vapour phase²¹. The use of molecular precursors make use of the existence of the preformed bonds, which can lead to material with fewer defects and/or better stoichiometry, and also avoiding toxic precursors. The two common techniques for synthesizing and controlling the size of nanoparticles are the hot injection and the heat up methods, which differ from each other by the temperature at which the precursors are introduced into the solvent.

The ‘hot injection’ method was forged by Bawendi et al²² for the fabrication of cadmium chalcogenide quantum dots²². It is the earliest method designed for the synthesis of uniform nanoparticles. It involves the injection of the precursors dissolved in a minimum amount of solvent into a preheated hot solvent. Upon injection, the precursors decompose or react to yield the nanoparticles. The hot-injection method has the advantage of yielding monodispersed nanoparticles. This method of nanoparticle synthesis has been extensively used for the synthesis of nanoparticles of numerous compositions^{23–25}. The ‘heat up’ method shares more resemblances with the precipitation method as demonstrated by LaMer than the ‘hot injection’, having all the

reagents together at the start of the reaction so proceeding through monomer accumulation, to nucleation and then to particle growth in order to produce nanoparticles²⁶. Regardless of the various synthetic methods reported, a tenacious deal is the necessity to adopt other synthetic routes that are environmentally friendly and economically viable. Recent attention has been on the use of greener methods for the preparation of nanoparticle. This approach consists of using non-toxic solvents and/or capping groups in the synthetic process²⁷⁻³¹. Chemical vapour deposition (CVD) is a commonly used synthetic method for the deposition of thin solid films of a material on a substrate. This method consists of the transportation of precursor solution into the reaction chamber and to the substrate through an inert carrier gas such as nitrogen or argon, or under vacuum. Since the innovative development of CVD, the method has progressed in a number of directions, resulting in the creation of a wide-range of variations of the process including low pressure-metal organic chemical vapour deposition (LP-MOCVD), metal organic chemical vapour deposition (MOCVD) and aerosol assisted chemical vapour deposition (AACVD)³²⁻³⁴. In this thesis, we have focused on the AACVD method. It is a simple and cheap process that offers the advantage of a uniform and large area deposition of the thin films over other deposition synthetic routes³⁴. Besides the various chemical methods, the fabrication of pure phase ternary materials or doped materials, without the presence of any other phase or impurity is difficult and remains interesting. Therefore, some nanochemists have focused their interest on such materials by using the melt method otherwise called as the solventless method. It is a simple and easy approach in which the solid-state decomposition of the precursors is executed only by heat action under inert conditions.^{35,36}

Controlling the morphology of nanomaterials during the synthesis remains a persistent challenge to researchers in general and to material chemists in particular. Various factors such as the nature of precursor, the monomer concentration, the capping agent, the temperature of the reaction and the reaction time have an influence on the particle size and shape. Some previous reports have elucidated the particle growth during preparation with the effect of kinetic/thermodynamic growth on the final morphology of the nanostructured materials.³⁷⁻³⁹

Many classes of inorganic complexes including dithioimidodiphosphinates^{40,41}, dithiophosphinates^{42,43}, thiosemicarbazides^{44,45}, xanthate⁴⁶⁻⁴⁸, dithiocarbamates^{37,38,49-51} and alkyl/aryl thiourea⁵²⁻⁵⁵ have been used for their suitability as precursors for the growth of metal sulfide nanostructures. Nyamen and co-workers synthesized multi-podal CdS nanostructures using

heterocyclic dithiocarbamate complexes as precursors⁵⁶, Mlowe et al⁵⁷ reported on the bis(piperidinedithiocarbamate)pyridinecadmium(II) for the synthesis of CdS nanoparticles and aerosol-assisted chemical vapour deposition (AACVD) of CdS thin films. Recently, Kun and co-workers synthesized heterocyclic bismuth(III) dithiocarbamate complexes for use as single source precursors for the synthesis of anisotropic Bi₂S₃ nanoparticles⁵⁷. Arain et al⁵⁸ used diethyl dithiocarbamate [Cd(S₂CNEt₂)₂] complex to deposit the cadmium sulphide thin film at much lower temperature by aerosol assisted chemical vapour deposition (AACVD) and to prepare the nanocrystals in oleylamine (OLA) at high temperature. Trindade et al⁴⁹ prepared some lead(II) dithiocarbamate complexes Pb(S₂CNRR')₂ and employed them as single molecule precursors to produce nanocrystalline PbS by thermolysis in trioctylphosphine oxide. Akhtar and co-workers⁵⁹ prepared a series of symmetrical and unsymmetrical N,N-dialkyldithiocarbamatelead(II) complexes with the general formula [Pb(S₂CNRR₂)₂] for use as single source precursors to grow PbS nanoparticles by thermolysis in oleylamine at temperature as low as 60 °C. Barreca and co-workers⁶⁰ reported the synthesis of cadmium bis(O-alkylxanthates) as potential molecular precursors for the chemical vapor deposition (CVD) of Cd(II) sulfide thin films. Al-Shakban et al⁶¹ reported on a simple, easily scalable route to monodispersed copper sulfide nanocrystals by the hot injection of a series of novel copper(I) xanthate single-source precursors [(PPh₃)₂Cu(S₂COR)] (R = isobutyl, 2-methoxyethyl, 2-ethoxyethyl, 1-methoxy-2-propyl, 3-methoxy-1-butyl, and 3-methoxy-3-methyl-1-butyl). Moloto et al⁶² synthesized the Cd(II) complexes of thiourea and N-alkylthioureas (with alkyl group or ethyl) for the use as single source precursors for the preparation of TOPO-capped CdS nanoparticles. Ramasamy et al⁶³ reported a series of new metal complexes of thiobiurets and dithiobiurets. They showed that the compounds are potentially useful as novel single source precursors for the deposition of metal sulfide thin films or nanoparticles. Bruce and co-workers⁵⁴ reported on cadmium complexes of N,N-diethyl-N'-benzoylthiourea and N,N-diethyl-N'-benzoylselenourea which have been used as single-source precursors for the preparation of HDA capped CdS and CdSe nanoparticles. In addition, Khan and co-workers⁶⁴ investigated the phase and shape of copper sulfide nanostructures using mixed solvent systems. In 2017, Masikane et al⁶⁵ reported lead(II) halide cinnamaldehyde thiosemicarbazone complexes as single source precursors for oleylamine-capped lead sulfide nanoparticles. Gervas et al^{66,67} synthesized rare pure phase Ni₃S₄ and Ni₃S₂ nanoparticles in different primary amine coordinating solvents and studied the effect of cationic disorder on the

energy generation and energy storage applications of $\text{Ni}_x\text{Co}_{3-x}\text{S}_4$ thiospinel. However, despite this considerable progress made on the use of xanthates, dithiocarbamates and thioureas as molecular precursors, it was found that heterocyclic thioureas, dithiocarbamates and xanthates complexes have not been extensively studied as precursors for the preparation of metal sulfide nanomaterials. The work contained in this thesis therefore reports on the synthesis and characterisation of some xanthate (ethyl xanthate), (dihexyl, diethyl, piperidine) dithiocarbamates and heterocyclic thiourea (morpholine and pyrrolidine benzoylthiourea) metal complexes of cadmium(II), indium(III), gallium(III), lead(II) and copper (II) respectively. Their utilization as molecular precursors for the preparation of the corresponding metal sulfide nanoparticles and thin films (CdS , PbS and Cu_xS_y) is also described. Moreover, we report also on the preparation of cadmium sulfide, indium and gallium-doped cadmium sulfide nanoparticles (CdS , $\text{Cd}_{1-x}\text{In}_x\text{S}$ and $\text{Cd}_{1-x}\text{Ga}_x\text{S}$) from ethyl xanthate complexes (Cd(II) , In(III) and Ga(III)) using melt method as synthetic route by mixing xanthate precursors of different metals while varying the range of mole percentage of the metal from 0 to 10%. Therefore, our aim is to investigate, the effect of the precursor type, the mixed solvent systems and the reaction temperature on the morphology, crystallographic phases and the optical properties of the synthesized nanostructured materials.

The work in this thesis is divided into three parts. The first chapter presents the literature survey on semiconductor nanomaterials, their synthesis, precursors and factors influencing these materials. Chapter two presents the experimental methods and the various techniques used for the characterization of both the precursors and the nanomaterials, including instrumental techniques used. Finally, chapter three presents and discusses the results obtained. This is followed by a general conclusion and perspectives.

CHAPTER 1: LITERATURE REVIEW ON SEMICONDUCTOR NANOMATERIALS

The synthesis, characterization and applications of nanomaterials have been investigated and their efficiency compared to the bulk materials has been well established. Their properties, however, are strongly dependent on their composition, arrangement of atoms and particle sizes.

1.1. Semiconductor Nanomaterials

A semiconductor is a solid substance that has a conductivity between that of a conductor and an insulator and they are typically used in the development of electronic chips, computing components and devices. They are commonly created using silicon, germanium or other pure elements. Semiconducting nanomaterials can exhibit a range of useful properties showing variable resistance, and sensitivity to light or heat. Since their properties can be modified by doping, or by the application of electrical fields or light, devices produced from semiconductors can find usefulness in amplification, switching, and energy conversion.

The current understanding of the properties of a semiconductor relies on quantum physics to explain the movement of charge carriers in a crystal lattice. Doping of semiconductors increases the number of charge carriers within the crystal. Briefly, a doped semiconductor that has mostly free holes is called "p-type", but when it has mostly free electrons, it is called as "n-type"⁶⁸. Some of the properties of semiconducting nanostructured materials were elucidated during the mid-19th and first decades of the 20th century. The first practical application of semiconductors in electronics was the fabrication of the cat whisker detector in 1904, an original semiconductor diode used in early radio receivers⁶⁹. Progresses in quantum physics allowed the development of more other applications such as the transistor in 1947⁷⁰ and the integrated circuit (laptops, scanners, cell phones) in 1958.⁷¹

1.2. Properties of semiconductor nanomaterials

Nanomaterials as opposed to other semiconductor materials are affected by factors such as surface area, quantum effects, surface atoms, surface energy and reduced imperfections. These factors can vary or enhance characteristic properties of the materials including optical and magnetic properties. Because of their small dimensions, nanomaterials have very large surface area to volume ratio, resulting in more “surface” dependent properties. The finite size of the particle confines the spatial distribution of the electrons, leading to quantized energy levels due to size effects⁷². The quantum confinement is a change of electronic and optical properties of a material of sufficiently small size, typically 10 nanometers or less (Figure 1). The bandgap increases as the size of the nanostructure decreases. This phenomenon, specifically result in electrons and holes being squeezed into a dimension that approaches a critical quantum measurement, called the exciton Bohr radius. The quantum confinement effect is observed when the size of the particle is too small to be comparable to the wavelength of the electron. For a better understanding of this effect, we separately define quantum and confinement. Confinement means to restrict the motion of an arbitrarily moving electron to specific energy levels (discreteness) and quantum reflects the atomic kingdom of particles. Consequently, as the size of a particle decrease to nanoscale, the decrease in confining dimension makes the energy levels discrete and this increases or enlarges the band gap and eventually the band gap energy. Since the band gap and wavelength are inversely related to each other the wavelength decrease with decrease in size.^{73,74}

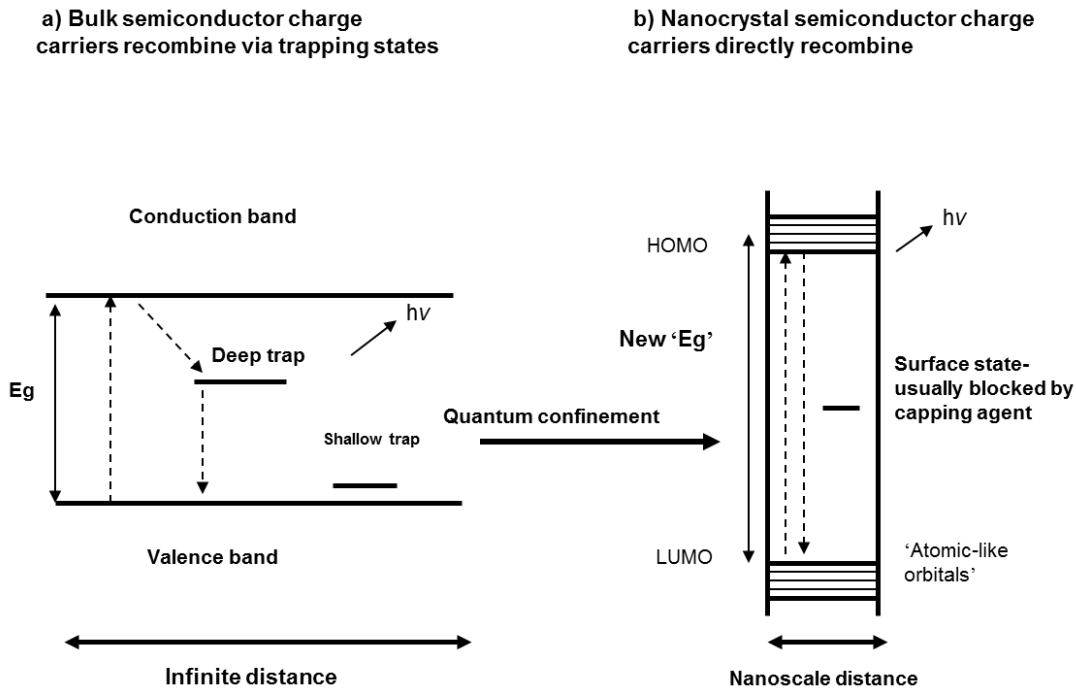


Figure 1. Spatial electronic state diagram for (a) bulk material and (b) nanomaterial semiconductor displaying the quantum confinement effect.⁷⁵

1.2.1. Optical properties

The most exciting aspect of nanomaterials is their novel optical properties, which vary from those of bulk materials. Applications based on optical properties of nanostructured materials include optical detector, sensor, solar cell, photocatalysis and biomedicine. Optical properties of nanocrystals depend on factors such as size, shape, surface characteristics, and additional variables including doping and interaction with the surrounding environment or other nanostructures. Similarly, shape can have an intense influence on optical properties of metal nanostructures. Figure 3 shows the effect of size on the optical properties of a metal (gold) and semiconductor (CdSe) nanoparticles. While the fluorescence spectra of CdSe, nanoparticles change color from blue at 2.3 nm through green to red at 5.5 nm, the color changes only faintly for gold nanoparticles as they increase in size^{76,77}. Nevertheless, the optical properties of nanoparticles change intensely when an anisotropic shape such as the growth of nanorods is added to the nanoparticle because the increase in the size of the materials leads to the increase of the surface/volume ratio. The surface states near to the band can interact with the intrinsic states, resulting in the variation of the energy

levels of nanomaterials. Moreover, due to decrease in the sizes, a large number of atoms are dropped off from the surface of the materials, which leads to an increase in the surface energy.

Some nanostructured materials present unique optical properties because of quantum size effect and this generally happens when the single nanocrystal dimensions are smaller than the de Broglie wavelength, where dipoles are formed by the merging of electrons and holes, leading to the formation of discrete energy levels²¹. The Fermi level of a body is a thermodynamic quantity, whose significance is the thermodynamic work required to add one electron to the body⁷⁸. In metal nanoparticles, Fermi level exists at the centre of the energy band with slight energy level spacing, thus guiding their optical and electrical properties to look like those of continuum. Whereas in the case of semiconducting nanomaterials, Fermi level exists between two energy and the band edges govern the low energy optical and electronic properties (Figure 2).

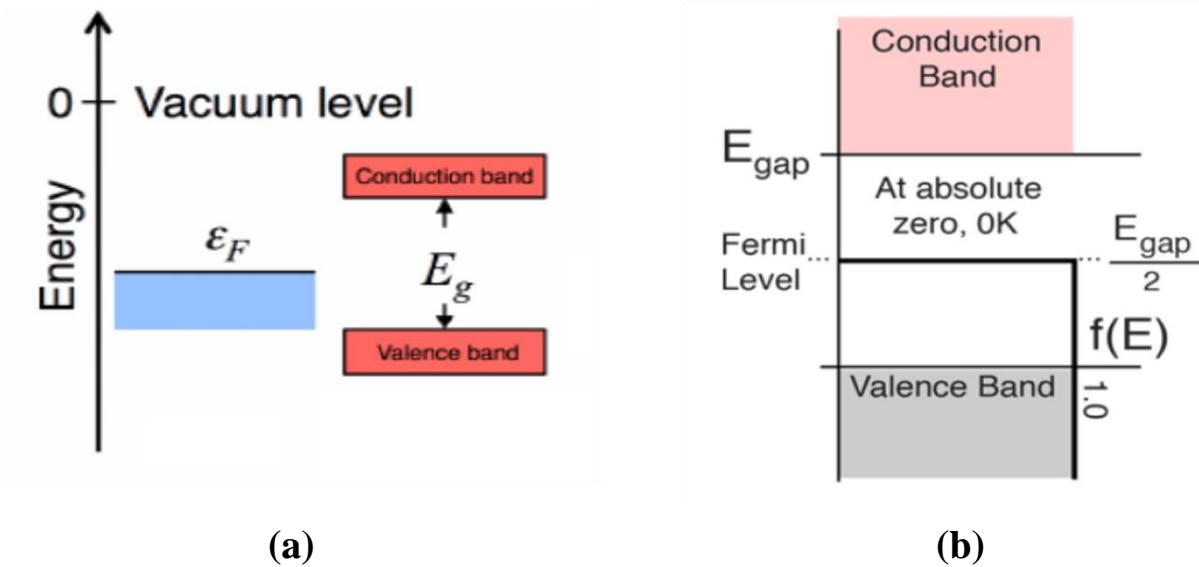


Figure 2. Schematic illustration of Fermi level context in (a); metal and (b); semiconducting nanomaterials.

Therefore, optical excitations depend on the size of the nanomaterial and this is the reason why with semiconducting nanomaterials, decreasing size leads to an increase in the energy gap due to the shifting of the absorption band in the direction of higher frequency region. This phenomenon is called ‘quantum confinement effect’. The energy difference between the completely filled valence band and empty conduction band is called ‘energy separation’^{79,80}. In the same way, some

reports on CdS nanoparticles have shown the presence of a red emission (± 700 nm) due to sulfur vacancies, and free-carrier recombination giving increase to a weak green fluorescence (515 nm)⁸¹. This can be prevented or reduced by the use of a capping group thus decreasing the possibility of charge carriers being imprisoned. This also includes capping of the quantum dots using materials with a higher band gap, for instance the preparation of cadmium sulfide (CdS) coated with CdSe nanoparticles²³, as well as the use of coordinating solvents.⁸²

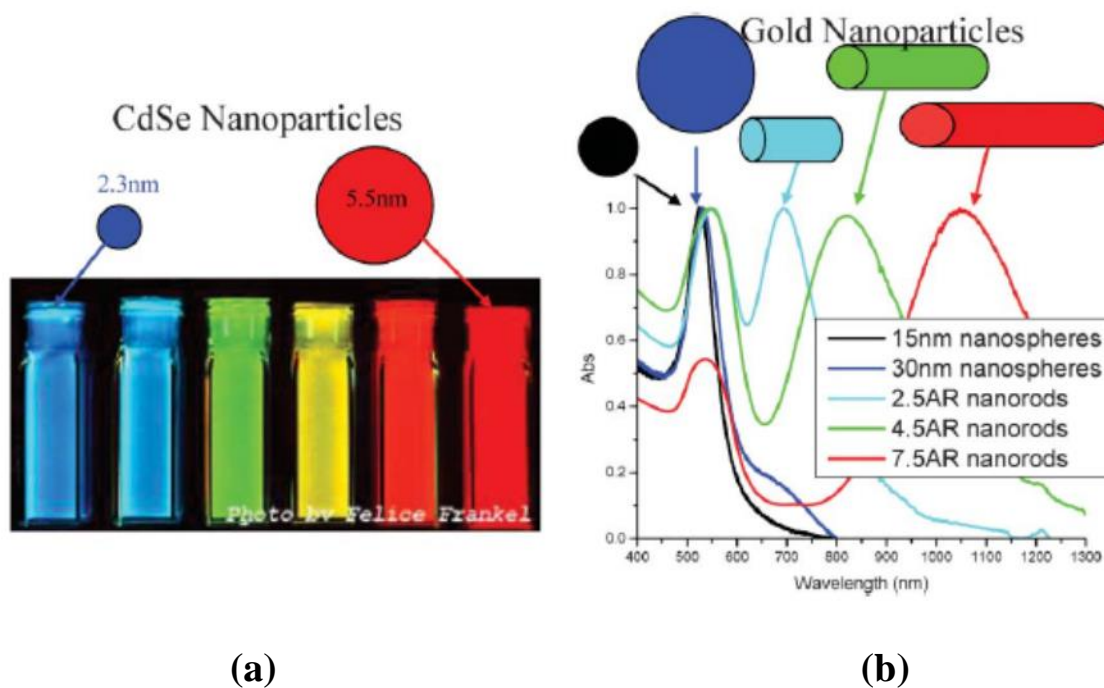


Figure 3. Fluorescence emission of (a); (CdSe) ZnS quantum dots of different sizes and (b); absorption spectra of different shapes and sizes of gold nanoparticles.⁷⁶

1.2.2. Magnetic properties

Like optical properties, factors such as size, shape, stoichiometry, crystal structure and interparticle interactions have an influence on the magnetic properties of nanomaterials. The intrinsic magnetic properties (saturation magnetization, coercive force and curie temperature) hang only on their composition and crystallographic structure in bulk materials while in nanomaterials, these properties are influenced by dimensional and surface effects. The progress made in the study of nanostructured materials has provided the opening to investigate the magnetic properties from the

bulk to the atomic scale. Thus, super paramagnetism, high magnetic coercivity and quantum tunneling are new properties occasionally displayed by these magnetic nanocrystals.⁸³

Magnetism results from magnetic moments related to individual electrons. Magnetic moments are from two major sources: ‘‘electron orbital motion and electron spin’’ (Figure 4), where the sum of these moments from electrons gives the net magnetic moment. Likewise, the magnetic property of a nanocrystal is also influenced by the response of electron and magnetic dipoles to an applied magnetic field and they are classified in different types including diamagnetism, paramagnetism and ferromagnetism.

In diamagnetism, there is no production of intrinsic electron magnetic moments. In paramagnetism, the atoms or molecules of the material have net orbital or spin magnetic moments, which are proficient of lining up in the direction of the applied field. Paramagnetism commonly happens in all atoms and molecules with unpaired electrons, nevertheless the force of the magnetism is small. In ferromagnetism, the materials display permanent magnetism without applying external field. Therefore, they create spontaneous magnetization essentially owing to the quantum mechanical exchange interaction. For instance, the magnets synthesized from yttrium-cobalt-samarium nanoparticles exhibit exceptional magnetic properties because of their high surface area⁸⁴. As a result, the nanostructured materials find several applications in biotechnology and automobile alternators, motors for ships, magnetic resonance imaging (MRI) in medical diagnosis and ultra-sensitive analytical instruments.⁸⁵

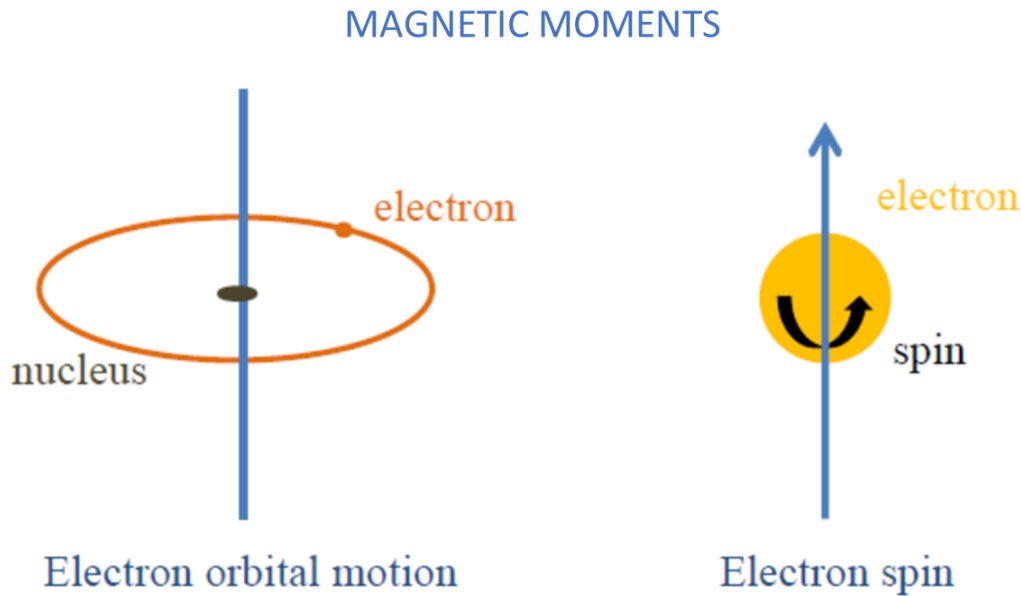


Figure 4. Magnetic moments rising from electron orbital motion (left) and electron spin (right).⁸⁶

1.3. Surface passivation of nanomaterials

In general, nanostructured materials have a large surface area and frequently form agglomeration because of the van der Waals attractive forces and the tendency of the system to reduce the total surface or interfacial energy. The agglomeration is composed of coagulation and flocculation, where coagulation is the formation of strong or compact crystallites and flocculation is the formation of a loose network of aggregates. The agglomeration of particles generally occurs during synthesis, drying, manipulating etc... Therefore, unwanted agglomeration needs to be avoided during synthesis and manipulating stages since monodispersed particles are usually required for several applications⁸⁷. Hence, surfactants are used as dispersants throughout the synthesis in order to produce non-agglomerated particles. A surfactant is an agent having an active surface, which can be partially soluble and possibly will reduce the interfacial tension via expanding upon the surface. A surfactant has an amphipathic structure composed of two constituents: a lyophobic group (solvent repulsive) and lyophilic group (solvent attractive). It can be anionic, cationic, zwitterionic (carrying both positive and negative charges), or non-ionic (carrying no charges). The

quality of a surfactant is estimated by its ability to reduce the surface steric barrier of a rising crystallite, displayed in the growth kinetics⁸⁷. The coordinating solvents (capping agents) typically behave as Lewis base compounds and covalently bound to surface metal atoms. They can either be a layer of a different material epitaxially grown onto the surface of the particle, or an organic group bonded directly to the surface⁸. So far, two principal approaches have been proposed for the surface derivatization of nanocrystals. The first approach is the growth of a second phase on the surface of a colloiddally synthesized material, referred to as an activation step. Examples include the post-treatment of CdS with hydroxy groups to form Cd(OH)₂, or the use of ligands like thiolates²¹ (Figure 5). Surface derivatization decreases the surface defects and therefore improves the possibility of electron-hole recombination. The second approach focuses on the derivatization of nanoparticles with solvent molecules, such as synthesizing nanoparticles from inorganic compounds, using tri-n-octylphosphine oxide (TOPO) as the solvent, which may then be replaced for alternative ligands like pyridine. Rossetti et al.⁸⁸ have previously reported a method for the fabrication of CdS nanoparticles by the controlled nucleation of CdS on mixing of dilute aqueous solutions of cadmium sulfate (CdSO₄) and ammonium sulfide ((NH₄)₂S). Similarly, Kortan et al.⁸⁹ synthesized CdSe capped, zinc sulfide (ZnS), ZnS/CdSe, and CdSe/ZnS nanoparticles from the inverse micellar solutions by addition of organoselenides (Silylchalcogenide chemicals) where they could control the growth of CdSe nanoparticles.

However, the selection of a surfactant should be done by taking into consideration many factors since they are different from each other. For instance, a molecule that binds tightly to the surface of the particle is not desired because it would affect the growth of the particle. While a softly coordinating agent would produce large crystals or aggregates. Therefore, for a perfect surface coating⁹⁰, some basic conditions such as preventing undesirable aggregation throughout chemical synthesis and the long-term storage, good solubility while maintaining the functionalities of the nanomaterials should be met. Chen and co-workers prepared an oleic acid (OA) capped lead sulfide (PbS) nanoparticles in which the effect of the capping agent has been clearly examined (Figure 6).⁹¹

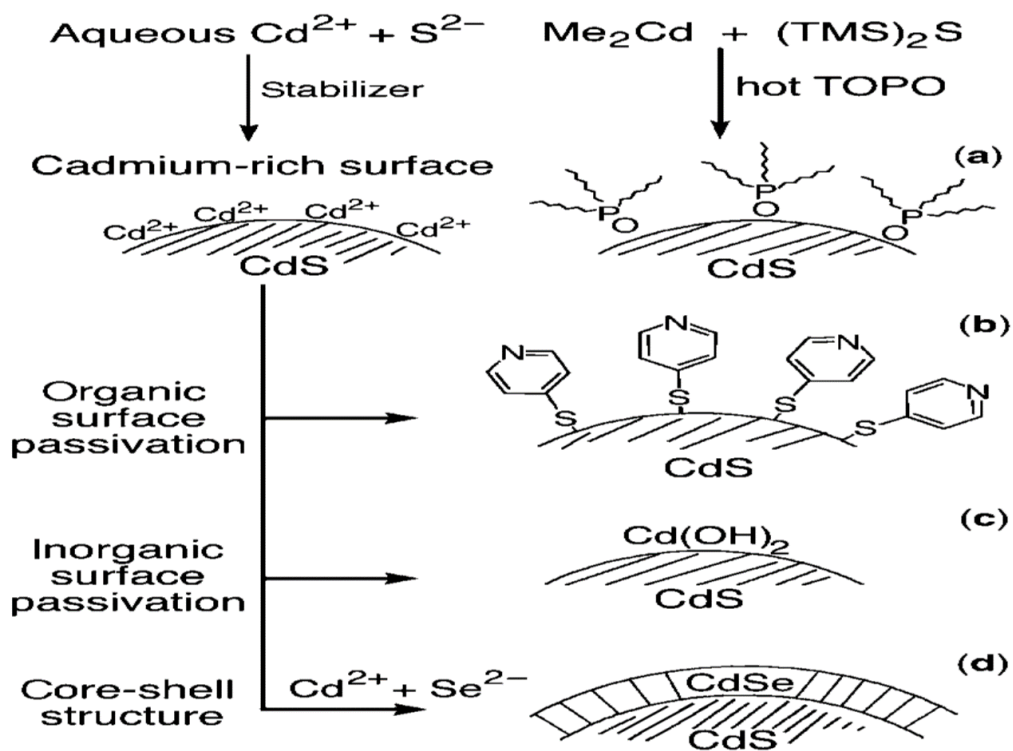


Figure 5. Scheme showing semiconductor nanoparticles capped with (a) TOPO, (b) an organic ligand, (c) inorganic ligand, and (d) a layer of a secondary semiconductor material.⁸

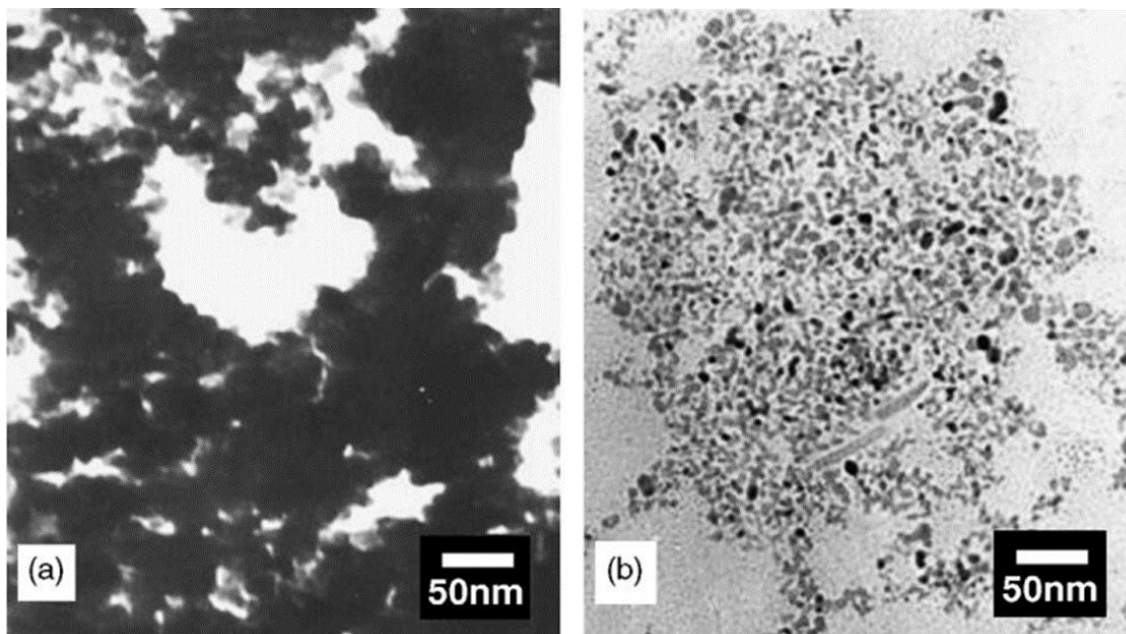


Figure 6. TEM images of: (a) non-capped PbS nanoparticles and (b) OA-capped PbS nanoparticles.⁹¹

1.4. Synthesis of nanomaterials

Over the past few years, a lot of progress has been made in the synthesis of semiconductor nanomaterials (nanoparticles and thin films) owing to their incredible applications in electronics, catalysis and biomedicine, since their morphology and size have an effect on their physical, chemical and biological properties at the nanometer range. A lot of progress has been made in the synthesis of materials in the nanoscale with better properties. Two approaches have attracted the attention of researchers in the preparation of advanced nanostructured materials namely, the ‘bottom-up’ and ‘top-down’ processes. The bottom-up approach consist of assemblies of atoms to produce nanosized and monodispersed materials. While the top-down approach breaks down or dis-assembles molecules to produce nanosized materials. Numerous synthetic procedures have been developed using both the bottom-up and top-down processes as seen in Figure 7. However, the bottom-up process is more advantageous because the control of the shape, size and crystallinity of nanomaterials is easier than when the top-down approach is employed. Moreover, the bottom-up process is easy and cheap and the nanoparticles synthesized are of high quality, monodispersed and have adaptable surface properties. This is confirmed by the model of variation of concentration

of Lamer and Dinegar. It includes three stages of which the first stage represents the formation of uniform particles by diffusion, while the second stage represents bigger size particles formation by the aggregation of smaller subunits, while stage three represents the formation of large particles by Ostwald ripening.^{92,93}

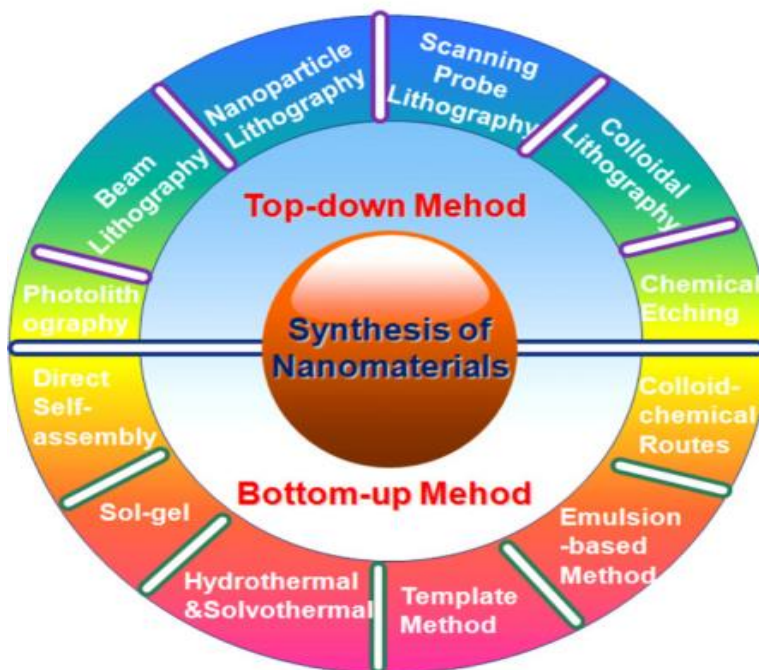


Figure 7. Scheme showing the various synthetic methods of Top-down and Bottom-up for synthesis of nanomaterials.

The first ‘‘top-down’’ route for the synthesis of nanostructured materials involves and includes size reduction of macroscopic units by physical techniques such as ball milling, arch discharge, spray pyrolysis and mechanical deformation. While the ‘‘bottom-up’’ approach involves the association of microscopic units by chemical routes and include hydrothermal, electrodeposition, chemical vapor deposition, sonochemical etc. Nanochemists generally use bottom-up methods over the top down approach for the synthesis of nanostructured materials. This is simply due to the fact that the top down route usually leads to the imperfection of the surface structure⁹⁴. Therefore material scientists have developed several methods to prepare nanomaterials of various shapes such as quantum dots, cubes, spheres, polyhedrons (0-D); rods, wires, tubes (1-D) and

prisms, plates, sheets, thin films (2-D) for the desired properties targeted to particular applications.^{1,7,95}

For the synthesis of group II-VI nanomaterials in particular, two chemical routes are known for developing nanomaterials. The first method is the conventional approach in which separate group II and VI precursors are employed either as elemental or molecular species. The second method includes the use of a single source precursor²¹. The use of single source precursors (SSPs) offer numerous key advantages over other synthetic methods such as the presence of preformed bonds and its ability to provide material with less defects and/or better stoichiometry⁹⁵. Preferably, synthetic chemical routes should result in the production of pure, monodispersed, crystalline particles stabilized from the surrounding chemical environment by a capping group. Various synthetic methods have been used for the preparation of metal sulfides nanostructures using inorganic compounds as molecular precursors. These methods include precipitation route, solution phase thermal decomposition, chemical vapour deposition and solventless methods.^{9,23,35,36,96-98}

1.4.1. Precipitation route

The main method of preparation of semiconductor nanoparticles was, until recently, classical colloid chemistry, involving controlled arrested precipitation from colloidal solutions^{88,99,100}. This is achieved by performing a precipitation reaction in a homogenous solution in the presence of stabilizing agents in order to favor the growth of nanocrystals and prevent them against agglomeration. Lamer and co-workers reported on the synthesis of highly monodispersed colloids and they suggested that nanosized particles can be easily synthesized if the nucleation and growth processes are well controlled⁹². The diagram known as the Ostwald ripening diagram illustrates that small particles, which are unstable, dissolve and then recrystallized to produce larger and more stable particles (Figure 8). In this diagram, the formation of the nuclei (seed) is readily started firstly by a rapid increase of the monomer concentration in the solution until a super saturation level, then secondly the growth of the particles from nuclei results in a progressive decrease of the monomer concentration and finally the coordinating solvents stabilize the surface of the resulting nanoparticles. We simply note that in this process, the control of reaction conditions and the crystalline phase is difficult to determine the final morphology of the nanocrystals.⁹³

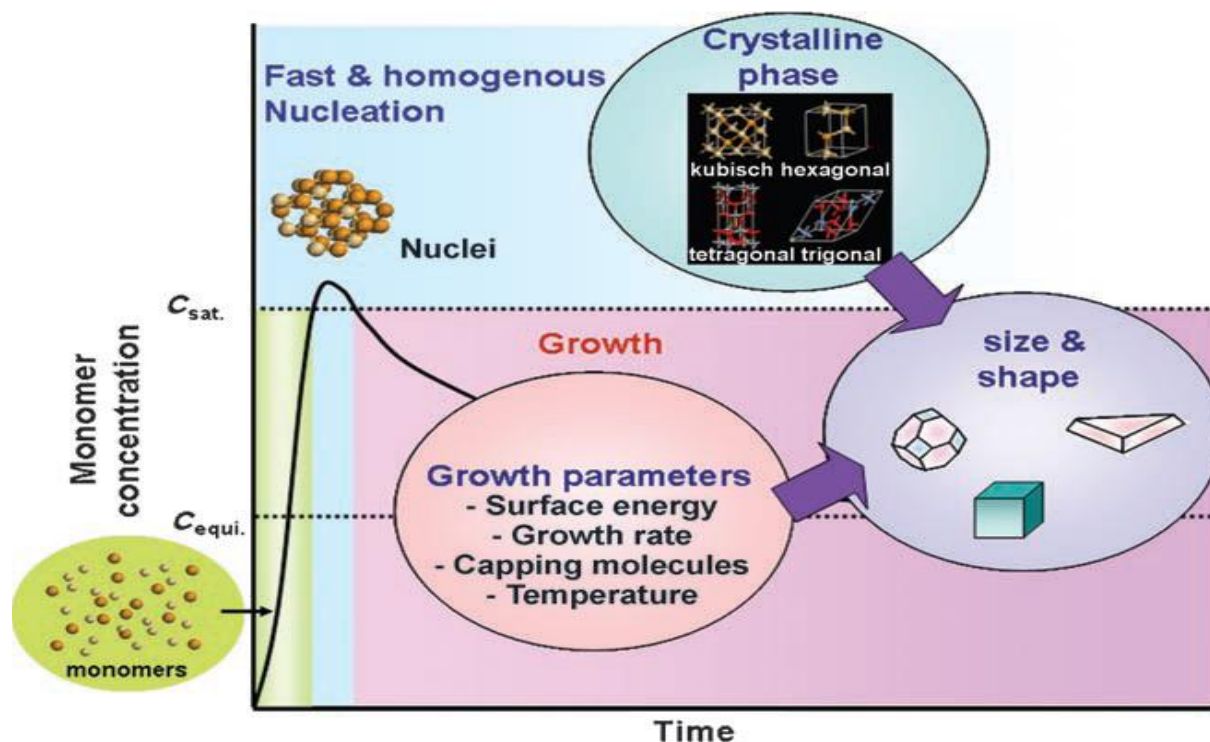


Figure 8. Process of the crystal growth of colloidal nanoparticles (Ostwald ripening).⁹³

The size of the crystals formed through this route depends on numerous variables such as the nature of precursor and concentration, reaction temperature, pH of the solution and capping agent. For instance, Rossetti and co-workers reported the preparation of CdS nanoparticles, involving the reaction between aqueous solutions of CdSO₄ and (NH₄)₂S, and they have determined the particle size by varying the nucleation kinetics by the control of pH.⁸⁸

Nevertheless, although the precipitation method works well and is the first route used for the preparation of high quality semiconductor materials, it is still problematic compared to other methods owing to air sensitivity and poor crystallinity of the materials.⁸

1.4.2. Solution phase thermal decomposition or the hot injection route

The thermal decomposition of precursors can be carried out in the solid, liquid and gas phase, although solution phase decomposition (single source precursor route) is undoubtedly the most extensively synthetic route used and it is our focus in this thesis. The difficulties related to the low temperature precipitation method could be overcome by the dissolution of molecular precursors in

a high boiling point solvent, followed by its decomposition at high temperature (from 200 to 300 °C).

The Hot injection method means the injection of reagents into hot solvents that involves the rapid nucleation and cooling below the solubility product.

1.4.2.1. Dual source precursor route

This method was pioneered by Bawendi and co-workers for the preparation of high quality cadmium chalcogenide CdE (E= S, Se and Te) quantum dots. They reported the injection into hot TOPO (tri-n-octylphosphine oxide) of a volatile dimethyl metal (Me_2M , M= Cd or Zn) and a chalcogen source which were previously dissolved in TOPO. Whilst for the selenium containing crystals, tri-n-octylphosphine selenide (TOPSe) was produced from dissolving selenium compound in TOP (tri-n-octylphosphine), as shown in (Figure 9). The rapid injection of TOPSe involves super saturation and the formation of seed. This is proceeded by a slow crystal growth, resulting in the production of passivated particles by the TOPO and/or TOPSe which coordinate to the surface metal atoms upon the crystal^{22,101}. Some compounds can be replaced with other organic molecules having different functional groups. Some examples of capping agents employed include tri-n-octylphosphine sulfide (TOPS), tri-n-butyl phosphine, pyridines, tris-(2-ethylhexyl)-phosphate and furans.^{102,103}

Generally, this chemical method gives high quality particles, having a low number of defects. Nonetheless, the reaction conditions are rough and involve hazardous, toxic, and pyrophoric material in the case of metal-alkyls. These compounds are injected into high boiling points solutions (around 350 °C), which would be unwanted for commercial utilization. Since dimethyl cadmium and dimethyl zinc are volatile, toxic and pyrophoric compounds having relatively low boiling points⁸. Consequently, there is need to consider new replacements methods, which are safe and environmental friendly for the fabrication of nanoparticles.

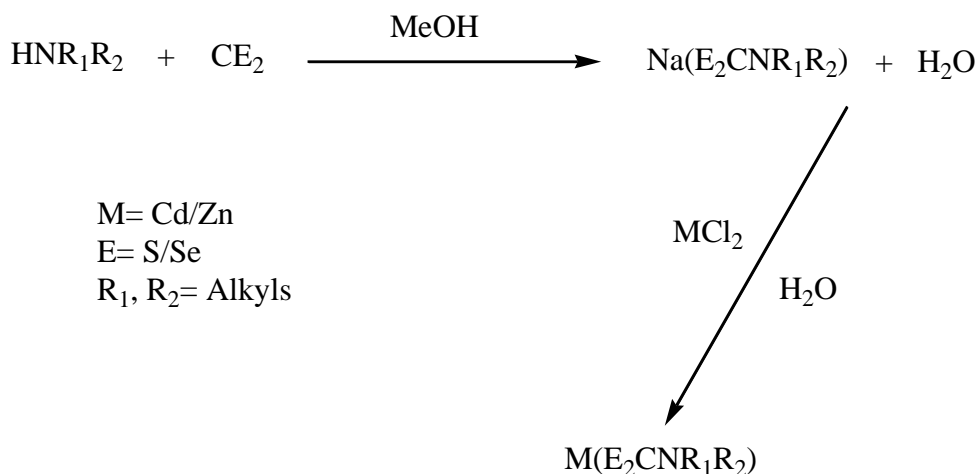


Figure 9. Reaction scheme for the synthesis of molecular precursors.¹⁰⁴

1.4.2.2. Greener precursor route

Ndifon and co-workers reported on low temperature synthesis of PbS and CdS nanoparticles in olive oil. They thermolysed the precursors at a relatively low temperature of 180 °C. The results revealed that distinct cube shaped PbS nanoparticles were obtained with the X-ray diffraction peaks assigned to the cubic rock salt phase. The optical properties of the olive oil capped CdS particles fabricated exhibited evidence of quantum confinement and the CdS particles produced were spherical in shape³¹. Similarly, Revaprasadu *et al*²⁷ described a synthesis and characterization of castor oil and ricinoleic acid capped CdS nanoparticles using single source precursors. The study showed that the optical properties of CdS were typical of particles that displayed quantum confinement effects. X-ray diffraction studies revealed the existence of both cubic and hexagonal phases depending on the reaction conditions. They found that ricinoleic acid capped CdS gave cubic phase particles whereas castor oil capped CdS gave both cubic and hexagonal phases dependent on the reaction temperature and the precursor used. The morphology of the particles varied from oval-short rods to spherical shaped particles with sizes ranging from 10 to 22 nm²⁷. Subsequent study by Bunge and co-workers¹⁰⁵ showed results associated with controlled growth of CdE (E= S, Se and Te) through the pyrolysis of CdO and Cd(OAc)₂, from 0.67 to 1 mole ratio for Cd to E. The work presented that the growth of CdS gave only spherical shaped while CdSe and CdTe gave rod like and tetrapod like shaped particles¹⁰⁵. Masikane *et al*¹⁰⁶ have done further work on castor oil and olive oil-capped In₂S₃ and CuInS₂ nanoparticles from xanthate complexes

using the hot injection method. They demonstrated that the capping agent and reaction temperature have an influence on the morphological, crystallographic and optical properties of the nanoparticles. Rod-like and irregular cubic-like morphologies were obtained in the β - In_2S_3 and CuInS_2 nanoparticles respectively. The crystallinity of the nanoparticles improved significantly with an increase in reaction temperature. They found that band gaps of between 3.5–4.3 eV and 1.15–1.5 eV were estimated for β - In_2S_3 and CuInS_2 nanoparticles respectively¹⁰⁶. This synthetic method is eco-friendly and uses relatively non-toxic chemicals.

1.4.2.3. Single source precursor route

Thermal decomposition of precursors is considered so far as a convenient and effective route to synthesize size and shape controlled nanoparticles¹⁰⁷. The morphology and chemical structure of metal sulfides nanoparticles can be controlled by regulating the experimental conditions such as the reaction time, the reaction temperature, the capping agent and the monomer concentration. Nanocrystalline semiconductor materials are produced by decomposition through injecting a solution of the single source precursor into a high boiling coordinating solvent generally at temperatures over 200 °C. Usually a mixture of tri-n-octylphosphine (TOP) or tri-n-octylphosphine oxide (TOPO) and long chain alkyl amine including oleylamine (OLA), hexadecylamine (HDA) and dodecylamine (DDA) is used, followed by refluxing for a specific duration (Figure 10). The nanocrystals are then separated by precipitating the mixture with ethanol^{9,108}. In addition, single source precursor route has many advantages including their significant volatility and stability to moisture when compared to other synthetic routes (such as colloidal routes and dual source organometallic precursor route)⁶⁰. The thermal decomposition of such compounds produce nanoparticles with great yields. Moreover, purification of the products is easier as only one compound is involved. The key advantages of single source precursor route over other conventional routes using dual sources reside in the fact that, they produce limited pre-reactions and high quality nanoparticles¹⁰⁹. The single source precursor route was used in this thesis owing to its simple nature, efficacy and reproducibility.

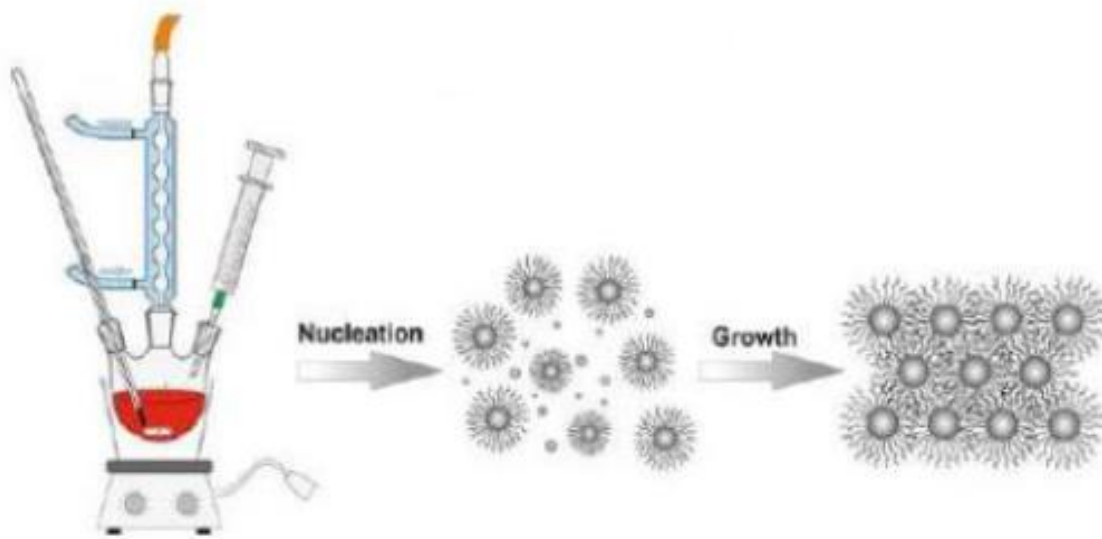


Figure 10. Schematic setup for hot injection route of nanocrystals.¹⁰⁷

1.4.3. Heat up route

This synthetic route has almost same resemblances with the precipitation route designed by LaMer. In this method, all the chemicals are mixed together at the beginning of the reaction. This takes place via monomer accumulation, to nucleation and afterwards to the growth of particle in order to produce nanocrystals²⁶. The reagents are dissolved in a hot coordinating solvent frequently in an oxygen free atmosphere at room temperature, and heated up to the required temperature. The reactions are usually performed during a long time allowing for the whole breakdown of the precursors. Several studies have been done using this route, although this method is more favourable for the fabrication of metal oxide nanoparticles.¹¹⁰⁻¹¹²

1.4.4. Deposition of thin films

A thin film is a layer of material ranging from fractions of a nanometer to several micrometers in thickness. The controlled deposition of thin film materials is a fundamental stage for many applications. Deposition of thin films classically consist of applying a thin film of material onto a substrate (Figure 11). A typical example is the mirror, which has a thin metal coating on the back of a sheet of glass to form a reflective interface. The development of the deposition methods of thin films during the 20th century have enabled a wide range of technological inventions in areas such as magnetic recording media, electronic semiconductor devices, light emitting diodes (LEDs)

and for both energy generation (thin film solar cells) and storage (thin film batteries). In addition, thin films play a significant role in the advance and study of materials with new and unique properties^{113,114}. However, various methods including chemical bath deposition (CBD), chemical vapour deposition (CVD) and atomic layer deposition (ALD) are commonly used for the deposition of thin films. In this work, we have focused on CVD technique because it is more advantageous compared to others since it uses gas phase precursor with very low pressures and also it is a simple, cheap and cost effective process.

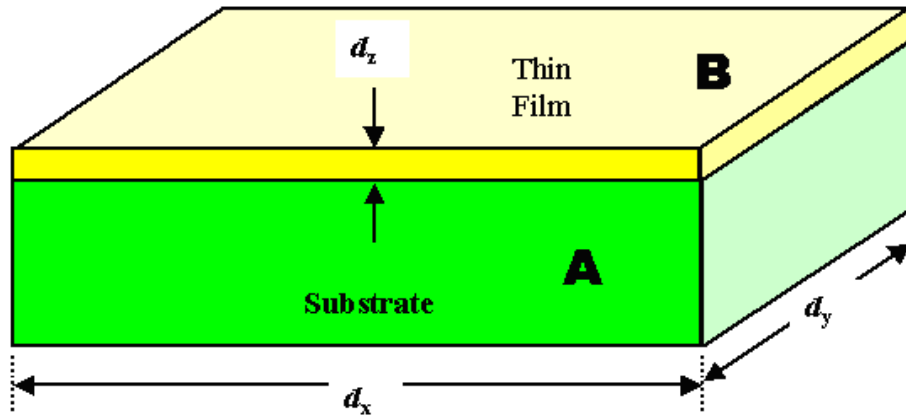


Figure 11. Schematic illustration of a deposited thin film material onto a substrate.

1.4.4.1. Description of chemical vapour deposition (CVD)

Chemical vapour deposition (CVD) is a useful synthetic route employed for the deposition of thin films of a material on a solid substrate. The CVD process consist of the transportation of molecular precursor into the reaction chamber and to the substrate by use of an inert carrier gas like nitrogen or argon, or under vacuum. The process includes important stages such as gas phase reaction of precursors, diffusion of precursors to substrate, surface reaction of adsorbed precursors, desorption and diffusion of by-products, diffusion of atoms to lowest energy substrate sites, nucleation and film growth (Figure 12). The expansion of the CVD method to low-pressure metal–organic chemical vapour deposition (LP-MOCVD), metal–organic chemical vapour deposition (MOCVD) and aerosol-assisted chemical vapour deposition (AACVD) has been driven by the commencement of CVD reactions from diverse sources of energy rather than thermal energy.¹¹⁵

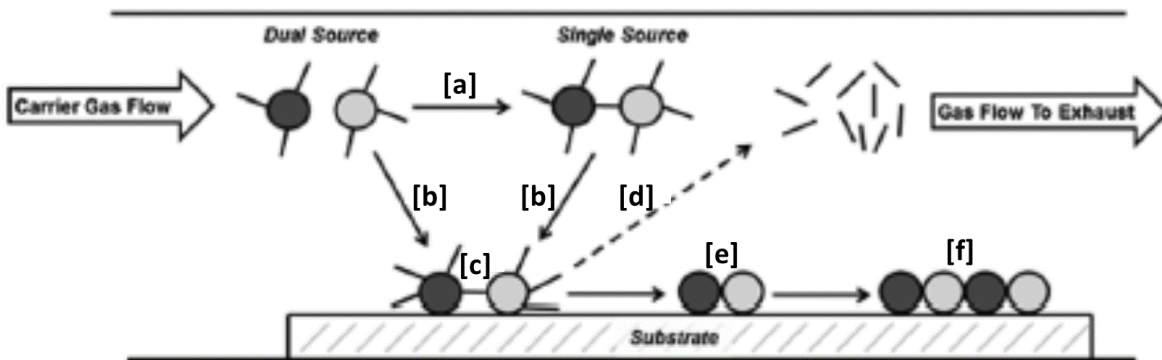


Figure 12. Schematic illustration of the process involved during chemical vapour deposition (CVD): [a] gas phase reaction of precursors; [b] diffusion of precursors to substrate surface; [c] surface reaction of adsorbed precursors; [d] desorption and diffusion of by-products; [e] diffusion of atoms to lowest energy substrate sites; [f] nucleation and film growth.¹¹⁵

1.4.4.2. Low pressure metal-organic chemical vapour deposition

This method uses metal organic complexes as molecular precursors rather than the inorganic precursors used in the conventional CVD. The precursor is expected to be volatile at a temperature below its decomposition temperature. It must also be stable and less toxic for easy usage and storage¹¹⁶. O'Brien and Trindade studied numerous inorganic precursors through sublimation experiments in order to check their volatility and suitability for LP-MOCVD growth. They discovered that $\text{Pb}(\text{S}_2\text{CN}^n\text{Bu}_2)_2$ was the best favorable precursor for the deposition of PbS films.⁹⁵

1.4.4.3. Metal-organic chemical vapour deposition (MOCVD)

This technique consist of depositing films through the decomposition of volatile organometallic precursors in TOP at relatively high temperatures (over 300 °C) and then injected into high boiling TOPO. This leads to the formation of the nanocrystals as an effect of the decomposition of the precursor, where a rapid burst of nucleation followed by Ostwald ripening occurs after the preliminary injection. The resulting nanoparticles are coated with TOPO to prevent agglomeration. The precipitates formed are separated by centrifugation and redispersed in toluene to provide an optically pure solution of TOPO-capped nanoparticles^{117,118}. Zhang et al reported work on this synthetic route where pure PbS microcrystallites with irregular polyhedral, cubic, and fish bone-,

star-, and flower-like morphologies were deposited using lead diethyldithiocarbamate as molecular precursor¹¹⁹. Nevertheless, this technique has some complications such as, the difficulty to control stoichiometry, impurity incorporation, undesirable side reactions and high processing temperature, which might be the origin of the inter-diffusion of layers.⁵⁹

1.4.4.4. Aerosol assisted chemical vapour deposition (AACVD)

AACVD is a liquid-phase variation of the conventional CVD process. In this process, the precursors are dissolved in a solvent from which an aerosol is produced by the use of an ultrasonic humidifier, creating a ‘precursor mist’, which is then transferred to the CVD reactor by a carrier gas (Figure 13). The solvent evaporates once the aerosol reaches the substrate because the increase in temperature leaves the vaporized precursor in its gaseous state, after which deposition onto the substrate can take place to yield the wanted material. Two possibilities exist for the reactions leading to the deposition of film. On the one hand, decomposition of the vaporized precursor can happen in the gas phase leading to the formation of intermediates, which then become adsorbed onto the substrate along with some unaffected vaporized precursor. Extra decomposition and heterogeneous reaction leads to the deposition of generally good quality and well-adhered thin films of the preferred material. On the other hand, if the substrate temperature is too high, decomposition and chemical reaction takes place mostly in the gas phase leading to homogeneous nucleation of particles. The adsorption of preformed particles tends to lead to the deposition of porous films on the substrate¹¹⁵. Though AACVD is not cheap due to the extra cost of solvents and equipment, it overcomes some of the limitations of MOCVD as it is a simple process that offers the advantage of a uniform and large-area deposition. Some researchers like Akhtar et al¹²⁰ reported investigations on the successful growth of PbS thin films on polyimide substrates by this method using $[\text{Pb}(\text{S}_2\text{COBu})_2]$ at temperatures as low as 150 °C¹²⁰. Likewise, Clark and co-workers¹²¹ also reported on the synthesis and characterization of PbS materials using N donor-adducts of ethyl and lead butyl xanthate by this route at a temperature of 200 °C and an argon carrier gas over two hours.¹²¹

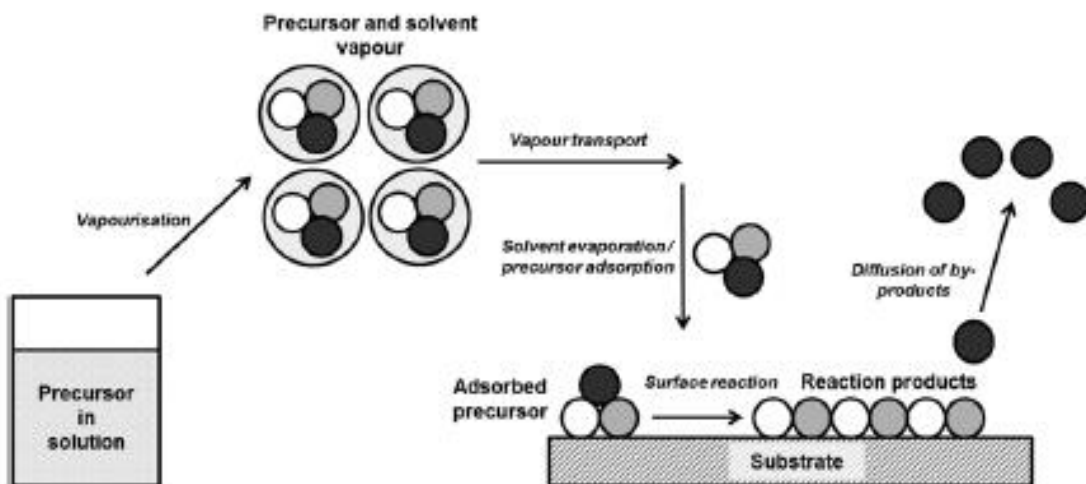


Figure 13. Setup of the AACVD technique.¹¹⁵

1.4.5. Solventless route (Melt method)

The solventless route is a simple melt method in which solid-state breakdown of the metal complexes is performed by an easy heat usage under inert atmosphere. The synthetic method is greatly suitable for scaling up compared to others techniques. The reaction conditions can be simply controlled because of the non-presence of any high boiling solvents or noxious precursors. This makes the production atomic scale nanomaterials to be effective, cheap and environmentally favourable³⁵. In some previous reports, various metal nanoparticles and binary metal chalcogenides with different shapes, such as nanospheres, nanorods, nanowires and nanodisks were formed by the decomposition of reactive melts of diverse single source precursors^{122–125}. Among these complexes, the usage of metal xanthate complexes is beneficial owing to their low decomposition temperature, which leads to the preparation of the desired material in a fairly short time. In addition, the by-products produced by the disintegration of metal xanthate complexes are highly volatile and can be taken away simply, resulting in the formation of materials with good purity and stoichiometric. In this thesis, we set our sights on this method to dope CdS nanoparticles with indium and gallium.

1.5. Single source precursors (SSPs)

A single source precursor is a compound or material that has a metal-sulfur, metal-selenide or metal-telluride bond available. It is used for the preparation of semiconductor nanomaterials. They are of a great importance for technological processing since they are prepared to contain the required elements in their exact stoichiometry and their nature affects the chemical composition, crystallographic structure and morphology of the resulting product. Furthermore, their use leads to the growth of nanomaterials under mild conditions with superior synthetic control over dispersity and crystallinity. Various reports on single source precursors have shown that, they are an effective approach to high quality, crystalline monodispersed semiconductor nanomaterials^{108,117,126}. One of the most important aspect in tuning the properties of a nanostructured material lies in the selection of a good single source precursor. Molecular precursors containing all the elements to be deposited can be suitably used as building blocks for the single-step transformation of molecules into nanostructured materials. The existence of preformed bonds can lead to a product with fewer defects and/or better stoichiometry. Hence, the formation metal sulfide is highly expected due to the presence of preformed metal sulfide (M-S) bonds and the absence of metal carbon (M-C) bonds in these single source precursors. Likewise, most of the single source precursors are air stable and consequently they are easy to manipulate and characterize. Another motivation for the use of single source precursors is their potential to decrease the environmental influence of material processing because of the limited solvent used during preparation. As a conclusion, the choice of a single source precursor should match with the above advantages in order to be a suitable precursor.

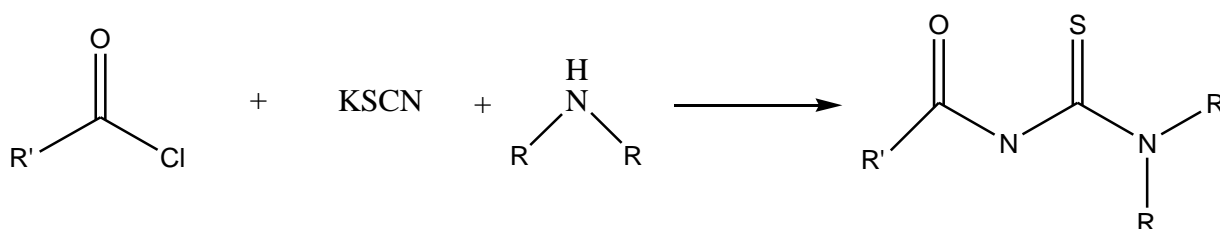
1.5.1. Sulfur based single source precursors

Several single source precursors have been used for the preparation of metal chalcogenide (MS, MSe and MTe) nanoparticles and thin films using different synthetic routes. However, the precursors employed for the fabrication of metal selenide and metal telluride nanomaterials are very unstable and change their form upon moderate heating. In addition, the reagents are highly toxics, dangerous, pyrophoric and very expensive. Whereas indispensable requirements such as nontoxicity, biocompatibility and water solubility of nanocrystals are desirable for instance for medical applications^{22,127,128}. Sulfur based precursors have been widely investigated, because they are less toxic or harmful, and therefore there are still avenues that need to be explored. In this

study, the focus is to explore sulfur based molecular precursors such as sulfur containing ligands to synthesize metal sulfide nanostructured materials.

1.5.2. Thiourea complexes as SSPs

Thioureas are well known ligands and are usually generalized as N,N-dialkyl-N'-acylthioureas; their first synthesis was reported by Douglass and Dains¹²⁹ in 1934. They are easily prepared by reacting acid chlorides with potassium thiocyanate to form acyl isothiocyanate, which on further reaction with an amine yield the acyl thiourea ligand in a simple one-pot method (Scheme 1).¹²⁹



Scheme 1. Global syntheses of thiourea ligand (R'= alkyl, aryl and R= alkyl).

Thiourea ligands easily react with metal salts to form metal complexes and the resulting complexes have been used as molecular precursors. Nair et al¹³⁰ described CdS nanoparticles synthesized by thermolysis using cadmium (Cd) complexes of alkyl-substituted thioureas (N,N'-dioctyl thiourea, N,N'-dicyclohexyl thiourea and N,N'-diisopropyl thiourea) as the sulfur source (precursor). The particles varied in shape from rods (15–25 nm in length) to spheres (up to 8 nm in diameter) showing the wurtzite CdS phase. Their optical properties were depended on their size and shape, which were also influenced by the length of the alkyl chain of the precursor type.¹³⁰

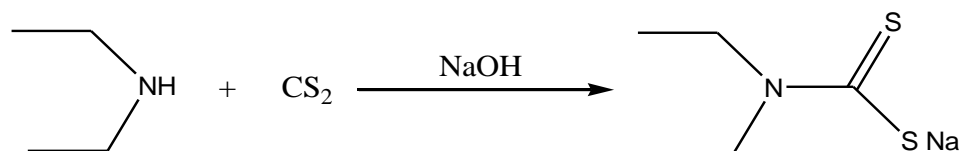
Similarly, O'Brien et al¹³¹ reported on the crystal structure of the copper(II) complex of 1,1,5,5-tetra-iso-propyl-2-thiobiuret [Cu(SO(N(CNiPr₂)₂)₂)₂], which was used to synthesize copper sulfide nanoparticles by solution thermolysis at different temperatures (200-280 °C). The nanocrystals had different morphologies (spherical, hexagonal disks and trigonal crystallites), depending on the reaction temperature, concentration of the complex and growth time. The Cu₇S₄ nanocrystals had a mixture of roxbyite (monoclinic) and anilite (orthorhombic) phases. Djurleite (Cu_{1.94}S) nanocrystals were obtained when a solution of the precursor in oleylamine was injected into hot dodecanethiol. The complex was also used to deposit copper sulfide thin films by aerosol assisted

chemical vapour deposition (AACVD) between 280-400 °C. The diffraction pattern showed predominantly a mixture of cubic CuS and hexagonal Cu₂S phases at all temperatures and the morphology of the copper sulfide thin films were spherical crystallites at 280 °C, cuboids at 320 °C and plate like crystallites between 360 and 400 °C.¹³¹

Moloto and co-workers¹³² also reported on the preparation of Cu_xS_y and PbS nanoparticles from alkylthiourea lead and copper complexes as precursors. They reacted a series of mono- and di-substituted alkylthiourea complexes (H₂NCSNHR and RHNCSNHR; R = CH₃, CH₂CH₃) with lead and copper to obtain PbS and Cu_xS_y nanocrystals with predominantly wurtzite facets shaped like tiny rods. The PbS and Cu_xS_y nanoparticles showed quantum confinement effects with a blue shift in their absorption spectra. Both the copper and lead sulfide nanoparticles had a truncated octahedral shaped, though some of the copper sulfide particles were triangular. The diffraction peaks of the PbS particles were indexed to the cubic rock salt structure, whilst those of copper sulfide particles obtained from the bulk solid matched to a mixture of sulfides of two principal ratios, Cu_{1.8}S (digenite) and Cu₃₁S₁₆ (djurleite).¹³²

1.5.3. Dithiocarbamate complexes as SSPs

Dithiocarbamates are generally prepared by reacting CS₂ with a secondary amine in presence of a base (Scheme 2). Different metal dithiocarbamate complexes have been synthesized and used for the preparation of metal sulfide nanostructures.



Scheme 2. Global syntheses of dithiocarbamate ligand.

Kun *et al*⁵⁷ reported on the synthesis of bismuth sulfide (Bi₂S₃) nanoparticles by thermolysis using catena-(μ₂-nitrate-O,O')bis(piperidinedithiocarbamato)bismuth(III) and tetrakis(μ-nitrate)tetrakis[bis(tetrahydroquinolinedithiocarbamato)bismuth(III)] complexes as molecular precursors. They obtained high quality, crystalline, long and short orthorhombic Bi₂S₃ nanorods whose length depended on the reaction temperature (190 to 270 °C)⁵⁷. O'Brien and co-workers⁴⁹

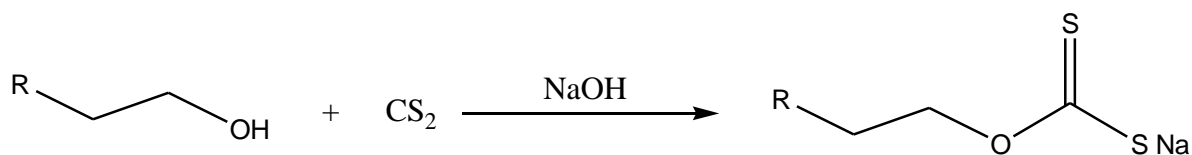
also reported the synthesis of PbS nanocrystallites using a novel single molecule precursor approach and elucidated the single-crystal structure of $\text{Pb}(\text{S}_2\text{CNEtPri})_2$. The results showed that the PbS nanocrystallites had a cubic (rock-salt) structure. They also found that the morphology and size of the synthesized PbS particles were strongly affected by the reaction temperature.⁴⁹

A series of symmetrical and unsymmetrical N,N-dialkyldithiocarbamatolead(II) complexes with the general formula $[\text{Pb}(\text{S}_2\text{CNRR}_2)_2]$ was also used for the synthesis of PbS by thermolysis and AACVD methods by Akhtar *et al*⁵⁹. They discovered that near spherical PbS nanoparticles were obtained at 60 °C, whereas at 80 °C, the PbS particles were cubic. They proposed a mechanism for the growth of spherical and cubic nanoparticles. The quality of PbS thin films deposited by AACVD method was influenced by reaction temperature, where deposition at higher temperatures resulted to an expected change in morphology⁵⁹. Nyamen *et al*^{31,56,108} also reported on the synthesis of multi-podal CdS nanostructures using heterocyclic dithiocarbamato complexes as precursors^{31,56,108}. They prepared two bis(dipiperidinyldithiocarbamato)cadmium(II) and bis(ditetrahydroquinolinyldithio-carbamato)cadmium(II) complexes which were used as molecular precursors for the preparation of oleylamine (OLA), decylamine (DA) and dodecylamine (DDA) capped CdS nanoparticles. They found that the amine capped CdS particles were blue shifted and the CdS crystals had different shapes, which varied with the reaction temperature and ranged from short and elongated nanorods (rods, bipods, tripods and tetrapods) to nanocubes (180 and 270 °C). The powder-x ray diffraction (P-XRD) patterns showed the wurtzite phase of CdS to be dominant⁵⁶. Additionally, Mlowe and co-workers⁹⁶ reported on cadmium dithiocarbamato complexes of piperidine and tetrahydroquinoline for the deposition of CdS thin films by AACVD at 350, 400 and 450 °C. They determined the X-ray single crystal structure of the bis(piperidine dithiocarbamato)cadmium(II) complex. They observed that the particle sizes were in the range between 50–110 nm and 100–220 nm for both complexes. Hence, the deposition temperature influenced the morphology, size and composition of the films.⁹⁶

1.5.4. Dithiocarbonato complexes (Xanthates) as SSPs

Xanthate ligands $[\text{RCOS}_2]^-$ are well known for their different coordination modes including monodentate, bidentate chelating or bridging. They are easily synthesized by reacting CS_2 and an alcohol in presence of a base (Scheme 3). Their properties can be improved by the choice of

suitable O-bond substituents. The metal xanthate complexes have shown interesting thermal properties hence their use as precursor for the growth of metal sulfide nanostructured materials.¹³³



Scheme 3. Global syntheses of xanthate ligand (R= alkyl).

O'Brien and co-workers¹³⁴ have extensively studied these complexes for metal sulfide nanoparticles and thin films using various synthetic routes. They investigated the size and morphological effect of PbS nanocrystals on polymer thin films from lead(II) xanthate and dithiocarbamate complexes. They showed the preparation of lead sulfide from molecular precursors within a polymer matrix to form networks of PbS nanocrystals by spin coating. They explored the effect of the alkyl chain length and showed that the xanthates complexes were more promising precursors giving nanocrystals with controlled sizes and shapes. The lead(II) octyl xanthate complex caused anisotropic growth, forming PbS nanowires within the polymer matrix. The P-XRD analysis of films deposited at various temperatures (80 to 275 °C) showed that the extent of precursor decomposition was temperature dependent, where the more prominent peak positions were indexed to PbS galena 00-005-0592¹³⁴. Recently, McNaughter et al¹³⁵ also investigated the effect of alkyl chain length on the structure of lead(II) xanthates and their decomposition to PbS in melt reactions. They decomposed the complexes at different temperatures (150-200 °C) to form PbS nanocrystals. Microscopic analyses showed that the choice of precursor had an influence on nanocrystal size with longer alkyl chains resulting in smaller cubic nanocrystals. In addition to cubes, anisotropic growth was detected from decomposition of some precursors. P-XRD results revealed that, after 30 minutes at 125 °C, the precursor only partially converts to PbS, while at 150 °C and higher, there is a complete conversion of the precursor to lead sulfide (ICDD # 00-005-0592) within 30 minutes.¹³⁵

In the same way, Mundher et al⁶¹ reported on novel xanthate complexes for the size-controlled synthesis of copper sulfide nanorods. They presented a simple, easily scalable route to monodisperse copper sulfide nanocrystals by the hot injection of a series of novel copper(I) xanthate single-source precursors [(PPh₃)₂Cu(S₂COR)] (R = isobutyl, 2-methoxyethyl, 2-

ethoxyethyl, 1-methoxy-2-propyl, 3-methoxy-1-butyl, and 3-methoxy-3-methyl-1-butyl). They found that the width of the rods was dependent on the length of the xanthate chain and a relationship between the ground-state energy of the precursor and the copper sulfide rod width was established through a computational study⁶¹. At long reaction times (1h), some complexes gave nanocrystals that were exclusively Cu₂S, whereas, at short reaction times (5s), all eight precursors generated Cu_{1.74}S, with a diffraction pattern identical to that of roxbyite (JCPDS 00–064–0278). Hence, the unit cells for the nanoparticles were in good agreement the literature values for the two phases⁶¹. Revaprasadu and co-workers¹³⁶ also described pure phase deposition of flower-like thin films by aerosol assisted chemical vapor deposition and solvent mediated structural transformation in copper sulfide nanostructures. They used bis(O-isobutyldithiocarbonato)copper(II) complex [Cu(SCSOCH₂CH(CH₃)₂)₂] as single source precursor to prepare both copper sulfide thin films and nanoparticles. They deposited copper sulfide thin films by the AACVD method and the nanoparticles were synthesized by hot injection route. The deposited copper sulfide thin films showed different morphologies from spherical to flower or flakes-like crystallites depending on the temperature of deposition. The P-XRD studies of the deposited films revealed the formation of pure covellite-hexagonal phases of copper sulfide, with high crystallinity at elevated temperature. The nanoparticles synthesized in dodecanethiol (DT), and 1-octadecene at 150 °C, 190 °C and 230 °C showed the formation of monodispersed nanoparticles of Cu_{1.78}S roxbyite phase with an average size of ca. 12 ± 1 nm. They discovered that when oleylamine was used as a capping solvent, covellite and digenite phases were obtained at temperatures of 110 °C and 190 °C respectively. Finally, rod shaped particles at 110 and 150 °C were observed, whereas at higher temperatures formation fairly spherical nanoparticles were observed¹³⁶. The deposition of cadmium sulfide and zinc sulfide (ZnS) thin films by AACVD from molecular precursors has also been reported by Memon et al¹³⁷. They used a new set of complexes with a general formula [M(S₂CNⁿ Bu₂)₂] [where M = Cd(II) (1) and Zn(II) (2)] to deposit thin films of cadmium sulfide and zinc sulfide. They found that, thin films of CdS deposited at low temperature (350 °C) consisted of densely packed granular crystallites with an average size of ca. 150 nm, while at higher temperatures (400 and 450 °C) particles with varying sizes and mixed morphologies were obtained. The ZnS thin films deposited at 400 °C showed rod-like structures, whereas dense globular-like structures were obtained at 450 °C. The P-XRD studies of the ZnS thin films deposited at 400 °C showed the formation of hexagonal phase (JCPDS 80-0007), while that of

CdS thin films deposited at various temperatures confirmed the formation of the wurtzite phase (ICDD-2306).¹³⁷

1.6. Critical parameters for growth and shape control of nanomaterials

The synthetic routes for the preparation of nanostructured materials can be classified into three groups. The grinding methods including wet and dry grinding, reactive grinding, gas-phase methods including chemical vapor deposition (CVD), laser ablation deposition (LAD), sputtering techniques and liquid-phase methods including forced hydrolysis, hydrothermal synthesis, sol-gel process and micro-emulsion. Apart from the size, other features including size distribution (as monodisperse as possible), effective suppression of agglomeration processes, and well-directed control of the surface functionalization have to be taken into consideration for the preparation of high quality nanomaterials. Moreover, the applicability of a method can be restricted by limiting conditions for specific compositions and materials properties. With grinding, the degree of agglomeration and contamination by material scratched from the grinding bulk must be estimated. Grinding routes are very important for practical purposes since, they lead to the obtaining large quantities of nanomaterials cheaply.

Gas-phase methods are commonly used as continuous processes that give crystalline nanoparticles with mostly non-covered surfaces. Nevertheless, due to the high synthesis temperatures (above 250 °C), such methods may help in the production of hard crystallites, which are challenging to obtain distinct primary particles. In addition, it can even prevent or hinder the formation of complexes with different phases. The formation of materials, which are metastable under the synthesis conditions, occurs only to a restricted degree. This is because gas-phase reactions are frequently based on thermodynamic control. Whereas with liquid-phase methods, there is an efficient control of particle size and agglomeration behaviour. The reactive surfaces can be protected with functionalized organic molecules, such as stabilizing agents (long chain alkyl compounds or polymers) directly after nucleation¹³⁸. The use of such stabilizers makes it possible to monitor the shape of nanoparticles, resulting in the formation of a wide variety of nanoparticles ranging from simple spheres to lentil like shaped and rod-shaped forms to tetrahedral, octahedral, cubes, or stellate shaped nanoparticles¹³⁹. The use of some high-molecular weight stabilizing agents may however be a handicap due to unwanted effects on the properties and function of the

nanoparticles. The preparation of high quality nanoparticles (those having a well-defined diameter, nearly monodisperse size distribution, and minimum degree of agglomeration) can basically be restricted into two main important conditions. The first one is the directed control of nucleation and nucleus growth and the second is the effective suppression of agglomeration processes. LaMer and Dinegar described nucleation as an endothermic process (Figure 14).⁹²

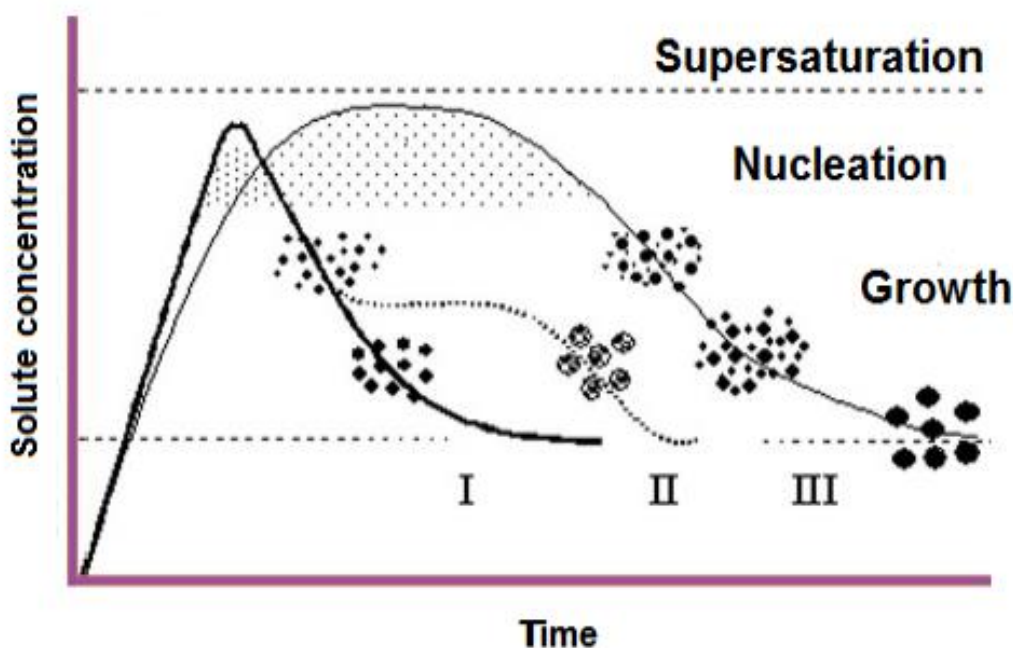


Figure 14. Schematic representation of the mechanism during growth of nanoparticle according to LaMer and Dinegar's model of variation of concentration versus time. Curve I shows formation of uniform particles by diffusion, curve II shows bigger size particles formation by aggregation of smaller subunits, and curve III shows formation of large particles by Ostwald ripening.⁹²

Energy is required to split bonds in the initial compounds, for the removal of solvate shells, and crossing the surface tension barrier of the solvent (endothermic processes). Whilst nucleus growth and Ostwald ripening are exothermic processes since they liberate the enthalpy of formation of the material including lattice binding energy. Therefore, agglomeration of the nanoparticles is also energetically favored, as it reduces surface area and saturates the bonding and coordination sites (Figure 15).

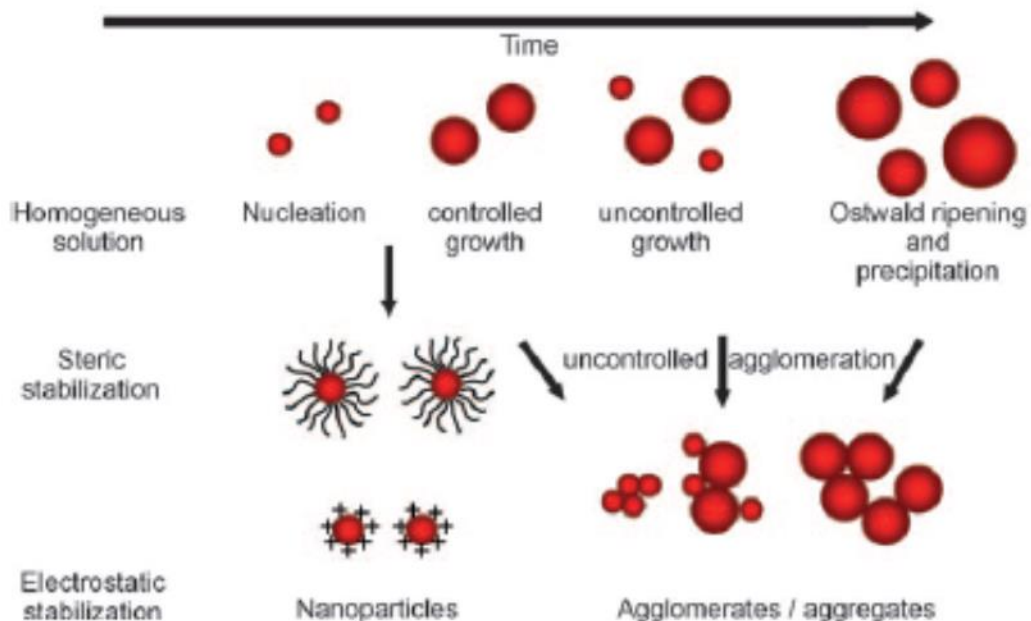


Figure 15. Schematic illustration of growth and stabilization of nanoparticles.¹⁴⁰

The preparation of nanoparticles is easy and nowadays, scientists have developed several methods in order to control reactions conditions. To avoid premature switch from nucleation to nucleus growth, the addition of a certain amount of activation energy (for instance performing the reaction at a higher temperature) is useful. The surfaces of the particles have to be saturated instantly after nucleation by electrostatic or steric stabilization to shield the nanoparticles from further growth or agglomeration (Figure 15). Electrostatic stabilization can be accomplished by targeted adsorption of ions like H^+ , OH^- , SO_4^{2-} , NO_3^- , $RCOO^-$, RSO_3^- and R_4N^+ on the particle surface. Steric stabilization is achieved by adsorption of long-chain organic molecules such as oleyl amine, oleic acid, trioctyl phosphine and trioctyl phosphine oxide¹³⁸. In addition, nucleus growth and agglomeration can also be monitored by complete separation of the reaction spaces. Further control can be achieved by high dilution or by continual removal of the nanomaterials already produced¹⁴¹. The potential of the “hot injection” method for preparing quantum dots has been demonstrated by Bawendi and co-workers.²²

1.7. Applications of semiconductor nanomaterials

Metal sulfide semiconducting nanomaterials have useful applications in several areas such as solar cells, sensing, health care delivery, photocatalysis and environmental pollution control. These applications are talked over in the next subparagraphs and they are because of their very small size being in the nanometer scale.

1.7.1. Solar cells

Solar cells have attracted the interest of many researchers due to attractive technologies that have emerged to substitute fossil fuels. Solar energy does not cause any pollution and it is abundant on earth. For economic reasons, further inexpensive materials (polymers) have been explored to move on from silicon and other costly semiconductors¹⁴². A solar cell is defined as a solid-state electrical device that transforms sunlight energy into electricity by the photovoltaic effect. It is based on a thin film made up of a mixture of inorganic nanostructured materials and a semi-conducting polymer inserted between two charge-collecting electrodes¹⁴³. The organic materials consisting of conjugated polymers absorb light as the donor and transport holes. These conjugated polymers contribute to the ease of processing, low cost, physical flexibility and large area coverage of the semiconductor. The inorganic materials (nanoparticles) are employed as the acceptors and electron transporters in the solar cell assembly. A solar cell is more effective to generate an electric field (heterojunction) at an interface among two different semiconductor materials^{15,144}. This property comes from their optical band since they can be modified through both material selection and quantum confinement and also owing to progress in the synthesis, which permit control over nanoparticle size and shape to improve performance.

1.7.2. Sensing

Over the past few years, a lot of considerable progress has been made in sensor technology. The principle of sensing is based on deposition of semiconductors on selected parts of a chip or on nano-cantilevers, which helps to evaluate gas mixtures by determining solubility, vapour pressure, melting point or reaction of the constituents from a variety of nanobased sensing material (semiconductor nanostructures). A selective tricking of biomolecules or cells through molecular recognition is permitted by biomolecules to perform some sensors^{145,146}. Such a complex miniaturized sensor, which is often termed lab-on-a-chip, requires a high degree of interdisciplinary

cooperation among chemists, biochemists, physicists, materials scientists and engineers. A great deal of collaboration is essential between researchers and scientists to make the production of such reduced composite sensor feasible.

1.7.3. Health care delivery

Semiconductor nanomaterials also provide interesting opportunities in medicine owing to their relatively small size when compared to a cell (10 – 100 μm) or a virus (20 – 450 nm), which allows them to move more or less easily inside an organism. For this, the nanomaterials are usually coated to make them biologically compatible. In other cases, hyperthermia is artificially induced by dispersing magnetic particles through the tissue and then applying an alternating magnetic field of necessary strength and frequency¹⁴⁷. Magnetic nanostructures have been used to improve the contrast of magnetic resonance (MR) imaging¹⁴⁸. Owing to complications in differentiating tumors from normal tissues in the body via a magnetic resonance imaging, patients are frequently injected with contrast agents, like gadolinium chelates and iron particles in order to selectively highlight the tumors. For example, in fluorescence imaging, the energy from an external source of light is adsorbed by the imaging agent injected near the tumor site (Figure 16, step A) and almost immediately is re-mitted at a longer, lower-energy wavelength which is easily detected by the detector (Figure 16, step B).⁷⁴

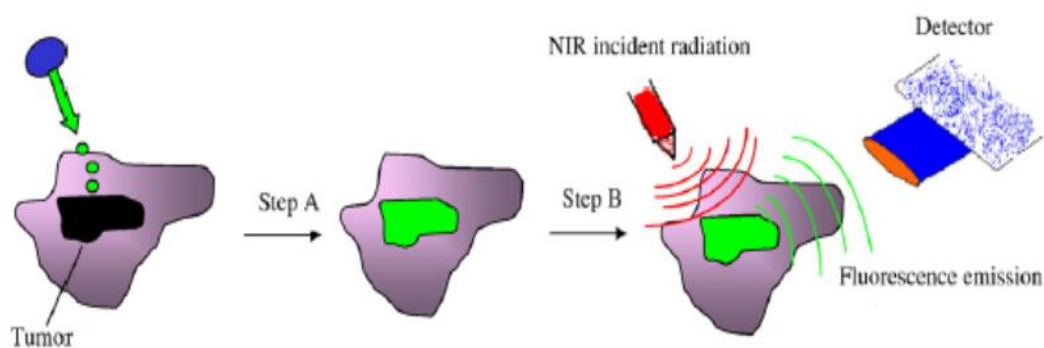


Figure 16. Schematic illustration of the application of the contrast agent on the tumor site (step A) followed by detection of reflected fluorescence emission from the contrast agent (step B).⁷⁴

1.7.4. Photocatalysis and environmental pollution control

Photocatalysis consist of adsorbing the contaminant organic molecules, from air or water, on the surface of semiconductor materials. The photocatalytic activity of nanomaterials has a very high rate compared to conventional materials owing to its higher number of active sites on the surface and its small sizes. The materials that have very small size will get a higher surface area to volume ratio and this makes its surface more active. For instance, nano aluminosilicates have been used as a solid-fuel in rocket propulsion and also as adsorbents to fix toxic transition metal ions for removal from waste¹⁴⁹. In the same way, zinc oxide has also been used as adsorbent for the degradation of chlorinated phenols¹⁵⁰. Nanostructured materials play a crucial role in the removal of organic pollutants from industrial wastes because of their very small sizes, therefore they are much appropriate for catalytic converters¹⁵¹. They are used to transform poisonous gases such as carbon monoxide and nitrogen oxide and also employed in power generation equipment to avoid environmental pollution arising from burning gasoline and coal.¹⁵²

1.8. Statement of the research problem

Over the past few decades, nanochemists have achieved prodigious progress for the effective synthesis of semiconductor nanomaterials. However, there is still a big challenge to produce high quality and shaped controlled nanocrystals. Many reports have proven that electronic properties are greatly dependent on the shape, size, phase and type of the metal chalcogenides precursor. Equally, the choice of the precursor employed depends on the ease of its decomposition, because impurities are included into some precursors after decomposition. Some of the metal chalcogenides nanostructured materials such as copper, nickel, cobalt, iron and manganese have numerous phases, thus, an impurity free pure phase is essential. Despite the exhaustive work reported so far on the use of complexes as precursors for the fabrication of nanostructures, one of the complications in the preparation of nanoparticles is the control of the growth of the particles through the variations of the reaction parameters (precursor type, capping agent, reaction temperature etc.) As a result, there is still need to investigate the effect of these parameters on the preparation of metal containing nanomaterials as novel precursors. In our continuing search for new single source precursors for the preparation of high quality and cheap metal sulfide nanomaterials, we found out that heterocyclic thiourea, dithiocarbamates and xanthates complexes have not yet been well explored for their use as starting materials. Following the interest on these

classes of compounds, our research group have recently investigated the use of heterocyclic benzoylthiourea, heterocyclic dithiocarbamates and xanthates complexes as single source precursors for the preparation of metal sulfide nanostructures.

We sought to enlarge the work on the utilization of dithiocarbamate and xanthate metal complexes as molecular precursors for the synthesis of binary metal sulfide materials. Finally, we doped CdS nanoparticles with indium and gallium at various percentages (0 to 10%) from ethyl xanthates complexes since they have been shown to improve on both the structural and optical properties of nanomaterials. The influence of some parameters (precursor type, reaction temperature and capping agent) on the morphology, crystallographic phase and optical properties of the prepared nanostructured materials was investigated.

1.9. Objectives

In this work, we synthesize ligands as proficient precursors for the production of high quality nanostructures.

1.9.1. Main objective

The main objective of this work is to synthesize high quality metal sulfide (MS) nanomaterials using metal heterocyclic benzoylthiourea, dithiocarbamates and xanthates. In this respect, we set to synthesize novel metal (M= Pb and Cu) morpholine benzoylthiourea, pyrrolidine benzoylthiourea, cadmium dithiocarbamate, cadmium, indium and gallium xanthate complexes for use as efficient precursors for the preparation of high quality PbS, Cu_xS_y , CdS, $\text{Cd}_{1-x}\text{In}_x\text{S}$ and $\text{Cd}_{1-x}\text{Ga}_x\text{S}$ nanomaterials.

1.9.2. Specific objectives

To attain our goal, we set to:

- prepare lead(II) and copper(II) metal complexes from the synthesized heterocyclic morpholine and pyrrolidine benzoylthiourea ligands using the method described by Douglass and Dains¹²⁹. Cadmium(II) complexes are prepared from the synthesized dihexyl, heterocyclic piperidine dithiocarbamate and commercial diethyl dithiocarbamate and ethyl xanthate ligands. In addition, indium(III) and gallium(III) complexes from the commercial ethyl xanthate are synthesized using a route described by Trindade and O'Brien²¹. The

ligands and complexes are characterized by elemental analysis, infrared spectroscopy, ^1H NMR and TGA/DTA analyses. The crystal structures of some of the complexes obtained will be also elucidated.

- use the prepared complexes as molecular precursors to synthesize lead sulfide (PbS), copper sulfide (Cu_xS_y) and cadmium sulfide (CdS) nanoparticles by thermolysis and also to prepare indium doped CdS and gallium doped CdS using the solventless method.
- characterize the metal sulfide nanomaterials by UV-visible and photoluminescence (PL) spectroscopies (determine their optical properties), transmission electron microscopy (TEM) and high-resolution transmission electron microscopy (HRTEM) techniques (for morphology and size) and X-ray diffraction (to elucidate their crystal structure).
- investigate the effect of the precursor type, the temperature reaction and the capping agent on the morphology and size of the synthesized nanoparticles.
- use the various complexes as molecular precursors to deposit PbS, Cu_xS_y and CdS thin films on glass substrate by the AACVD technique.
- use the cadmium, indium and gallium ethyl xanthate complexes to synthesize undoped CdS, indium doped CdS and gallium doped CdS nanoparticles by the solventless technique.
- characterize the deposited thin films, the undoped and doped CdS nanoparticles by: scanning electron microscopy (SEM) technique (morphology), P-XRD technique and energy dispersive X-ray spectroscopy technique (to elucidate their elemental composition)

CHAPTER 2: EXPERIMENTAL METHODS

The different synthetic methods and techniques of characterization used in this work are described in this chapter.

2.1. Reagents

Benzoyl chloride 99%, morpholine 99%, pyrrolidine 99%, potassium thiocyanate 98.5%, cadmium(II) chloride 99.99%, copper(II) chloride 97%, dodecanethiol (DT) 98.5%, gallium(III) chloride 99.99%, hexadecylamine (HDA) 98%, indium(III) chloride 98%, oleylamine (OLA) 98%, tri-n-octylphosphine (TOP) 90%, 1-octadecene 90%, sodium diethyl dithiocarbamate trihydrate 97%, dihexylamine 97%, potassium ethyl xanthogenate 96%, piperidine 99%, carbon disulfide 99.5% and Castor Oil (CO) were purchased from Sigma-Aldrich. Lead(II) nitrate 99%, ethanol 99.5%, acetone, chloroform, dichloromethane, petroleum ether, methanol 99.5%, sodium hydroxide 98%, cadmium(II) chloride monohydrate 99%, tetrahydrofuran and toluene were purchased from Merck. All the reagents were used as received without any further purification.

2.2. Syntheses of the ligands and complexes as SSPs

The heterocyclic morpholine, pyrrolidine thiourea and the heterocyclic piperidine dithiocarbamate ligands with their corresponding Pb(II), Cu(II) and Cd(II) metal complexes were prepared using the methods described by Douglass *et al*¹²⁹ and O'Brien *et al*⁴⁵ which have been summarized in 2.2.1. – 2.2.6 below.

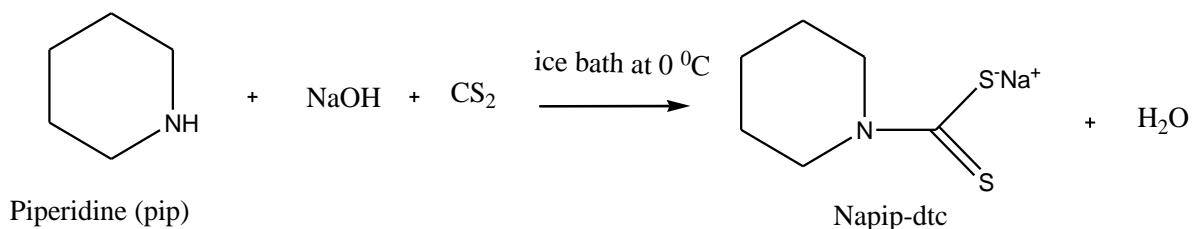
2.2.1. Syntheses of N-morpholine and N-pyrrolidine-N'-benzoylthiourea ligands

Benzoyl chloride (2.0 mL; 17 mmol) was dissolved in 50 mL of acetone and the resulting mixture added dropwise to a suspension of potassium thiocyanate (1.67 g; 17 mmol) in 30 mL of acetone. The reaction mixture was heated under reflux for 30 min, then cooled to room temperature. A solution of the corresponding amine (morpholine/pyrrolidine; 17 mmol) in 10 mL of acetone was added and the resulting mixture stirred for 2 h. Distilled water (250 mL) was added to the resultant solution and the solid product filtered off, then dried in air and purified by recrystallization in ethanol:dichloromethane (1:1) mixture.

2.2.2. Synthesis of sodium piperidine dithiocarbamate ligand

Carbon disulfide (6.0 mL, 100 mmol) was added in small portions to an equimolar mixture of sodium hydroxide (4.0 g, 100 mmol) and piperidine (9.9 mL, 100 mmol) and the mixture cooled in an ice bath at 0 °C. The reaction mixture was stirred at room temperature for 30 min; the solidified mass was then dried in air and recrystallized in a mixture of acetone/petroleum ether. The final compound was washed with chloroform and dried by suction.

The chemical reaction for the synthesis of the piperidine dithiocarbamate ligand is shown in Scheme 4.

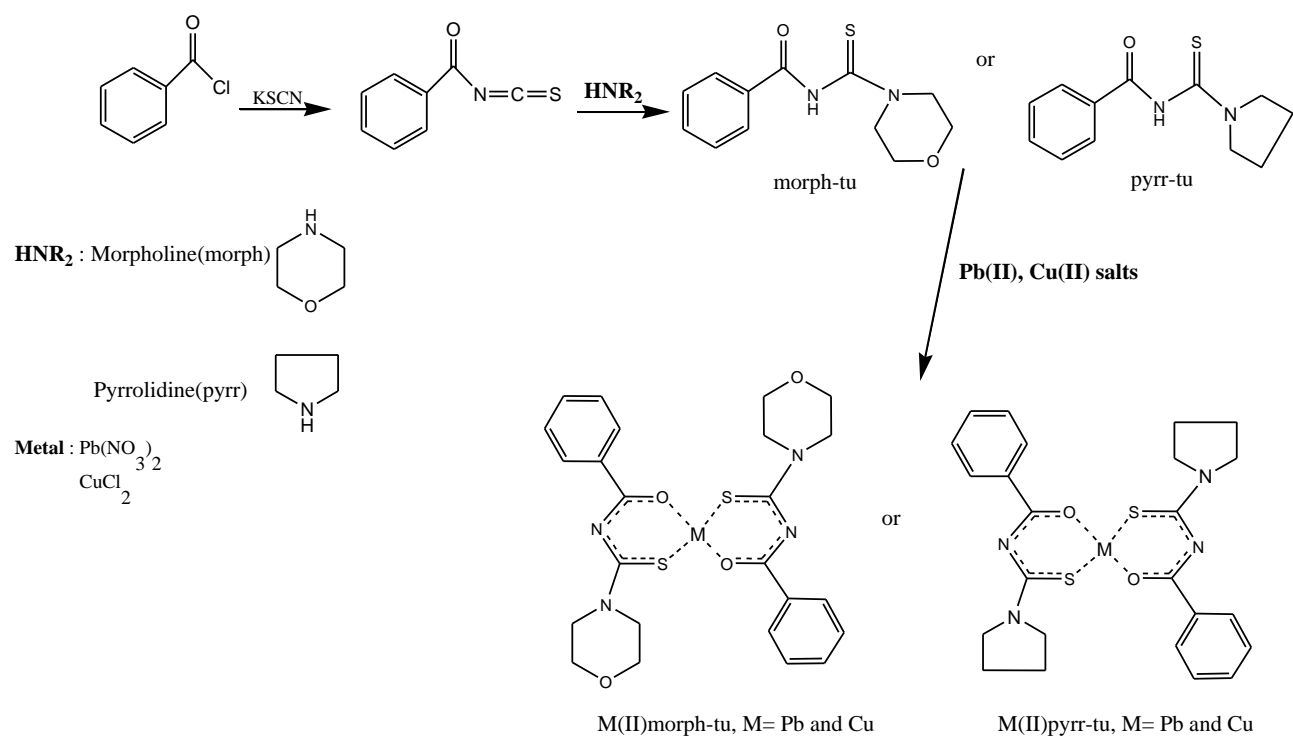


Scheme 4. Chemical reaction scheme for the synthesis of the piperidine ligand.

2.2.3. Syntheses of metal(II) N-morpholine and N-pyrrolidine [M(morph/pyrr-tu)₂] complexes, M= (Pb and Cu)

The metal salt (2 mmol) (lead nitrate and copper chloride) was each dissolved in 20 mL of water and added dropwise to a solution of the corresponding ligand (4 mmol) (N-morpholine and N-pyrrolidine-N'-benzoylthiourea) in 50 mL of ethanol at room temperature. The resulting mixture was stirred for 30 min and the final product obtained was filtered off, washed with distilled water and dried at room temperature, and purified by recrystallization in ethanol:dichloromethane (1: 1).

The chemical reaction for the synthesis of the thiourea ligands and their corresponding Pb(II) and Cu(II) complexes is shown in Scheme 5.

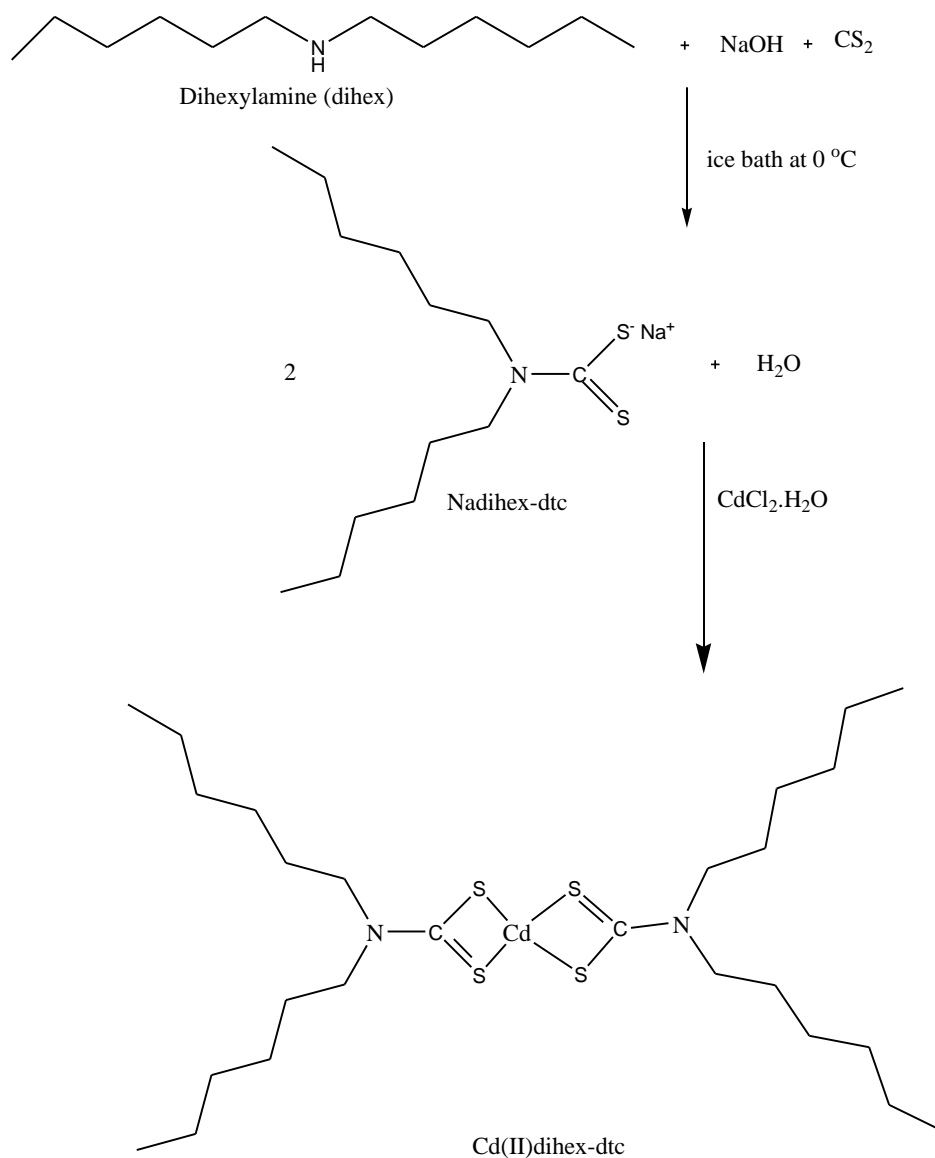


Scheme 5. Chemical reaction scheme for the syntheses of the thiourea complexes.

2.2.4. Synthesis of cadmium(II) dihexyl dithiocarbamate complex

Carbon disulfide (1.2 mL, 20 mmol) was added in small portions to an equimolar mixture of sodium hydroxide (0.8 g, 20 mmol) and dihexylamine (4.7 mL, 20 mmol). The mixture was cooled in an ice bath at 0 °C. After 15 min, cadmium chloride (2.0 g, 10.0 mmol) dissolved in distilled water (30.0 mL) was added dropwise to the corresponding solution of the dithiocarbamate ligand while stirring. The reaction mixture was stirred for 1 h and the precipitate formed was filtered off, washed with excess distilled water and dried overnight at room temperature.

The chemical reaction for the preparation of the dihexyl dithiocarbamate ligand and its Cd(II) complex is shown in Scheme 6.



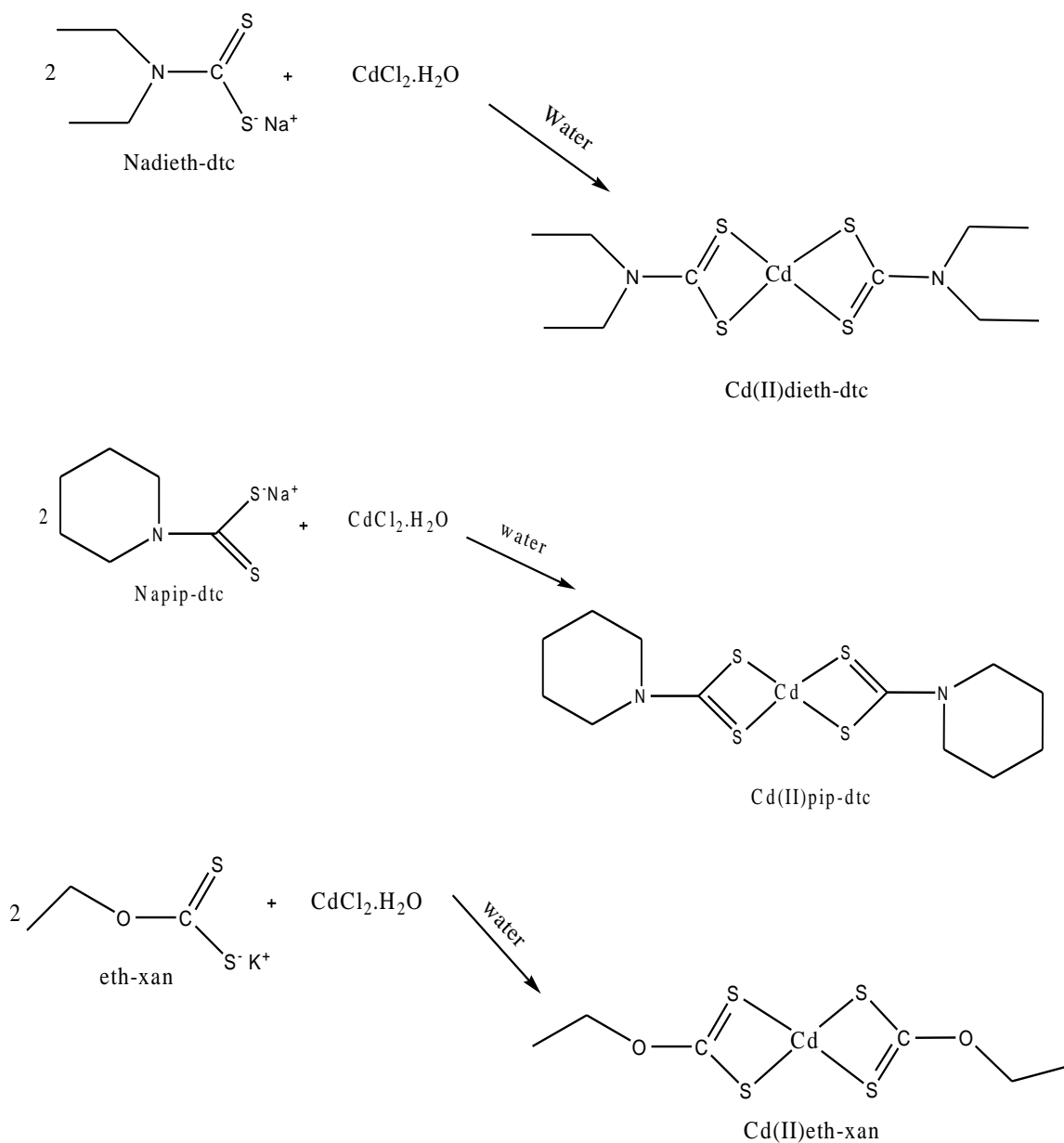
Scheme 6. Chemical reaction scheme for the synthesis of the Cd(II) dihexyl dithiocarbamate complex.

2.2.5. Syntheses of cadmium(II) diethyl dithiocarbamate, piperidinyl dithiocarbamate and ethyl xanthate complexes

Cadmium chloride monohydrate (1.0 g, 5.0 mmol) was dissolved in distilled water (25.0 mL) and the solution added dropwise to a solution of the dithiocarbamate or xanthate ligands (10.0 mmol).

The reaction mixture was stirred for 1 h, and the precipitate formed was filtered off, washed with excess distilled water and dried overnight at room temperature.

The chemical reaction for the preparation of the Cd(II) diethyl, piperidine dithiocarbamate and Cd(II) ethyl xanthate complexes is shown in Scheme 7.



Scheme 7. Chemical reaction scheme for the syntheses of the Cd(II) diethyl, piperidine dithiocarbamate and Cd(II) ethyl xanthate complexes.

2.2.6. Syntheses of cadmium(II), indium(III) and gallium(III) ethyl xanthate complexes

2.2.6.1. Synthesis of bis(ethylxanthato)cadmium(II)

Cadmium chloride (1.83 g, 10.0 mmol) was dissolved in distilled water (20.0 mL) and the solution added dropwise to a stirred solution of potassium ethyl xanthogenate ligand (3.21 g, 20.0 mmol). After an hour, the resulting pale yellowish precipitate was filtered, washed with excess distilled water and allowed to dry overnight at room temperature in air.

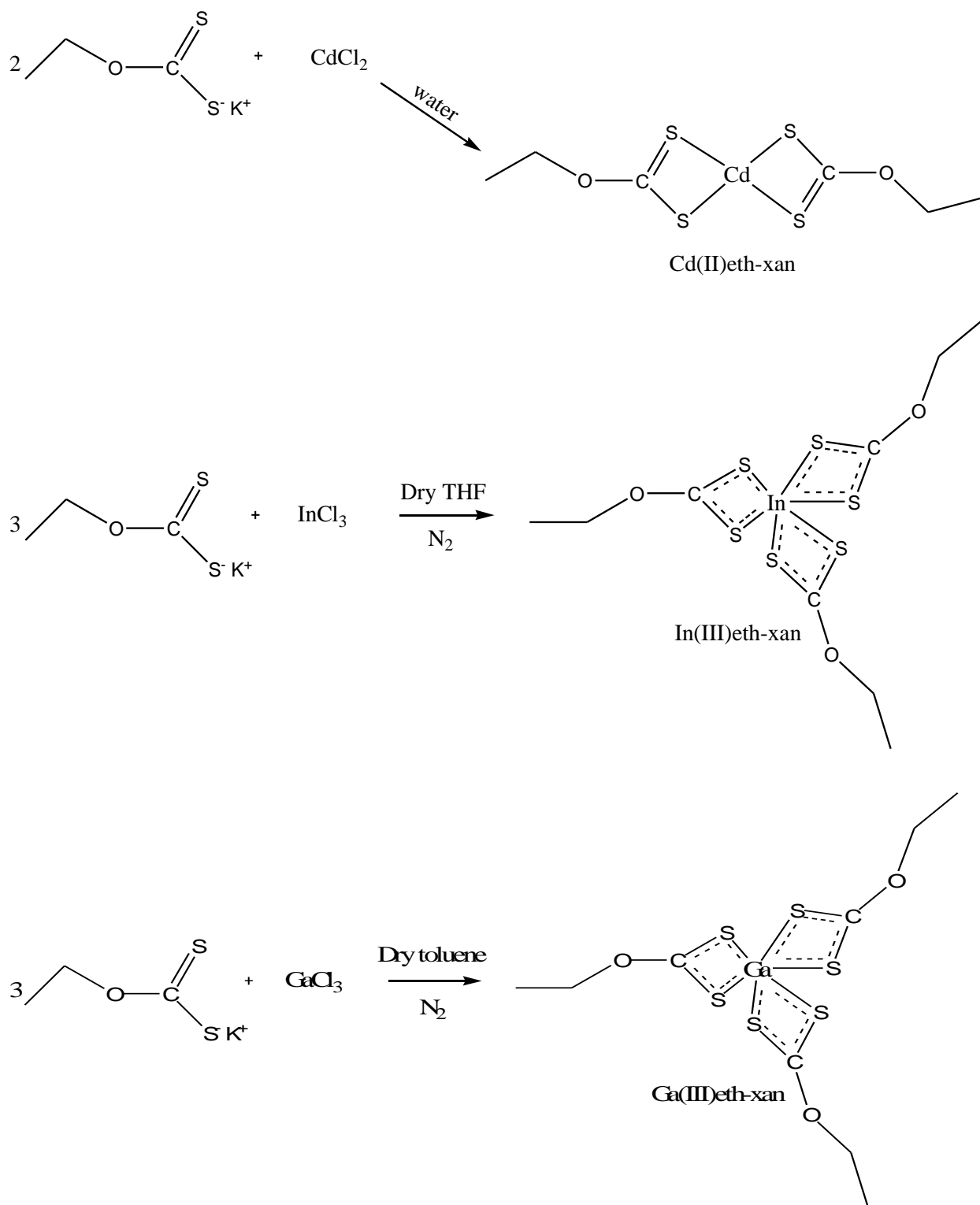
2.2.6.2. Synthesis of tris(ethylxanthato)indium(III)

Potassium ethyl xanthogenate (2.18 g, 13.56 mmol) was dissolved in dry tetrahydrofuran (100 mL) under N₂. A colourless solution of indium(III) chloride (1.00 g, 4.52 mmol) in 5 mL tetrahydrofuran was added dropwise to the potassium xanthate solution and the mixture stirred for an hour. The mixture was then filtered to remove KCl and the tetrahydrofuran was removed *in vacuo*, resulting in a cream coloured powder. The product was recrystallized in chloroform to give colourless crystals.

2.2.6.3. Synthesis of tris(ethylxanthato)gallium(III)

Gallium(III) chloride (2.01 g, 11.40 mmol) was dissolved in 10 mL of dry toluene under N₂. Potassium ethyl xanthogenate (5.50 g, 34.20 mmol) was dissolved in dry toluene (50 mL), added dropwise to the gallium chloride solution and the mixture stirred for three hours at room temperature under N₂. KCl was removed by filtration and the toluene was removed *in vacuo*, resulting in the formation of a cream coloured powder.

The chemical reaction for the preparation of the Cd(II), In(III) and Ga(III) ethyl xanthate complexes is shown in Scheme 8.



Scheme 8. Chemical reaction scheme for the syntheses of the Cd(II), In(III) and Ga(III) ethyl xanthate complexes.

2.3. Syntheses of organically capped metal sulfide nanoparticles using the hot injection route

The lead sulfide (PbS), copper sulfide (Cu_xS_y) and cadmium sulfide (CdS) were prepared from the molecular precursors through the hot injection method as reported by O'Brien and Pickett.³⁷

Figure 17 shows the schematic set up for the preparation of metal sulfide PbS, Cu_xS_y and CdS nanoparticles.

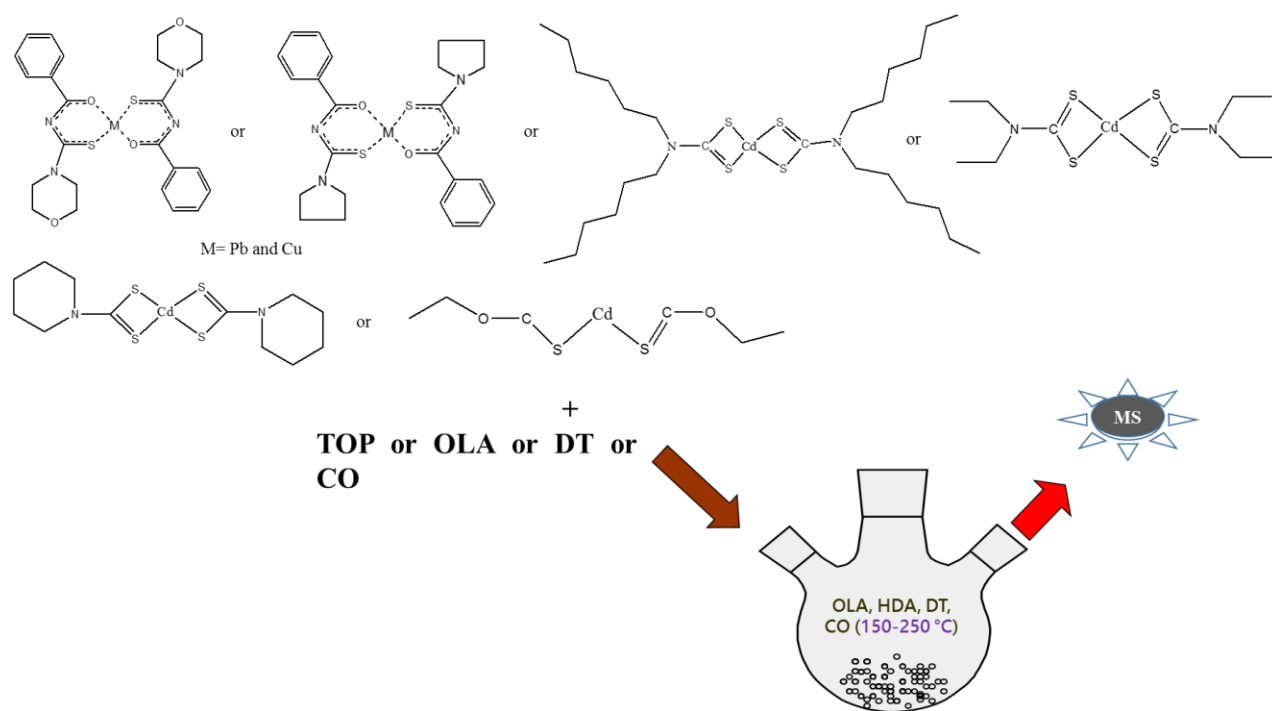


Figure 17. Schematic set up for the preparation of metal sulfide nanoparticles.

2.3.1. Syntheses of lead sulfide (PbS) nanoparticles

A specified amount of 0.3 mmol (0.2 g) of the $[\text{Pb}(\text{morph-tu})_2]$ or $[\text{Pb}(\text{pyrr-tu})_2]$ complex was each dissolved in 3.0 mL of the dispersion solvent (oleylamine or castor oil). The solution was injected into 5.0 mL of hot capping agent (OLA or CO) in a three-necked flask to the desired temperature (150 - 250 °C). The solution turned black and a drop in temperature of 10 - 20 °C was observed, then the reaction was allowed to stabilize to the desired temperature (150 - 250 °C). After a reaction

time of 30 mins, aliquots of samples were taken and methanol was added, resulting in the formation of a flocculent precipitate. The precipitate was separated by centrifugation and then dispersed in toluene to give blackish OLA- or CO-capped PbS nanoparticles (see Image 1).



Image 1. a) Some tubes of synthesized a) OLA-capped PbS and b) CO-capped PbS nanoparticles.

The above reaction procedure is detailed in Table 1.

Table 1. Reaction parameters for the syntheses of PbS nanoparticles

Precursor-Mass (g)	Dispersion solvent (mL)	Capping agent (mL)	Volume of the capping agent (mL)	Temperature of the reaction (°C)	Time of the reaction (min)
[Pb(morph-tu) ₂]-0.2	OLA	OLA	5	150	30
				200	30
				250	30
[Pb(pyrr-tu) ₂]-0.2	OLA	OLA	5	150	30
				200	30
				250	30
[Pb(morph-tu) ₂]-0.2	CO	CO	5	150	30
				200	30
				250	30
[Pb(pyrr-tu) ₂]-0.2	CO	CO	5	150	30
				200	30
				250	30

2.3.2. Syntheses of copper sulfide (Cu_xS_y) nanoparticles

Briefly, 5.0 mL of the capping agent (OLA or dodecanethiol) was placed in a three-necked flask and purged with N_2 , after applying vacuum for few minutes at room temperature, using a Schlenk line to evacuate any air. The capping agent was slowly heated to the desired temperature (150 - 250 °C) and the temperature was maintained for 10 mins. A specified amount (0.35 mmol) of the precursors ($[\text{Cu}(\text{morph-tu})_2]$ or $[\text{Cu}(\text{pyrr-tu})_2]$) was each dispersed in 3.0 mL of the dispersion solvent (OLA and/or DT) and injected into the pre-heated capping agent. Upon injection, the colourless solution turned brownish, and a drop in temperature of 15 - 20 °C was observed, the temperature was quickly maintained to desired temperature (150 - 250 °C). After a reaction time of 30 min, aliquots of samples were taken and methanol was added, this resulted to the formation of a flocculent precipitate. The precipitate was separated by centrifugation and then dispersed in toluene to obtain dark brownish OLA- or DT-capped Cu_xS_y nanoparticles (see Image 2).



Image 2. Some tubes of synthesized a) DT-capped Cu_xS_y and b) OLA-capped Cu_xS_y nanoparticles.

The above reaction procedure is detailed in Table 2.

Table 2. Reaction parameters for the syntheses of Cu_xS_y nanoparticles.

Precursor-Mass (g)	Dispersion solvent (mL)	Capping agent (mL)	Volume of the capping agent (mL)	Temperature of the reaction (°C)	Time of the reaction (min)
[Cu(morph-tu) ₂]-0.2	OLA	OLA	5	150	30
				200	30
				250	30
[Cu(pyrr-tu) ₂]-0.2	OLA	OLA	5	150	30
				200	30
				250	30
[Cu(morph-tu) ₂]-0.2	OLA	DT	5	150	30
				190	30
				230	30
[Cu(pyrr-tu) ₂]-0.2	OLA	DT	5	150	30
				190	30
				230	30
[Cu(morph-tu) ₂]-0.2	DT	DT	5	150	30
				190	30
				230	30
[Cu(pyrr-tu) ₂]-0.2	DT	DT	5	150	30
				190	30
				230	30

2.3.3. Syntheses of cadmium sulfide (CdS) nanoparticles

A specified amount of 1.2 mmol of the [Cd(dihex-dtc)₂] or [Cd(dieth-dtc)₂] or [Cd(pip-dtc)₂] or [Cd(eth-xan)₂] complex was each dissolved in 6.0 mL of tri-n-octylphosphine (TOP). The solution was injected into 6.0 mL of hot capping agent (OLA or hexadecylamine) in a three-necked flask at 250 °C. The solution turned yellow and a drop in temperature of 20 - 30 °C was observed, then the reaction was allowed to stabilize at 250 °C. After a reaction time of 1 h, aliquots of samples were taken and methanol was added, resulting in the formation of a flocculent precipitate. The precipitate was separated by centrifugation and then dispersed in toluene to give yellowish OLA- or HDA-capped CdS nanoparticles (see Image 3).

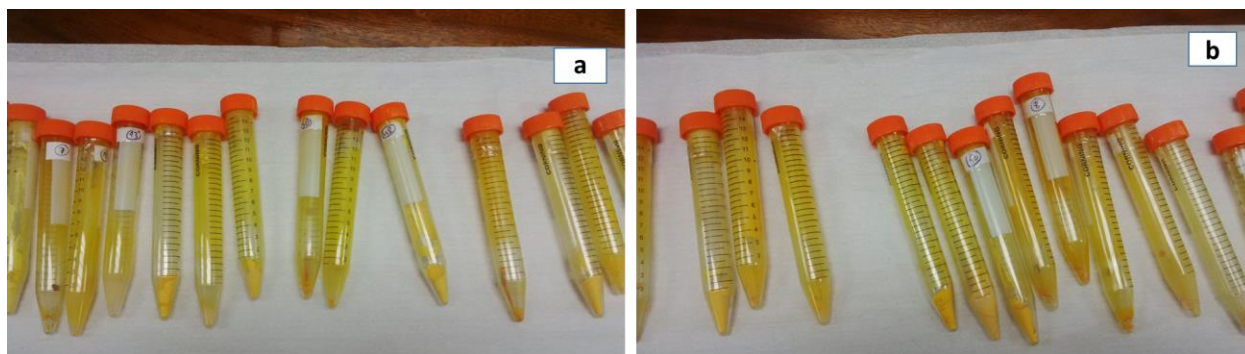


Image 3. Some tubes of synthesized a) OLA-capped and b) HDA-capped CdS nanoparticles.

The above reaction procedure is detailed in Table 3.

Table 3. Reaction parameters for the syntheses of CdS nanoparticles.

Precursor-Mass (g)	Dispersion solvent (mL)	Capping agent (mL/g)	Amount of the capping agent (mL/g)	Temperature of the reaction (°C)	Time of the reaction (h)
[Cd(dihex-dtc) ₂]-0.8	TOP	OLA	6	250	1
[Cd(dieth-dtc) ₂]-0.5	TOP	OLA	6	250	1
[Cd(pip-dtc) ₂]-0.5	TOP	OLA	6	250	1
[Cd(eth-xan) ₂]-0.4	TOP	OLA	6	250	1
[(dihex-dtc) ₂]-0.8	TOP	HDA	6	250	1
[Cd(dieth-dtc) ₂]-0.5	TOP	HDA	6	250	1
[Cd(pip-dtc) ₂]-0.5	TOP	HDA	6	250	1
[Cd(eth-xan) ₂]-0.4	TOP	HDA	6	250	1

2.4. Synthesis of undoped CdS, In-doped and Ga-doped CdS nanoparticles by solventless method

The undoped CdS, In-doped CdS and Ga-doped CdS nanoparticles were synthesized from the single source precursors through the solventless technique as reported by Abe and co-workers.¹²²

2.4.1. Synthesis of undoped CdS nanoparticles

Complex of Cd(II)eth-xan (0.20 g, 0.56 mmol) was finely ground and heated under N₂. The powder was heated to 300 °C and held at this temperature for 1 h before being allowed to cool to room temperature where a red powder was obtained.

2.4.2. Syntheses of In-doped and Ga-doped CdS nanoparticles

Complexes of Cd(II)eth-xan and In(III)eth-xan were mixed and finely ground in mass ratios varying from 2 to 10 %. The mixture was then heated under N₂ to 300 °C and held at this temperature for 1 h before being allowed to cool to room temperature where red In-doped CdS nanocrystals were obtained. The same procedure was repeated using the Cd(II)eth-xan and Ga(III)eth-xan complexes (see Image 4).

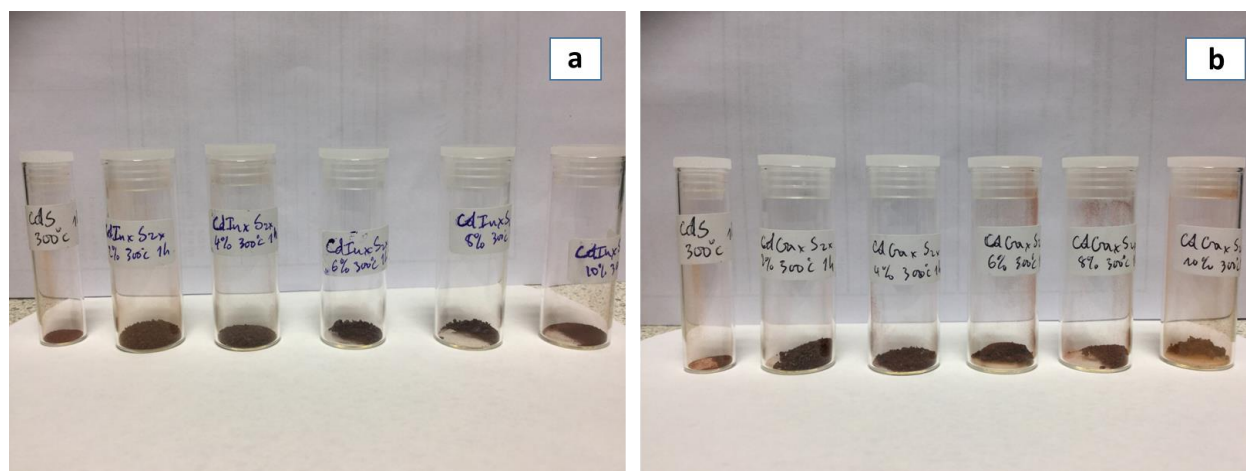


Image 4. Synthesized a) Undoped CdS, In-doped CdS and b) Undoped CdS, Ga-doped CdS nanoparticles.

The above reaction procedure is detailed in Table 4.

Table 4. Reaction parameters for the syntheses of undoped CdS, In-doped CdS and Ga-doped CdS nanoparticles

Composition [In]/[In]+[Cd]	Ratio (Cd:In:S)	Mmol of In (mass in grams)	Mmol of Cd (mass in grams)	T °C	Time (h)
-	50:0:50 (only CdS)	-	0.56 (0.20)	300	1
0.02	49:1:50	0.104 (0.05)	5.121 (1.82)	300	1
0.04	48:2:50	0.104 (0.05)	2.508 (0.89)	300	1
0.06	47:3:50	0.104 (0.05)	1.637 (0.58)	300	1
0.08	46:4:50	0.104 (0.05)	1.202 (0.43)	300	1
0.1	45:5:50	0.104 (0.05)	0.940 (0.33)	300	1

Composition [Ga]/[Ga]+[Cd]	Ratio (Cd:Ga:S)	Mmol of Ga (mass in grams)	Mmol of Cd (mass in grams)	-	-
-	50:0:50 (only CdS)	-	0.56 (0.20)	300	1
0.02	49:1:50	0.115 (0.05)	5.653 (2.00)	300	1
0.04	48:2:50	0.115 (0.05)	2.769 (0.98)	300	1
0.06	47:3:50	0.115 (0.05)	1.807 (0.64)	300	1
0.08	46:4:50	0.115 (0.05)	1.326 (0.47)	300	1
0.1	45:5:50	0.115 (0.05)	1.038 (0.37)	300	1

2.5. Syntheses of some metal sulfide thin films by the aerosol-assisted chemical vapour deposition (AACVD) technique

0.2 g of each molecular precursor was dissolved in 25 mL of chloroform and/or tetrahydrofuran (THF) in a two-necked 100 mL round-bottom flask with a gas inlet that allowed the carrier gas (argon) to pass into the solution to assist the transport of the aerosol. This flask was connected to the reactor tube by a piece of reinforced tubing. The argon flow rate was controlled by a Platon flow gauge. Seven glass substrates (approx. 1 x 2 cm) were placed inside the reactor tube in a Carbolite furnace. The precursor solution in a round-bottom flask was kept in a water bath above

the piezoelectric modulator of a Pifco ultrasonic humidifier (Model No. 1077). Aerosol droplets of the precursor were transferred into the hot wall zone of the reactor by carrier gas. Both the solvent and the precursor were evaporated and the precursor vapor reached the heated substrate surface where thermally induced reactions and film deposition took place. The reaction temperatures were varied between 350 - 450 °C (see Image 5).

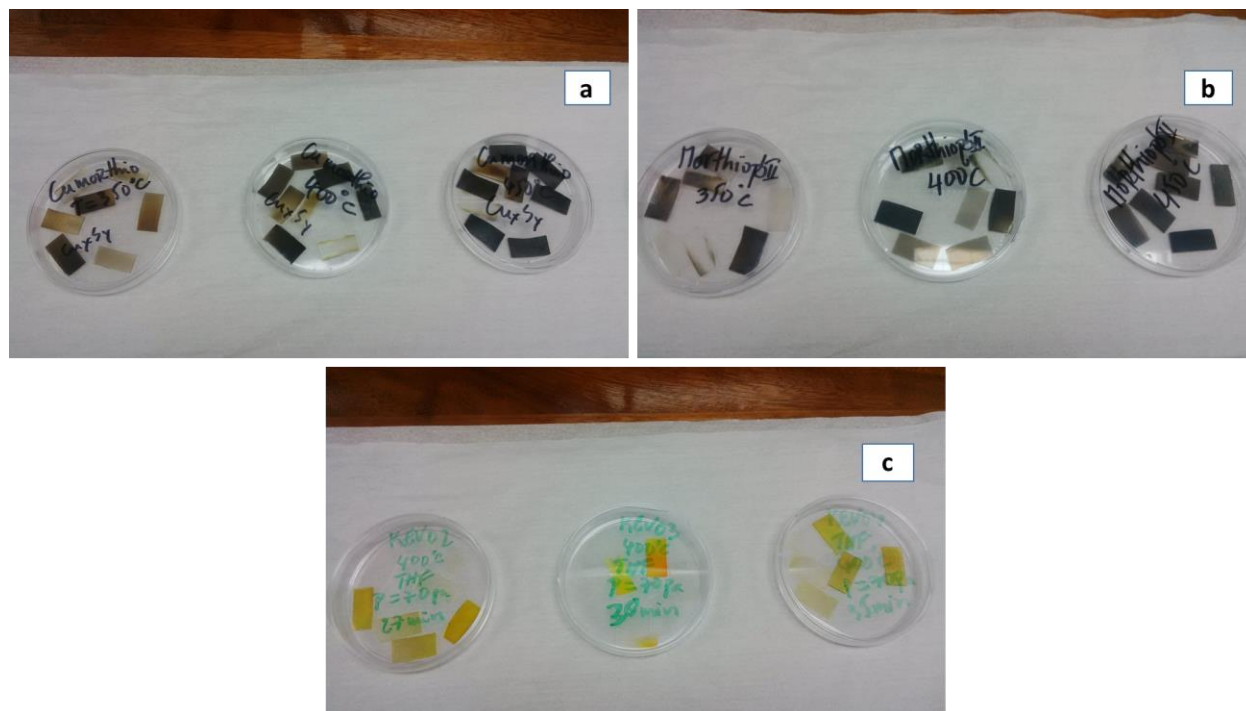


Image 5. Glass substrate of deposited a) Cu_xS_y , b) PbS and c) CdS thin films.

Figure 18 presents a schematic set up for an AACVD reaction and Table 5 provides the reaction parameters for the deposition of PbS , Cu_xS_y and CdS thin films.

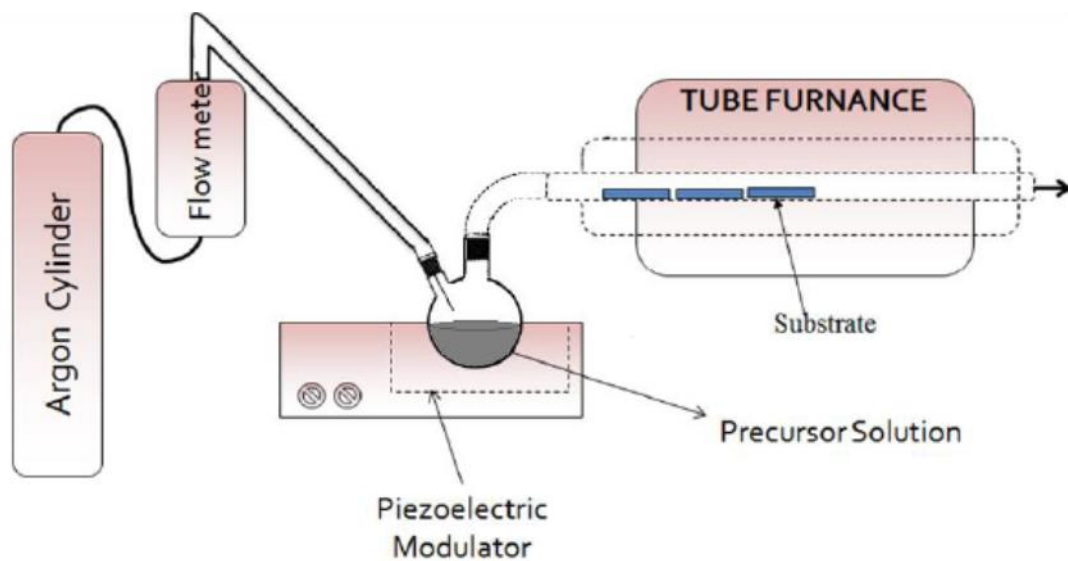


Figure 18. Schematic set up for an AACVD reaction.

Table 5. Reaction parameters for the deposition of PbS, Cu_xS_y and CdS thin films.

Precursor-Mass (g)	T (°C)	Time (min)	Flow rate (cm ³ /min)	Solvent (volume in mL)	Substrate
[Pb(morph-tu) ₂]-0.2	350-400-450	40	140	Chloroform (25)	Glass
[Pb(pyrr-tu) ₂]-0.2	350-400-450	25	140	Chloroform (25)	Glass
[Cu(morph-tu) ₂]-0.2	350-400-450	30	140	Chloroform (25)	Glass
[Cu(pyrr-tu) ₂]-0.2	350-400-450	20	140	Chloroform (25)	Glass
[Cd(dihex-dtc) ₂]-0.2	400-450	30	140	THF (25)	Glass
	450	40	140	THF+chloroform (25)	Glass
[Cd(dieth-dtc) ₂]-0.2	400-450	25	140	THF	Glass
	450	35	140	THF+chloroform (25)	Glass
[Cd(pip-dtc) ₂]-0.2	400-450	35	140	THF	Glass
	450	45	140	THF+chloroform (25)	Glass
[Cd(eth-xan) ₂]-0.2	400-450	30	140	THF	Glass
	450	40	140	THF+chloroform	Glass

2.6. Characterization of the ligands and the metal complexes

The prepared precursors were characterized by analytical techniques such as C, H, N elemental analysis, melting points analyses. Thermo gravimetric analysis (TGA), infra-red spectroscopy (IR) and nuclear magnetic resonance (NMR).

2.6.1. Elemental analyses

Elemental microanalysis (C, H, N) is a direct technique for determining the analytic data of a sample by providing a precise and accurate atomic composition analysis of a sample. Elemental analysis was performed on a Perkin-Elmer automated model 2400 series II CHNS/O analyzer at the Chemistry Department, University of Zululand, South Africa. Other elemental analysis were done using a Flash 2000 Thermo Scientific elemental analyzer and TGA data obtained with Mettler Toledo TGA/DSC1 star^e system between 30–600 °C at a heating rate of 10 °C min⁻¹ under nitrogen flow at the School of Chemistry, University of Manchester, UK.

2.6.2. Melting point determination

The melting point of a compound is the temperature where it changes state from solid to liquid. It depends on the pressure and is commonly identified at a standard pressure such as one atmosphere (atm) or 100 kilopascals (kPa). Melting points of the samples were recorded on the Barloworld SMP10 Melting Point Apparatus at the Chemistry Department, University of Zululand, South Africa (Image 6), the School of Chemistry, University of Manchester, UK (Image 6) and at the Department of Inorganic Chemistry, University of Yaounde I, Cameroon (Image 7).



Image 6. Barloworld SMP10 Melting Point Apparatus.



Image 7. Melting Point Apparatus.

2.6.3. Thermal analyses

Thermogravimetric analysis (TGA) provides the amount and rate of change in the weight of a sample as a function of temperature in a known atmosphere. TGA analysis are employed to find the composition of compounds and to forecast their thermal stability at temperatures up to 1000 °C. Thermogravimetric analysis was carried out at 20 °C/min heating rate from 30 °C to 700 °C under N₂ gas flow rate of 10 mL/min, using a Perkin Elmer Pyris 6 TGA equipped with a closed

perforated aluminium pan. The DSC analysis was carried out at 20 °C/min heating rate up to 700 °C using a Perkin-Elmer DSC 4000 series, previously calibrated with an indium metal. Both TGA and DSC were performed under N₂ gas at the Chemistry Department of the University of Zululand in South Africa (Image 8).



Image 8. Perkin-Elmer Pyris 6 Thermogravimetric analyzer.

2.6.4. Infra-red analyses

Infrared (IR) spectroscopy is a useful spectroscopic method employed by chemist and others researchers to determine the chemical functional groups present in a compound. It is also an instrument, which is significantly used for structural interpretation and sample identification. Infrared spectra were recorded on a Bruker FT-IR Tensor 27 spectrophotometer directly on small samples of the samples in the wavenumber range of 200 – 4000 cm⁻¹, equipped with a standard ATR crystal cell detector at the Chemistry Department of the University of Zululand, South Africa (Image 9).

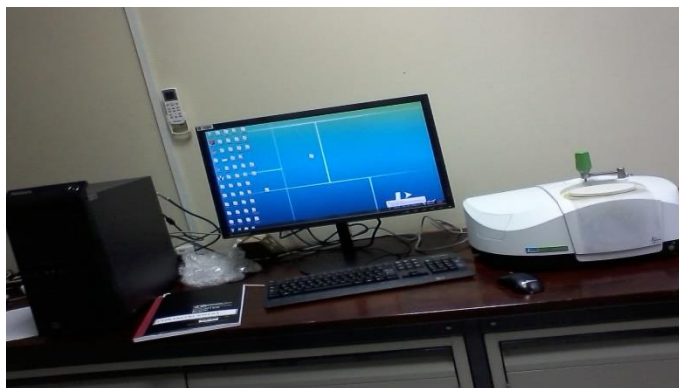


Image 9. Bruker FT-IR tensor 27 spectrophotometer.

2.6.5. ^1H Nuclear magnetic resonance (NMR) analyses

Nuclear magnetic resonance (NMR) spectroscopy is a technique that gives complete information concerning the structure and the environment of compounds. The ^1H NMR spectra of both the ligands and metal complexes were obtained using a Bruker advance III 400 MHz spectrophotometer equipped with trimethylsilane as an internal standard reference. They were performed at the University of KwaZulu-Natal, South Africa and at the School of Chemistry, University of Manchester, UK (Image 10).



Image 10. Nuclear magnetic resonance Bruker advance III 400 MHz spectrophotometer.

2.6.6. Single crystal X-ray crystallography

Single X-ray diffraction data was recorded on a Bruker Apex Duo equipped with an Oxford Instruments Cryojet operating at 100(2) K and an Incoatec microsource operating at 30 W power. The data were collected with Mo K α ($\lambda = 0.71073 \text{ \AA}$) radiation at a crystal-to-detector distance of 50 mm. Data were collected using omega and phi scans with exposures taken at 30 W X-ray power and 0.50° frame widths using APEX2¹⁵³. The data were reduced with the programme SAINT¹⁵³ using outlier rejection, scan speed scaling, as well as standard Lorentz and polarization correction factors. A SADABS semi-empirical multi-scan absorption correction¹⁵³ was applied to the data. Direct methods, SHELX-2016¹⁵⁴ and WinGX¹⁵⁵, were used to solve the data. All non-hydrogen atoms were located in the difference density map and refined anisotropically with SHELX-2016.¹⁵⁴ All hydrogen atoms were included as idealized contributors in the least squares process.

2.7. Characterization of the organically capped metal sulfide nanoparticles and thin films

The main importance of nanotechnology is based on the statement that the properties of materials change dramatically when their dimension is reduced to the nanometer range. However, ongoing research is still moving on the synthesis of nanostructured materials and their characterization still represents a challenge to researchers. It is therefore important to use every given opportunity to study and fully understand the characterisation of nanomaterials since it plays a decisive role in the determination of their different properties through different aspects like the morphology, crystal structure, chemistry and electronic structure.

2.7.1. Optical spectroscopies

Optical spectroscopies are based on the interaction of light with matter as a function of wavelength or energy to give information concerning a material. The absorption or emission (photoluminescence) experiments with visible and UV light aims at disclose the electronic structure while Raman will provide the fingerprint of the material.

2.7.1.1. UV-visible spectroscopy

UV-visible spectroscopy involves a light source, reference, sample beams, a monochromator and a detector. The UV-visible spectrum of a sample is found by exposing the sample to ultraviolet light from a light source like xenon lamp. For PbS samples and CdS thin films, a Perkin Elmer Lambda 1050 UV/Vis/NIR spectrophotometer was used to carry out UV-Vis absorption measurements (Image 11). While for CdS nanoparticles, optical absorption measurements were carried out on a Varian Cary 50 UV-Visible spectrophotometer using quartz cuvettes (1 cm path length), using toluene as reference solvent (Image 12).



Image 11. Perkin Elmer Lambda 1050 UV/Vis/NIR spectrophotometer.



Image 12. Varian Cary 50 Conc UV-visible spectrophotometer.

2.7.1.2. Photoluminescence spectroscopy

Photoluminescence spectroscopy is a contactless technique for probing the electronic structure of materials. In this technique, the light fixed onto a sample is absorbed and transmits excess energy into the material in a process called phot-excitation. A Perkin-Elmer LS 55 spectrofluorimeter was used to measure the photoluminescence properties of the CdS thin films (Image 13).



Image 13. Perkin-Elmer LS 55 spectrofluorimeter.

2.7.1.3. Raman spectroscopy

Raman is a spectroscopic technique used to observe vibrational, rotational, and other low-frequency modes in a system. Raman spectroscopy is frequently used to provide a structural fingerprint by which a material can be recognized¹⁵⁶. Raman spectra were measured using a Renishaw 1000 micro-Raman system equipped with a 514 nm laser at the School of Chemistry of the University of Manchester, UK.

2.7.2. Electron beam techniques

Electron beams are used to produce images of materials. These imaging techniques give a highly magnified image of the surface or the bulk of the sample. Nanostructures can only be analyzed via these imaging methods. Therefore, transmission electron microscopy (TEM), high-resolution transmission electron microscopy (HRTEM), scanning electron microscopy (SEM) and energy dispersive X-ray spectroscopy (EDX) are among the most important instruments used to investigate the internal structure of a material.

2.7.2.1. Transmission electron microscopy (TEM) and high resolution TEM (HRTEM)

Transmission electron microscopy (TEM) is a microscopic method in which a beam of electrons is transmitted through an ultra-thin specimen and interacts as it crosses via the sample. The formation of an image occurs from the electrons transmitted via the specimen, it is magnified and focused by an objective lens and appears on an imaging screen. TEM permits the investigation of the internal

structure of the materials in the micro and nano range, while HRTEM is an imaging method of the transmission electron microscope that permits the imaging of the crystallographic structure of a sample at an atomic scale.

Samples were arranged by evaporating drops of diluted solution of nanoparticles on Formvar-coated Cu grids (150 mesh) for TEM and holey carbon grids for HRTEM analyses. A JEOL 1400 TEM and JEOL 2100 HRTEM were used for respective analyses, at an accelerating voltage of 120 kV and 200 kV, respectively. A Megaview III camera was used for TEM and the images were captured using iTEM software. While a Gatan camera and Gatan software were used for HRTEM.

2.7.2.2. Scanning electron microscopy (SEM) and energy dispersive X-ray analysis (EDX)

The as-deposited thin films were carbon coated before performing scanning electron microscopy (SEM) and energy dispersive X-ray spectroscopy (EDX) analyses. This allows to investigate the morphology of the films and to find out the elemental composition of the films respectively.

The surface morphology and structure of the film was determined using a Zeiss Sigma VP-03-67 field emission gun scanning electron microscopy (FEGSEM), equipped with an Oxford instrument X-max 50 EDX detector (Image 14) and Philips XL30 FEG microscope, with an energy-dispersive X-ray spectroscopy (EDX) DX4 detector. The analyses were carried out at the Department of Chemistry, University of Zululand, South Africa and at the School of Chemistry, University of Manchester, UK.



Image 14. Scanning Electron Microscope.

2.7.3. X-ray diffraction technique

X-ray diffraction (XRD) is a versatile technique that provides detailed information about the chemical composition, crystallographic and microstructure of the samples. The analysis of the diffraction pattern reveals information such as lattice parameter, crystal structure, sample orientation and particle size. The Bragg equation allows for the finding of the lattice parameters: $2d\sin\theta = n\lambda$ where d is the lattice spacing.¹⁵⁷

Powder diffraction patterns of the nanomaterials were recorded at room temperature in the high angle 2θ range ($20 - 90^\circ$) using an Advanced Bruker AXS D8 diffractometer, equipped with nickel-filtered Cu $K\alpha$ radiation ($\lambda = 1.542 \text{ \AA}$) at 40 kV and 40 mA at the Chemistry Department, University of Zululand, South Africa. The scan speed and step sizes were $0.05^\circ/\text{min}$ and 0.00657° respectively (Image 15). Furthermore, analyses were also carried out using an X-Pert diffractometer with a Cu- $K\alpha_1$ source ($\lambda = 1.54059 \text{ \AA}$), the samples were scanned between 20° and 70° , the applied voltage was 40 kV, and the current was 30 mA at the School of Chemistry, University of Manchester, UK.

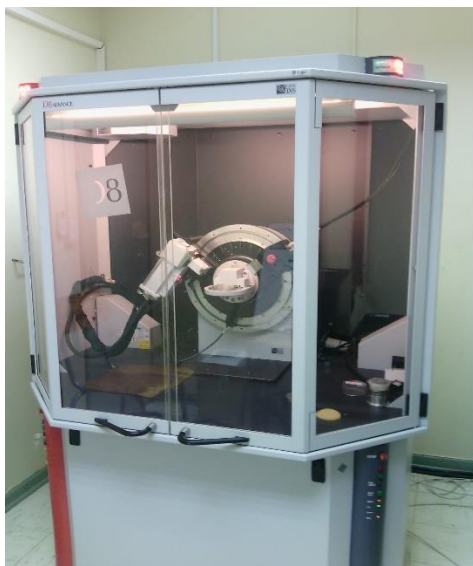


Image 15. Bruker AXS D8 diffractometer.

CHAPTER 3: RESULTS AND DISCUSSION

This chapter focuses on the results and discussion of the synthesized precursors and metal sulfide nanomaterials.

3.1. Syntheses and characterisation of precursors

Ligands and their respective metal complexes were prepared as described in subsection 2.2 and then characterised using some analytical techniques reported in subsection 2.6.

3.1.1. Syntheses and characterization of heterocyclic thiourea ligands and lead complexes

Heterocyclic morpholine thiourea (morph-tu) and pyrrolidine thiourea (pyrr-tu) ligands and the corresponding lead complexes were prepared as presented in scheme 5, page 43. The resulting products were characterized using known analytical methods such as elemental analysis, thermogravimetric analysis (TGA), infrared analysis (IR), ^1H nuclear magnetic resonance ($^1\text{HNMR}$) analysis and single crystal X-ray crystallography.

The N-morpholine- N' -benzoylthiourea ligand was a white powder and its corresponding Pb(II) complex was a white microcrystal whilst the N-pyrrolidine- N' -benzoylthiourea ligand and its Pb(II) complex were yellow. The compounds were air and moisture stable, easy to synthesize and soluble in some organic solvents such as chloroform. The elemental analysis data for the ligands and lead complexes are detailed in Table 6.

Table 6. Elemental analyses data for the ligands and lead complexes.

Compounds	Yield (%)	Form (color)	MPt (°C)	Elemental analysis Found (calcd)%			Molecular formula
				C	H	N	
morph-tu	75	Precipitate (white)	144-146	57.98 (57.58)	5.62 (5.64)	11.07 (11.19)	C ₁₂ H ₁₄ N ₂ O ₂ S
pyrr-tu	73	Precipitate (yellow)	130-133	61.92 (61.51)	5.89 (6.02)	11.08 (11.96)	C ₁₂ H ₁₄ N ₂ OS
[Pb(morph-tu)₂]	91	Microcrystal (white)	167-169	39.85 (40.84)	3.69 (3.71)	7.93 (7.94)	C ₂₄ H ₂₆ N ₄ O ₄ PbS ₂
[Pb(pyrr-tu)₂]	74	Precipitate (yellow)	154-157	41.14 (42.78)	3.51 (3.89)	7.43 (8.31)	C ₂₄ H ₂₆ N ₄ O ₂ PbS ₂

[morph-tu]: N-morpholine-N'-benzoylthiourea

[pyrr-tu]: N-pyrrolidine-N'-benzoylthiourea

[Pb(morph-tu)₂]: bis(N-morpholine-N'-benzoylthioureato)lead(II)

[Pb(pyrr-tu)₂]: bis(N-pyrrolidine-N'-benzoylthioureato)lead(II)

The IR results revealed that the medium peak appearing at 3239 cm⁻¹ for (morph-tu) and 3148 cm⁻¹ for (pyrr-tu) is attributed to the stretching of the N-H group adjacent to the carbonyl group. This N-H bond is replaced by the C=N bond upon complexation of the ligand to the metal ion by action of a base. The appearance of two new peaks in the IR spectra of the complexes is observed at 1587 cm⁻¹ and 1586 cm⁻¹ respectively for complexes Pb-morph-tu and Pb-pyrr-tu and attributed to the C=N bond. The strong band at 1663 cm⁻¹ for (morph-tu) and 1643 cm⁻¹ for (pyrr-tu) is attributed to the vibration of the C=O of carbonyl groups which shifts to lower wavenumbers upon complexation. Deprotonation involved delocalization of C=O stretching vibration which is in agreement with the literature^{158,159} thus confirming the coordination to the central metal ion through oxygen atom of the carbonyl group.

The ¹H NMR data of the ligands showed that the amide proton, N-H peak is observed at 9.68 and 9.65 ppm for (morph-tu) and (pyrr-tu), respectively. The multiplet peaks in the ¹H NMR spectra assigned to the aromatic protons are observed in the 8.00-7.54 and 8.02-7.50 ppm range in both

ligands respectively. Two signals indexed to the methylene protons of morpholine and pyrrolidine are also observed in the 4.27-3.84 and 3.80-3.70 ppm range (see Table 7).

Table 7. Spectroscopic data for the ligands and lead complexes.

Compounds	¹ H NMR (400 MHz) δ in (ppm)	ν(N-H) (cm ⁻¹)	ν(C=O) (cm ⁻¹)	ν(C=S) (cm ⁻¹)	ν(C=N) (cm ⁻¹)
morph-tu	9.68 (s, 1H, NH) 8.00 (m, 2H, Ar-H) 7.60 (m, 1H, Ar-H) 7.54 (m, 2H, Ar-H) 4.27 (s, 4H, CH ₂) 3.84 (t, 4H, CH ₂)	3239 (br)	1663 (s)	1000 (s)	-
pyrr-tu	9.65 (s, 1H, NH) 8.02 (m, 2H, Ar-H) 7.70 (m, 1H, Ar-H) 7.50 (m, 2H, Ar-H) 3.80 (t, 4H, CH ₂) 3.70 (t, 4H, CH ₂)	3148 (br)	1643 (s)	979 (s)	-
[Pb(morph-tu)₂]	-	-	1473 (s)	-	1587 (s)
[Pb(pyrr-tu)₂]	-	-	1487 (s)	-	1586 (s)

s= strong, br= broad.

The TGA profiles of both complexes showed a two-step decomposition pattern. The first step gave a loss of 58% (54.19%, corresponding to 2MB = 2morpholinylbenzamide) Pb-morph-tu complex (1) (Figure 19; step ii) and 52% (52.01%, corresponding to 2PB = 2pyrrolidinylbenzamide) Pb-pyrr-tu complex (2) (Figure 19; step iv) at 282 and 293 °C, respectively corresponding to the loss of the organic moiety. The second decomposition steps at 485 and 493 °C with mass losses of a further 10% (calcd: 7.38%; corresponding to 2CN = 2cyanide, step i) (1) and 9% (7.73%; corresponding to 2CN = 2cyanide; step iii) (2) occurred, respectively¹⁶⁰. The final residues of 33.00% (calc. 33.90%) (1) and 39% (calc. 35.51%) (2) closely correspond to the theoretical values of PbS, respectively. The higher experimental residues for (2) can be attributed to carbonaceous contamination from aryl and heterocyclic groups.

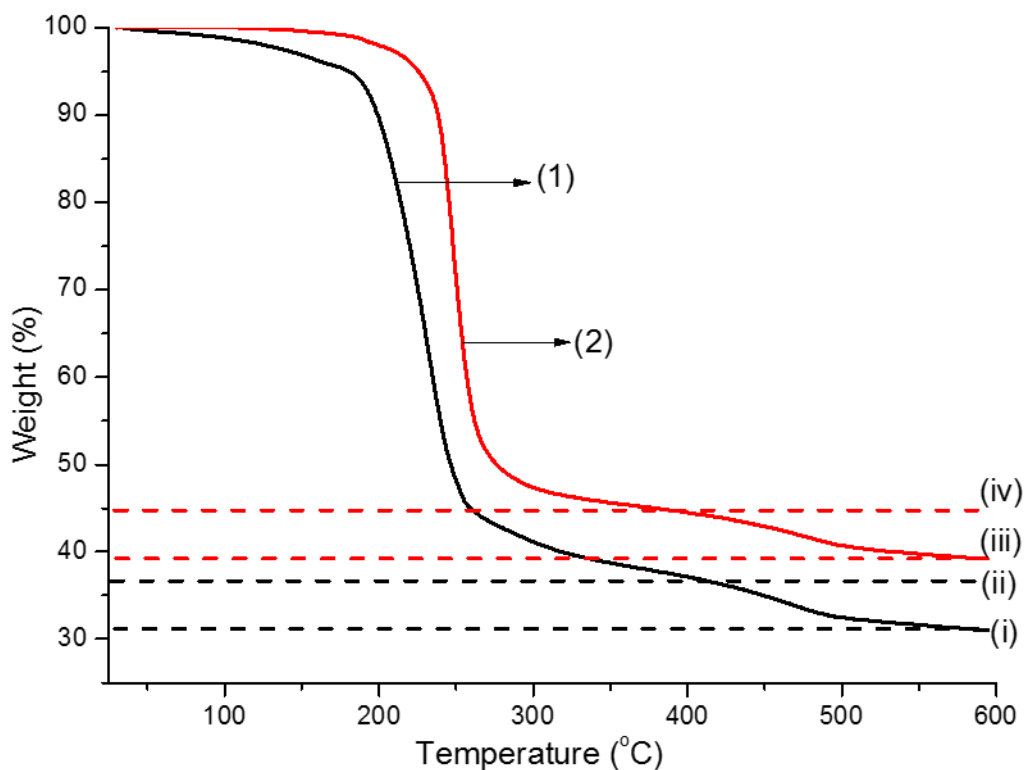


Figure 19. Thermogravimetric analysis (TGA) plots of Pb(II) complexes (1) and (2) at a heating rate of $10\text{ }^{\circ}\text{C min}^{-1}$ under nitrogen atmosphere.

3.1.1.1. Crystal structure of the Pb-morphTU complex

Thin colourless, plate-like crystals of Pb-morphTU complex (1) were grown from a 1:1 mixture of dichloromethane and ethanol. The data were collected with Mo $K\alpha$ ($\lambda = 0.71073\text{ \AA}$) radiation at a crystal-to-detector distance of 50 mm. Data were collected using omega and phi scans with exposures taken at 30 W X-ray power and 0.50° frame widths using APEX2¹⁵³. Direct methods, SHELX-2016¹⁵⁴ and WinGX¹⁵⁵, were used to solve the data. All non-hydrogen atoms were located in the difference density map and refined anisotropically with SHELX-2016¹⁵⁴. All hydrogen atoms were included as idealized contributors in the least squares process. Their positions were calculated using a standard riding model of SHELX with C-Haromatic distances of 0.93 \AA and $U_{iso} = 1.2\text{ Ueq}$ and C-Hmethylene distances of 0.99 \AA and $U_{iso} = 1.2\text{ Ueq}$. The Pb(II) cation is four-coordinated with the coordination sphere comprising two bidentate N-morpholine-derived benzoylthioureato ligands. The ligands are coordinated through the carbonyl oxygen atom and a deprotonated thiol group yielding a monoanionic ligand and neutral lead(II) chelate. The

coordination geometry of the lead(II) complex can be described as hemidirected¹⁶¹ i.e. the bonds between the ligand and metal occupy only part of the encompassing globe of the metal ion, The compound crystalized in the monoclinic space group $P2_1/n$ with a single molecule in the asymmetric unit ($Z = 4$). Crystal and structure refinement data are given in Table 8. The contents of the asymmetric unit and the Difference Fourier map of Pb-morphotu complex (1) are shown in Figure 20, the latter illustrates the likely position of the lone pair of electrons on the lead(II) ion.

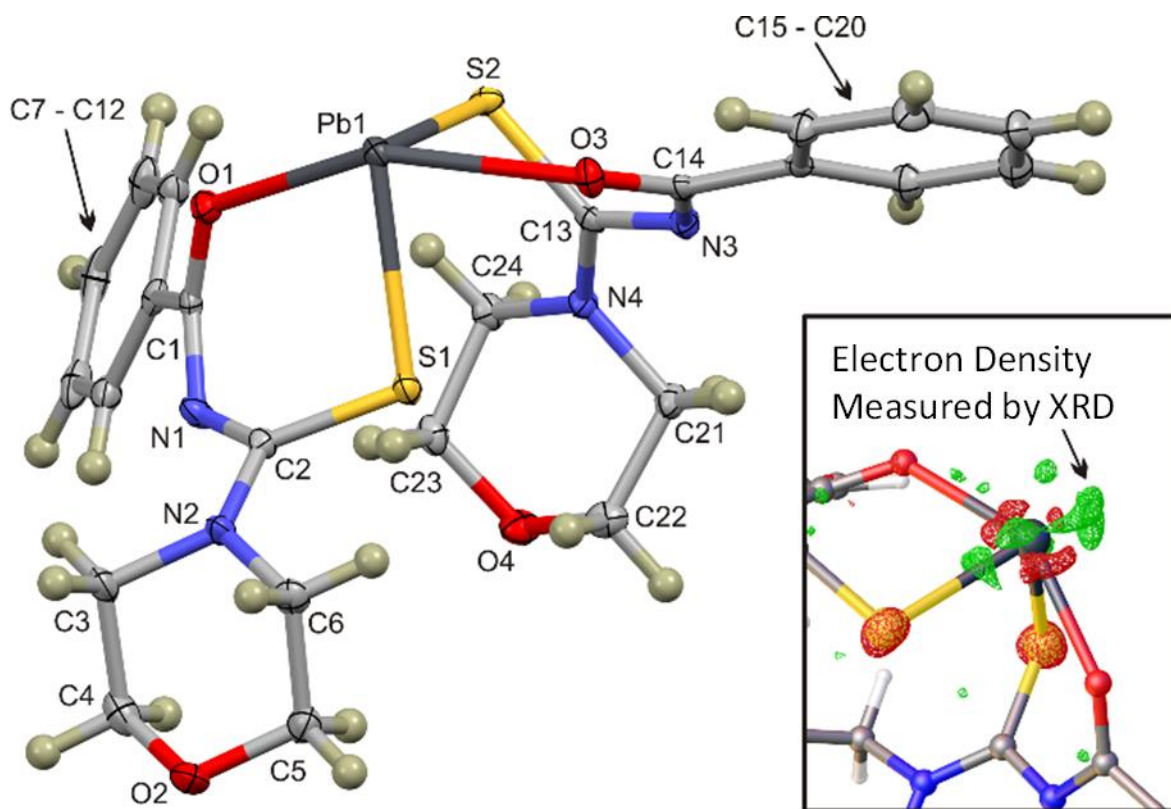


Figure 20. Thermal displacement plot (50% probability) of (1) showing the distorted trigonal bipyramidal geometry as well as the void in the coordination sphere, as conventionally attributed to the electron density. Hydrogen atoms are rendered as spheres of arbitrary radius. [Inset] Difference Fourier map showing the probable location of the electron density residing on the lead (II) ion. The contour has $\rho = -1.8 e$, the red and green grids indicate electron density maxima and minima, respectively. The plot was rendered using OLEX2¹⁶². CCDC reference number 1545392.

Table 8. Crystal data and structure refinement details for Pb-morphotu complex (1).

Crystal Data	Complex (1)
Chemical formula	C ₂₄ H ₂₆ N ₄ O ₄ PbS ₂
Molar mass (g mol ⁻¹)	705.80
Crystal system, space group	Monoclinic, P2 ₁ /n
Temperature (K)	100(2)
a, b, c (Å)	13.430(2), 8.0145(13), 23.392(4)
α, β, γ (°)	90, 92.456(5), 90
V (Å ³)	2515.6(7)
Z	4
Radiation type	Mo Kα
μ (mm ⁻¹)	6.91
Crystal size (mm)	0.6 × 0.05 × 0.02
Data Collection	
Diffractometer	Bruker APEXII CCD diffractometer
Theta (max)	28.234
F000	1376.0
h, k, lmax	17, 10, 31
Absorption correction	Multi-scan, SADABS
T _{min} , T _{max}	0.645, 0.746
No. of measured, independent and observed [I > 2σ(I)] reflections	23490, 6186, 5398
R _{int}	0.035
Refinement	
wR2 (reflections)	0.0517 (6186)
R[F ² > 2σ(F ²)], wR(F ²), S	0.024, 0.052, 1.05
No. of reflections	6186
No. of parameters	316

H-atom treatment	H-atom parameters constrained
Data completeness	0.995
$\Delta\rho_{\max}, \Delta\rho_{\min}$ (e \AA^{-3})	1.00, -0.64
S	1.052

Table 9. Selected bond parameters describing Pb-morphthu complex.

Bond	Length (\AA)	Bond	Angle ($^{\circ}$)
Pb1–O1	2.448(2)	O1–Pb1–S1	79.63(5)
Pb1–O3	2.455(2)	S1–Pb1–O3	76.81(6)
Pb1–S1	2.687(1)	O3–Pb1–S2	76.24(5)
Pb1–S2	2.689(1)	S2–Pb1–O1	85.11(5)
C1–O1	1.262(4)	S1–Pb1–S2	96.07(2)
C14–O3	1.275(4)	O1–Pb1–O3	147.99(7)
		O1–C1–C7	118.3(3)
		O3–C14–C15	117.1(3)

The data in Table 9 illustrate the bond parameters associated with the metal ion coordination sphere. The bond parameters are comparable to those of related four-coordinate hemi-directed lead(II) chelates with pseudo trigonal bipyramidal geometry^{163–165}. The C–O bond of the metal have a mean bond length of 1.268(6) \AA .

The structure packs as inversion dimers (Figure 21) supported by complementary Pb–S interactions between the lead ion and sulfur atom of an adjacent molecule with an interaction distance of 3.6157(9) \AA . This motif leads to the formation of a four-membered ring. Interactions of this type are common, but not ubiquitous in comparable O₂S₂ lead(II) complexes^{163,164}, as seen in many related cadmium complexes. The dimeric structures are linked into a one-dimensional supramolecular structure (Figure 22) through C–H \cdots O interactions with a C \cdots O interaction

distance of 3.399(4) Å. This structure propagates collinear to the b-axis. Bond length cannot be definitively linked to bond strength due to various packing constraints in the crystal lattice. However, both the Pb···S and C–H···O interactions are significantly shorter than the sum of the van der Waals radii of the interacting atoms, 0.304 and 0.204 Å, respectively. This short bond length suggests a genuine and indeed moderately strong interaction. In the case of the C–H···O interaction, this statement is further supported by the fact that the bond angle (171.4°) does not deviate significantly from the ideal angle of 180°.

The dimeric structure indicates weak stabilizing Pb···Pb interactions. The separation of the metal ions comprising the dimer measures 3.9777(7) Å. In the literature there is debate as to whether Pb–Pb bonds exist or would be better described as van der Waals interactions¹⁶⁶. The van der Waals parameter for a bond of this nature is 4.04 Å, thus the distance noted in the present compound is only modestly shorter and may indicate weak stabilizing van der Waals interactions between the metal ions. If the Pb···Pb contact and lone pair are considered part of the coordination sphere then the chelate could be loosely categorized as a distorted octahedron.

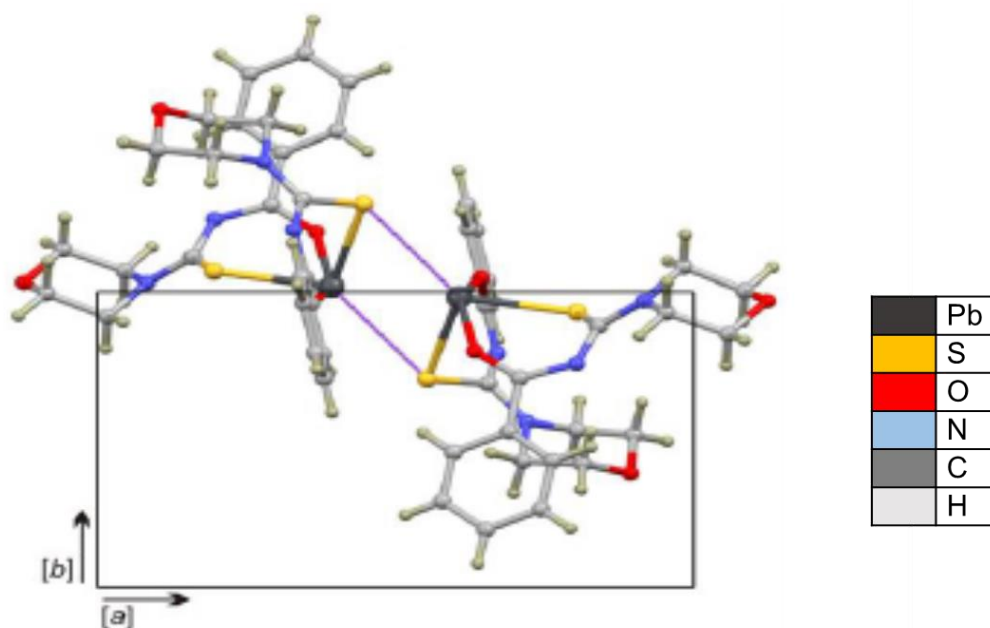


Figure 21. Dimeric structure of Pb-morphu stabilized by Pb···S and weak Pb···Pb interactions.

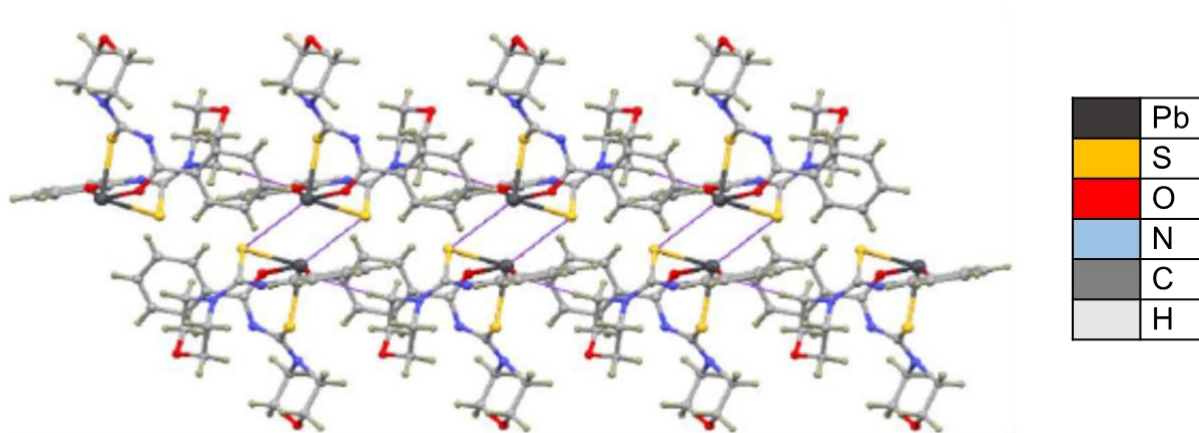


Figure 22. One-dimensional polymer of Pb-morphthu comprising dimeric molecules cross-linked by short, 3.399(4) Å, C, C-H...O interactions. Respective symmetry codes: 1-x, -y, 2-z and x, -1+y, z. Interactions are shown as dashed purple tubes, all atoms are rendered as spheres of arbitrary radius.

3.1.2. Syntheses and characterization of heterocyclic thiourea ligands and copper complexes

The heterocyclic morpholine and pyrrolidine thiourea ligands and the corresponding copper(II) complexes were synthesized as shown in scheme 5, page 43. The resulting compounds were characterized using common analytical methods such as elemental analysis, thermogravimetric analysis (TGA), infrared analysis (IR), ^1H nuclear magnetic resonance ($^1\text{HNMR}$) analysis and single crystal X-ray crystallography.

The prepared compounds were obtained as greenish powders. The products were obtained in good yields, and the purity was confirmed by microanalysis. The elemental analysis data for the ligands and copper complexes are detailed in Table 10.

Table 10. Elemental analyses data for the ligands and copper complexes.

Compounds	Yield (%)	Form (color)	MPt (°C)	Elemental analysis Found (calcd)%			Molecular formula
				C	H	N	
morph-tu	75	Precipitate (white)	144-146	57.98 (57.58)	5.62 (5.64)	11.07 (11.19)	C ₁₂ H ₁₄ N ₂ O ₂ S
pyrr-tu	73	Precipitate (yellow)	130-133	61.92 (61.51)	5.89 (6.02)	11.08 (11.96)	C ₁₂ H ₁₄ N ₂ OS
[Cu(morph-tu)₂]	90	Microcrystal (green)	204-206	51.04 (51.28)	4.64 (4.66)	9.74 (9.47)	C ₂₄ H ₂₆ N ₄ O ₄ CuS ₂
[Cu(pyrr-tu)₂]	84	Precipitate (green)	190-192	53.89 (54.37)	4.78 (4.94)	10.09 (10.57)	C ₂₄ H ₂₆ N ₄ O ₂ CuS ₂

[morph-tu]: N-morpholine-N'-benzoylthiourea

[pyrr-tu]: N-pyrrolidine-N'-benzoylthiourea

[Cu(morph-tu)₂]: bis(N-morpholine-N'-benzoylthioureato)copper(II)

[Cu(pyrr-tu)₂]: bis(N-pyrrolidine-N'-benzoylthioureato)copper(II)

The IR studies revealed that the medium peak appearing at 3239 cm⁻¹ for (morph-tu) and 3148 cm⁻¹ for (pyrr-tu) is attributed to the stretching of the N-H bond adjacent to the carbonyl group. This N-H bond is replaced by a C=N bond upon complexation of the ligand to the metal ion by action of a base. The appearance of one new peak, a C=N for each complex in the IR spectra of the complexes is observed at 1588 cm⁻¹ and 1574 cm⁻¹ respectively for Cu-morph-tu and Cu-pyrr-tu and attributed to the C=N vibration of the bond. The intense band at 1663 cm⁻¹ for (morph-tu) and 1643 cm⁻¹ for (pyrr-tu) is attributed to the vibration of the C=O of carbonyl which shifts to lower wavenumbers upon complexation. Deprotonation involves delocalization of C=O stretching vibration which is in agreement with the literature^{158,159}, confirming the coordination to the central metal ion through the oxygen atom of the carbonyl group.

The ¹H NMR data of the ligands showed that the amide proton, N-H peak is observed at 9.68 and 9.65 ppm for (morph-tu) and (pyrr-tu), respectively. The multiplet peaks in the ¹H NMR spectra assigned to the aromatic protons are observed in the 8.00-7.54 and 8.02-7.50 ppm range in both

ligands respectively. Two signals indexed to the methylene protons of morpholine and pyrrolidine are also observed in the 4.27-3.84 and 3.80-3.70 ppm range (see Table 11).

Table 11. Spectroscopic data for the ligands and copper complexes.

Compounds	¹ H NMR (400 MHz) δ in (ppm)	ν(N-H) (cm ⁻¹)	ν(C=O) (cm ⁻¹)	ν(C=S) (cm ⁻¹)	ν(C=N) (cm ⁻¹)
morph-tu	9.68 (s, 1H, NH)	3239 (br)	1663 (s)	1000 (s)	-
	8.00 (m, 2H, Ar-H)				
	7.60 (m, 1H, Ar-H)				
	7.54 (m, 2H, Ar-H)				
	4.27 (s, 4H, CH ₂)				
	3.84 (t, 4H, CH ₂)				
pyrr-tu	9.65 (s, 1H, NH)	3148 (br)	1643 (s)	979 (s)	-
	8.02 (m, 2H, Ar-H)				
	7.70 (m, 1H, Ar-H)				
	7.50 (m, 2H, Ar-H)				
	3.80 (t, 4H, CH ₂)				
	3.70 (t, 4H, CH ₂)				
[Cu(morph-tu)₂]	-	-	1472 (s)	-	1588 (s)
[Cu(pyrr-tu)₂]	-	-	1473 (s)	-	1574 (s)

s= strong, br= broad.

The TGA plot of Cu-morphtu complex (3) showed a two-step decomposition pattern, while Cu-pyrrtu complex (4) undergoes a single step decomposition (Figure 23). The first step gave a loss of 71.24% (69.03%, indicating the loss of 2MB = 2morpholinylbenzamide) (3) (step ii) and 70.13% (72.92%, indicating the loss of 2PB+2CN where 2PB = 2pyrrolidinylbenzamide and 2CN = 2cyanide) (4) (step iii) at 315 and 327 °C, respectively matching to the loss of the organic moiety. The second decomposition step at 386 °C with mass loss of 10.43% (calc: 9.26% corresponding to the loss of 2CN, step i) (3) occurred¹⁶⁰. The final residues of 16.90% (calc. 17.00%) (3) and 20.45% (calc. 18.03%) (4), corresponds to the theoretical values of CuS, respectively. The higher experimental residues for (4) can be attributed to the carbon contamination from aryl and heterocyclic groups.

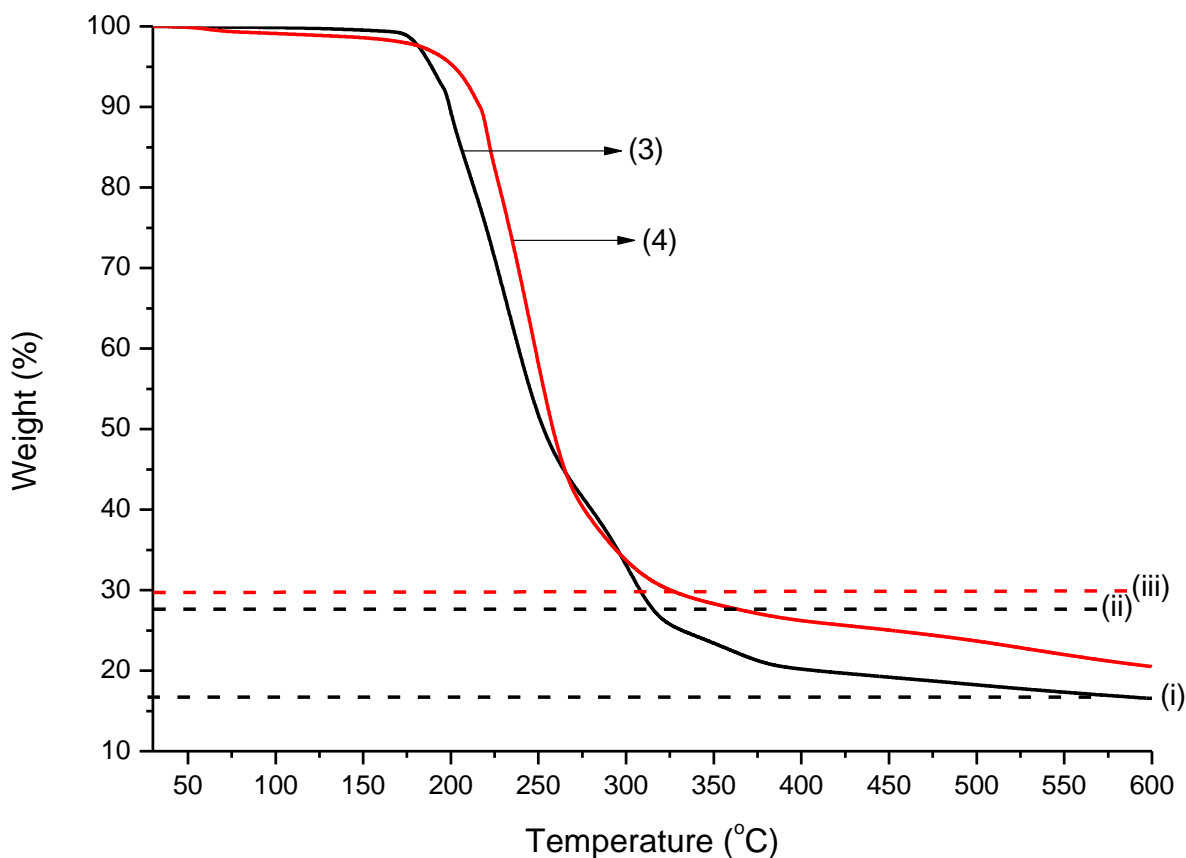


Figure 23. Thermogravimetric analysis (TGA) plots of Cu(II) complexes (3) and (4) at a heating rate of $10\text{ }^{\circ}\text{C min}^{-1}$ under nitrogen atmosphere.

3.1.2.1. Crystal structure of the Cu-morphtu complex

Green single crystals of Cu-morphtu complex suitable for X-ray crystal structure determination were grown from a 1:1 mixture of dichloromethane and ethanol. X-ray data were collected on a dual source Rigaku FR-X rotating anode diffractometer using Cu $K\alpha$ ($\lambda = 1.5418\text{ \AA}$) radiation at 150K, and reduced using CrysAlisPro¹⁶⁷. All non-hydrogen atoms were located in the difference density map and refined anisotropically with SHELX-2016¹⁵⁴. Structures were solved and refined using SHELX-2016 implemented through Olex2¹⁶⁸. All hydrogen atoms were included as idealised contributors in the least squares process. The Oak Ridge Thermal Ellipsoid Plot (ORTEP) crystal structure of bis(N-morpholine- N^2 -benzoylthioureato)copper(II) complex, is presented in

Figure 24 while the corresponding crystal data and selected bond parameters are described in Table 12 and Table 13, respectively.

The complex crystallizes in the triclinic crystal system, with space group P-1. Its molecular structure adopts a slightly square planar geometry with an asymmetric trans configuration. The Cu–S and Cu–O bond lengths are longer due to the Jahn–Teller effect¹⁶⁹. In two six membered (NC₂SO–Cu) rings of each specie, the Cu–S bond distances ranging from 2.2759 to 2.2797 Å and Cu–O bond distances ranging from 1.907 to 1.912 Å were observed. While the relatively long C–S and short C–O average bond lengths of 1.730(4) Å and 1.266(5) Å are consistent with mostly single and double-bond character, respectively.

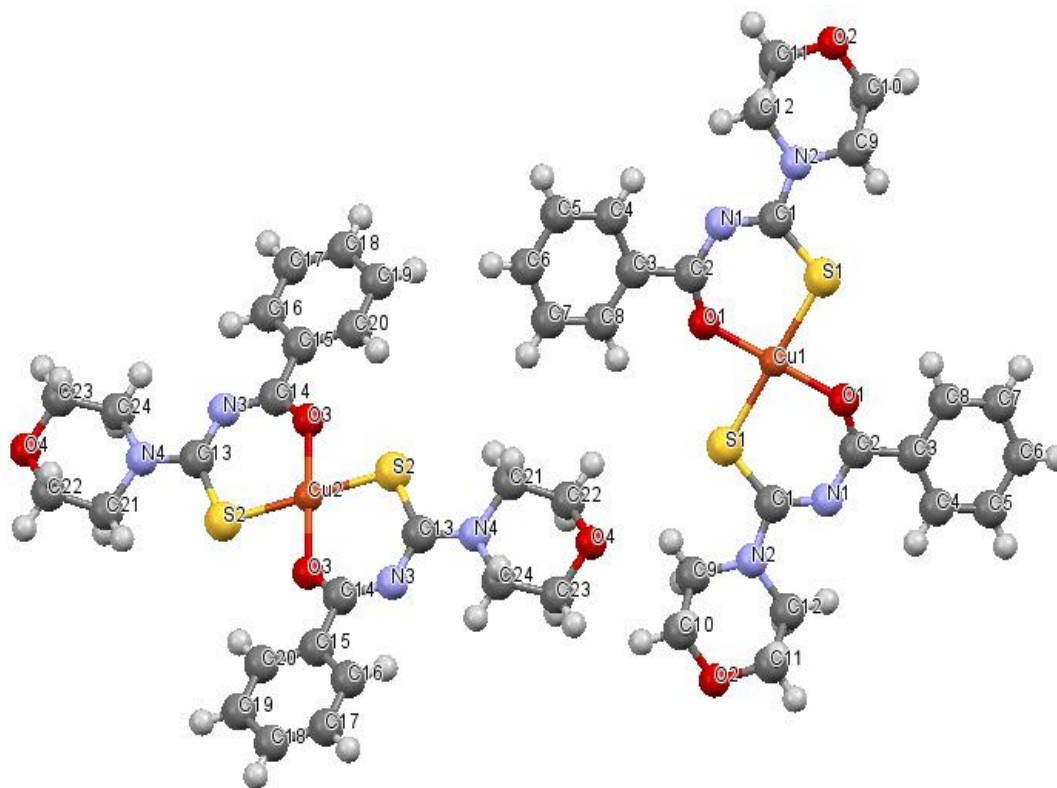


Figure 24. Single X-ray crystal structure of bis(N-morpholine-N²-benzoylthioureato)copper(II) complex.

Table 12. Crystal data and structure refinement details for Cu-morphotu complex (3).

Crystal Data	Complex (3)
Chemical formula	C ₂₄ H ₂₆ N ₄ O ₄ CuS ₂
Molar mass (g mol ⁻¹)	562.15
Crystal system, space group	Triclinic, P-1
Temperature (K)	150
a, b, c (Å)	4.1050(3), 16.3094(9), 17.7108(6)
α, β, γ (°)	81.492(4), 86.958(4), 82.974(5)
V (Å ³)	1163.15(11)
Z	2
Radiation type	Cu Kα
μ (mm ⁻¹)	3.352
Crystal size (mm)	0.6 × 0.05 × 0.02
Diffractometer	Rigaku FR-X rotating anode diffractometer
Dcalc (g cm ⁻³)	1.605
F(000)	582.0
h, k, lmax	4, 20, 21
Nref	4464
Tmin, Tmax	0.687, 1.000
Data completeness	0.935
Theta (max)	75.031
R(F ²) (observed reflections)	0.0534 (3925)
wR(F ²) (all reflns)	0.1446 (4464)
S	1.115
Npar	319

Table 13. Selected bond parameters describing Cu-morphu complex (3).

Bond	Length (Å)	Bond	Angle (°)
Cu1-S1	2.2797	S1-Cu1-O1	93.35
Cu1-O1	1.907	S1-Cu1-S1	180
Cu1-S1	2.2797	S1-Cu1-O1	86.65
Cu1-O1	1.907	O1-Cu1-S1	86.65
S1-C1	1.730(4)	O1-Cu1-O1	180
O1-C2	1.256(4)	S1-Cu1-O1	93.35
N1-C1	1.336(4)	S2-Cu2-O3	93.45
N1-C2	1.337(4)	S2-Cu2-S2	180
Cu2-S2	2.2759	S2-Cu2-O3	93.45
Cu2-O3	1.912	O3-Cu2-S2	86.55
Cu2-S2	2.2759	O3-Cu2-O3	180
Cu2-O3	1.912	S2-Cu2-O3	93.45
O3-C14	1.266(5)		
N3-C13	1.335(4)		
N3-C14	1.326(4)		

3.1.3. Dithiocarbamates (dihexyl, diethyl, piperidine) and Cd(II) complexes

Dithiocarbamates and Cd(II) complexes were synthesized as described in subsection 2.2.2, 2.2.4, 2.2.5 and their proposed chemical structures are included in page 44-45. Then they were characterised using some analytical methods reported in subsection 2.6.

3.1.3.1. Syntheses and characterization of dithiocarbamate ligands and cadmium complexes

The piperidinyl dithiocarbamate ligand, its corresponding cadmium(II) complexes synthesized from dihexyl/diethyl dithiocarbamates and ethyl xanthate were obtained in good yields as described in scheme 4, 6 and 7. These synthesized compounds were confirmed by Infrared (IR), microanalysis and Thermogravimetric analysis (TGA). The piperidinyl dithiocarbamate ligand and

its complex and the diethyl dithiocarbamate complex were white powders while dihexyl dithiocarbamate and ethyl xanthate complexes were yellow precipitates. The complexes are air and moisture stable at room temperature. Some elemental analytical data for the ligand and the cadmium complexes are shown in Table 14.

Table 14. Elemental analytical data for the ligand and cadmium complexes.

Compounds	Yield (%)	Form (color)	Elemental analysis Found (calcd)%			Molecular formula
			C	H	N	
Na(pip-dtc)	88	Precipitate (white)	32.57 (32.87)	6.29 (6.44)	5.96 (6.39)	C ₆ H ₁₄ NO ₂ S ₂ Na
[Cd(dihex-dtc) ₂]	88	Precipitate (yellow)	48.56 (49.30)	8.43 (8.27)	4.34 (4.42)	C ₂₆ H ₅₂ CdN ₂ S ₄
[Cd(dieth-dtc) ₂]	94	Precipitate (white)	29.19 (29.37)	4.77 (4.93)	6.73 (6.85)	C ₁₀ H ₂₀ CdN ₂ O ₄ S ₄
[Cd(pip-dtc) ₂]	83	Precipitate (white)	45.57 (45.40)	3.61 (3.81)	5.73 (5.29)	C ₁₂ H ₂₀ CdN ₂ S ₄
[Cd(eth-xan) ₂]	96	Precipitate (yellow)	20.32 (20.31)	2.67 (2.84)	- -	C ₆ H ₁₀ CdO ₂ S ₄

Na(pip-dtc): sodium piperidine dithiocarbamate

[Cd(dihex-dtc)₂]: bis(dihexyldithiocarbamato)cadmium(II)

[Cd(dieth-dtc)₂]: bis(diethyldithiocarbamato)cadmium(II)

[Cd(pip-dtc)₂]: bis(piperdinyldithiocarbamato)cadmium(II)

[Cd(eth-xan)₂]: bis(ethylxanthato)cadmium(II)

The IR results spectra of the cadmium piperidine dithiocarbamate (c), cadmium dihexyl dithiocarbamate (a) and cadmium diethyl dithiocarbamate (b) showed a $\nu(\text{C}=\text{N})$ band at 1480, 1490 and 1495 cm^{-1} respectively, indicating partial double bond character. The C–N stretching vibration usually appears in dithiocarbamates as a strong band around 1500 cm^{-1} . The position of

this band is indicative of the degree of the double bond character in the C–N bond ($\nu(\text{C}=\text{N}) = 1690\text{--}1640\text{ cm}^{-1}$; $\nu(\text{C}-\text{N}) = 1350\text{--}1250\text{ cm}^{-1}$)¹⁷⁰. The $\nu(\text{C}-\text{N})$ band is higher for complex (b) than for complex (a) and for complex (c) respectively. This may be due to the inductive effects of the alkyl chain length in dihexyl dithiocarbamate and the ring in piperidine dithiocarbamate, resulting in a decrease in the double bond character of the C–N bond¹⁷¹. The IR spectra of the cadmium ethyl xanthate (d) showed $\nu(\text{C}-\text{O})$ band at 1200 cm^{-1} . The $\nu(\text{C}=\text{S})$ band is observed in the $999\text{--}975\text{ cm}^{-1}$ range in the spectra of the piperidine dithiocarbamate ligand. The increase of the band for the different complexes from that of the free ligand, together with a strong band (or two very close bands) attributed to $\nu(\text{C}-\text{S})$, is indicative of a bidentate or slightly anisobidentate dithiocarbamate¹⁷². While a new additional band, is present in the $350\text{--}390\text{ cm}^{-1}$ region toward the end of the IR spectra, which probably corresponds to $\nu(\text{Cd}-\text{S})$ band that was not appearing in the spectra of the ligands. The IR data are detailed in Table 15.

Table 15. Spectroscopic data for the ligand and cadmium complexes.

Compounds	$\nu(\text{O}-\text{H})$ (cm^{-1})	$\nu(\text{C}=\text{N})$ (cm^{-1})	$\nu(\text{C}=\text{S})$ (cm^{-1})	$\nu(\text{Cd}-\text{S})$ (cm^{-1})	$\nu(\text{C}-\text{O})$ (cm^{-1})
Na(pip-dtc)	3367	1468	967	-	-
[Cd(dihex-dtc) ₂]	-	1490	980	390	-
[Cd(dieth-dtc) ₂]	-	1495	970	380	-
[Cd(pip-dtc) ₂]	3324	1480	970	388	-
[Cd(eth-xan) ₂]	-	-	-	350	1200

The TGA profiles of the complexes are presented in Figure 25. All the complexes showed a single step decomposition at 320, 334, 340 and 186 °C, displaying a weight loss of 76.2, 62.1, 63.2 and 57.6% (calc: 77.2, 64.7, 66.6 and 59.3%) corresponding to the loss of the organic moiety for dihexyl dithiocarbamate (a), diethyl dithiocarbamate (b), piperidinyl dithiocarbamate (c) and ethyl xanthate (d) complexes, respectively. The final residues of 23.8, 37.9, 36.8 and 42.4 % were close to the calculated values of 22.8, 35.3, 33.4 and 40.7 % for CdS respectively. Piperidinyl dithiocarbamate cadmium(II) complex was more stable than diethyl dithiocarbamate and dihexyl dithiocarbamate cadmium(II) complexes respectively (see Table 16 showing decomposition

patterns). The ethyl xanthate cadmium(II) complex was less stable due to the resonance effect resulting from the oxygen being more electronegative than nitrogen.

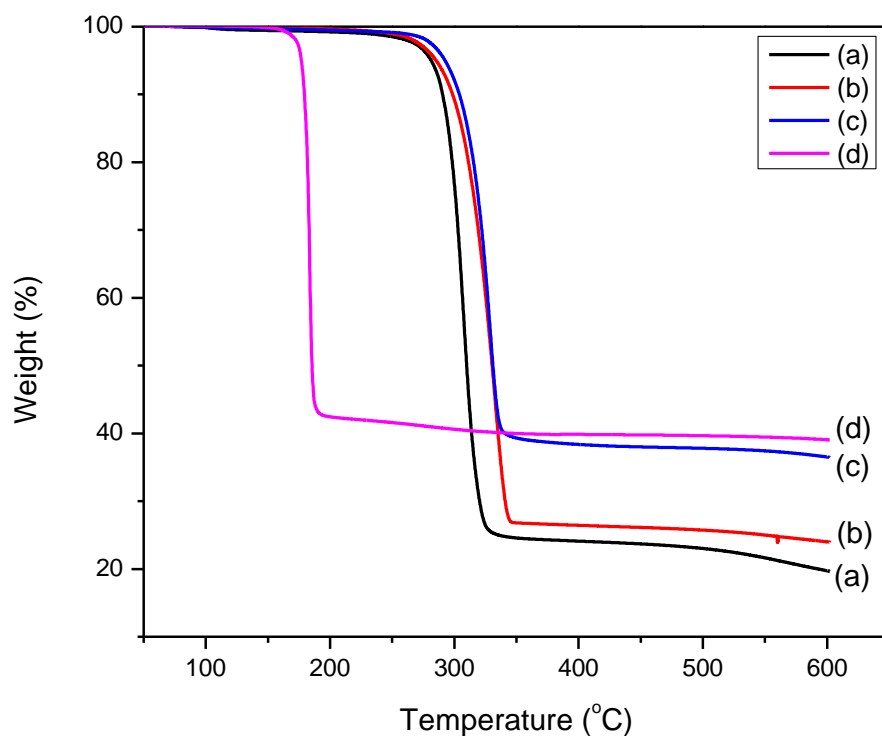


Figure 25. Thermogravimetric analysis (TGA) plots of complexes from Cd(II) dihexyl (a), Cd(II) diethyl (b), Cd(II) piperidinyl dithiocarbamates (c) and Cd(II) ethyl xanthate (d) at a heating rate of $10\text{ }^{\circ}\text{C min}^{-1}$ under nitrogen atmosphere.

Table 16. Data from decomposition patterns.

Complexes	T ($^{\circ}\text{C}$)	Weight loss (%)		Residue (%)	
		(Exp.)	(Calc.)	(Exp.)	Calc.)
(a)	320	76.2	77.2	20.1	22.8
(b)	340	62.1	64.7	31.1	35.3
(c)	334	63.2	66.6	36.8	33.8
(d)	186	57.6	59.3	39.2	40.7

3.1.4. Ethyl xanthate metal complexes of (Cd(II), In(III) and Ga(III))

Cadmium(II), indium(III) and gallium(II) of ethyl xanthate complexes were made up as described in subsection 2.2.6 and their proposed chemical structures are presented in page 46-47. Then they were characterised using some analytical methods reported in subsection 2.6.

3.1.4.1. Syntheses and characterization cadmium(II), indium(III) and gallium(III) complexes of ethyl xanthate

The Cd(II), In(III) and Ga(III) complexes synthesized from ethyl xanthate were obtained in good yields as described in scheme 8. These synthesized compounds were confirmed by microanalysis, ¹H NMR and Thermogravimetric analysis (TGA). The Cd(II) and Ga(III) ethyl xanthate complexes were pale yellowish and cream powder precipitates respectively while colourless crystals were obtained from In(III) ethyl xanthate complex. The Cd(II) and In(III) complexes are air and stable at room temperature while Ga(III) complex is air sensitive. Some elemental analytical and spectroscopic data of the complexes are shown in Table 17 and 18 respectively.

Table 17. Elemental analytical data of the complexes.

Compounds	Yield (%)	Form (color)	MPt (°C)	Elemental analysis			
				Found (calcd)%			
				C	H	S	M(metal)
[Cd(eth-xan) ₂]	96	Precipitate (pale yellowish)	168	20.72 (20.31)	2.80 (2.84)	36.22 (36.15)	31.35 (31.68)
[In(eth-xan) ₃]	60	Microcrystal (colourless)	> 250	22.95 (22.60)	2.94 (3.16)	39.84 (40.21)	23.64 (24.00)
[Ga(eth-xan) ₃]	65	Precipitate (cream powder)	87-88	23.88 (24.96)	3.46 (3.49)	41.52 (44.34)	16.80 (16.12)

[Cd(eth-xan)₂]: bis(ethylxanthato)cadmium(II)

[In(eth-xan)₃]: tris(ethylxanthato)indium(III)

[Ga(eth-xan)₃]: bis(ethylxanthato)gallium(III)

The ^1H NMR spectra of these complexes exhibited characteristic resonances due to the ligand proton at room temperature (Table 18). For any particular metal, we noticed that the ^1H NMR data of the metal complexes of the ligand protons were not much affected by the complexation with ethyl xanthate protons.

Table 18. Spectroscopic data of the complexes.

Compounds	^1H NMR (400 MHz) δ in (ppm)	Molecular formula
Cd(eth-xan)₂	4.5 - 4.47 (q, 4H, CH ₃) 1.51 (t, 6H, CH ₂)	C ₆ H ₁₀ CdO ₂ S ₄
In(eth-xan)₃	4.51 (q, 6H, CH ₃) 1.49 (t, 9H, CH ₂)	C ₉ H ₁₅ InO ₃ S ₆
Ga(eth-xan)₃	4.55 - 4.50 (q, 6H, CH ₃) 1.49 - 1.47 (t, 9H, CH ₂)	C ₉ H ₁₅ GaO ₃ S ₆

The TGA plots of complexes are presented in Figure 26. The TGA profile of Cd(II) ethyl xanthate (Figure 26a) showed a single step decomposition at 180 °C while In(III) ethyl xanthate (Figure 26b) and Ga(III) ethyl xanthate (Figure 26c) showed two step decomposition patterns with the first turning points at 163 and 138 °C respectively. The two-step decomposition suggest the removal of one ligand before the other, with a possible Chugeav elimination mechanism³⁶ (Figure 27). The final weight percentages of 40.62, 35.51 and 26.28 of the residues were close to the expected values of 40.70, 34.05 and 23.50 for CdS, In₂S₃ and GaS respectively, see Table 19 showing decomposition patterns.

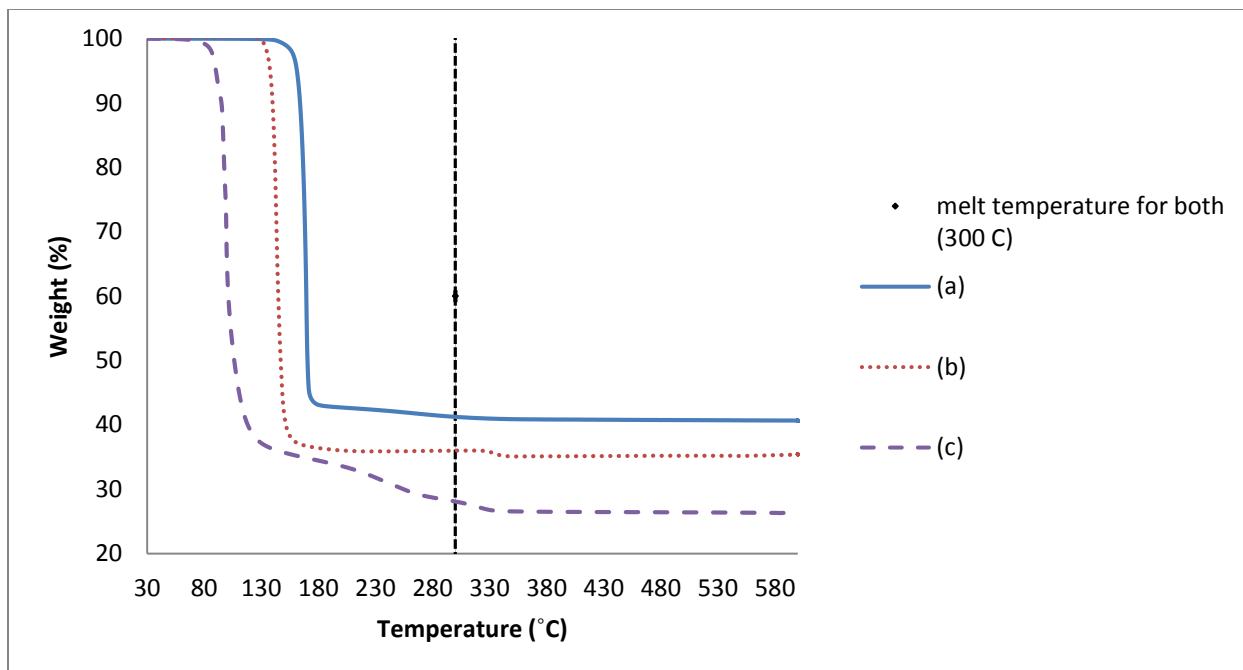


Figure 26. TGA curves for (a) Cd(eth-xan)₂, (b) In(eth-xan)₃ and (c) Ga(eth-xan)₃.

Table 19. Data from decomposition patterns.

Precursors	1 st turning point / °C	Observed percentage weight, %	Calcd percentage weight, %
(a)	169	40.62	40.70 (for CdS)
(b)	145	35.51	34.05 (for In ₂ S ₃)
(c)	94 – 101	26.28	23.50 (for GaS)

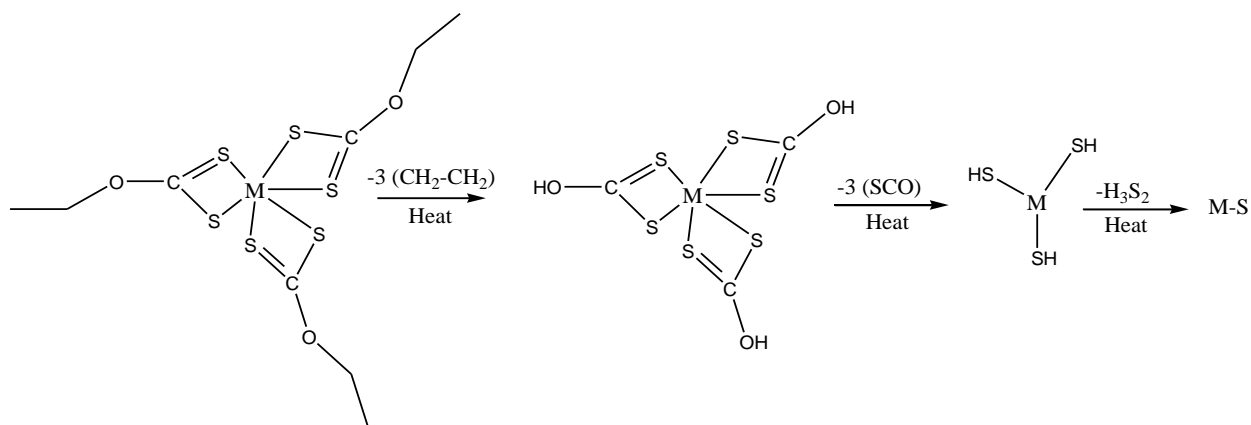


Figure 27. Proposed decomposition of metal ethyl xanthate complexes by a modified Chugaev elimination mechanism.

At about 200 °C, the metal complexes of ethyl xanthate decompose and the alkene is formed by an intramolecular elimination. In a 6-membered cyclic transition state, the hydrogen atom is removed from the carbon atom β to the xanthate oxygen in a *syn*-elimination. The side product decomposes to carbonyl sulfide (OCS) and hydrogen sulfide.

3.2. Organically-capped PbS nanoparticles

The synthesis of semiconductor nanoparticles has been widely investigated over the past years due to their tunable electronic and morphological properties, which make them useful in different applications⁶⁵. Among these various semiconductors, PbS is a II-VI group semiconductor nanomaterial which has unique quantization effects. PbS has a direct band gap of 0.41 eV, a large excitonic Bohr radius of 18 nm^{173,174} and it also displays interesting physical and chemical properties in the nano-size regime. Consequently, PbS nanostructured materials have potential applications in solar cells¹⁷⁵, near infrared (NIR) communications¹⁷⁶, thermal and biological imaging¹⁷⁷, infrared (IR) detectors¹⁷⁸ and light emitting diodes (LEDs).¹⁷⁹

The hot injection is a usual route to synthesize high quality PbS nanoparticles, which can use either multiple or single source precursors (SSPs)^{66,173,180–182}. For instance, Joo and co-workers used lead chloride and sulfur source dissolved in oleylamine as dual sources to synthesize PbS particles¹⁸³. The use of SSPs has lately been favored for size and shape-control, owing to high quality nanostructured materials obtained previously^{30,66,173,180}. Most of the reports on lead complexes employed as SSPs for PbS nanomaterials has been ruled by dithiocarbamates, xanthates and

thiosemicarbazides^{30,65,116,126,173}. Other analogous compounds continue to receive significant attention principally in other fields of research. This is the case of thioureas, which predominate in biological applications^{129,184,185}. Merdivan and co-workers have explored the use of such compounds as ligands for numerous metal complexes^{160,186}. Though diverse preparation protocols have been established for PbS nanostructures^{49,187,188}, very few allow easy access to size, shape and morphology control. As a result, solvent-based preparation protocols such as the solvothermal method¹⁸⁹⁻¹⁹¹, address this matter by using coordinating solvents that play a major role in lowering the decomposition temperature, and stabilizing nanomaterials during and after preparation. Long alkyl chain amines (hexadecylamine and oleylamine) have taken priority owing to high efficiency in producing good quality nanostructures^{192,193}. The use of castor oil as coordinating solvent has also been identified as a green alternative to amines.³⁰

PbS nanoparticles with various morphologies (spheres, cubes, nanorods, dendrites etc.) have been prepared using diverse routes with the goal of finding a way to monitor their shape, size and self-assembly. To achieve this purpose, researchers used some parameters such as the precursor nature, the monomer concentration, the capping agent nature, the reaction time and the reaction temperature.

3.2.1. Preparation and characterization of PbS nanoparticles using lead N-morpholine-N'-benzoylthiourea as precursor in oleylamine and castor oil solvents

PbS nanoparticles were prepared as described in section 2.3.1, page 48. A specified amount of 0.3 mmol (0.2 g) of Pb-morphthu complex previously dispersed in 3.0 mL of OLA was injected into 5.0 mL of hot capping agent (OLA or CO) at a desired temperature. The procedure was repeated varying some parameters such as the nature of the capping agent and the reaction temperature.

Our goal is to study the effect of the capping agents (OLA and CO), on the morphology and optical properties of PbS nanoparticles at various reaction temperatures.

3.2.1.1. Syntheses of oleylamine OLA-capped PbS nanoparticles

The preparation of PbS nanoparticles in 5 mL of OLA using the Pb-morphthu complex at 150 °C led to the formation of spherical to oval shaped PbS crystals with an average size of 29.2 ± 3 nm (Figure 28a). At the reaction temperature of 200 °C, elongated PbS nanorods were obtained with

an average breadth of 21.90 ± 4.20 nm and length of 66.00 ± 10.40 nm which are aggregates forming a long chain (Figure 28b). When the temperature was raised from 200 °C to 250 °C, cubic shaped PbS nanoparticles were obtained with an average size of 37.53 ± 4.93 nm (Figure 28c).

Some studies reported that primary amines such as oleylamine preferentially coordinate to the [111] facets of PbS thereby preventing the formation of [100] terminated cubes. Warner and co-workers reported on the formation of PbS nanocubes prepared in oleylamine mentioning the presence of lead acetate in the synthetic procedure which prevents the formation of spherical PbS nanoparticles.¹⁹⁴

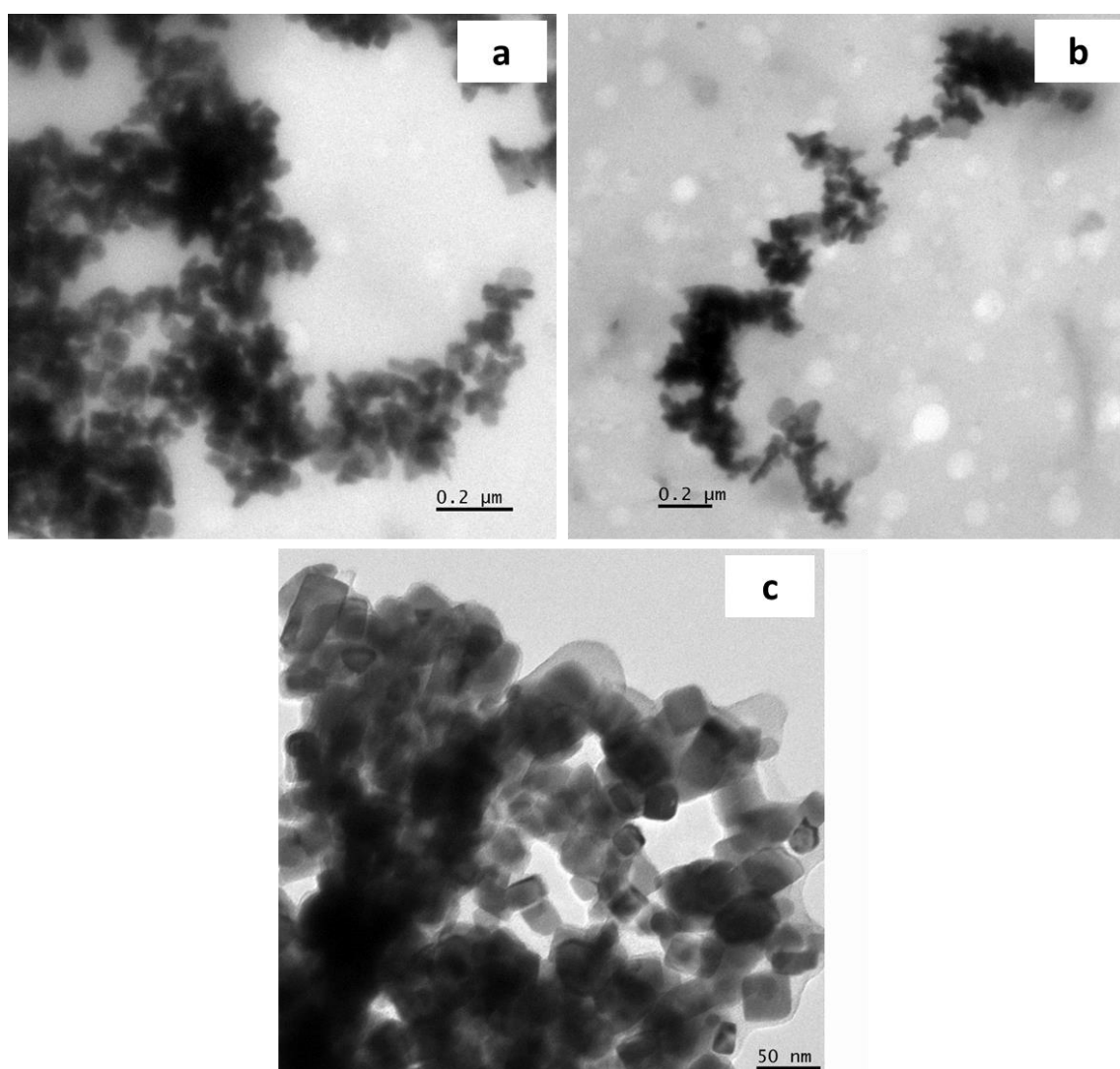


Figure 28. TEM images of PbS nanoparticles prepared from Pb-morphu in OLA at a) 150 °C, b) 200 °C and c) 250 °C.

The powder X-ray diffraction patterns of the PbS nanoparticles prepared in OLA at the different temperatures (150, 200 and 250 °C) reveal the characteristic (111), (200), (220), (311), (222), (400), (331), (420) and (422) peaks of cubic rock salt PbS (card #: 00-005-0592) (Figure 29). No any other peak was observed suggesting that pure PbS was obtained.

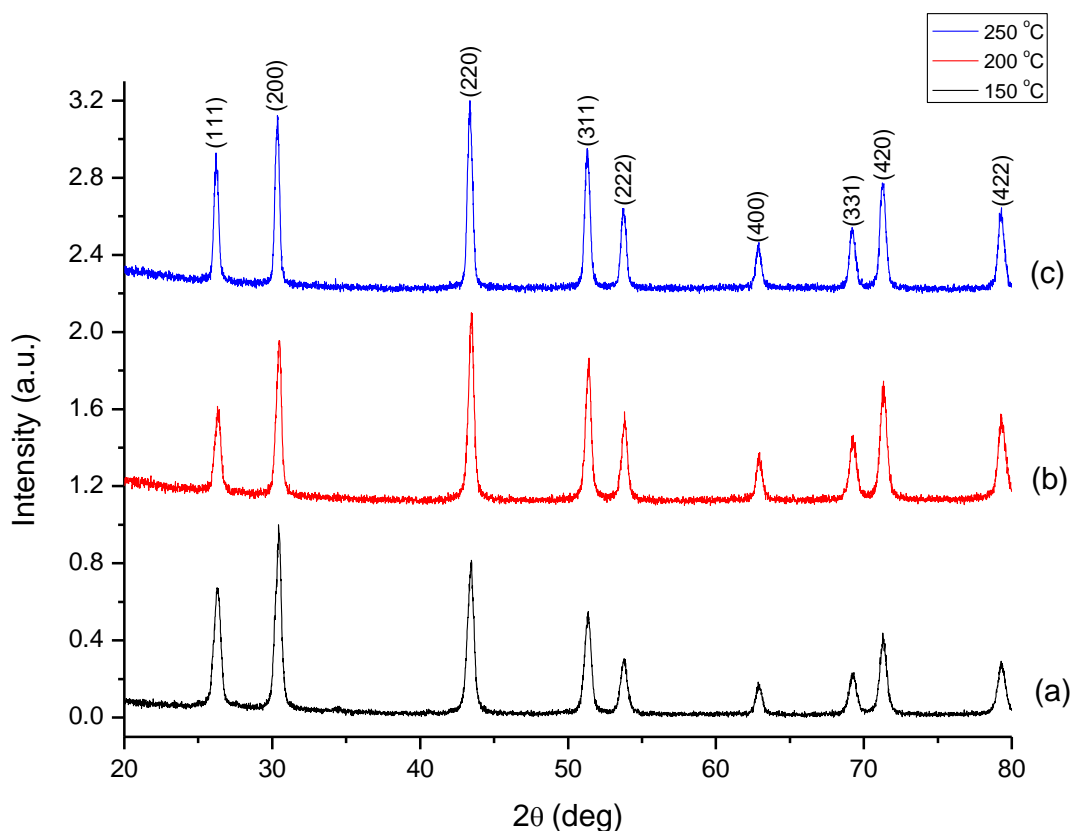


Figure 29. Powder X-ray diffractograms of PbS nanoparticles prepared from Pb-morphu in OLA at a) 150 °C, b) 200 °C and c) 250 °C.

The optical properties (NIR UV) of the PbS nanoparticles synthesized from the hot injection of Pb-morphu complex in 5 mL of oleylamine (OLA) at different temperatures (150, 200 and 250 °C) are showed in Figure 30. The absorption spectra displayed broad absorption band edges at around 400-900 nm, 600-1200 nm and 700-1200 nm respectively showing a blue shift compared to the bulk PbS (3100 nm)¹⁹⁵. An increase of the absorption band edge as the reaction temperature was raised from 150 °C to 250 °C is observed. This may possibly be the result of position-dependent quantum confinement effects.⁶⁵

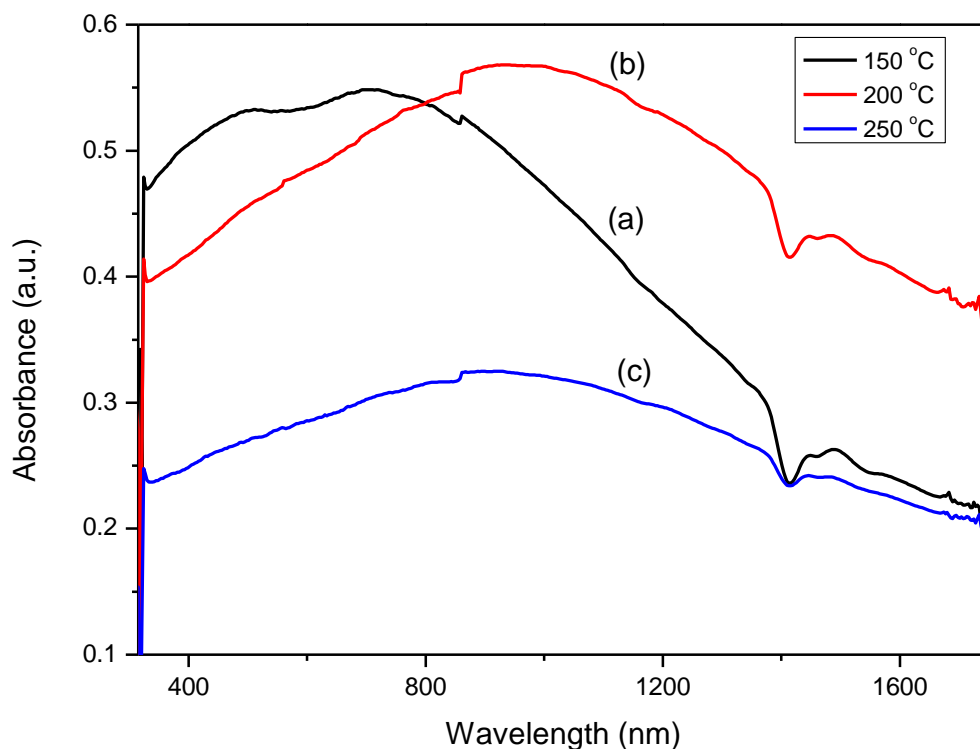


Figure 30. NIR UV absorption spectra of PbS nanoparticles prepared from Pb-morphthu in OLA at a) 150 °C, b) 200 °C and c) 250 °C.

3.2.1.2. Syntheses of castor oil CO-capped PbS nanoparticles

The use of coordinating solvents in the preparation of PbS nanoparticles has shown to be very efficient. Different shapes PbS nanoparticles were found when the Pb-morphthu was thermolysed in oleylamine (OLA). We changed the amine-capping agent to the use of castor oil (CO) as a coordinating solvent in the synthesis of PbS nanoparticles while hoping to have an efficient greener capping in the PbS nanoparticles preparation.

A mass of 0.2 g of the Pb-morphthu previously dispersed in 3 mL of CO was injected into 5 mL of hot castor oil at various reaction temperatures of 150 °C, 200 °C and 250 °C. The TEM image of the Pb-morphthu complex thermolysed at 150 °C gave spherical to cubic shaped PbS particles with an average size of 9.83 ± 1.97 nm (Figure 31a). The diffraction rings in the selected area electron diffraction (SAED) patterns from Pb-morphthu complex at 150 °C (Figure 31b) confirms the

formation of crystalline PbS nanoparticles composed of polycrystals of the cubic rock salt phase. An increase of temperature from 150 °C to 200 °C resulted in a change of the PbS particles to predominantly cubic or close to cubic with a considerable increase in the average size of 26.16 ± 3.63 nm was observed (Figure 31c). When the reaction temperature was increased to 250 °C, cubic shaped PbS nanoparticles were formed with an average size of 74.04 ± 8.96 nm (Figure 31d).

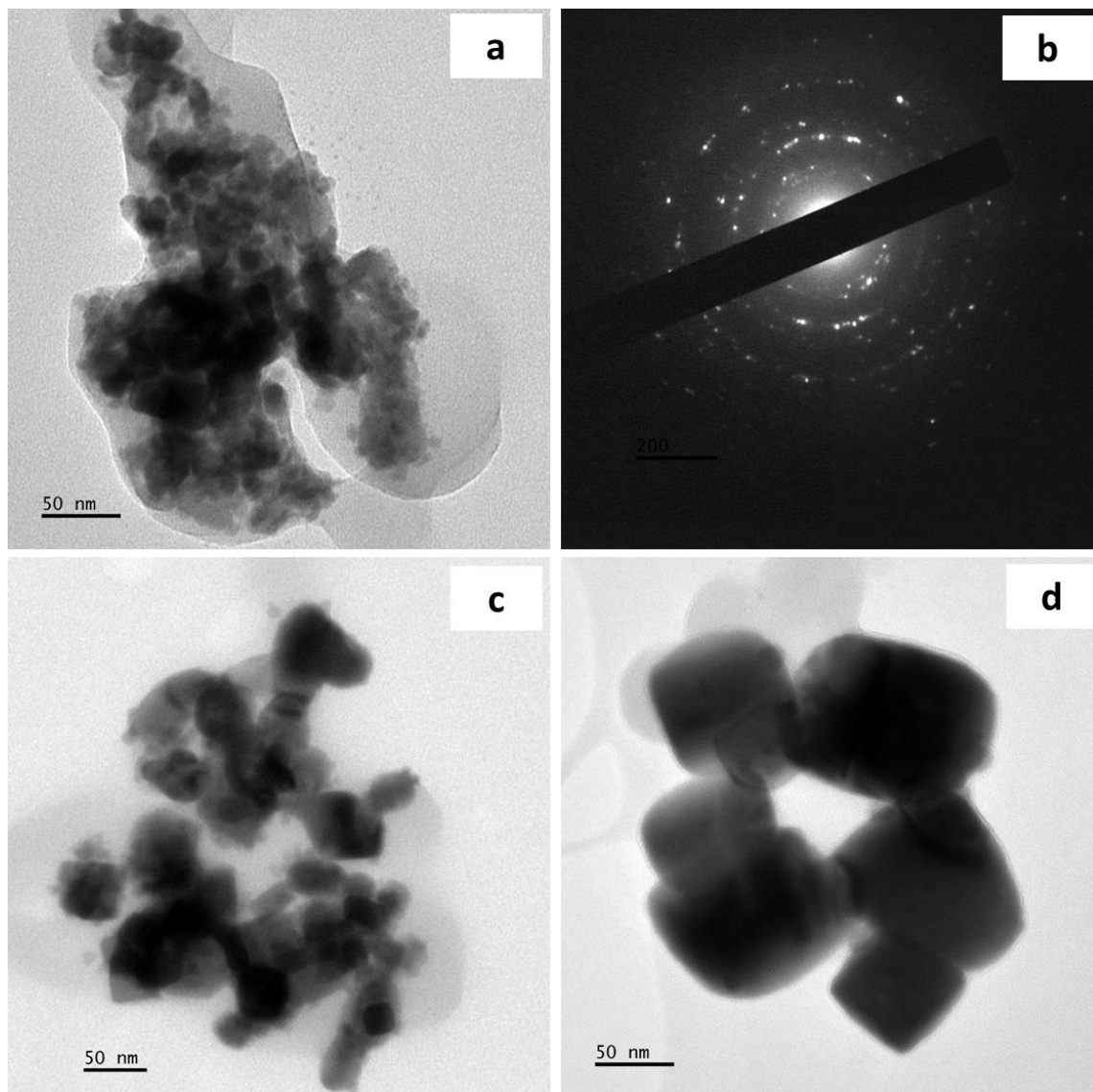


Figure 31. TEM images of PbS nanoparticles prepared from Pb-morphu in CO at a) 150 °C with corresponding b) SAED image, c) 200 °C and d) 250 °C.

The powder X-ray diffraction patterns of the PbS particles prepared in CO is presented in Figure 32. All the peaks are indexed to the cubic rock salt phase of PbS. A slight decrease in the intensity of peaks at 250 °C is observed (Figure 32c). This might be due to the by-products resulting from the decomposition of the complex.

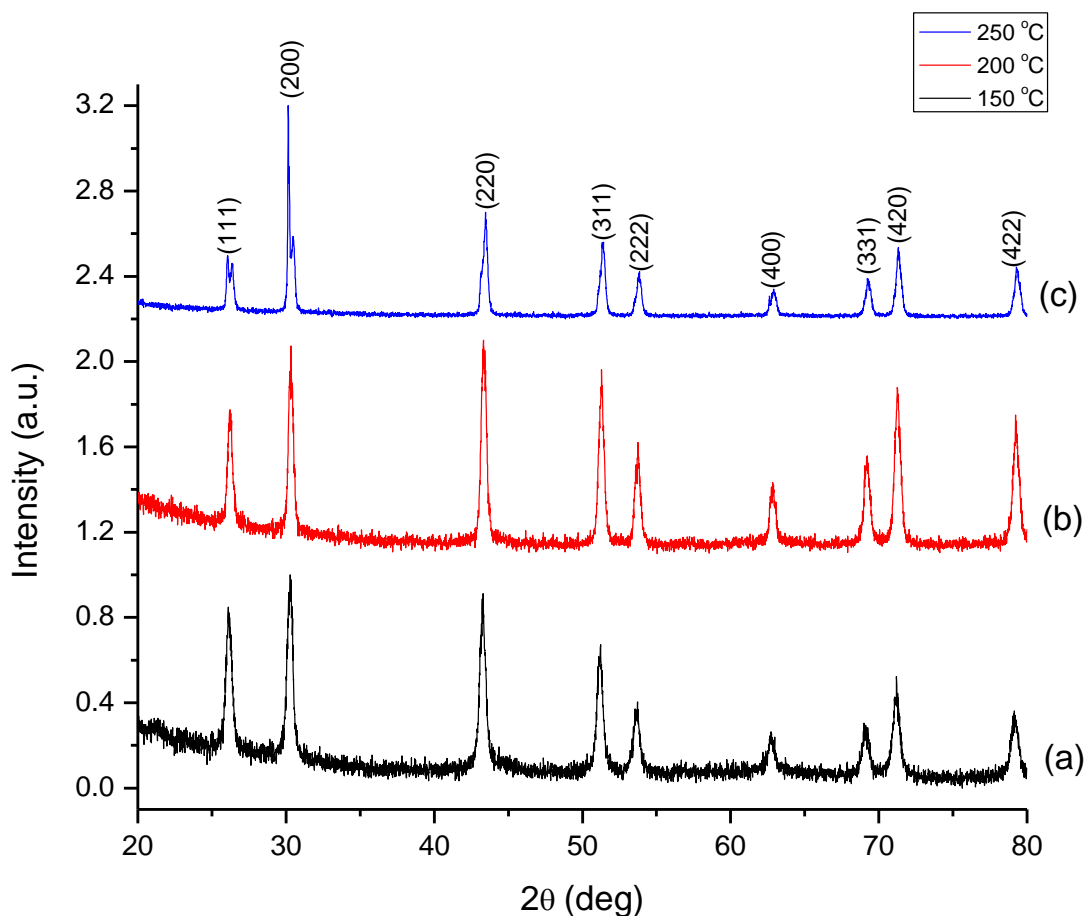


Figure 32. Powder X-ray diffractograms of PbS nanoparticles prepared from Pb-morphu in CO at a) 150 °C, b) 200 °C and c) 250 °C.

The NIR UV spectra of the PbS particles showed that absorption bands of particles prepared from the thermolysis of Pb-morphu complex in 5 mL of castor oil (CO) at all reaction temperatures (150, 200 and 250 °C) are blue shifted as compared to bulk PbS (3100 nm). Figure 33 shows absorption spectra of castor oil capped PbS nanoparticles displaying broad absorption band edges at around 380-500 nm, 600-900 nm and 1200-1700 nm corresponding to 150, 200 and 250 °C respectively. However, a small red shift of the absorption peaks as the reaction temperature was

raised from 150 °C to 250 °C is observed. This result could be due to position-dependent quantum confinement effects.

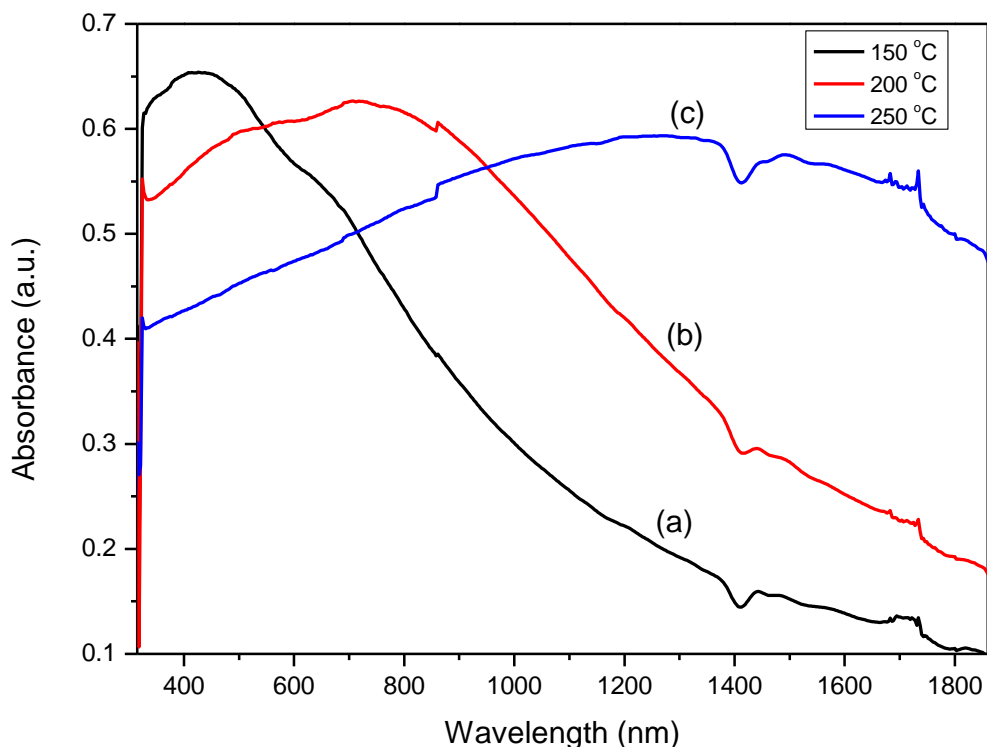


Figure 33. NIR UV absorption spectra of PbS nanoparticles prepared from Pb-morphu in CO at a) 150 °C, b) 200 °C and c) 250 °C.

To conclude, we can say that varying the reaction temperature (150 °C, 200 °C and 250 °C) and the capping agents (OLA and CO) in a reaction resulted in the formation of different PbS nanoparticles shapes. Likewise, the Pb-morphu precursor might have an influence on the final morphology of PbS particles. The utilization of long chain amines as coordinating solvents has proven to be very successful in the synthesis of nanocrystals. Li and co-workers reported that the high reaction temperature (250 – 350 °C) simplifies the dynamic bonding of the surface ligands to the nanoparticles in the hot injection technique¹⁹⁶. In addition, the crystallinity of the particles is improved by high temperature. At high temperatures, the influence of the surface ligands are

reduced through the dynamic bonding nature of the ligands leading to thermodynamically stable shaped nanoparticles such as spheres. Whereas the low temperatures methods provide more flexibility in shape control with anisotropic shaped particles such as rods formed through careful utilization of surfactants.

3.2.2. Preparation and characterization of PbS nanoparticles using lead N-pyrrolidine-N'-benzoylthiourea as precursor in oleylamine and castor oil solvents

PbS nanoparticles were prepared as described in section 2.3.1, page 48 where a mass of 0.2 g of the Pb-pyrrtu complex previously dispersed in 3.0 mL of OLA was injected into 5.0 mL of hot capping agent (OLA or CO) at a desired temperature. The procedure was repeated varying some parameters such as the nature of the capping agent and the reaction temperature. Our aim in this section, is to study the effect of the capping groups (OLA and CO), on the shape and optical properties of PbS nanoparticles at various reaction temperatures.

3.2.2.1. Syntheses of oleylamine OLA-capped PbS nanoparticles

The Pb-pyrrtu complex was thermolysed in OLA at 150 °C, the TEM images showed agglomerates spherical PbS particles with an average size of 9.5 ± 0.6 nm (Figure 34a). When the reaction temperature was increased to 200 °C, a change in the PbS particle from spherical to cubic was observed as shown in Figure 34b. The average size of the PbS particles was 21.2 ± 2 nm. The diffraction rings in the selected area electron diffraction (SAED) patterns from Pb-pyrrtu complex at 200 °C (Figure 34c) approves the formation of crystalline PbS nanoparticles composed of polycrystals of the cubic rock salt phase. When the reaction temperature was increased from 200 °C to 250 °C, cubic shaped PbS particles with an average size of 41.0 ± 4 nm were obtained as presented in Figure 34d. These results are close to those found by Nyamen and co-workers¹⁷³. This evolution in shape and size from spherical to cubes can be attributed to the increase of reaction temperature. It can also be proposed that, the nature of the precursor does also involve in the shape evolution of the PbS particles. Primary amines such as OLA selectively adsorb onto different facets allowing the growth along a certain facet and prevents the growing along another one. The decomposition profile of the complex may also play a role in the growth mechanism and final morphology. However, few reports endeavor to link the nature of the precursor to the growth

dynamics of the particles, therefore no conclusive evidence on how the nature of the precursor affects the morphology of the nanoparticles has been elucidated.^{54,197}

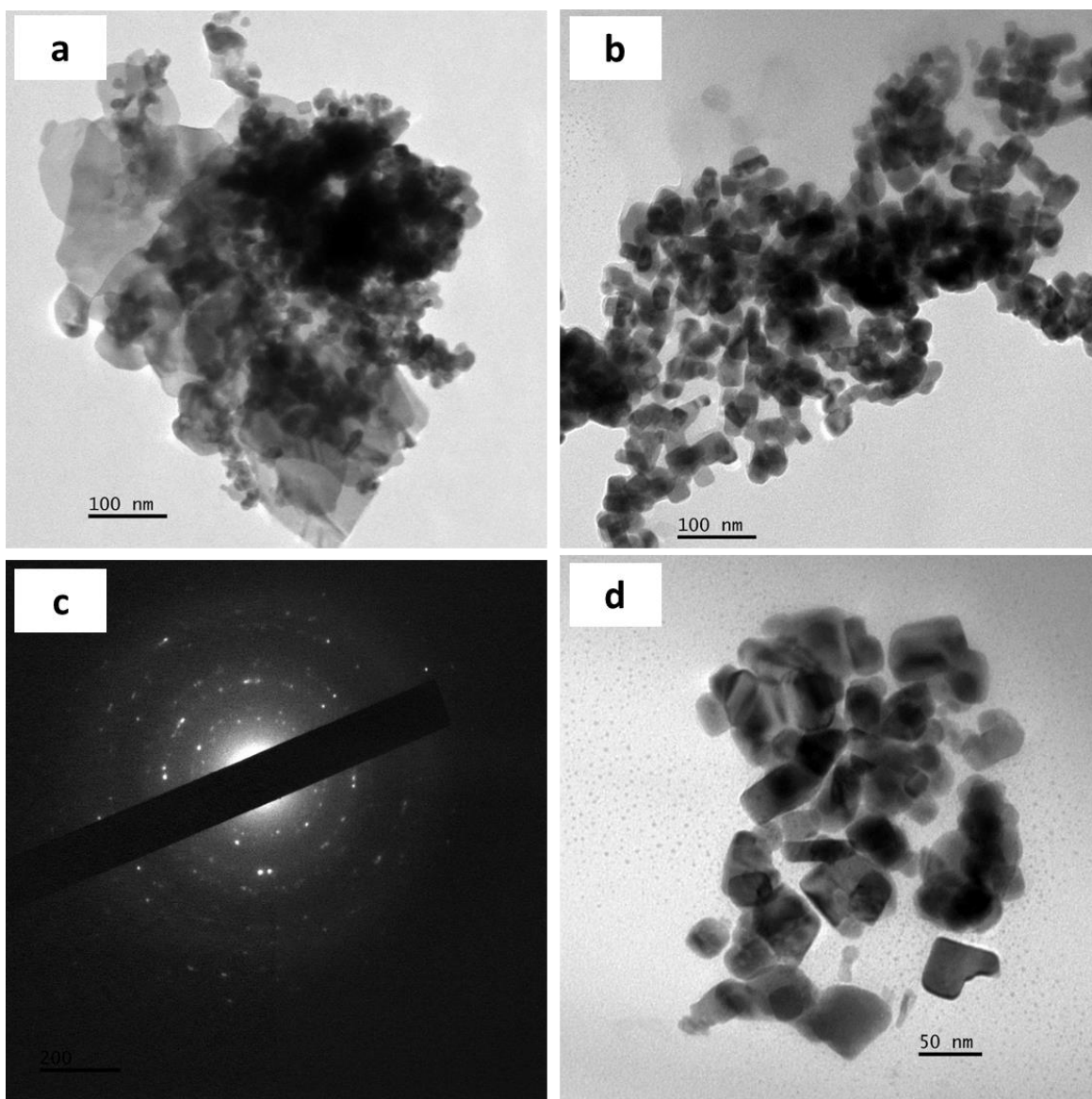


Figure 34. TEM images of PbS nanoparticles prepared from Pb-pyrrtu in OLA at a) 150 °C, b) 200 °C with corresponding c) SAED image and d) 250 °C.

The powder X-ray diffraction patterns of the PbS nanoparticles prepared in OLA at various reaction temperatures confirmed the crystalline nature of the material. The characteristic planes of cubic rock salt PbS are observed (Figure 35).

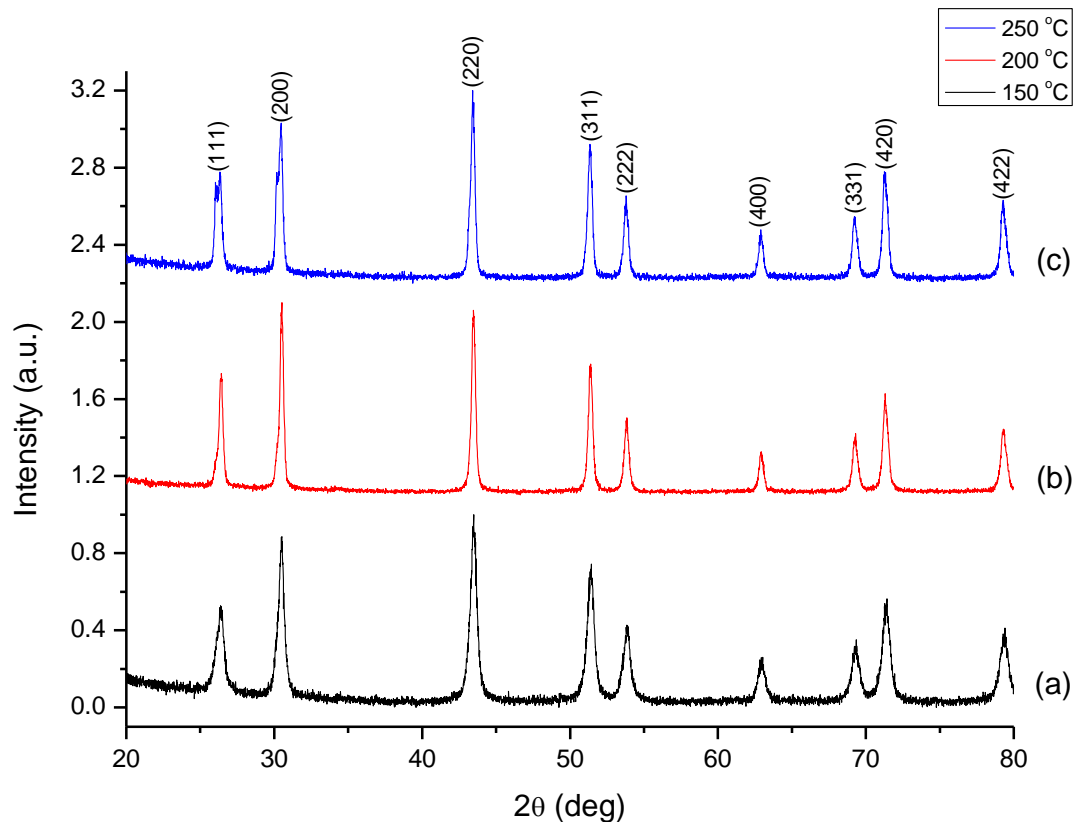


Figure 35. Powder X-ray diffractograms of PbS nanoparticles prepared from Pb-pyrriu in OLA at a) 150 °C, b) 200 °C and c) 250 °C.

The optical properties (NIR UV) of the PbS nanoparticles synthesized from the thermolysis of Pb-pyrriu complex in 5 mL of oleylamine (OLA) at various temperatures (150, 200 and 250 °C) are presented in Figure 36. The absorption spectra showed broad absorption band edges at around 450-700 nm, 700-1100 nm and 800-1300 nm respectively showing a blue shift compared to the bulk PbS (3100 nm). We also note an increase of the absorption band edge as the reaction temperature was increased from 150 °C to 250 °C is observed. This can be the result of position-dependent quantum confinement effects.

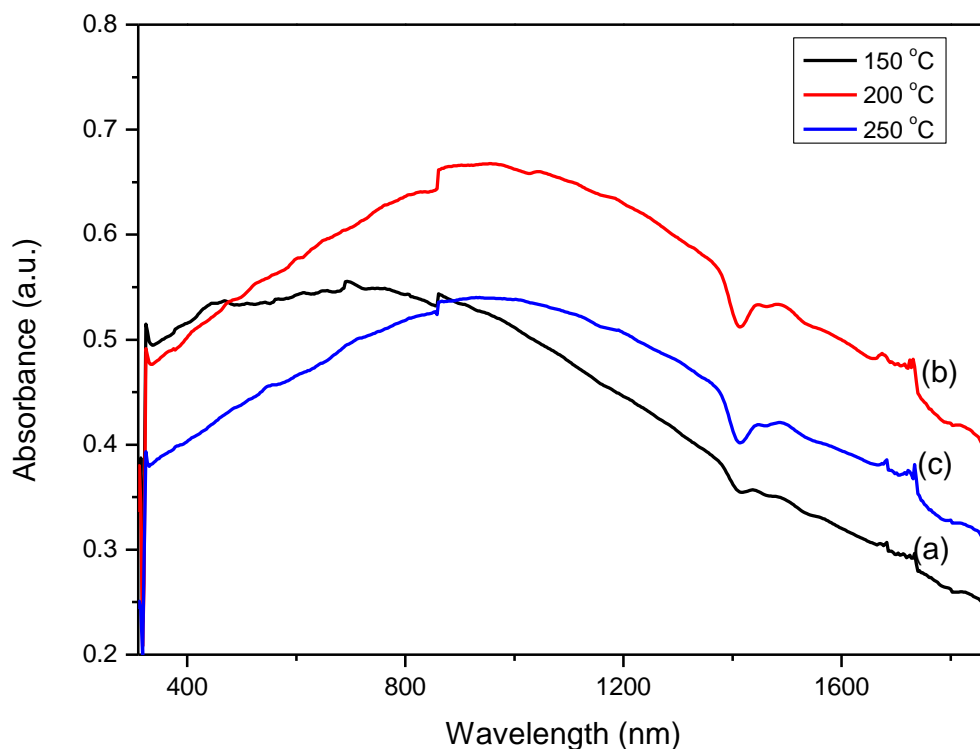


Figure 36. NIR UV absorption spectra of PbS nanoparticles prepared from Pb-pyrirtu in OLA at a) 150 °C, b) 200 °C and c) 250 °C.

3.2.2.2. Syntheses of castor oil CO-capped PbS nanoparticles

The Pb-pyrirtu complex was thermolysed in CO at 150 °C, 200 °C and 250 °C. At the reaction temperature of 150 °C, spherical to cubic shaped PbS particles were obtained (Figure 37a) with an average size of 17.2 ± 3 nm. When the reaction temperature was raised to 200 °C, predominantly cubic shaped PbS particles which an average size of 35.8 ± 5 nm were obtained (Figure 37c). The diffraction rings in the selected area electron diffraction (SAED) patterns from Pb-pyrirtu complex at 150 °C and 200 °C (Figure 37b and 37d) settle the obtaining of crystalline cubic rock salt phase PbS nanoparticles, respectively. When the reaction temperature was increased from 200 °C to 250 °C, well cubic shaped PbS nanoparticles with an average size of 74.4 ± 11 nm were obtained (Figure 37e). The increase of size of the nanoparticles with the reaction temperature can be

clarified through the Ostwald ripening process where small particles dissolve to form bigger particles.³⁹

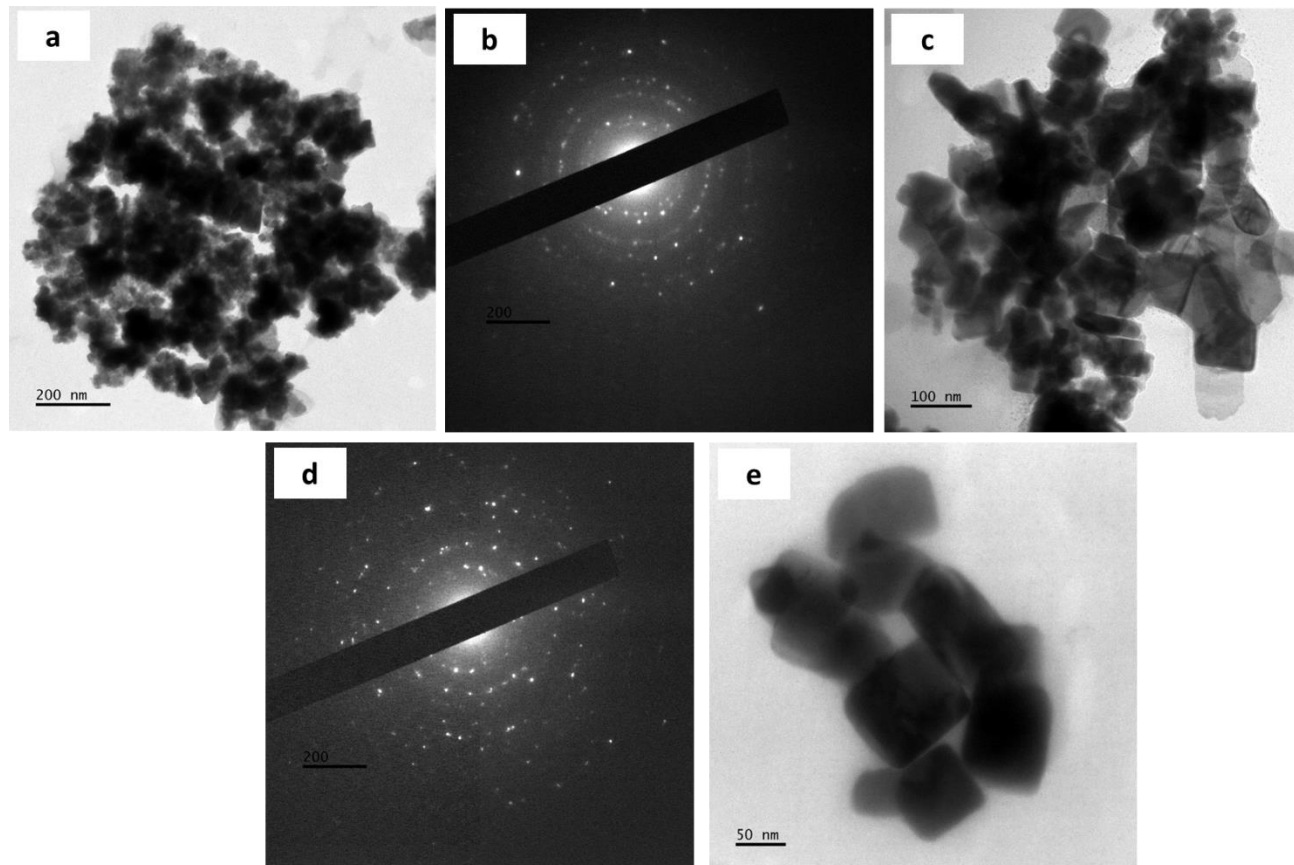


Figure 37. TEM images of PbS nanoparticles prepared from Pb-pyrtru in CO at a) 150 °C with corresponding b) SAED image, c) 200 °C with corresponding d) SAED image and e) 250 °C.

The P-XRD patterns of the PbS particles confirmed the high crystallinity of the particles and the characteristic planes of the cubic rock salt PbS (Figure 38). In addition, no other peak as impurity was observed.

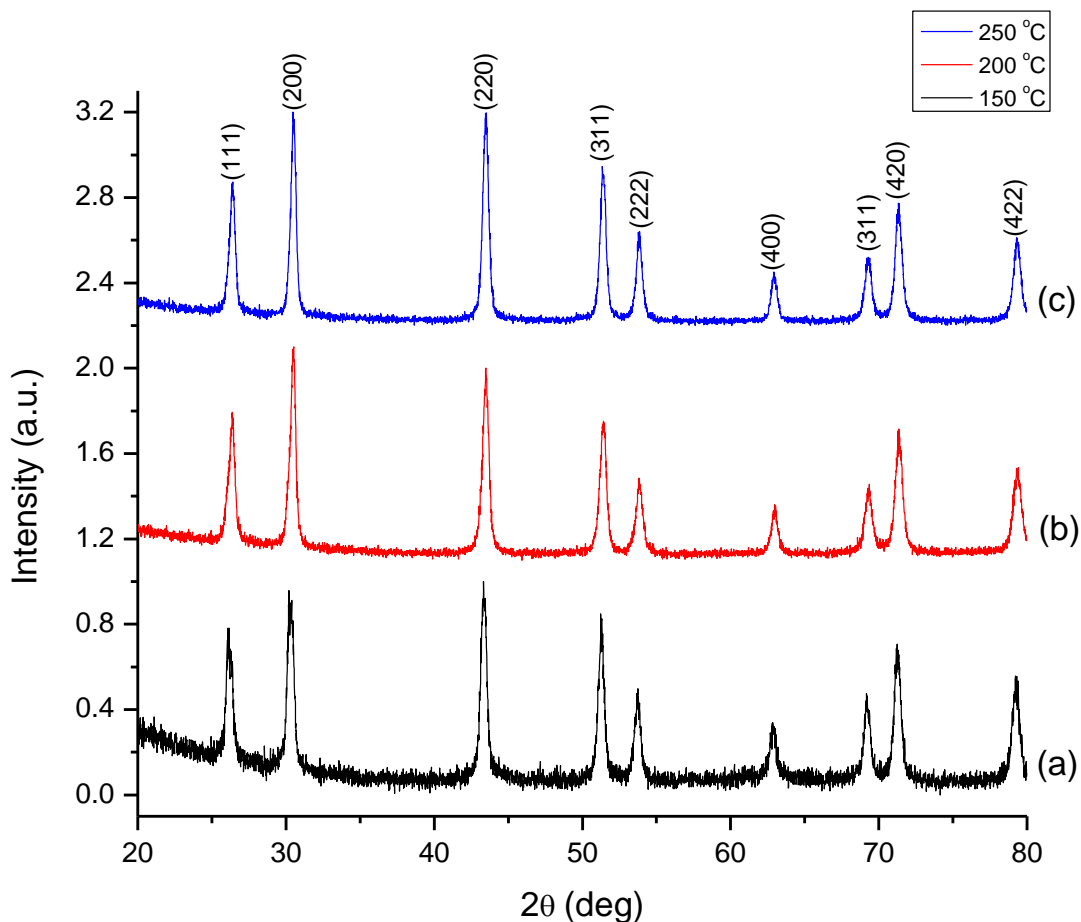


Figure 38. Powder X-ray diffractograms of PbS nanoparticles prepared from Pb-pyrrtu in CO at a) 150 °C, b) 200 °C and c) 250 °C.

The NIR UV spectra of the PbS particles showed that absorption bands of particles prepared from the hot injection of Pb-pyrrtu complex in 5 mL of castor oil (CO) at all various temperatures (150, 200 and 250 °C) are blue shifted as compared to bulk PbS (3100 nm). Figure 39 presents absorption spectra of castor oil capped PbS nanoparticles showing broad absorption band edges at around 380-500 nm, 600-900 nm and 1200-1700 nm corresponding to 150, 200 and 250 °C respectively. Nonetheless, a small red shift of the absorption peaks as the reaction temperature was increased from 150 °C to 250 °C is observed. This result possibly will be due to position-dependent quantum confinement effects.

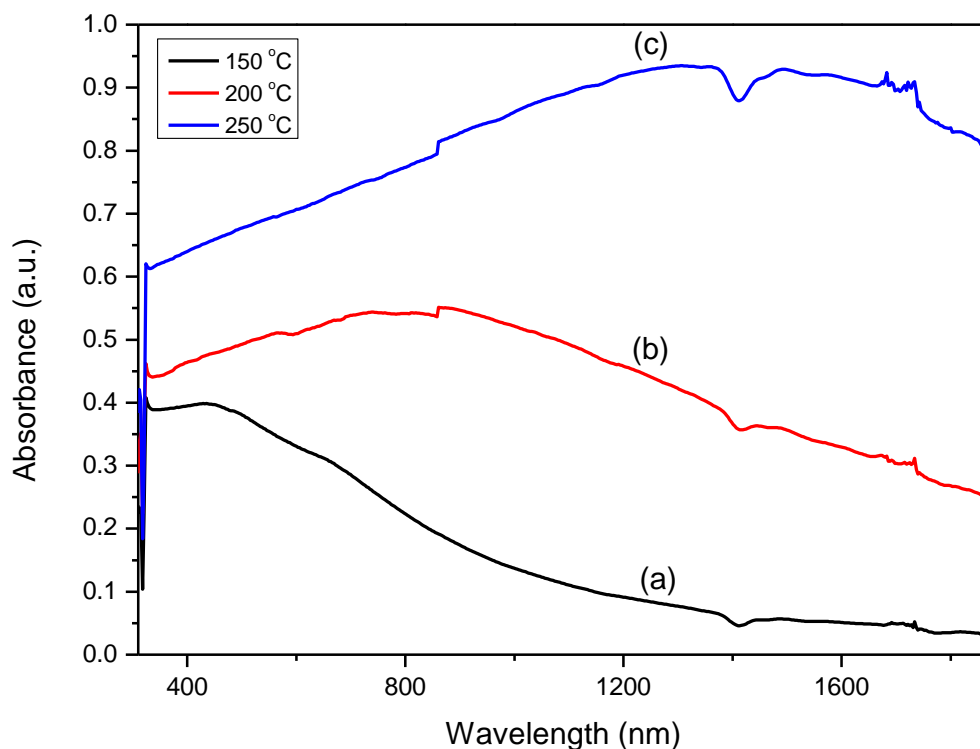


Figure 39. NIR UV absorption spectra of PbS nanoparticles prepared from Pb-pyrirtu in CO at a) 150 °C, b) 200 °C and c) 250 °C.

To summarize, we have reported the preparation and characterization of lead morpholine and lead pyrrolidine benzoylthiourea complexes and their utilization as molecular precursors for the fabrication of PbS particles. The hot injection of the complexes in capping agents such as OLA and CO gave PbS particles with different morphologies. The OLA-capped PbS nanoparticles were regular spherical shaped at low temperature (150 °C) but transformed to rods and cubic shaped at higher temperatures (200 °C and 250 °C) for the Pbmorphtu complex. While the thermolysis of the Pbpyrrtu complex gave spherical shaped particles at low temperature (150 °C) and cubes at high temperatures (200 °C and 250 °C). Whereas, in CO, the particles obtained were very crystalline, with the formation of spherical and cubic shaped particles in the thermolysis of the Pbmorphtu complex at low temperature (150 °C) and high temperatures (200 °C and 250 °C) respectively. The optical properties of the PbS nanoparticles prepared from the Pb-morphtu complex showed a considerable blue shift as compared to the bulk PbS (3100 nm). However, a

smooth decrease in the optical absorption from the near UV to the NIR was always detected with the increase of the reaction temperature. This is due to the increase in particle size with temperature. The same tendency was observed with the Pb-pyrrtu precursor.

The reaction temperature has proven to have a great influence on the shape and size of the prepared PbS nanoparticles. In addition, the nature of the lead complex showed some effect on the evolution of the shape of the PbS particles. We also noticed that the PbS nanocrystals fabricated in our work are slightly bigger than the particles prepared by the hot injection method. This can be explained by the influence of the precursor nature on the growth mechanism, which results in the formation of large facet particles.

3.3. Organically-capped Cu_xS_y nanoparticles

Copper sulfide is a p-type semiconductor, which has found applications in diverse fields such as, photo catalysis, solar cells, sensors, lithium ion batteries and supercapacitors^{198–200}. It has an indirect band gap of ~1.2 eV (for chalcocite) and 1.5 eV (for digenite)²⁰¹. It is found in many stoichiometric compositions ranging from the copper rich phase of chalcocite Cu_2S , djurleite $\text{Cu}_{1.96}\text{S}$, digenite $\text{Cu}_{1.8}\text{S}$, anilite $\text{Cu}_{1.75}\text{S}$ to copper poor phase of covellite CuS and villamaninite CuS_2 .^{202–204}

Previous reports on the synthesis of copper sulfide nanostructures resulted in the formation of spheres, hexagons, triangular nanoplates, nanorods, nanodiscs and nanowires^{205–207}. Khan and co-workers have prepared copper sulfide nanoparticles with various shapes and super-lattices using the bis(O-isobutyldithiocarbonato)copper(II) complex via the hot injection route⁶⁴. Mundher and co-workers reported on the preparation of monodisperse copper sulfide nanorods via the hot injection of novel xanthate copper complexes. They showed that the width of the obtained rods is dependent on the length of the xanthate chain²⁰⁸. Similarly, Chen et al synthesized nanoplates of Cu_2S and nanoflakes of CuS following the thermal decomposition of $[\text{Cu}(\text{acac})_2]$ (acac = acetylacetonate) with elemental sulfur in oleylamine^{209,210}. They also synthesized Cu_2S nanoparticles using cysteine as the sulfur source. As a result, thermal decomposition of precursors including $[\text{Cu}(\text{acac})_2]$ or CuCl_2 and elemental sulfur or dodecanethiol, revealed hexagonal nanodisks of CuS , Cu_7S_4 and Cu_2S .^{206,211,212}

3.3.1. Preparation and characterization of Cu_xS_y nanoparticles using copper N-morpholine-N'-benzoylthiourea as precursor in oleylamine and 1-dodecanethiol solvents

Copper sulfide nanoparticles were prepared as described in section 2.3.2, page 69. Firstly, a three-necked flask was purged with N_2 , after applying vacuum for few times at room temperature, using a Schlenk line to evacuate any air. Then, a mass of 0.2 g of the Cu-morphtu complex previously dispersed in 3 mL of (OLA and/or DT) was injected into 5 mL of hot OLA or DT at a wanted temperature. The procedure was repeated varying some parameters such as the nature of the capping agent and the reaction temperature. Our aim here is to study the effect of reaction temperature and coordinating solvents, such as, oleylamine and 1-dodecanethiol, on the shape and crystal phase of the as-synthesized copper sulfide nanoparticles.

3.3.1.1. Syntheses of oleylamine OLA-capped Cu_xS_y nanoparticles

Oleylamine (OLA) has a dual role in being an effective coordinating solvent, and also it is known to help in the decomposition of the precursor^{213,214}. When the Cu-morphtu complex was dispersed in OLA, the color of the complex started changing from green to greenish brown, which may indicate the interaction of OLA with the complex and its decomposition. The solution was then directly injected into the hot OLA at the preferred growth temperatures (150 – 250 °C).

The TEM images shown in Figure 40 revealed that the as-synthesized nanoparticles from Cu-morphtu complex at 150 °C (Figure 40a) have apparently spherical morphology with an average size of 13 ± 1 nm. When the temperature was raised to 200 °C, an increase of the average size (15.9 ± 2 nm) of the particles and agglomeration (Figure 40b) occurred. When the reaction was carried out at 250 °C the size further increased (49.6 ± 11 nm) with a broader size distribution, some elongated particles also start to appear (Figure 40c) due to interparticle aggregation. The diffraction rings in the selected area electron diffraction (SAED) patterns from Cu-morphtu complex at 250 °C (Figure 40d) confirms the formation of crystalline copper sulfide nanoparticles composed of polycrystals of the roxbyite phase.

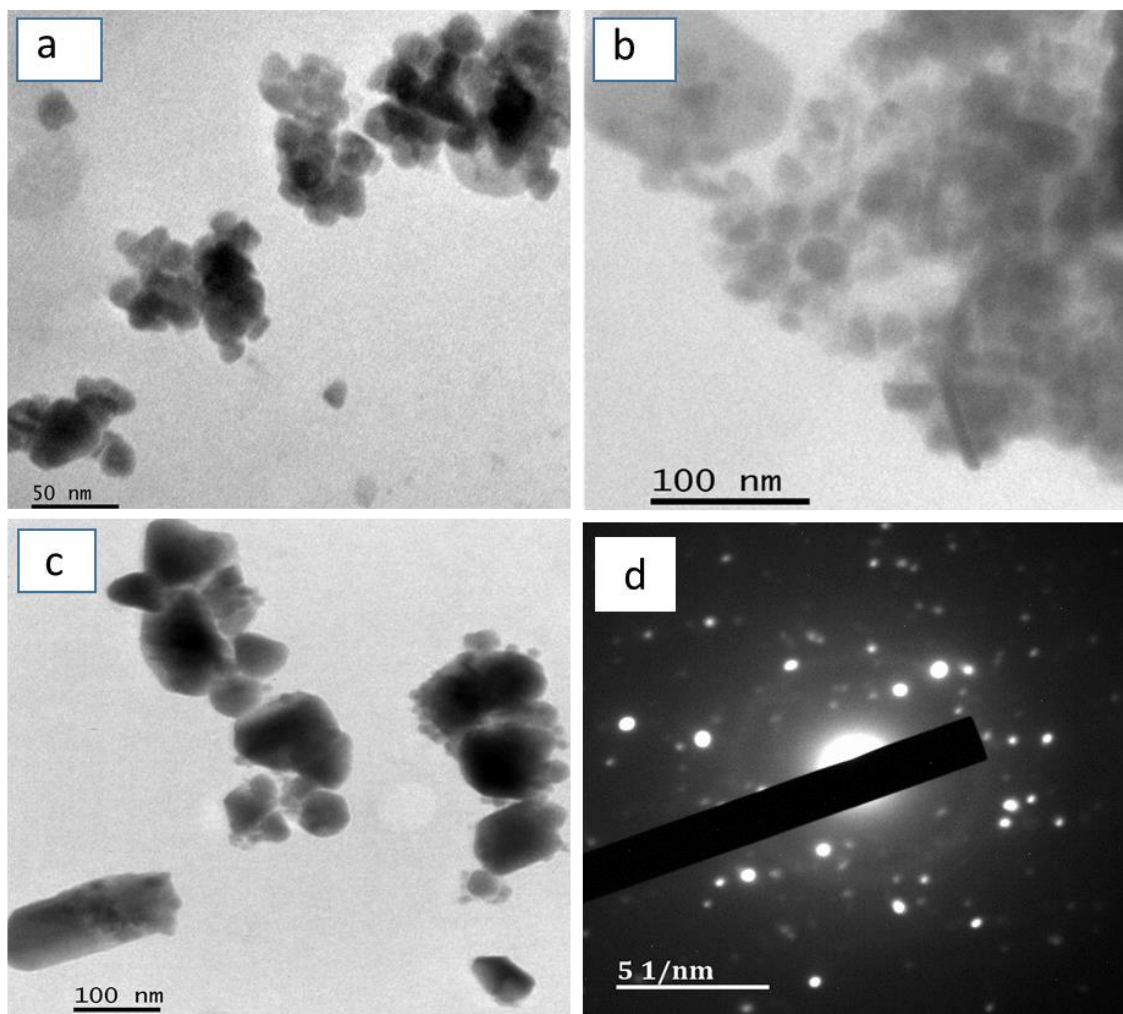


Figure 40. TEM images of copper sulfide nanoparticles prepared at (a) 150 °C, (b) 200 °C and (c) 250 °C, from Cu-morphu complex respectively when OLA is used both as dispersion solvent and capping agent; (d) showing the selected area electron diffraction (SAED) patterns of nanoparticles prepared at 250 °C from Cu-morphu complex.

The powder X-ray diffraction peaks of the nanoparticles prepared from Cu-morphu complex (Figure 41) are indexed to the roxbyite phase (ICDD# 00-023-0958) with no presence of any other phase as an impurity. As such, the peak width broadness is in accordance with the small size of the nanospheres. The intensity of the peaks increases slightly with increasing temperature. However, the peak present at the 2θ value of 46.5° was the most intense at all temperatures, which may indicate a preferred orientation along that plane.

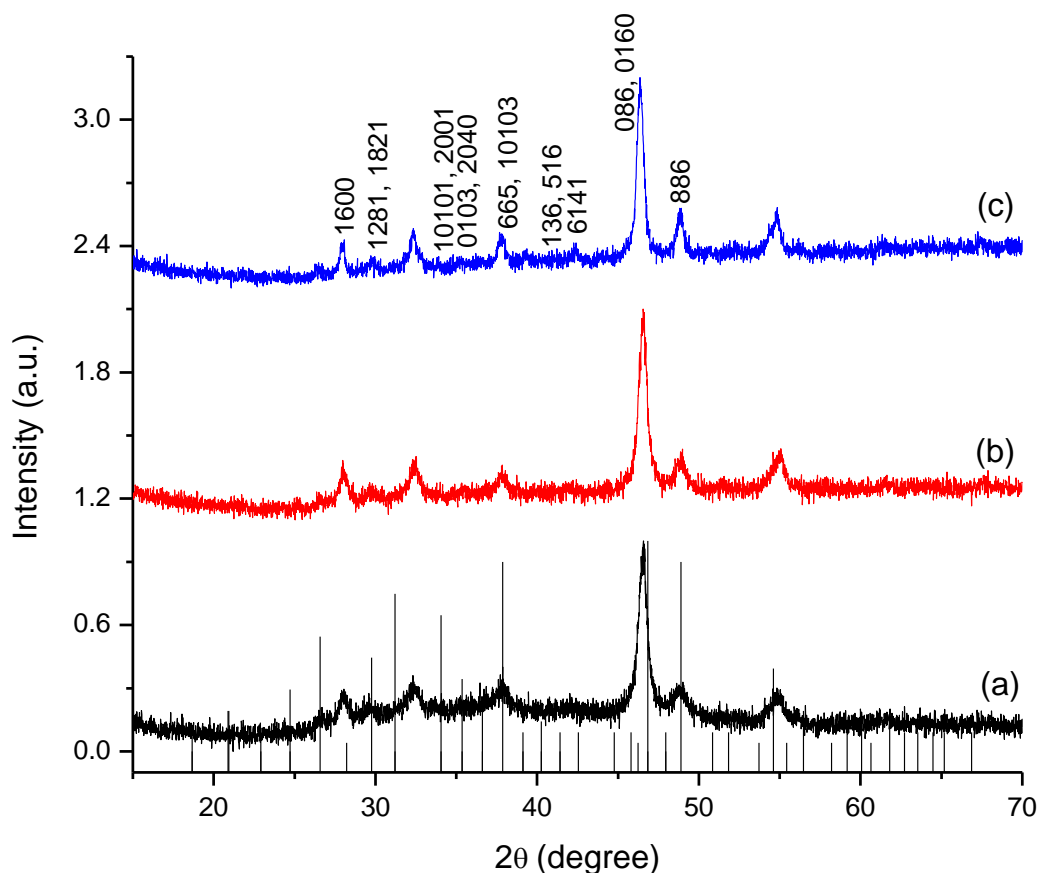


Figure 41. P-XRD of nanoparticles prepared from Cu-morphu complex in OLA at (a) 150 °C, (b) 200 °C and (c) 250 °C when OLA is used both as dispersion solvent and capping agent.

3.3.1.2. Syntheses of 1-dodecanethiol DT-capped Cu_xS_y nanoparticles

3.3.1.2.1. OLA as dispersion solvent in DT

In an attempt to investigate the effect of capping agent, we replaced OLA by a comparatively weak coordinating solvent DT. The solution was then directly injected into hot DT at the wanted growth temperatures (150 - 230 °C).

Nearly uniform monodispersed spherical CuS nanoparticles were obtained from Cu-morphu complex prepared at reaction temperature of 150 °C with an average size of 7.1 ± 0.5 nm and 190 °C (Figure 42a-b). As the temperature was elevated to 190 °C, a considerable increase in the size

of the particles (12.1 ± 1 nm) was observed, but the morphology remained spherical (Figure 42b). Mixed morphology was obtained at higher temperature of 230 °C, and some rod-like particles with an average length of 30.2 ± 5 nm and an average breadth of 7.2 ± 1 nm were also formed along with the spherical particles (Figure 42c-d). The change in growth kinetics of the different planes can lead to the formation of elongated or rod-like particles. The OLA may act as a strong base to deprotonate the thiol, creating an ionic environment, which probably caused limited growth of some of the planes and eventually leads to the formation of nanorods. The HRTEM image of the sample prepared at 230 °C is shown in (Figure 42e) from Cu-morphthtu precursor. The lattice fringes indicate the highly crystalline nature of the nanoparticles. The d-spacings measured from the lattice fringes of the different crystallites correspond approximately to the roxbyite $\text{Cu}_{1.75}\text{S}$ phase. For example d-spacing of 3.25 Å from Cu-morphthtu complex (Figure 42e) can be indexed to (1600) plane of roxbyite phase. The SAED pattern (Figure 42f) contains information from a large number of nanoparticles and the polycrystalline diffraction rings can be indexed to the roxbyite $\text{Cu}_{1.75}\text{S}$ phase within measurement errors.

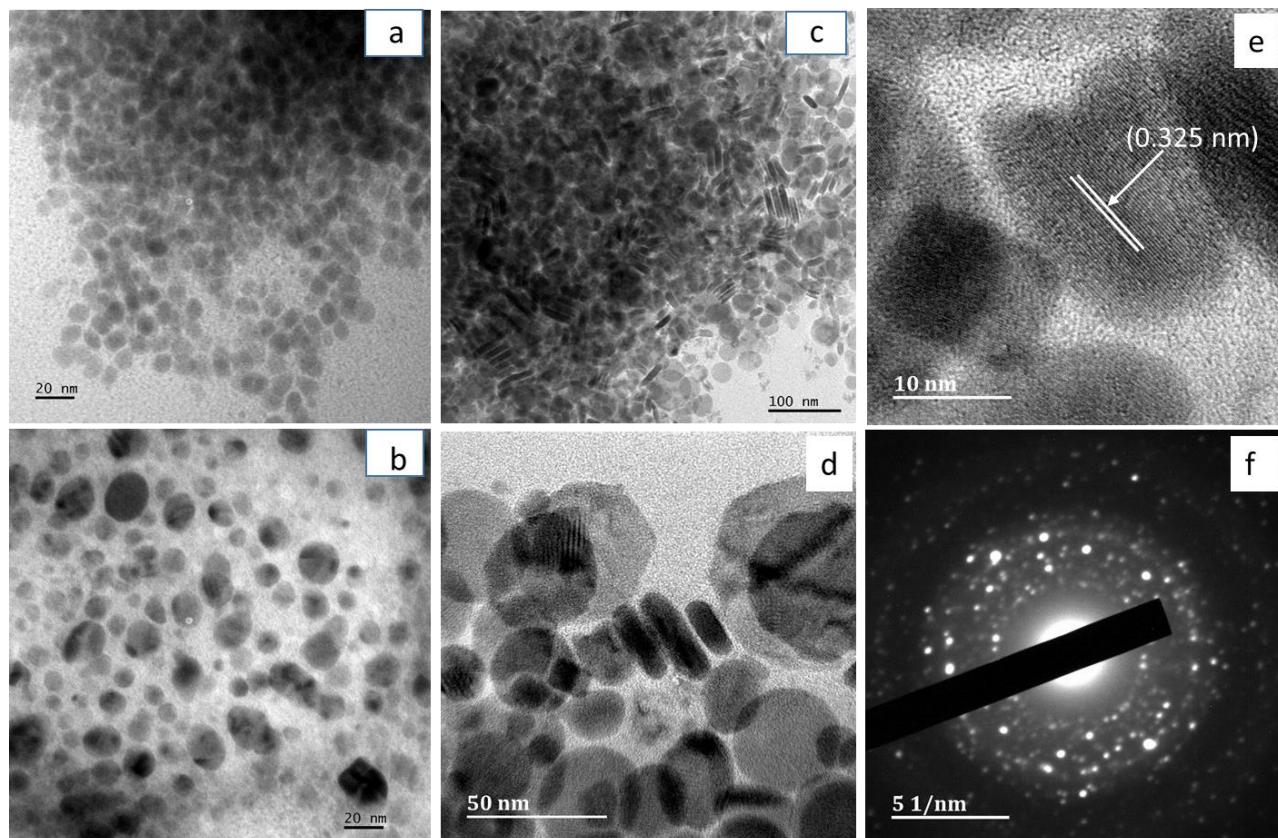


Figure 42. TEM images of nanoparticles prepared at (a) 150 °C, (b) 190 °C and (c-d) 230 °C, from Cu-morphtho complex when OLA is used as dispersion solvent in DT. (e): HRTEM image at 230 °C from Cu-morphtho complex; (f) showing the selected area electron diffraction (SAED) pattern of nanoparticles prepared at 230 °C from Cu-morphtho complex.

The diffraction patterns of the nanoparticles produced from Cu-morphtho complex is presented in Figure 43. Since copper sulfide has various possible crystallographic phases having almost the same stoichiometry, it is difficult to assign the peaks. However, the P-XRD results revealed that the most prominent reflection peaks match well with the pure $\text{Cu}_{1.75}\text{S}$ Roxbyite phase (ICDD # 00-023-0958), although some few minor intensity peaks confirm the presence of the Anilite phase as an impurity. The intensity of the peaks increases slightly with increasing temperature.

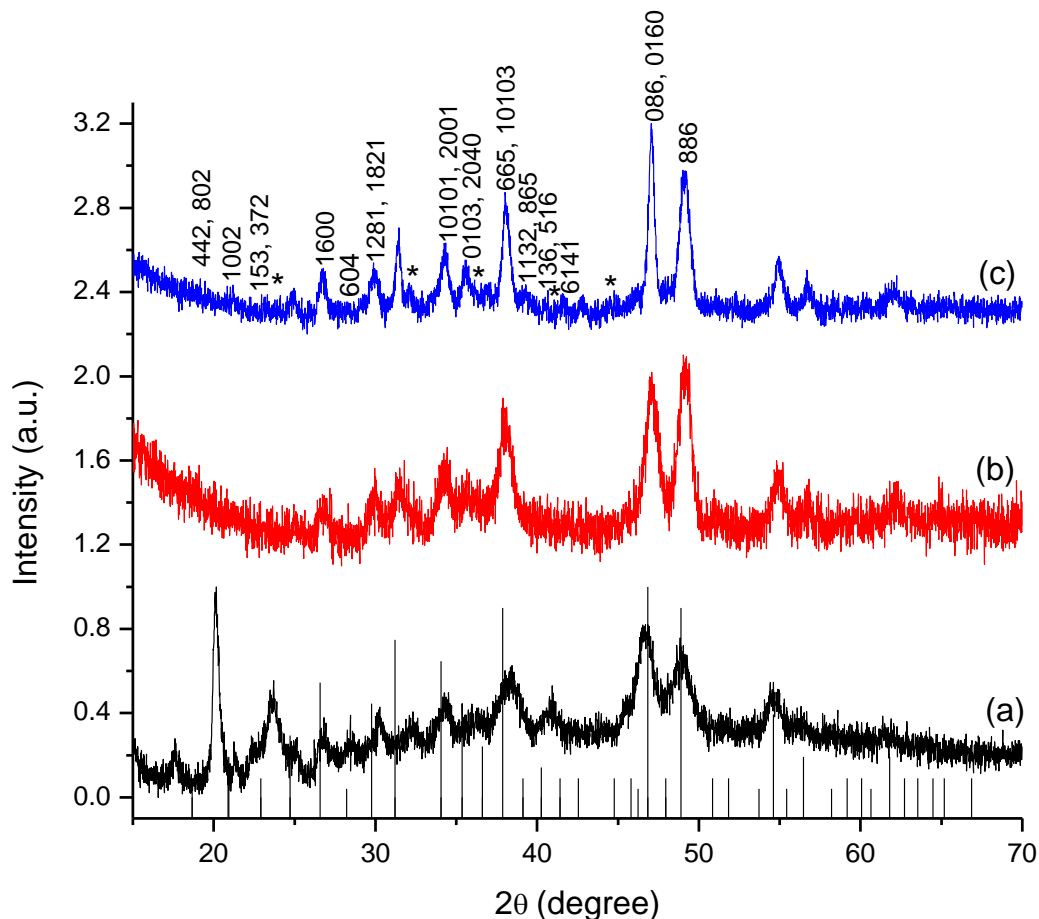


Figure 43. P-XRD of nanoparticles obtained from Cu-morphu complex at (a) 150 °C, (b) 190 °C and (c) 230 °C when OLA is used as dispersion solvent in DT. The (*) represents the presence of Anilite phase (ICDD: 00-033-0489).

3.3.1.2.2. Dodecanethiol (DT) as dispersion solvent in DT for Cu-morphu

The effect of DT was observed by using DT alone as a capping agent and dispersion medium, while keeping all the other parameters constant.

The TEM images (Figure 44) showed that the synthesized nanoparticles from Cu-morphu complex at 150 °C are fairly monodispersed with uniform spherical morphology (11.7 ± 1 nm) (Figure 44a). The size of the particles increased faintly (31.3 ± 4 nm) with change in temperature to 190 °C (Figure 44b). When the reaction was carried out at 230 °C the size was further increased,

leading to the formation of poly-dispersed spherical particles with an average size of 53 ± 7 nm (Figure 44c).

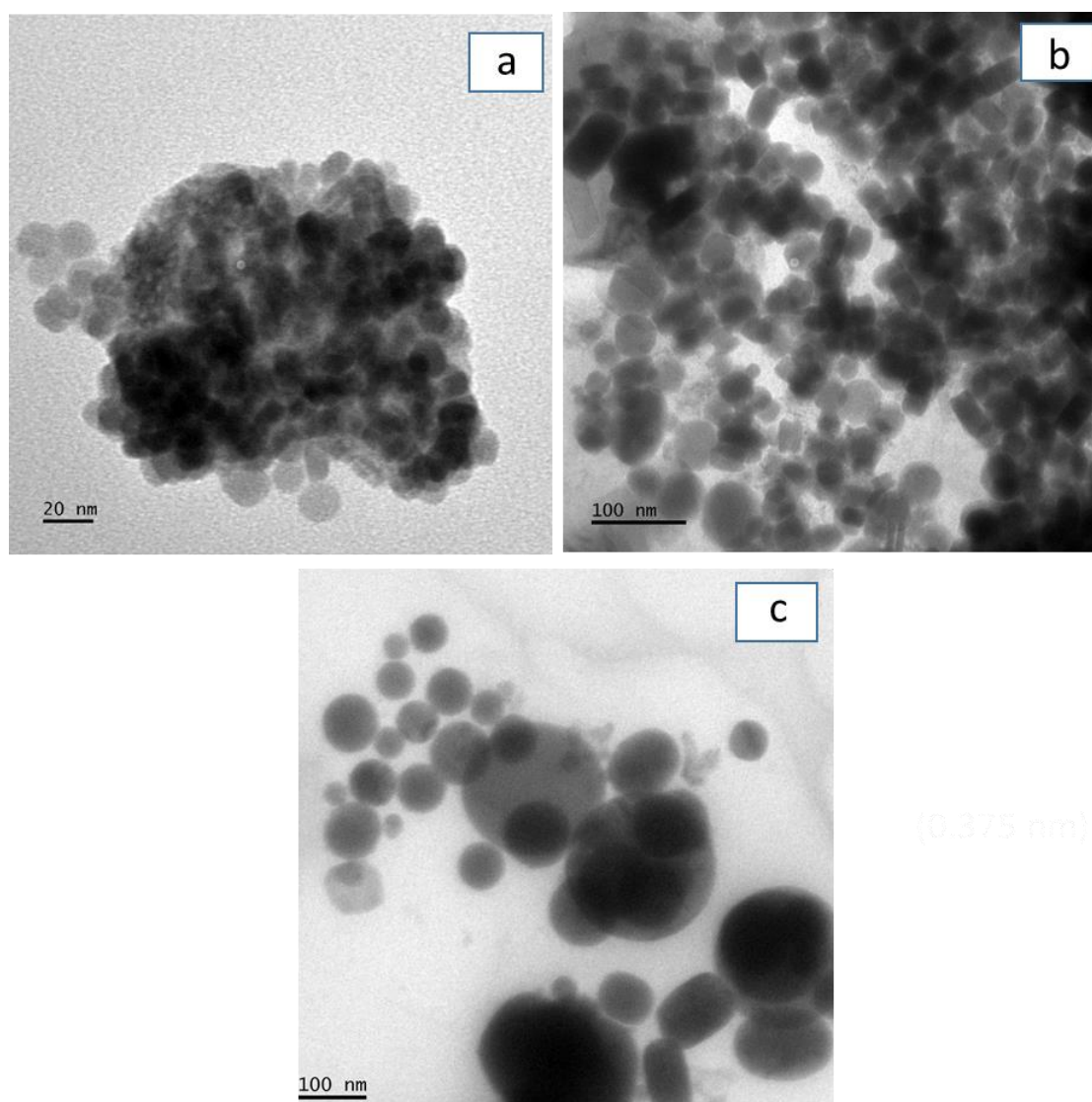


Figure 44. TEM images of nanoparticles prepared at (a) 150 °C, (b) 190 °C and (c) 230 °C, from Cu-morphu complex when DT is used both as dispersion solvent and capping agent.

The P-XRD patterns showed that, nanoparticles with the roxbyite ($\text{Cu}_{1.75}\text{S}$) phase (ICDD# 00-023-0958) were obtained (Figure 45), when Cu-morphu precursor was decomposed at different temperatures (150, 190 and 230 °C). It was also noticed that, the intensity of the peaks increases significantly with the increase of the reaction temperature.

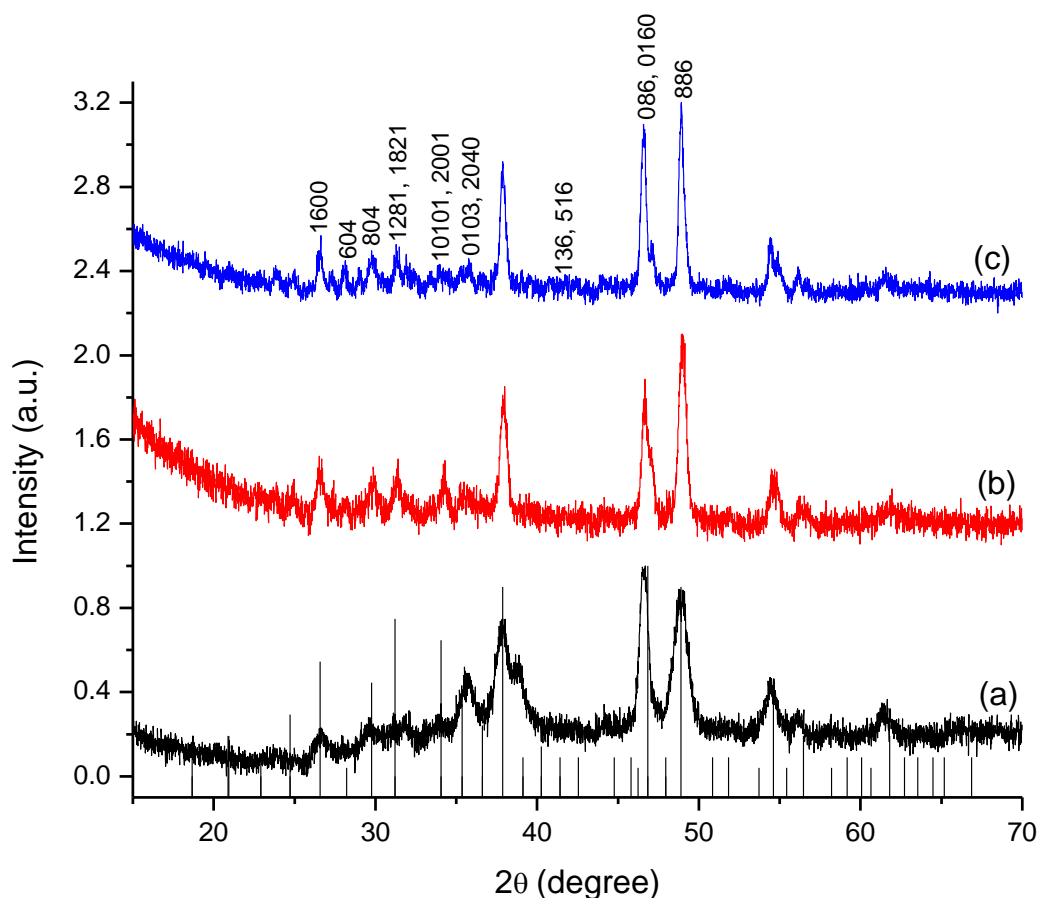


Figure 45. P-XRD pattern of $\text{Cu}_{1.75}\text{S}$ nanoparticles obtained from Cu-morphu complex (a) 150 °C, (b) 190 °C and (c) 230 °C when DT is used both as dispersion solvent and capping agent.

3.3.2. Preparation and characterization of Cu_xS_y nanoparticles using copper N-pyrrolidine-N'-benzoylthiourea as precursor in oleylamine and 1-dodecanethiol solvents

Copper sulfide nanocrystals were synthesized as detailed in section 2.3.2, page 50 and summarised here. A three-necked flask was purged with N_2 , after applying vacuum for few times at room temperature, using a Schlenk line to evacuate any air. A mass of 0.2 g of the Cu-pyrtru complex previously dispersed in 3 mL of (OLA and/or DT) was injected into 5 mL of hot OLA or DT at a desired temperature. The procedure was repeated varying some parameters such as the nature of the capping agent and the reaction temperature. In this paragraph, our purpose is to investigate the influence of the reaction temperature and capping groups, such as oleylamine and 1-dodecanethiol, on the morphology and crystallographic phase of the as prepared copper sulfide nanocrystals.

3.3.2.1. Syntheses of oleylamine OLA-capped Cu_xS_y nanoparticles

Once the complex was dispersed in OLA, the color of the Cu-pyrrtu complex began to change from green to greenish brown, which may indicate the interaction of OLA with precursor and its decomposition. Then, the solution was injected into the hot OLA at the desired growth temperatures (150 – 250 °C).

The TEM images presented in Figure 46 show that the as-prepared copper sulfide nanoparticles from Cu-pyrrtu complex at 150 °C (Figure 46e) agglomerated spherically shaped nanoparticles along with some rod-like shaped (average length 15 ± 2 nm; average breadth 7.5 nm) were obtained. While at 200 °C (Figure 46f) uniform spherical nanoparticles with an average size of 15.8 ± 1 nm were observed and when the temperature was raised to 250 °C (Figure 46g) non uniform cubic shaped nanoparticles with an average size of 61.8 ± 11 nm were formed. The selected area electron diffraction (SAED) pattern from Cu-pyrrtu complex at 250 °C (Figure 46h) approves the formation of crystalline copper sulfide nanoparticles composed of polycrystals of the roxbyite phase.

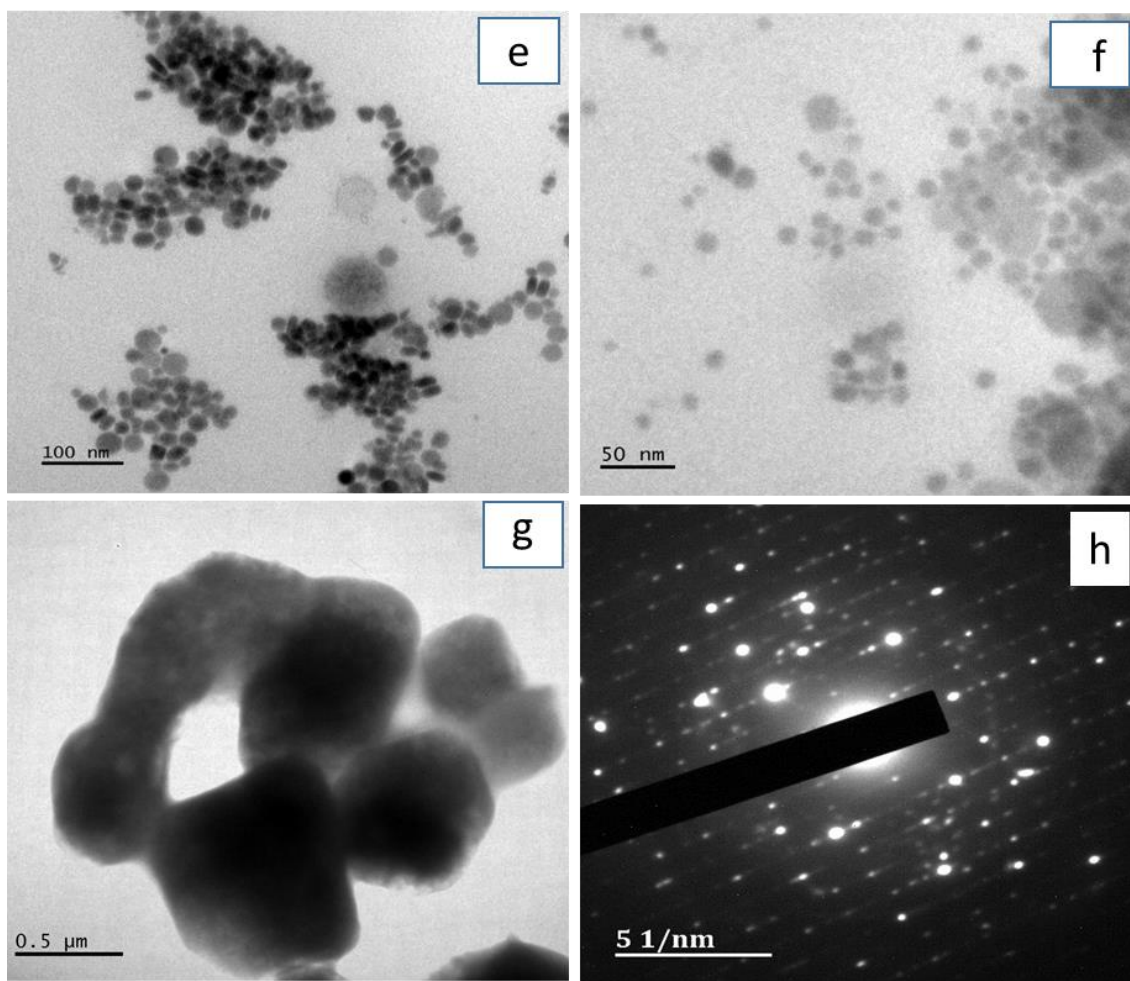


Figure 46. TEM images of copper sulfide nanoparticles synthesized at (e) 150 °C, (f) 200 °C and (g) 250 °C, from Cu-pyrrtu complex when OLA is used both as dispersion solvent and capping agent; (h) showing the selected area electron diffraction (SAED) pattern of nanoparticles prepared at 250 °C from Cu-pyrrtu precursor.

The diffraction peaks of the nanoparticles prepared from Cu-pyrrtu complex (Figure 47) matched the roxbyite phase (ICDD# 00-023-0958) with no presence of any other phase as an impurity. The powder X-ray diffraction results show that at low temperatures (150 and 200 °C), intense peaks were observed (Figure 47a-b), whereas at 250 °C a decrease in the intensity of the peaks was observed (Figure 47c).

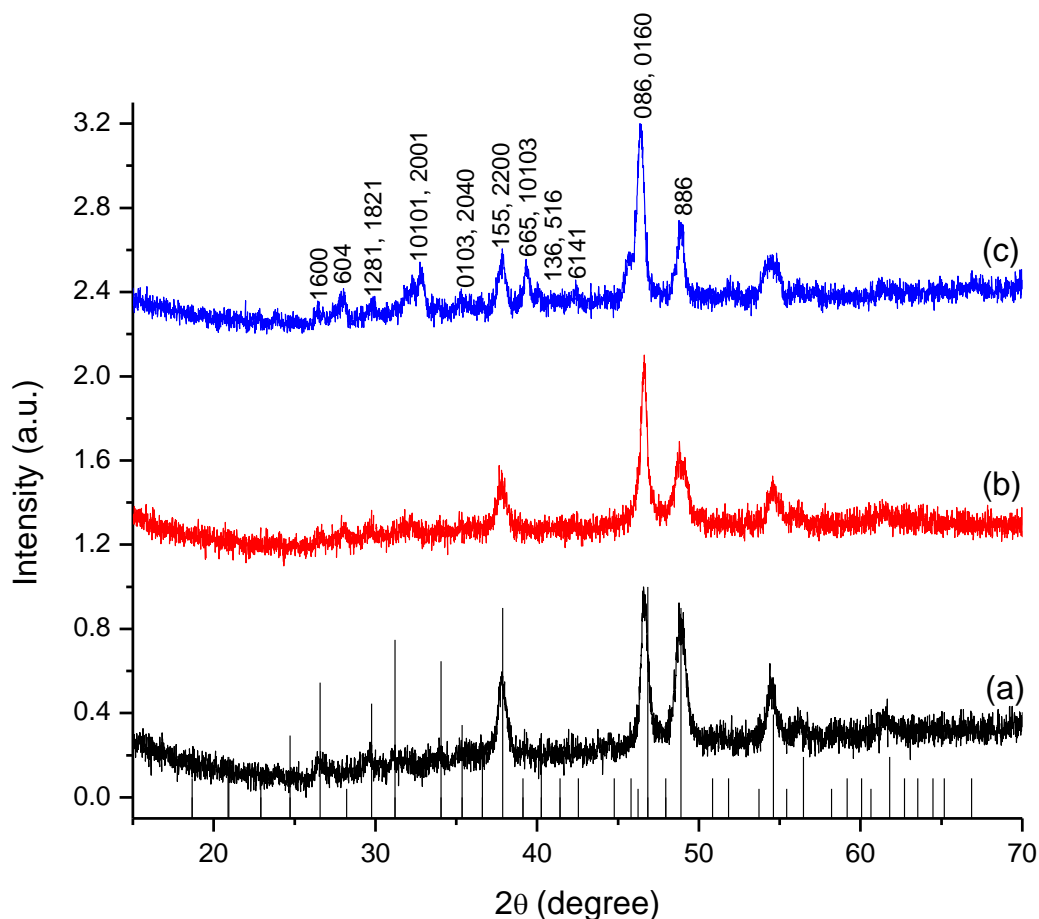


Figure 47. P-XRD of nanoparticles prepared from Cu-pyrrtu complex in OLA at (a) 150 °C, (b) 200 °C and (c) 250 °C when OLA is used both as dispersion solvent and capping agent.

3.3.2.2. Syntheses of 1-dodecanethiol DT-capped Cu_xS_y nanoparticles

3.3.2.2.1. OLA as dispersion solvent in DT

In order to explore the effect of capping group, we changed OLA by a comparatively weak coordinating solvent, DT. Then, the solution was injected into hot DT at the preferred growth temperatures (150 - 230 °C).

Approximately uniform monodispersed spherical copper sulfide nanoparticles were obtained from Cu-pyrrtu complex prepared at reaction 150 °C with an average size of 3.3 ± 1 nm and 190 °C (Figure 48g-h). As the temperature was raised to 190 °C, an increase in the size of the particles was observed significantly, but the morphology remained spherical with an average size of $8.4 \pm$

1 nm (Figure 48h). Mixed morphology was obtained at higher temperature of 230 °C, and some rod-like particles (average length 50.6 ± 5 nm and average breadth 9.7 ± 1 nm) were also formed along with the spherical particles (Figure 48i-j). The HRTEM image of the Cu-pyrrtu sample synthesized at 230 °C is presented in (Figure 48k) from Cu-pyrrtu precursor. The lattice fringes indicate the highly crystalline nature of the nanoparticles. The d-spacings measured from the lattice fringes of the different crystallites correspond approximately to the roxbyite $\text{Cu}_{1.75}\text{S}$ phase. For instance d-spacing of 3.95 Å from Cupyrrtu complex (Figure 48k) can be indexed to (1002) peak of roxbyite phase. The SAED pattern (Figure 48l) holds information from a large number of nanoparticles and the polycrystalline diffraction rings can be indexed to the roxbyite $\text{Cu}_{1.75}\text{S}$ phase within measurement errors.

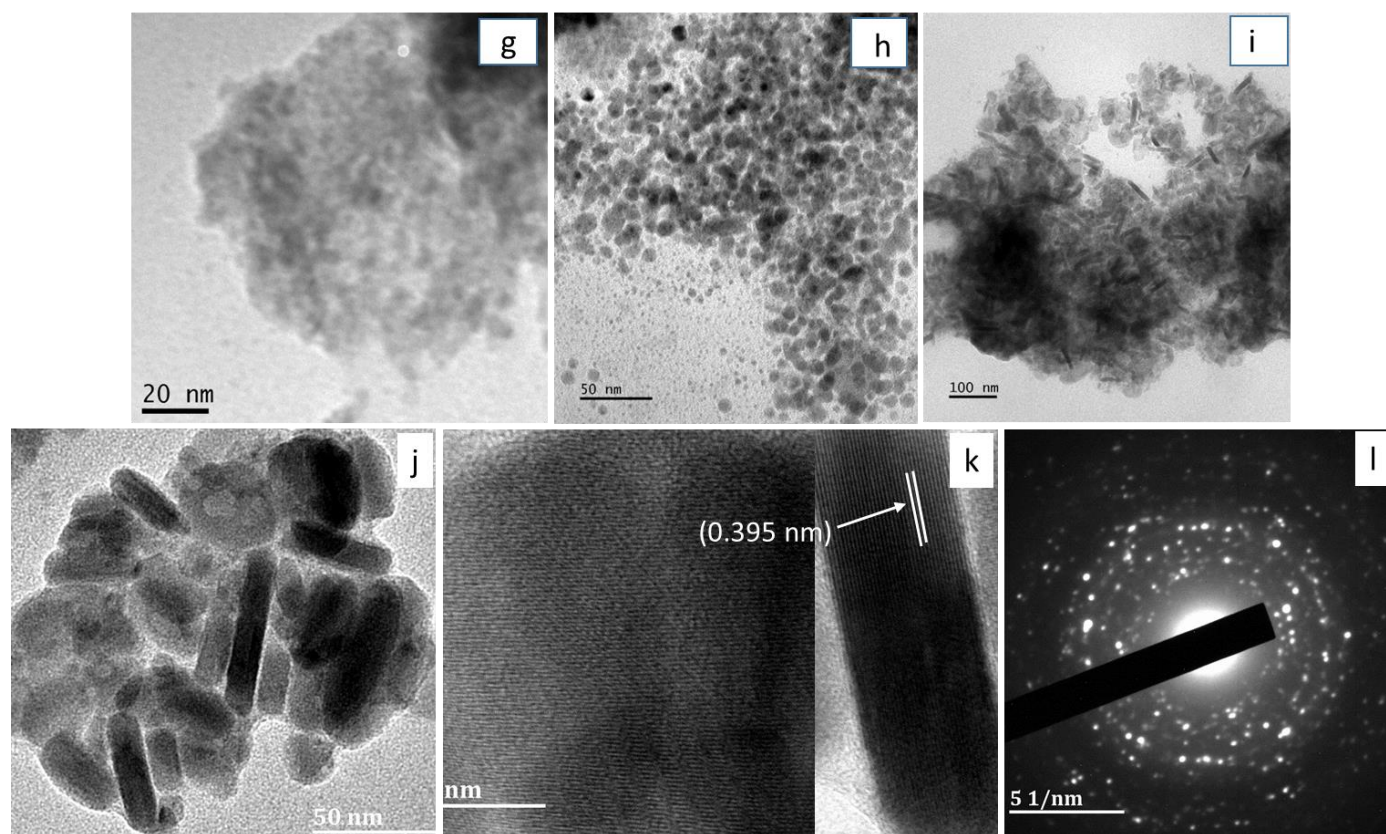


Figure 48. TEM images of nanocrystals fabricated at (g) 150 °C, (h) 190 °C and (i-j) 230 °C, from Cupyrrtu complex when OLA is used as dispersion solvent in DT. HRTEM image (k) at 230 °C from Cu-pyrrtu precursor; (l) showing the selected area electron diffraction (SAED) pattern of nanocrystals prepared at 230 °C from Cu-pyrrtu complex.

The diffraction pattern of the nanoparticles produced from Cu-pyrrtu complex is shown in Figure 49. The P-XRD results showed that, the most prominent reflections planes indexed well with the $\text{Cu}_{1.75}\text{S}$ Roxbyite phase (ICDD# 00-023-0958), although a negligible impurity of the Anilite phase also appears at higher temperature. At low temperatures (150 and 190 °C), the P-XRD patterns are broad but at 230 °C the roxbyite phase is more pronounced (49c).

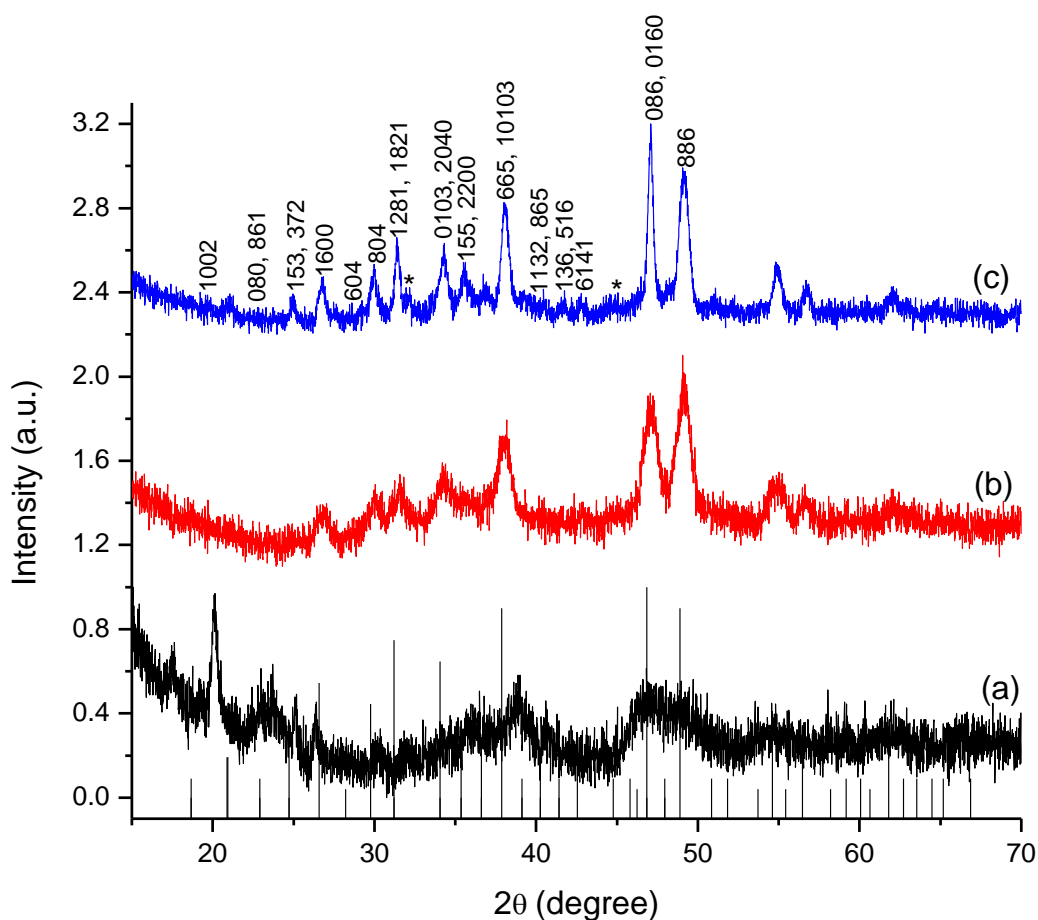


Figure 49. P-XRD of nanoparticles obtained from Cu-pyrrtu complex at (a) 150 °C, (b) 190 °C and (c) 230 °C when OLA is used as dispersion solvent in DT. The (*) represents the presence of Anilite phase (ICDD: 00-033-0489).

3.3.2.2.2. DT as dispersion solvent in DT for Cu-pyrrtu

The influence of DT was observed by using DT as a capping agent and dispersion solvent, while keeping constant all the parameters.

The TEM images (Figure 50) showed that the prepared nanocrystals from Cu-pyrrtu complex at 150 °C are almost monodispersed spherical morphology with an average size of 6.3 nm (Figure 50d). When the reaction temperature was elevated to 190 °C, the spherical nanoparticles became faceted in six equivalent directions resulting in hexagonal nano-disks with an average size of 86 ± 40 nm (Figure 50e). When the reaction was carried out at 230 °C, the size was further increased, resulting in the formation of poly-dispersed spherical particles with an average size of 18.9 ± 5 nm (Figure 50h). The HRTEM image (Fig. 50f) for the sample prepared from Cu-pyrrtu complex at 190 °C displays plane or standing hexagonal nanodisks. The fine determined lattice fringes indicate the highly crystalline nature of the nanocrystals. The d-spacing determined from the lattice fringes of the different crystallites match to the roxbyite $\text{Cu}_{1.75}\text{S}$ phase. For instance, spacing of 3.75 \AA (Figure 50f) can be indexed to (153, 372) plane of roxbyite phase. The SAED pattern (Figure 50g) contains information from a large number of nanoparticles and the polycrystalline diffraction rings can be matched to the roxbyite $\text{Cu}_{1.75}\text{S}$ phase within measurement errors.

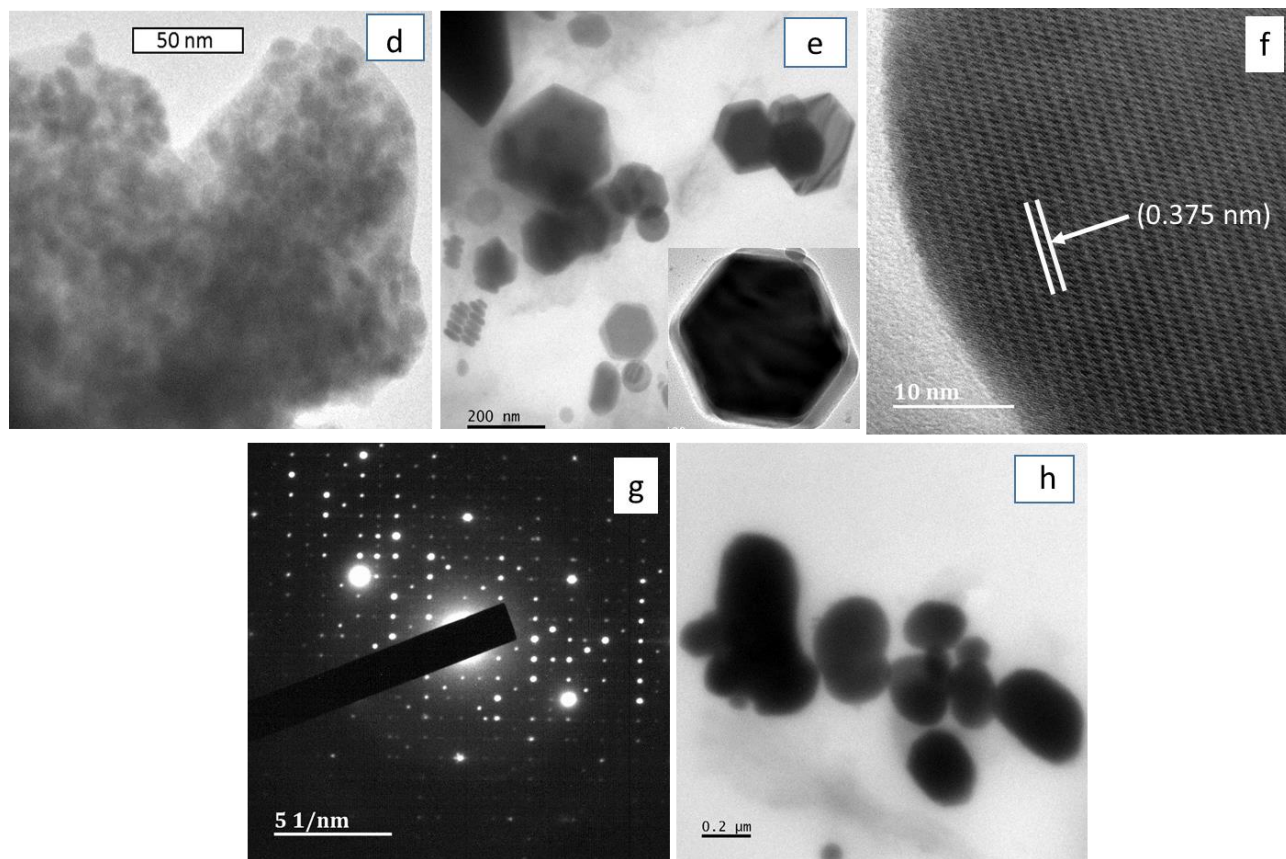


Figure 50. TEM images of nanoparticles prepared at (d) 150 °C, (e) 190 °C and (h) 230 °C, from Cu-pyrrtu complex when DT is used both as dispersion solvent and capping agent. HRTEM

image (inset f) at 190 °C from Cu-pyrrtu complex. (Inset g) showing the selected area electron diffraction (SAED) pattern of nanoparticles prepared at 190 °C from Cu-pyrrtu.

The P-XRD patterns revealed that, nanocrystals with the roxbyite ($\text{Cu}_{1.75}\text{S}$) phase (ICDD# 00-023-0958) were obtained (Figure 51), when Cu-pyrrtu complex was used at various temperatures (150, 190 and 230 °C). It is also observed that, the intensity of the peaks increased considerably with increase of the reaction temperature.

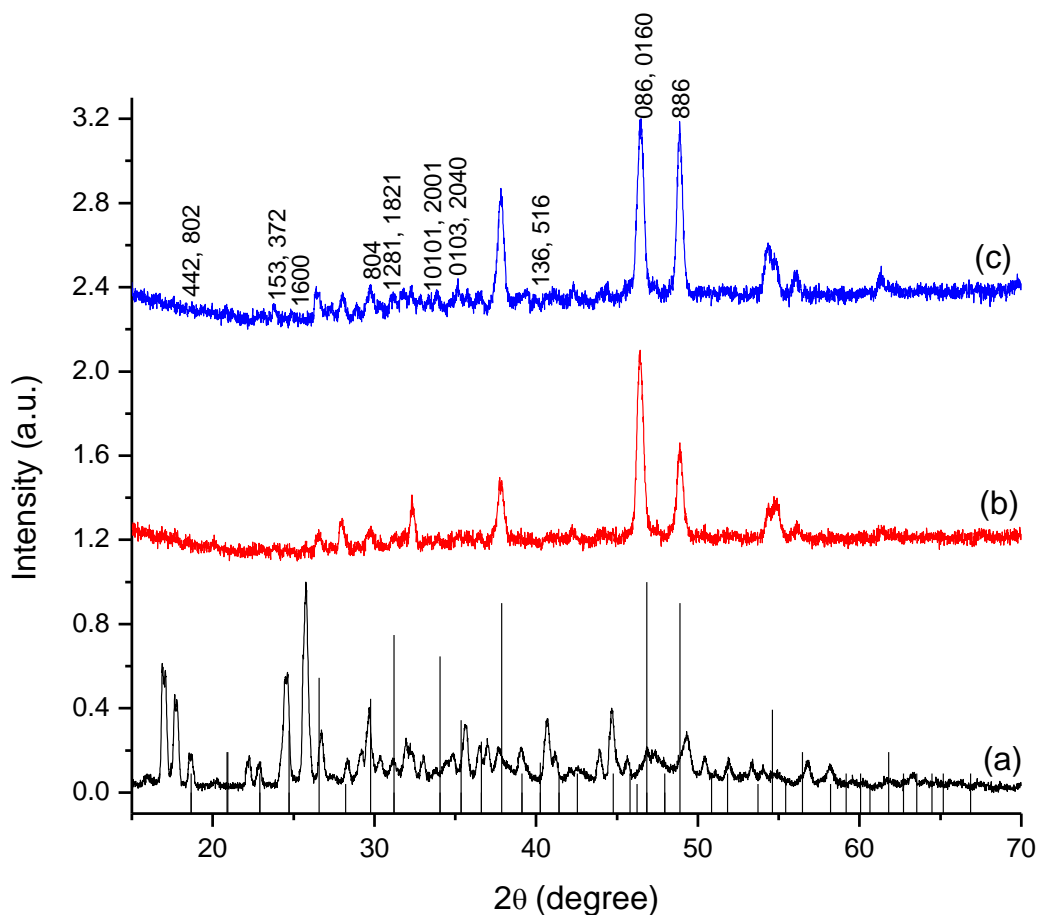


Figure 51. P-XRD pattern of $\text{Cu}_{1.75}\text{S}$ nanoparticles obtained from Cu-pyrrtu complex at (a) 150 °C (b) 190 °C and (c) 230 °C when DT is used both as dispersion solvent and capping agent.

As a conclusion, we have stated on the synthesis and characterization of copper morpholine and copper pyrrolidine benzoylthiourea complexes and their use as single source precursors for the fabrication of Cu_xS_y nanocrystals. The thermolysis of these precursors in capping groups such as,

OLA and DT produced copper sulfide with diverse shapes and sizes. The morphology of the particles obtained at a comparatively lower temperature is somewhat more uniform compared to the morphology of particles at higher temperature. Therefore, the rate of the reaction is significantly affected with increase in temperature and higher rate of precursor decomposition provides higher monomer concentration. The increase in monomer concentration leads to enhanced nucleation and growth of the nanoparticles²¹⁵. Better capping of the nanoparticles can be achieved at lower temperature, as the higher temperature reduces the affinity of ligands for effective capping.

3.4. Organically-capped CdS nanoparticles

Among the various semiconductors, cadmium sulfide nanoparticles have been widely investigated owing to their size dependent unique optical and electronic properties. Cadmium sulfide (CdS) is a II–VI semiconductor with a direct band gap of 2.42 eV, which has been recognized as an significant material for applications in solar cells, light-emitting diodes for flat-panel displays, gas sensors, and heterogeneous photocatalysis.^{216–219}

One of the main synthetic methods to high-quality CdS nanoparticles is the thermolysis of metal complexes as molecular precursors in high-boiling solvents. This method allows for the control of particle size and shape by varying reaction conditions such as precursor type, capping agent and reaction temperature. For example, Peng and co-workers showed the influence of these reaction parameters on the particle morphology²²⁰. Various classes of precursors such as dithiocarbamates, xanthates, thiourea, and dithioimidodiphosphinates have been used to fabricate CdS nanostructured materials^{9,221–223}. The control of the CdS shape in the form of spheres, rods, bipods and tetrapods has been attained by using these classes of complexes. So far, there has been no clear indication, on how the precursor composition does affect the morphology of the particles, although it has been deduced that the alkyl chain length of the coordinating solvents plays a role in the final shape of the particles. At first, phosphine-based capping agents such as tri-*n*-octylphosphine oxide were employed for passivation. Alkyl amine capping agents, such as hexadecylamine and oleylamine, surpassed phosphine-based capping agents, owing to the effectiveness with which they can be adsorbed by the CdS nanoparticle core, which authorizes for shape control.^{224,225}

3.4.1. Preparation and characterization of CdS nanoparticles using cadmium dihexyl, diethyl, piperidine dithiocarbamate and cadmium ethyl xanthate as precursors in oleylamine and hexadecylamine solvents

CdS nanoparticles were prepared as described in section 2.3.3, page 51 where a specified amount of 1.2 mmol of the precursor previously dispersed in 6.0 mL of tri-n-octylphosphine (TOP) was injected into 6.0 mL of hot capping agent (HDA or OLA) at 250 °C.

Primary amines have been widely employed as capping groups in the synthesis of CdS nanostructured materials since long alkyl chain amines are proven to be appropriate surfactants for semiconducting nanomaterials.^{23,37,54,108,221}

In this section, we investigate the effect of the precursor type on the morphology and electronic properties of CdS nanoparticles synthesized in hexadecylamine (HDA) and oleylamine (OLA) used as coordinating solvents.

3.4.1.1. Syntheses of hexadecylamine HDA-capped CdS nanoparticles

The final morphology of nanoparticles in any solution is directed by the preferred growth regime of the reaction. The reaction can proceed in either a kinetic or a thermodynamic growth regime^{220,226}. The TEM images of HDA capped CdS nanoparticles (Figure 52) show that, spherical shaped particles with a mean diameter of 12.9 ± 2 nm were obtained from Cd(II) dihexyl dtc complex. Rod shaped with a length of 29.9 ± 5 nm and a breadth of 11.3 ± 2 nm were obtained from Cd(II) diethyl dtc complex with an aspect ratio of 2.64. When the precursor was changed from alkyl to heterocyclic, oval to rod shaped particles with an average particle size of 13.6 ± 3 nm were obtained from Cd(II) piperidine dtc complex. Whereas when the precursor was changed from xanthate, spherical to oval shaped particles with a mean diameter of 9.4 ± 2 nm from Cd(II) ethyl xanthate were obtained and their particles size distribution are presented in Figure 53.

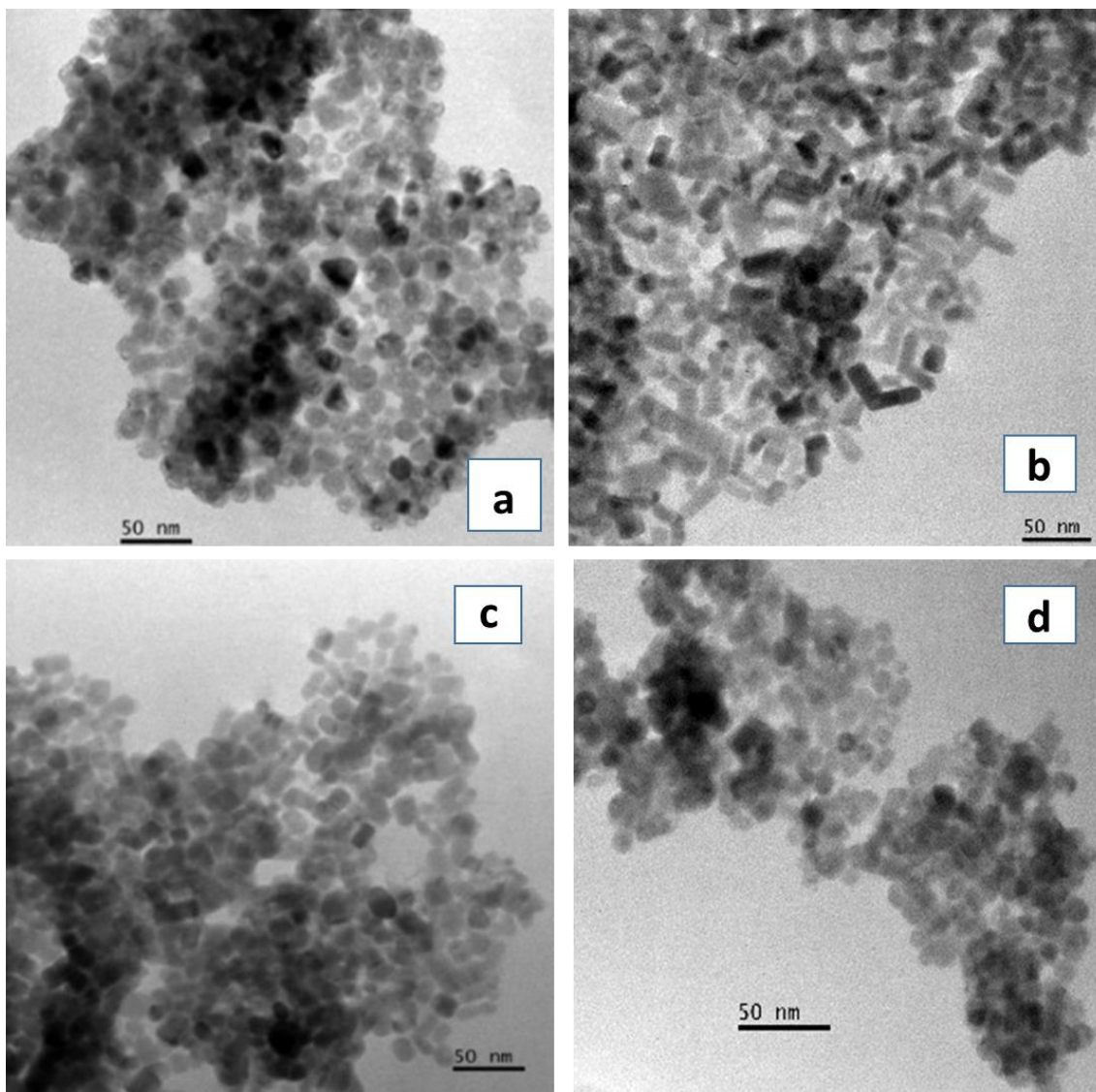


Figure 52. CdS nanoparticles prepared from a) Cd(II) dihexyl dtc, b) Cd(II) diethyl dtc, c) Cd(II) piperidine dtc and d) Cd(II) ethyl xanthate complexes.

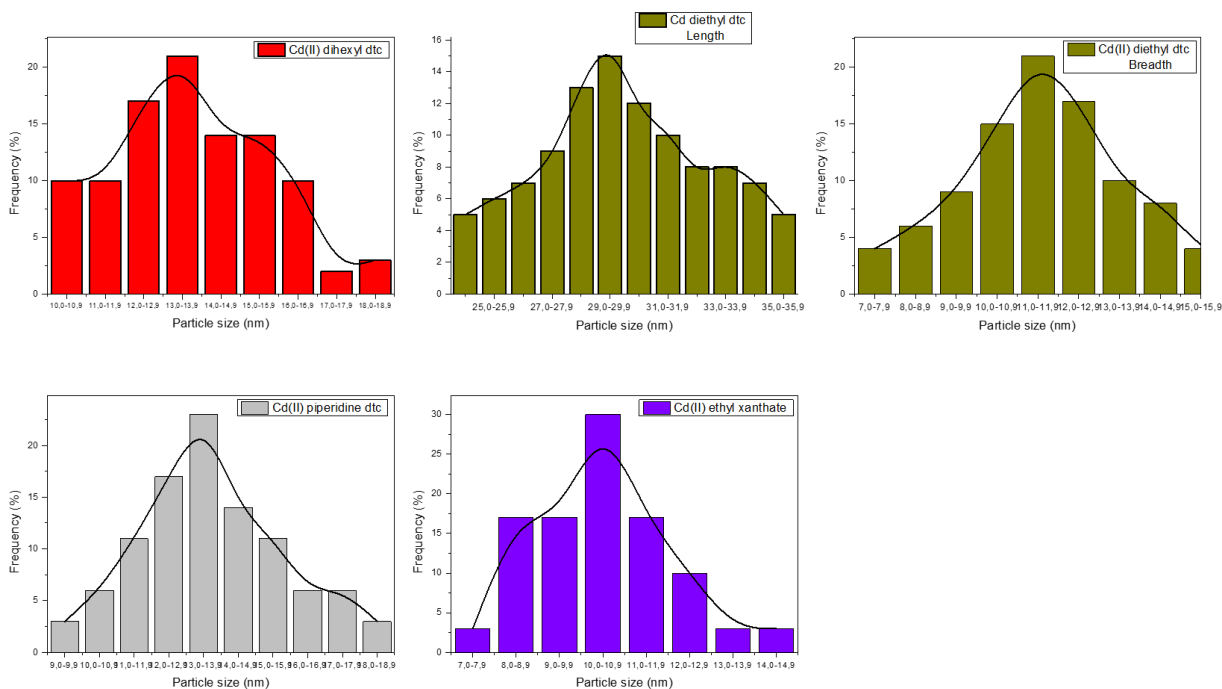


Figure 53. Particle size distribution of the prepared CdS nanocrystallites synthesized from a) Cd(II) dihexyl dtc, b) Cd(II) diethyl dtc, c) Cd(II) piperidine dtc and d) Cd(II) ethyl xanthate complexes.

The P-XRD patterns of the HDA capped CdS nanoparticles revealed the hexagonal wurtzite crystalline system (card number: 01-077-2306) (Figure 54). Diffraction peaks at $2\theta = 24.84^\circ$, 26.53° , 28.22° , 43.74° , 47.89° and 51.89° which correspond to the (100), (002), (101), (110), (103) and (112) planes of hexagonal CdS respectively were observed and the broadness of the XRD diffraction peaks was indicative of relatively small particle size and heterogeneous particle size distribution²²⁷. Also the higher intensity (002) peak in p-XRD pattern of CdS nanoparticles indicated that the nanoparticles were preferably elongated along the c-axis²²⁸. However the weaker (102) plane confirms the wurtzite phase is dominant and a non-indexed peak at $2\theta = 23.27^\circ$ was observed. The non-indexed peak in the spectra could be attributed to the capping group or the impurities present from the decomposition of the complex.

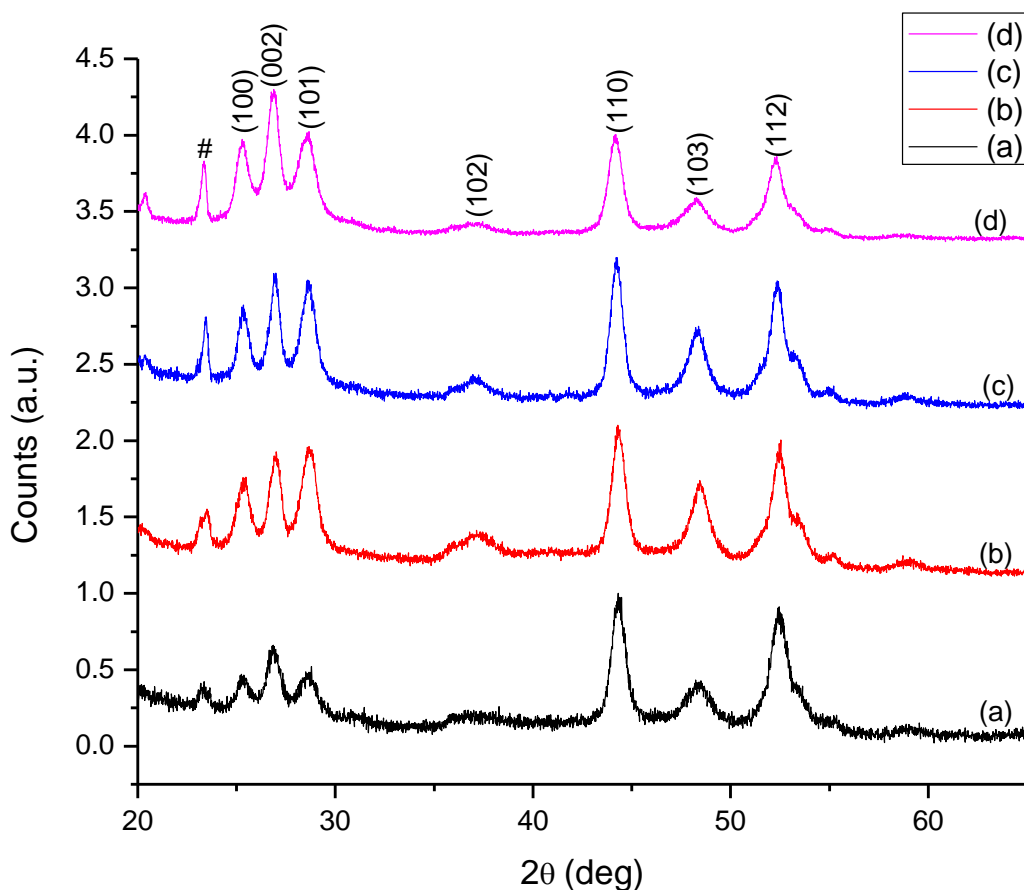


Figure 54. P-XRD patterns of HDA capped CdS nanoparticles prepared from a) Cd(II) dihexyl dtc, b) Cd(II) diethyl dtc, c) Cd(II) piperidine dtc and d) Cd(II) ethyl xanthate complexes.

The optical properties (UV-visible) of the CdS nanoparticles prepared from Cd(II) dihexyl dtc, Cd(II) diethyl dtc, Cd(II) piperidine dtc and Cd(II) ethyl xanthate were investigated (Figure 55). The absorption band edges are 505 nm, 485 nm, 500 nm and 490 nm respectively displaying a considerable blue shift of 10 nm, 30 nm, 15 nm and 25 nm compared to the bulk CdS (515 nm). This is the result of a typical quantum confinement. We noticed that CdS nanoparticles prepared from Cd(II) diethyl dtc were more blue shifted than those prepared from other precursors and this might be due to the effect of HDA.

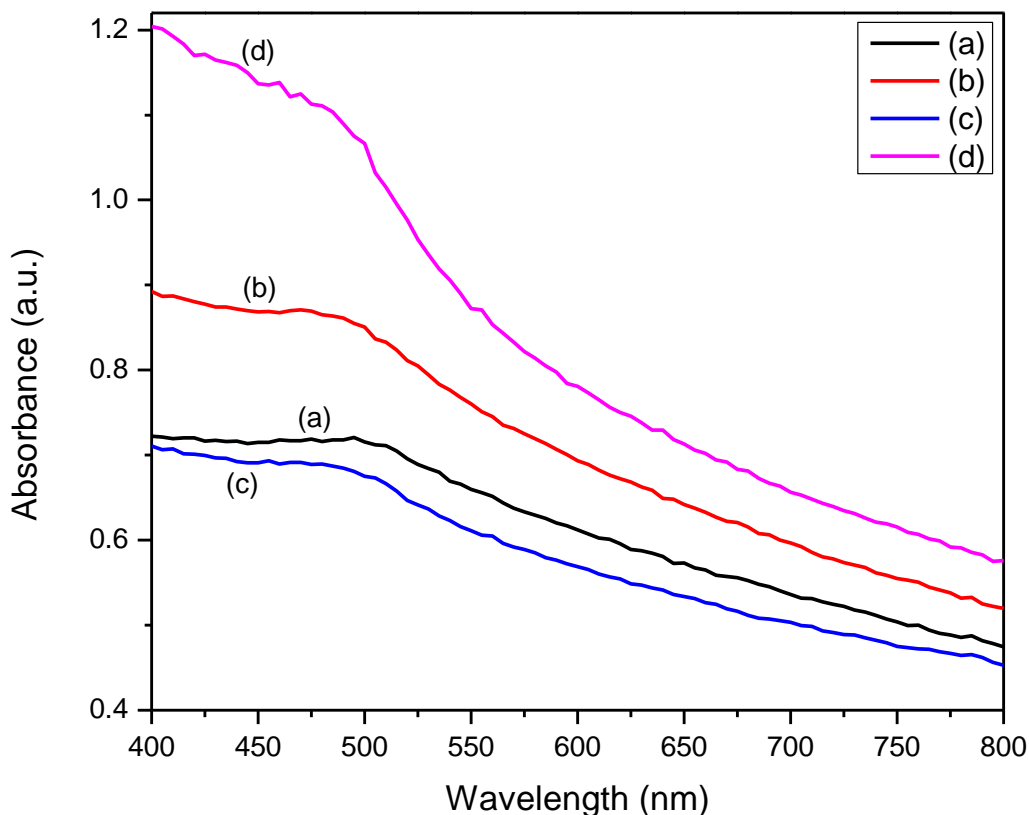


Figure 55. UV-visible absorption spectra of HDA capped CdS nanoparticles prepared from a) Cd(II) dihexyl dte, b) Cd(II) diethyl dte, c) Cd(II) piperidine dte and d) Cd(II) ethyl xanthate complexes.

The capping group has a primordial role in determining the final morphology of the nanocrystals since a compound that binds toughly to the surface of the particle is inappropriate, as it would not allow the particle to grow well. Whereas, a weak capping agent would produce large particles or aggregates²²⁹. Hexadecylamine (HDA) is a C₁₆ long chain primary amine which adsorbs through its amine group on the surface of the CdS nanoparticles and this results in the formation of anisotropic morphology.⁵⁶ We reported the synthesis of HDA-capped CdS nanoparticles where the nanocrystals obtained were high quality and monodispersed. The precursor type also has an effect on the morphology and optical properties of the CdS nanoparticles.

3.4.1.2. Syntheses of oleylamine OLA-capped CdS nanoparticles

Herein, we have modified a reaction parameter by increasing the length of the carbon chain of the linear shape amine from a C₁₆ amine (hexadecylamine) to a C₁₈ branched shaped amine (oleylamine) while we have kept constant the other parameters.

The TEM images of OLA capped CdS nanoparticles are shown in Figure 56, spherical to cubic shaped particles with an average size of 13.9 ± 3 nm were obtained from Cd(II) dihexyl dte complex. Oval shaped with an average size of 16.7 ± 3 nm were obtained from Cd(II) diethyl dte complex. When the precursor was changed from alkyl chain to heterocyclic, oval shaped particles with an average size of 9.9 ± 2 nm were obtained from Cd(II) piperidine dte complex. Whereas when the precursor was changed from xanthate, spherical to oval shaped particles with an average size of 9.5 ± 2 nm from Cd(II) ethyl xanthate were obtained and their corresponding particles size distribution are presented in Figure 57.

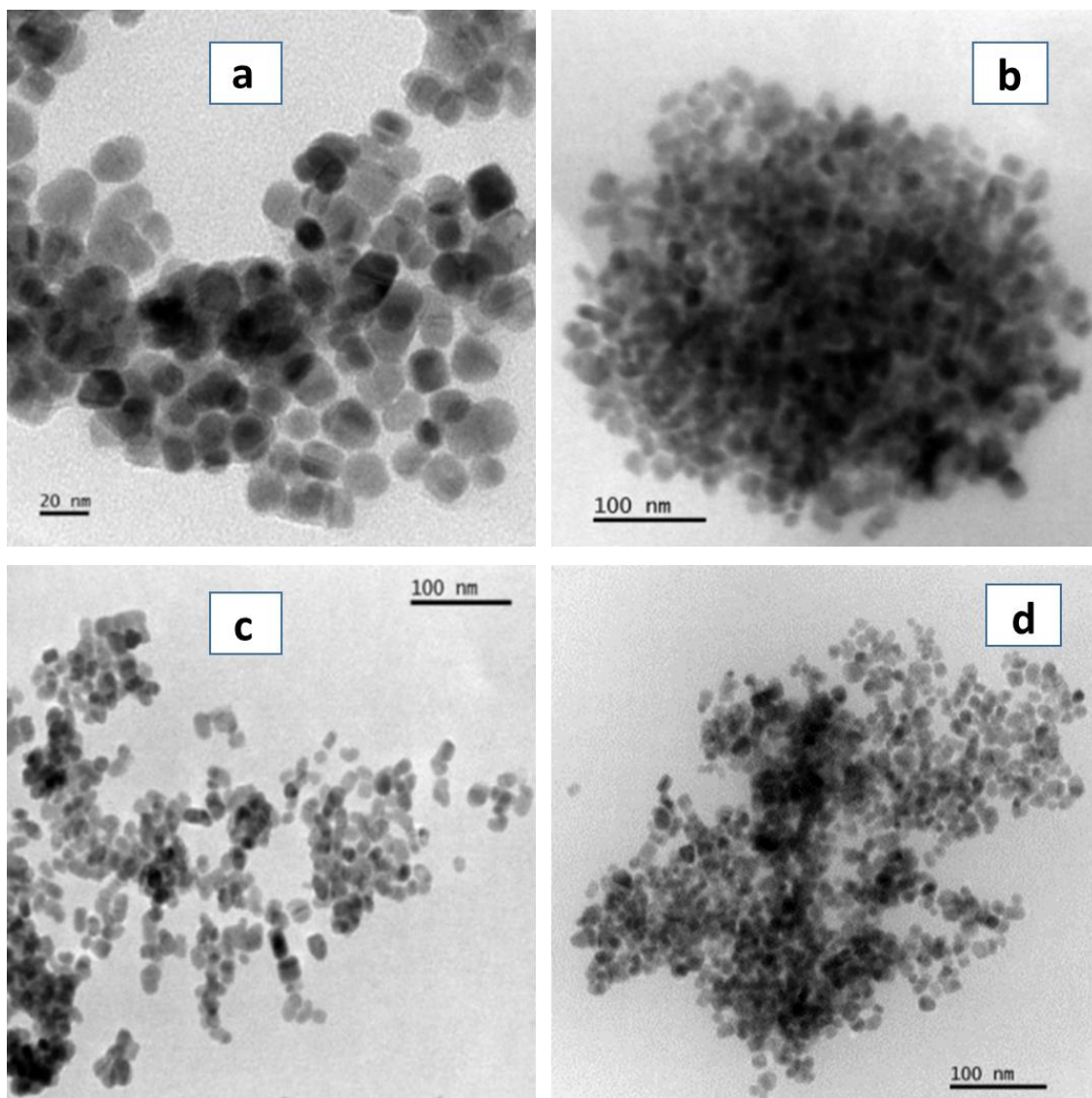


Figure 56. CdS nanoparticles synthesized from a) Cd(II) dihexyl dtc, b) Cd(II) diethyl dtc, c) Cd(II) piperidine dtc and d) Cd(II) ethyl xanthate complexes.

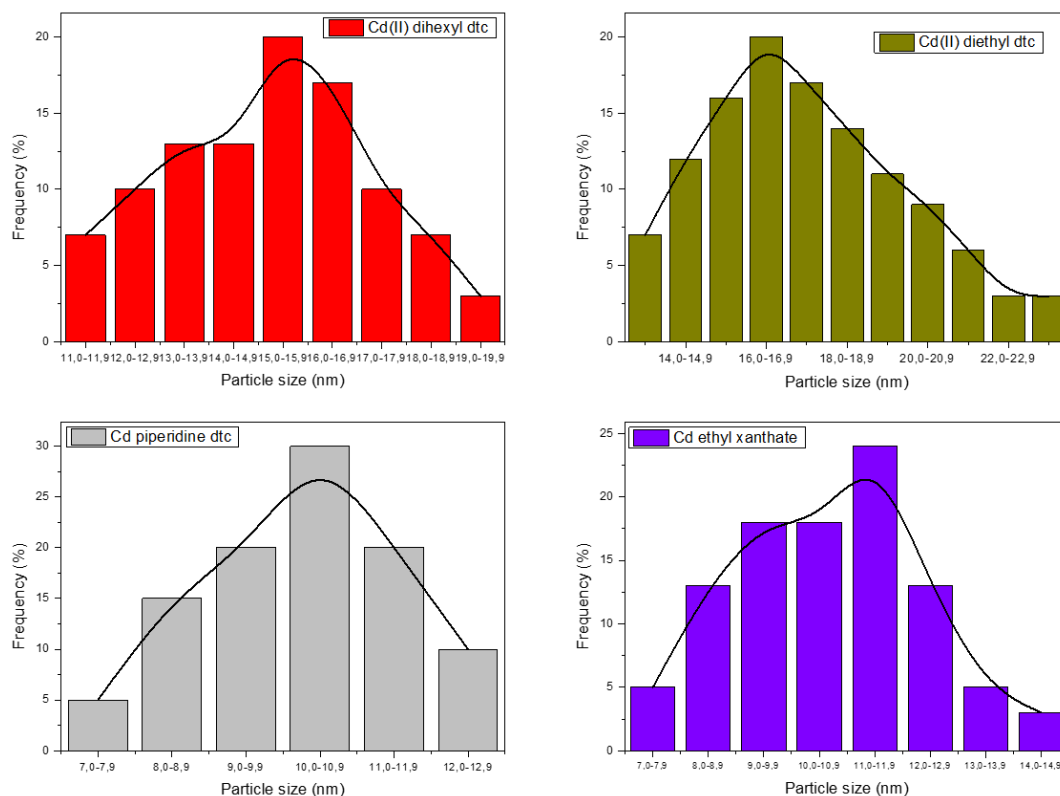


Figure 57. Particle size distribution of the prepared CdS nanocrystallites prepared from a) Cd(II) dihexyl dte, b) Cd(II) diethyl dte, c) Cd(II) piperidine dte and d) Cd(II) ethyl xanthate complexes.

The powder X-ray diffraction patterns of the OLA capped CdS nanocrystals synthesized are shown in Figure 58. The diffraction peaks of the CdS samples matched well with the wurtzite crystalline system (card number: 01-077-2306). Furthermore, no any other peak was observed, suggesting that pure CdS was obtained. The crystal phase of the CdS particles was not influenced by the difference in chemical composition for each single-source precursor.

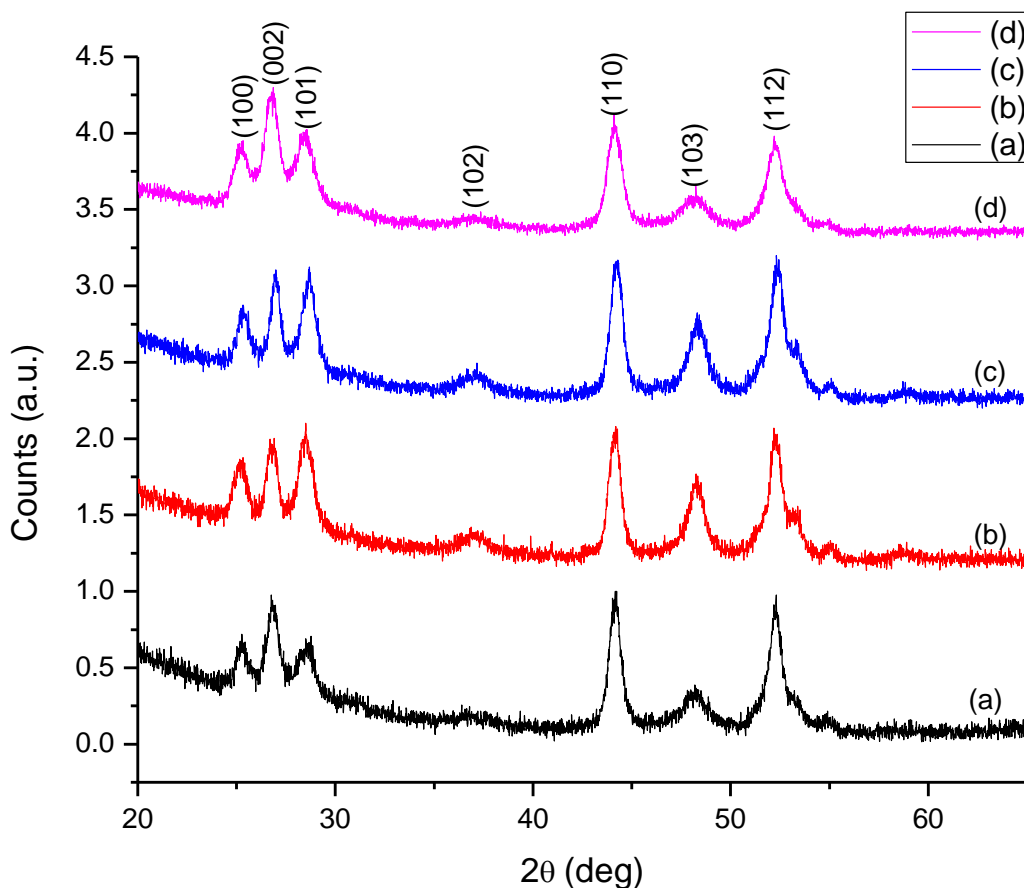


Figure 58. P-XRD patterns of OLA capped CdS nanoparticles prepared from a) Cd(II) dihexyl dte, b) Cd(II) diethyl dte, c) Cd(II) piperidine dte and d) Cd(II) ethyl xanthate complexes.

The absorption spectra of the CdS nanocrystals prepared with OLA are presented in Figure 59. The absorption band edges are approximately 490 nm, 480 nm, 495 nm and 485 nm from Cd(II) dihexyl dte, Cd(II) diethyl dte, Cd(II) piperidine dte and Cd(II) ethyl xanthate complexes respectively, showing a blue shift compared to the bulk CdS (515 nm) and a characteristic of quantum confinement. This result was justified by Yu and co-workers, in which they showed that the linear shape of some capping groups allow oxygen to attain the surface of particle, which oxidize the surface and decrease the emission quantum yield while capping group with branched arrangements protect the surface in a more suitable way.²³⁰

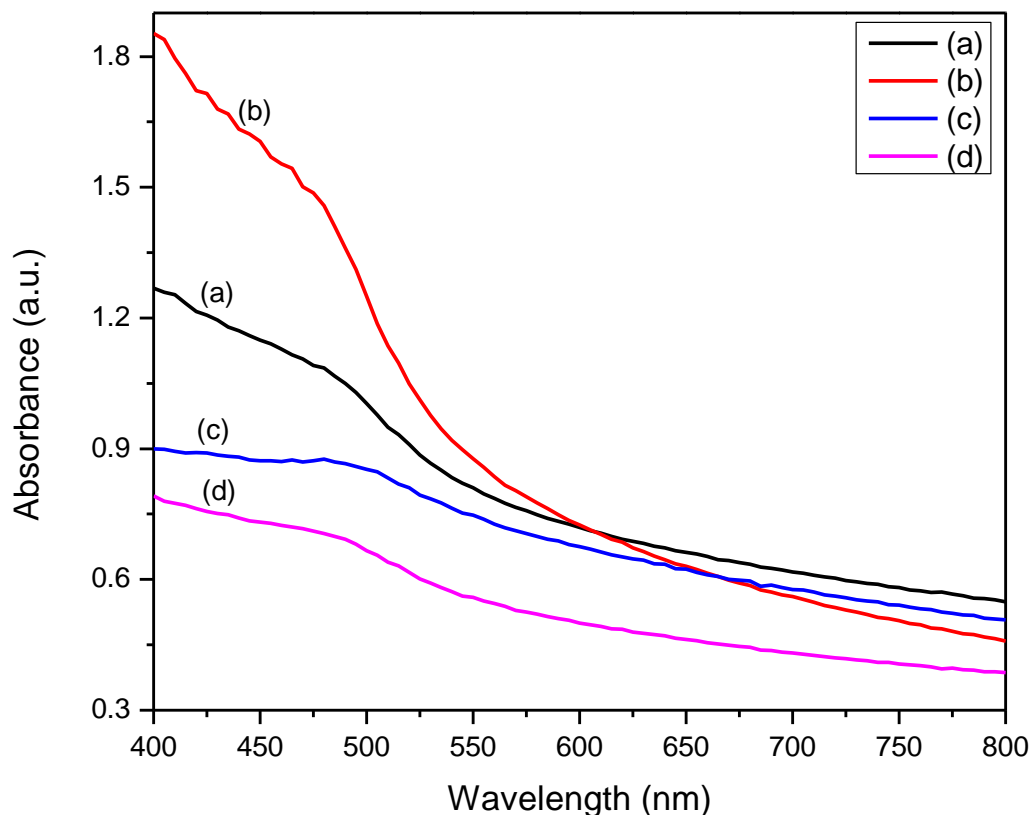


Figure 59. UV-visible absorption spectra of OLA capped CdS nanoparticles prepared from a) Cd(II) dihexyl dte, b) Cd(II) diethyl dte, c) Cd(II) piperidine dte and d) Cd(II) ethyl xanthate complexes.

3.4.2. Study the effect of precursor type and capping group on the morphology and size of CdS nanoparticles

The capacity to control the physical and the chemical properties of semiconducting nanoparticles depends on the fine-tuning of their morphology. The size and shape dependent optical properties of such nanostructured materials (spherical, cubic, rod shaped) have been proven being direct dependent on the resulting morphology in the case of semiconductor colloidal nanoparticles⁴⁴. According to this statement, the growth of semiconductor nanoparticles can be observed by the progressive evolution of the UV-visible absorption curve. This enables an understanding of the relationship between reaction parameters and the resultant morphology.^{56,108}

In this section, we investigate the effect of nature of the precursor and the capping agent on the size and shape of the prepared CdS nanoparticles.

3.4.2.1. Effect of the precursor type

This study was achieved by thermolysing 1.2 mmol of each complex (Cd(II) dihexyl dte (C₁₂), Cd(II) diethyl dte (C₄), Cd(II) piperidine dte (C₅) and Cd(II) ethyl xanthate (C₂)) at 250 °C in 6 mL of OLA.

Figure 60 shows results of the UV-visible absorption and the corresponding TEM images of the CdS nanoparticles prepared. The particles are all blue shifted as compared to the bulk CdS (515 nm). It is noticed from the Figure 60 that similar morphologies were obtained using different precursor and the shape and size of CdS nanoparticles varied little when Cd(II) piperidine dte and Cd(II) ethyl xanthate complexes were used and much when Cd(II) dihexyl dte and Cd(II) diethyl dte complexes were used. However we also noticed that the size of the CdS nanoparticles obtained from the Cd(II) ethyl xanthate complex was smaller compared to those from Cd(II) dithiocarbamates complexes. The variation of the precursor type did not affect much the shape of CdS nanoparticles but the difference happened on the optical properties.

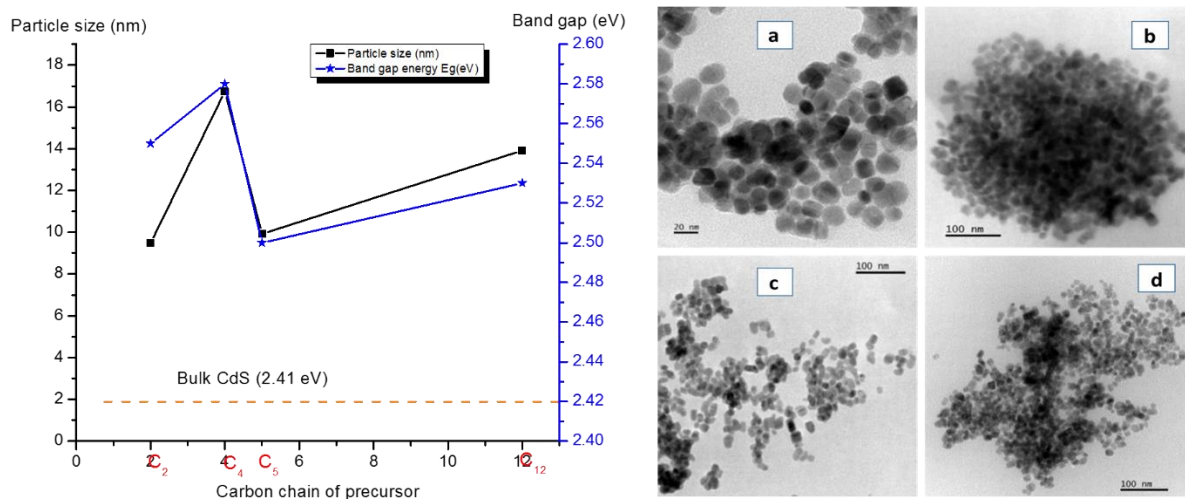


Figure 60. Plots of band gap energy and average particle sizes versus the precursor type. Corresponding TEM images at 250 °C from a) Cd(II) dihexyl dtc, b) Cd(II) diethyl dtc, c) Cd(II) piperidine dtc and d) Cd(II) ethyl xanthate complexes.

3.4.2.2. Effect of the capping agent

This study was achieved by thermolysing 1.2 mmol of each complex (Cd(II) dihexyl dtc (C_{12}), Cd(II) diethyl dtc (C_4), Cd(II) piperidine dtc (C_5) and Cd(II) ethyl xanthate (C_2)) at 250 °C in 6 g or mL of HDA and OLA.

Figure 61 shows results of the UV-visible absorption of the CdS nanoparticles prepared from the thermolysis of different complexes in 6 g or mL of HDA and OLA at 250 °C. It is seen that when OLA was used as capping agent, the average size of the CdS nanoparticles obtained from Cd(II) diethyl dtc (C_4) complex was higher followed by Cd(II) dihexyl dtc (C_{12}), Cd(II) piperidine dtc (C_5) and Cd(II) ethyl xanthate (C_2) complexes respectively. While when HDA was used as capping agent, the average size of the CdS nanoparticles obtained from Cd(II) diethyl dtc (C_4) complex was higher than complexes from Cd(II) piperidine dtc (C_5), Cd(II) dihexyl dtc (C_{12}), and Cd(II) ethyl xanthate (C_2). This observation can be explained by the fact that the longer the carbon chain, the better the capping group^{56,108}. In general, the CdS nanoparticles prepared at higher temperature, favor the thermodynamic growth regime resulting in quite well-defined isotropic particles (spherical, oval and cubes)²³¹. The OLA capped CdS nanoparticles are more blue shifted than the corresponding HDA capped CdS nanoparticles. A potential reason to explain this phenomenon

could be due to the fact that higher reaction temperature results in the formation of irregular nanoparticles with reduced crystallinity due to random, faster nucleation and with the rapid growth affecting the ligand configuration at the nanocrystal surface.²³²

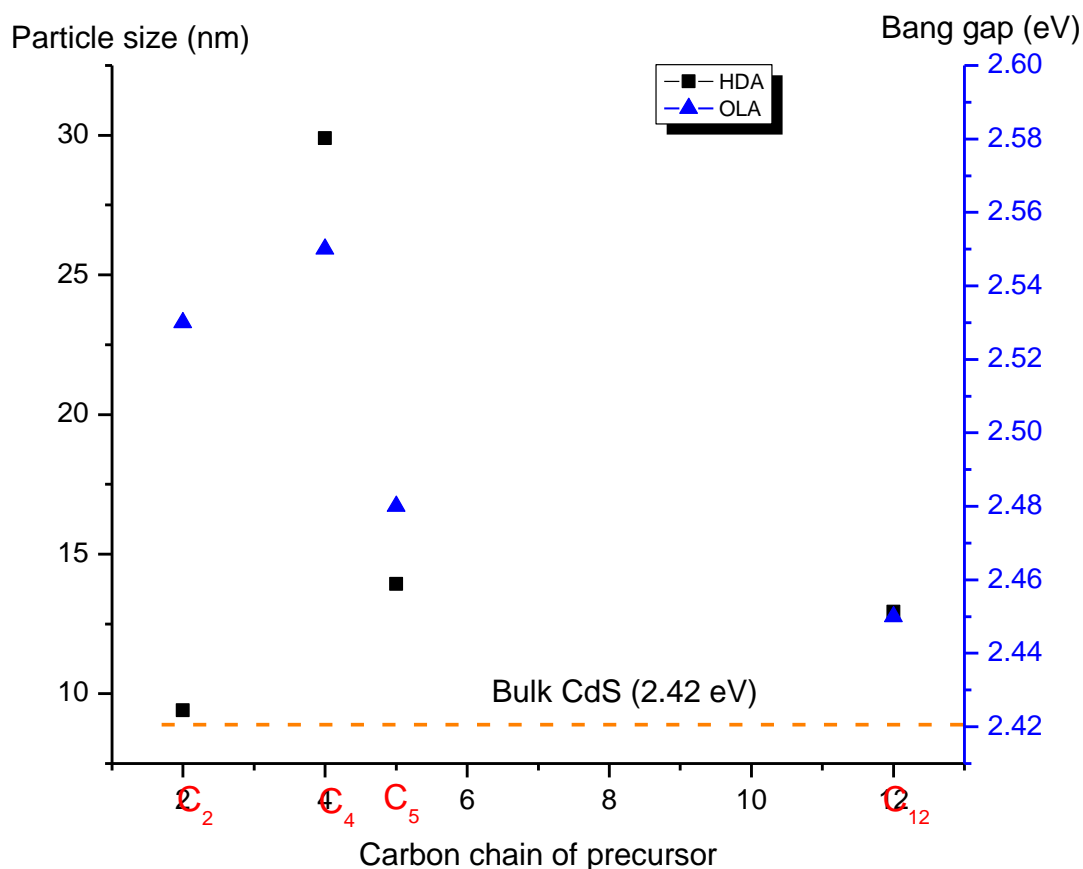


Figure 61. Plots of band gap energy and average particle sizes versus the precursor type of CdS nanoparticles synthesized from Cd(II) dihexyl dte (C₁₂), Cd diethyl dte (C₄), Cd(II) piperidine dte (C₅) and Cd(II) ethyl xanthate (C₂) in HDA and OLA.

In summary, we showed that CdS is a material whose morphology can be handled through the variation of the reactions parameters (the precursor type and the capping group) by the thermolysis of molecular precursors. By changing the nature of the precursor and the capping agent, spherical, oval cubic and rod shaped particles were formed while the optical properties displayed a blue shift as compared to the bulk CdS (515 nm) in general.

3.5. Undoped CdS, In-doped and Ga-doped CdS nanoparticles

Doped semiconductors have generated a lot of interest since they have been shown to improve on both the electrical and optical properties of nanomaterials^{233,234}. Several reports have been made on the synthesis of doped CdS nanomaterials using cobalt, zinc and gallium^{36,233,235,236}. Our interest in this work has been focused on the synthesis of cadmium sulfide nanoparticles doped with indium and gallium as dopants since both are predominantly used in electronics as a semiconductor substrates because of their properties. The annealing method is a rapid process, which facilitates the swift formation of the crystallites with improved grain structure from a single source precursor (SSP). SSPs are compounds which contain the desired elements and decompose to materials with a specific composition. Recently, complexes containing (O-alkyl)xanthate ($-S_2COAk$) ligands have been employed and proven to be potentially useful as SSPs for the preparation of metal sulfide nanomaterials. Metal xanthate complexes are preferred precursors for the low temperature growth of metal chalcogenide nanocrystals, through the Chugaev elimination reaction.^{36,135}

In this section, we report the characterisation of CdS, $Cd_{1-x}In_xS$ and $Cd_{1-x}Ga_xS$ nanoparticles by melt method. The samples, $Cd_{1-x}In_xS$ and $Cd_{1-x}Ga_xS$ were prepared in the range of mole percentage of the metal from 2 to 10%. The crystalline and structural properties of the nanoparticles are investigated.

3.5.1. Syntheses and characterization of In-doped CdS nanoparticles

The samples were prepared as described in section 2.4.1 and 2.4.2, page 52-53. The undoped CdS was observed to be the wurtzite structure (Figure 62). Upon introduction of indium, no additional phases were observed and the reflections of the hexagonal wurtzite phase shifted to higher two theta (2θ) values suggesting that doping was successful (Figure 62). This is consistent with substitutional doping of In(III) in the tetrahedral Cd(II) sites of wurtzite CdS due to the smaller ionic radius of In(III), 76 pm, as compared to Cd(II), 92 pm, resulting in the unit cell to decrease in size. The lattice parameters (a and c) of undoped CdS and CdS:In nanoparticles (Figure 63) were determined by cell refinement using hexagonal CdS as the starting point (a value of 4.137 Å and c value of 6.7144 Å)²³⁷. The refinements showed that there were near linear decrease in the size of the unit cell in both a=b and c with increase mole fraction of indium precursor (Figure 63). Ravichandran and co-workers reported on the influence of indium (In) doping on CdS thin films

by varying the In doping level from 0 to 8%. They found a reduction in the crystal quality with the increase of In-doping amount up to 8%²³⁸. As compared to the undoped CdS sample, the broadening of the reflections increased with the increasing of mole fraction of the doping. This could indicate the reduction of particle size, which may be due to the marginal lowering of lattice parameter suggesting that incorporation of indium in the lattice structure is limited.

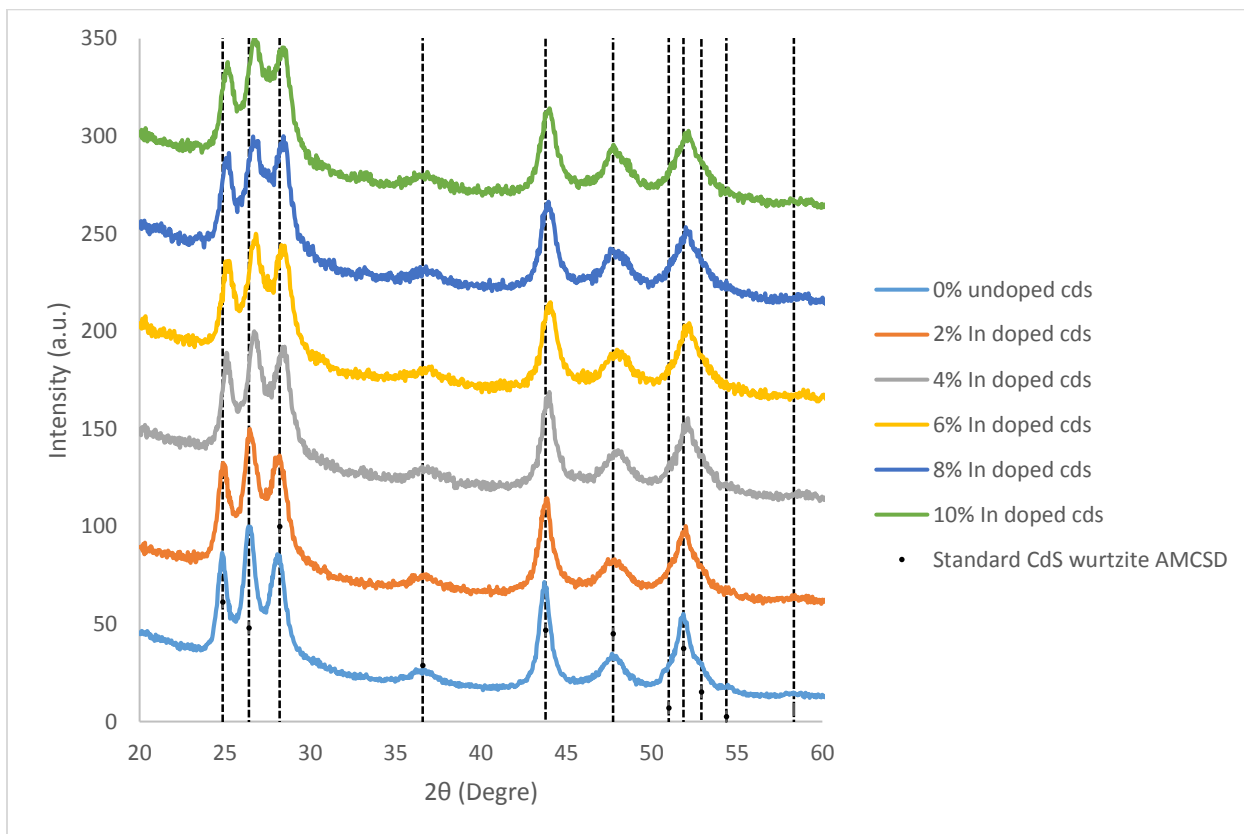


Figure 62. P-XRD patterns of In-doped CdS nanoparticles.

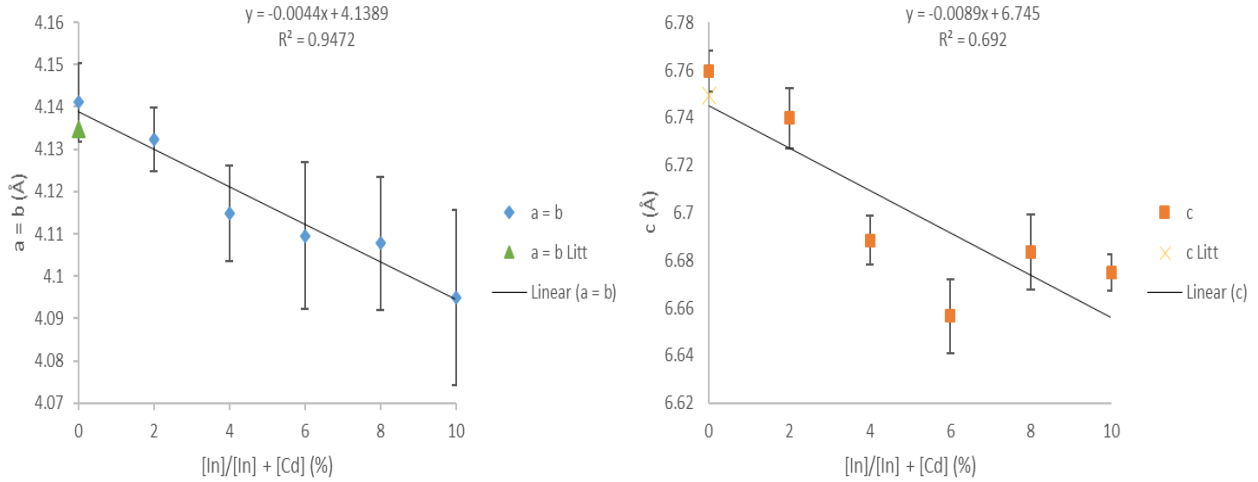


Figure 63. Lattice constant as a function of [In]/[In]+[Cd] ratio.

The SEM images of undoped CdS and In-doped nanoparticles are shown in Figure 64. The samples are composed of irregular shaped grains of different sizes. A smooth and uniform surface coverage morphology is observed for 8 and 10 % doping. Figure 64b shows the morphology of 2% In-doped CdS nanoparticles. Compared to undoped CdS, the surface morphology changes and is respectively to be non- uniform and continuous showing hexagonal-like shaped grains with voids that appear in the picture. As the concentration was raised from 2 to 4 % (Figure 64c), a small amount of undefined crystallites shaped grains were also present. The surface topography at 6% varied significantly and some big undefined shape grains (Figure 64d) were also observed. Figure 64e-f show the surface morphology of 8 and 10% In-doped CdS samples. It is observed that the morphology is uniform and very compact as compared to that of 2, 4 and 6%. Furthermore, the grains are almost uniformly distributed along the entire surface with a denser structure.

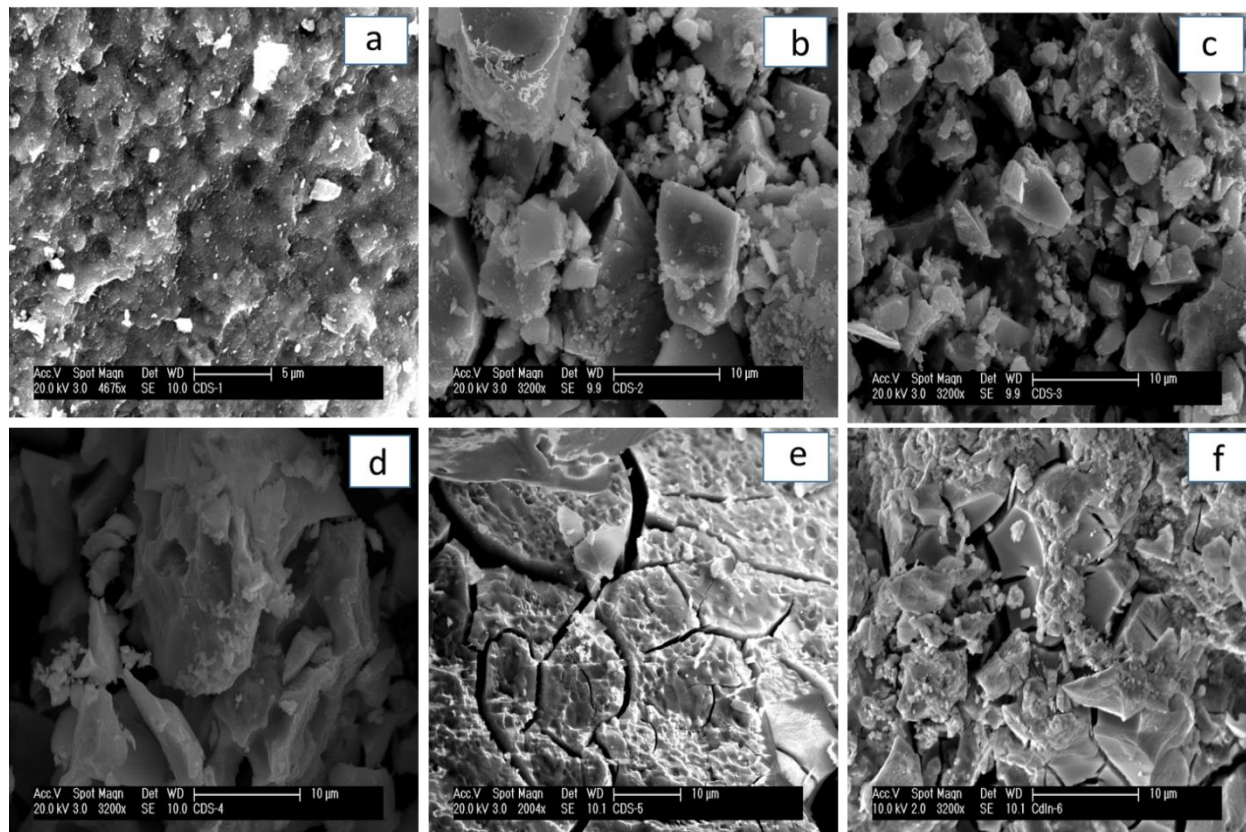


Figure 64. Secondary electron microscopy SEM images (20 kV) of Cd_{1-x}In_xS nanoparticles in the composite range ($0 \leq x \leq 0.1$): a) pure CdS; b) 0.02% indium; c) 0.04% indium; d) 0.06% indium; e) 0.08% indium; and f) 0.1% indium. (Magnification scales of doped CdS samples are 10 μm).

The incorporation of In atoms in CdS nanoparticles was also confirmed by EDX measurements (Table 20), and Figure 65 displays the elemental mapping patterns of undoped CdS, In-doped CdS nanocrystals and indicate the presence of Cd, In and S in the melt nanocrystal. However, some In atoms deficiencies are observed and might be due to the uneven distribution during the synthesis process.

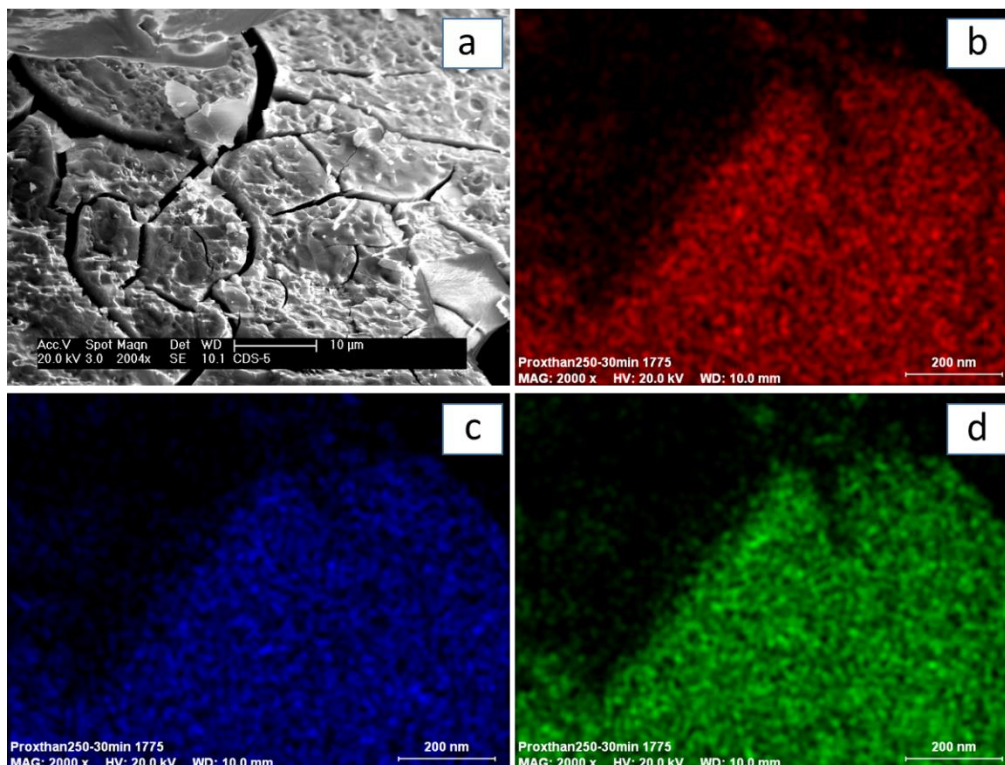


Figure 65. Elemental mapping distributions (20 kV) of Cd, In and S (colored images); a) In-doped CdS at 8%, b) Cd, c) In and d) S emission at 8% indium-doped CdS nanoparticles. (All EDX scale bar correspond to 200 nm).

Table 20. EDX of In-doped CdS.

$\text{Cd}_{1-x}\text{In}_x\text{S}$ ($0 \leq x \leq 0.1$)	0	0.02	0.04	0.06	0.08	0.10
Cd	49.19%	48.00%	47.18%	46.47%	47.50%	44.68%
S	50.81%	50.79%	50.76%	50.33%	48.22%	51.05%
In	/	1.21%	2.06%	3.20%	4.27%	4.27%

The Raman spectra of undoped CdS and In-doped CdS nanoparticles are presented in Figure 66. The fundamental peaks at 297.5 and 599 cm^{-1} correspond to the 1LO and 2LO of the bulk CdS hexagonal structure^{239,240}, whereas the synthesized CdS samples have 1LO and 2LO at 303 and 600 cm^{-1} respectively. The shift in peak position of CdS nanoparticles towards inferior wavelength side was noticed. Some previous reports showed that phonon confinement, strain, defects and broadening associated with the size distribution, were significant features, which affect the phonon

properties²⁴¹. It is also observed from the Figure 66 that the characteristic peaks of the Raman spectra of CdS samples are slightly broad compared to the doped CdS samples. This may be due to the increasing of compositional and structural disorders.²⁴²

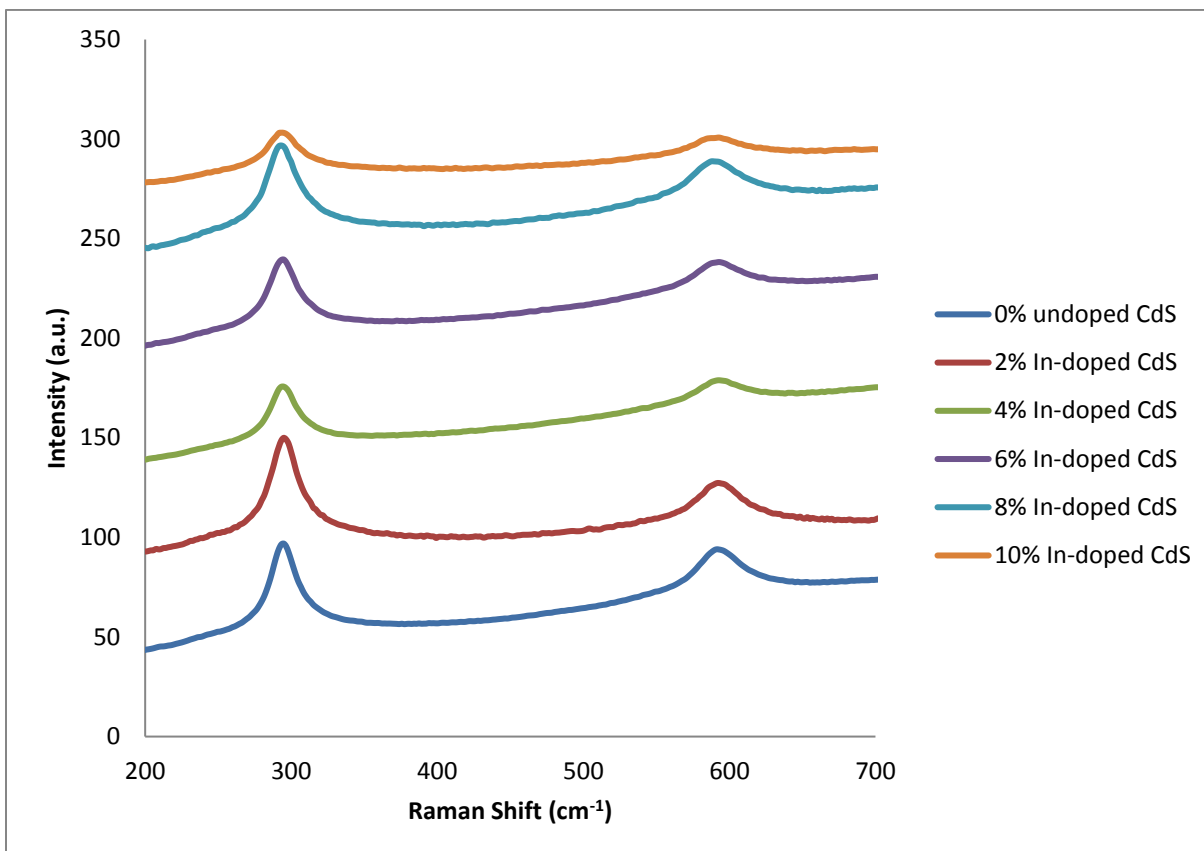


Figure 66. Raman spectra of In-doped CdS nanoparticles.

3.5.2. Syntheses and characterization of Ga-doped CdS nanoparticles

The samples were synthesized as detailed in section 2.4.1 and 2.4.2, page 52-53. The undoped CdS and Ga-doped CdS nanoparticles obtained were found to be the hexagonal structure (Figure 67). Upon introduction of gallium, no additional phases were observed and the reflections shifted to higher two theta values as the ionic radius of Ga(III) is 61 pm as compared to Cd(II), 92 pm (Figure 67). The lattice parameters (a and c) of undoped CdS and CdS:Ga (Figure 68) samples were found by cell refinement using hexagonal CdS as the standard reference (a value of 4.137 Å and c value of 6.7144 Å)²³⁷. When the mole fraction of gallium precursor was increased there was a linear

decrease in $a=b$ and a slight decrease in c (Figure 68). It is known that interstitial incorporation of Ga atoms in CdS gives rise to a deterioration in the crystal structure²⁴³. Some reports exhibited that some dopant metal ions go to interstitial defect sites causing enhanced disorder and increasing the degree of polycrystallinity. Such increase of polycrystallinity might be the reason for lowering of particle size.^{235,243}

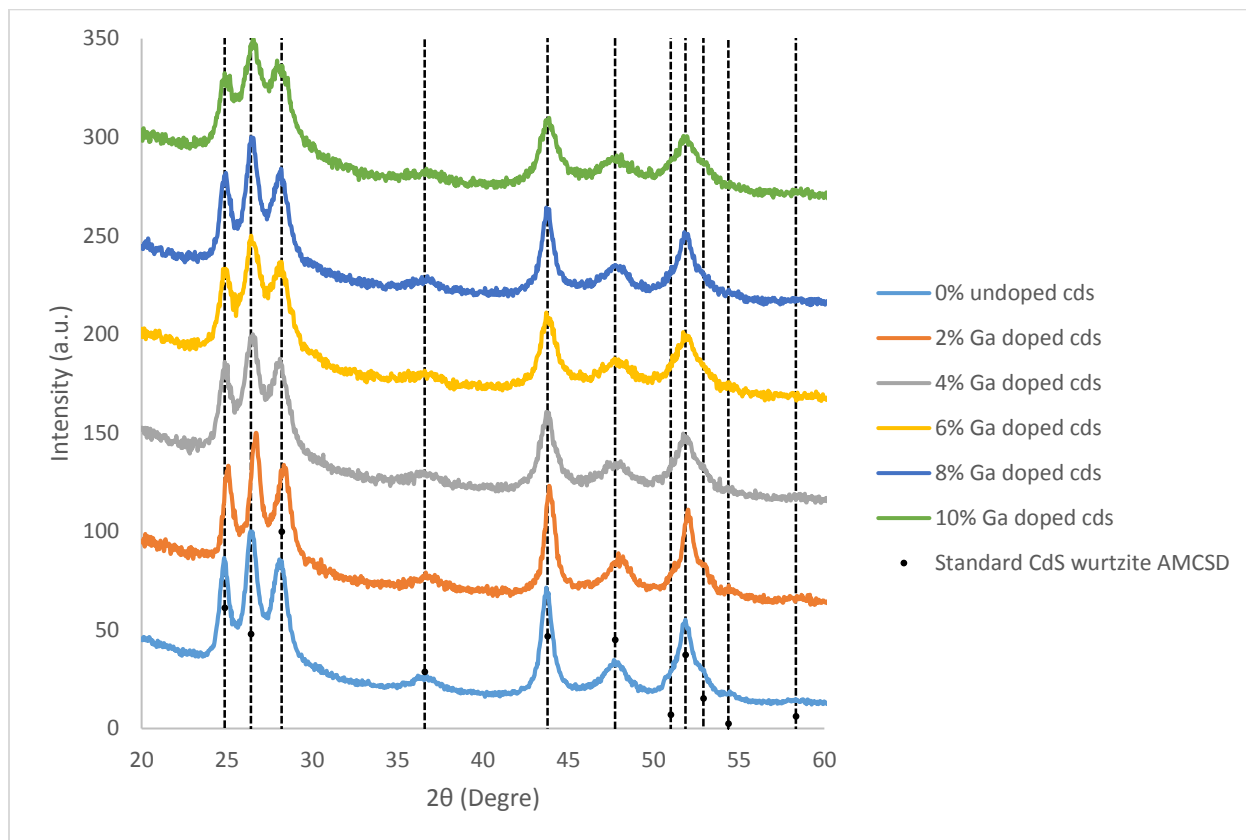


Figure 67. P-XRD patterns of Ga-doped CdS nanoparticles.

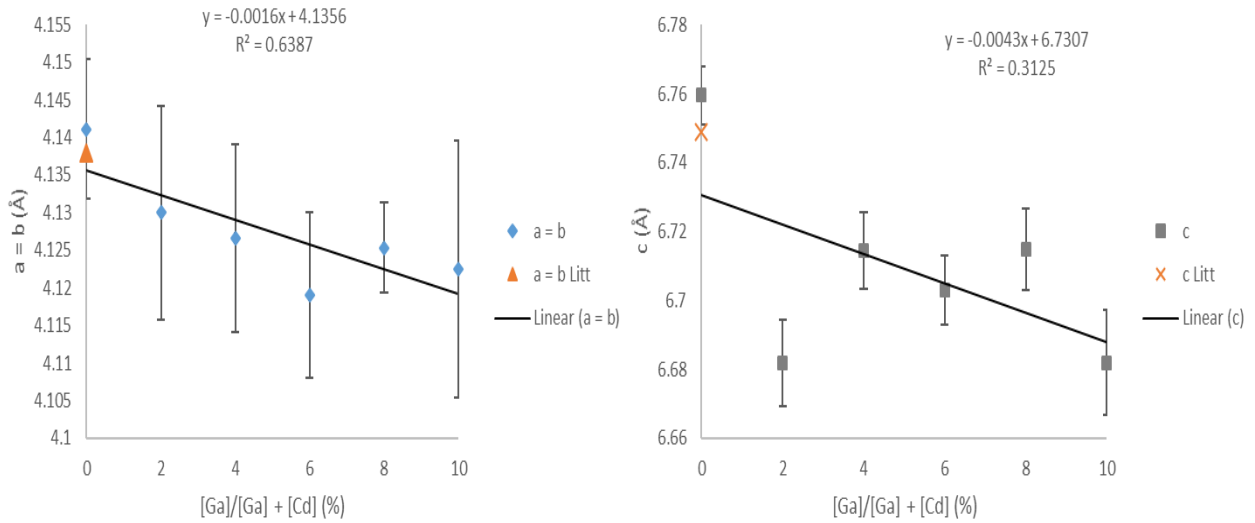


Figure 68. Lattice constant as a function of [Ga]/[Ga]+[Cd] ratio.

SEM images of the undoped CdS and Ga-doped CdS nanoparticles are presented in Figure 69. A smooth and uniform surface coverage morphology is observed for all the Ga-doped CdS nanoparticles. Figure 69b displays the morphology of 2% Ga-doped CdS nanoparticles and it is observed that the surface morphology changed as compared to the undoped CdS sample. When the concentration was increased from 2 to 4 % (Figure 69c), in addition to hexagonal-like shaped grains, a small amount of undefined crystallites shaped grains were also present. The surface topography at 6% still changed considerably. The shape of the grains starts to round and form defined grain (Figure 69d). There is an increase in grain sizes as well, probably due to an expansion in the volume of unit cell²⁴³, which is in agreement with P-XRD results. Figure 69e-f show the surface morphology of 8 and 10%, we noticed that the morphology is uniform and compact compared to that of 2, 4 and 6%.

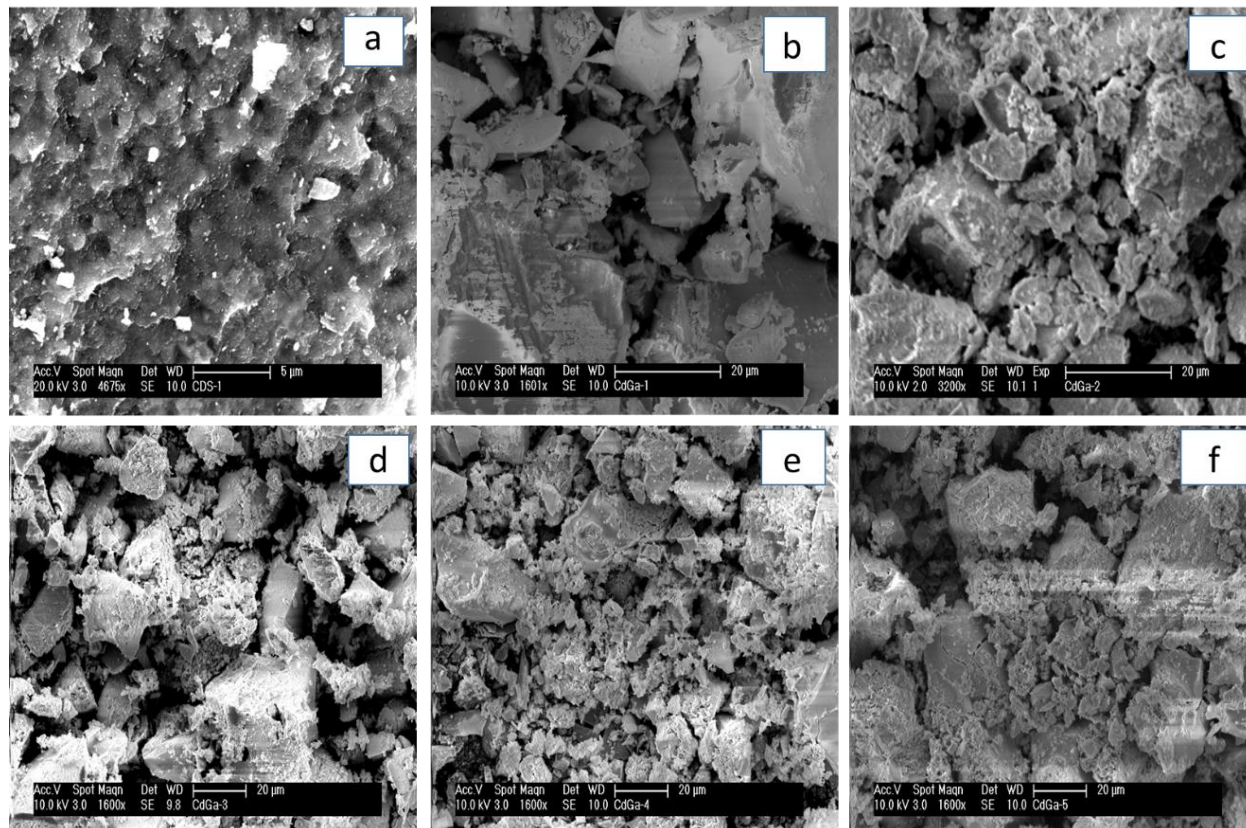


Figure 69. Secondary electron microscopy SEM images (10 kV) of $\text{Cd}_{1-x}\text{Ga}_x\text{S}$ nanoparticles in the composite range ($0 \leq x \leq 0.1$): a) pure CdS; b) 0.02% gallium; c) 0.04% gallium; d) 0.06% gallium; e) 0.08% gallium; and f) 0.1% gallium. (Magnification scales of doped CdS samples are $20 \mu\text{m}$).

Moreover, the incorporation of Ga atoms in CdS nanoparticles was also confirmed from EDX (Table 21), Figure 70 show the elemental mapping distributions of undoped CdS and Ga-doped CdS nanocrystals and specify the existence of Cd, Ga and S in the melt nanoparticle. Nevertheless, some Ga atoms deficiencies are detected.

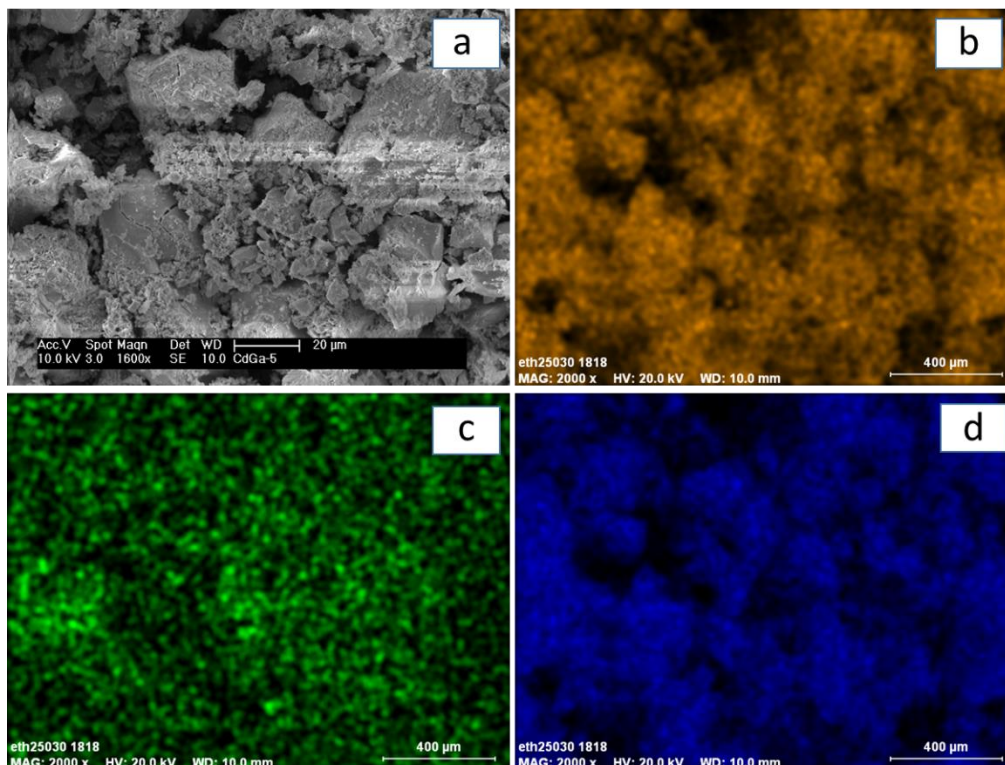


Figure 70. EDX spectrum mapping of the elemental distributions (20 kV) of Cd, Ga and S (colored images); a) Ga-doped CdS at 10%, b) Cd, c) Ga and d) S emission at 10% gallium-doped CdS nanoparticles. (All EDX scale bar correspond to 400 μm).

Table 21. EDX of Ga-doped CdS nanoparticles.

$\text{Cd}_{1-x}\text{Ga}_x\text{S}$ ($0 \leq x \leq 0.1$)	0	0.02	0.04	0.06	0.08	0.10
Cd	49.19%	48.00%	47.18%	46.47%	45.41%	44.24%
S	50.81%	50.79%	50.76%	50.33%	50.33%	50.56%
Ga	/	0.88%	2.16%	2.94%	4.25%	5.20%

Figure 71 presents the Raman spectra of undoped CdS and Ga-doped CdS nanoparticles. In general, the characteristic peaks of the longitudinal optical (LO) modes of CdS are observed from the Raman spectra. The fundamental peaks at 297.5 and 599 cm^{-1} correspond to the 1LO and 2LO of the bulk CdS hexagonal structure^{239,240}, while the prepared CdS nanoparticles have 1LO and 2LO at 303 and 600 cm^{-1} correspondingly. The shift in peak position of CdS nanoparticles towards

lower wavelength side was observed. We also noticed that the shift in 1LO and 2LO peak positions of CdS nanoparticles are in good agreement with the bulk CdS.

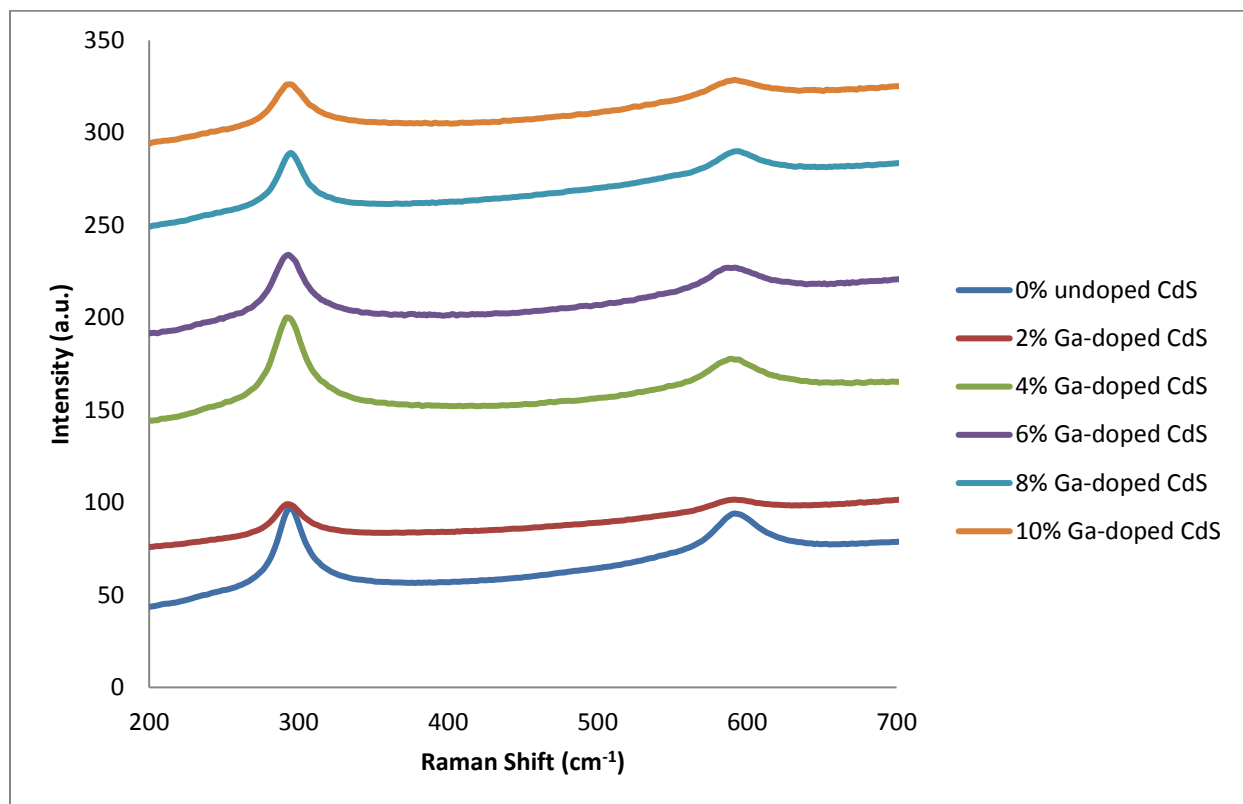


Figure 71. Raman spectra of Ga-doped CdS nanoparticles.

To summarize, In-doping and Ga-doping with various concentrations have an important influence on the morphology of CdS nanoparticles. Crystallographic analysis revealed that wurtzite CdS crystallites incorporated In³⁺ and Ga³⁺ was obtained without any phase change or formation of additional phases. This was confirmed by observation of the expected decrease in unit cell size.

3.6. Deposition of lead sulfide, copper sulfide and cadmium sulfide thin films

PbS, Cu_xS_y and CdS have been used for a wide-ranging of technological applications such as sensors, photocatalysts, photovoltaic cells, electro-optic modulators, sensors, photo luminescent devices, antireflection coatings, lithium ion batteries and supercapacitors due to their unique size dependent, optical and electronic properties^{244–247}. Many methods including spray pyrolysis²⁴⁸, chemical bath deposition (CBD)²⁴⁹, successive ionic layer absorption²⁵⁰ and chemical vapour deposition (CVD)^{63,251,252} have been used.

The use of single source precursors in aerosol assisted chemical vapor deposition (AACVD) can have the advantage of avoiding toxic precursors and eliminating undesired effects of the anions of the metal salt. AACVD is a simple and cost effective technique, which is well known to produce high quality thin films. Dithiocarbamates²⁵³, thiosemicarbazides²⁵⁴, xanthates⁴⁷, imidodiphosphinates⁴¹, N-alkyl thioureas¹³², dichalcogenophosphinates⁴³ and dichalcogenophosphates²⁵⁵ metal complexes have been investigated for the preparation of some metal sulfide thin films.

In this paragraph, we aim to explore the use of heterocyclic thiourea lead and copper complexes, heterocyclic dithiocarbamate and xanthate cadmium complexes as molecular precursors for the deposition of PbS, Cu_xS_y and CdS thin films by the AACVD method.

3.6.1. Syntheses and characterization of lead sulfide thin films

In this section, we report the deposition of PbS thin films on glass substrate at various temperatures by AACVD from N-morpholine and N-pyrrolidine lead (II) N'-benzoylthioureato complexes used as single source precursors. These lead complexes and thin films were characterized as reported in section 2.6 and 2.7.

The films deposited by AACVD were investigated by powder X-ray diffraction. The recorded patterns for films obtained using Pb-morpho complex (**1**) and Pb-pyrro complex (**2**) are summarized in the Figures 72 and 73. The films deposited are all of well-defined galena PbS with the halite structure (ICDD 05-0592). The deposited films all gave very sharp peaks in the p-XRD and indeed at values greater than ca 60° of the 2θ the peaks for 1.5405 Å and 1.54434 Å of Cu K alpha radiation are seen. These results indicate good crystallinity. There are many literature studies of PbS: the original mineralogical study in 1925²⁵⁶ gave 5.3 Å lattice parameter, whilst Wyckoff in 1963 gives 5.9363 Å²⁵⁷ and one at 298 K by Noda 1987²⁵⁸ gives 5.9315 Å.

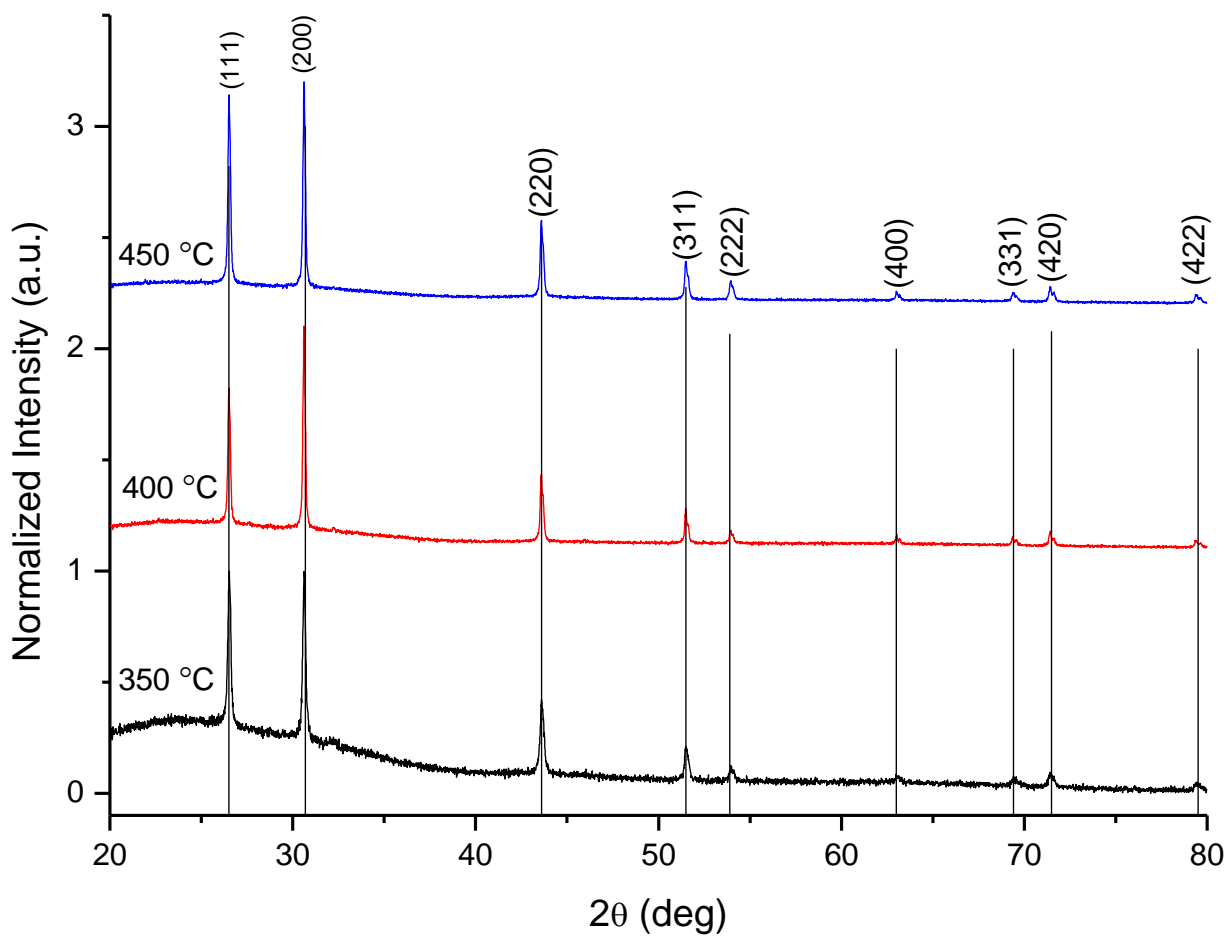


Figure 72. P-XRD patterns of PbS thin films deposited from complex (1) at temperatures 350, 400 and 450 °C.

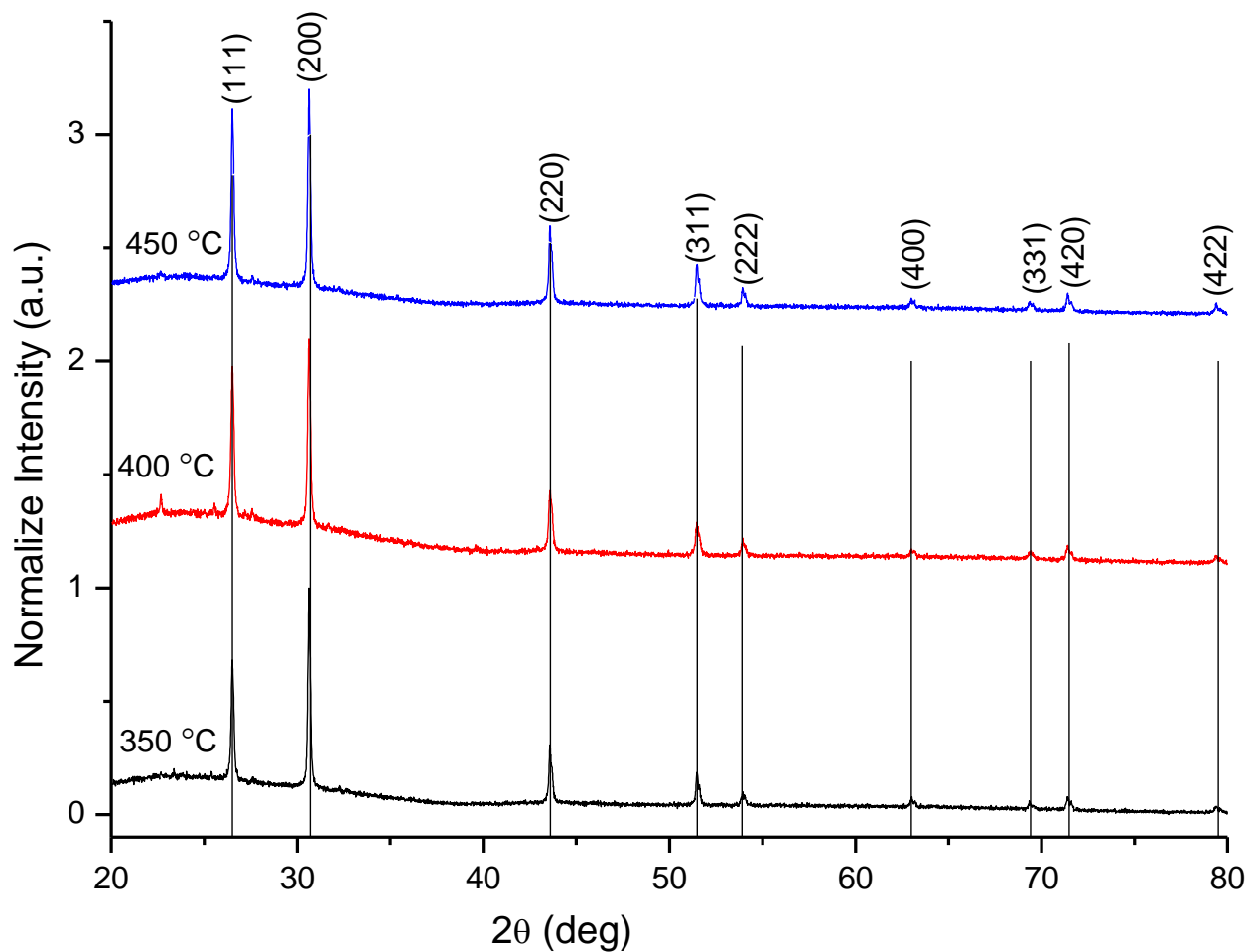


Figure 73. P-XRD patterns of PbS thin films deposited from complex (2) at temperatures 350, 400 and 450 °C.

Table 22. Calculated lattice parameter/Å (Calculated for all peaks below $2\theta = 60^\circ$).

Temp./°C	Complex (1)	Complex (2)
350	5.930(5)	5.933(4)
400	5.931(6)	5.932(4)
450	5.923(6)	5.932(4)
Average	5.928(4)	5.932(5)

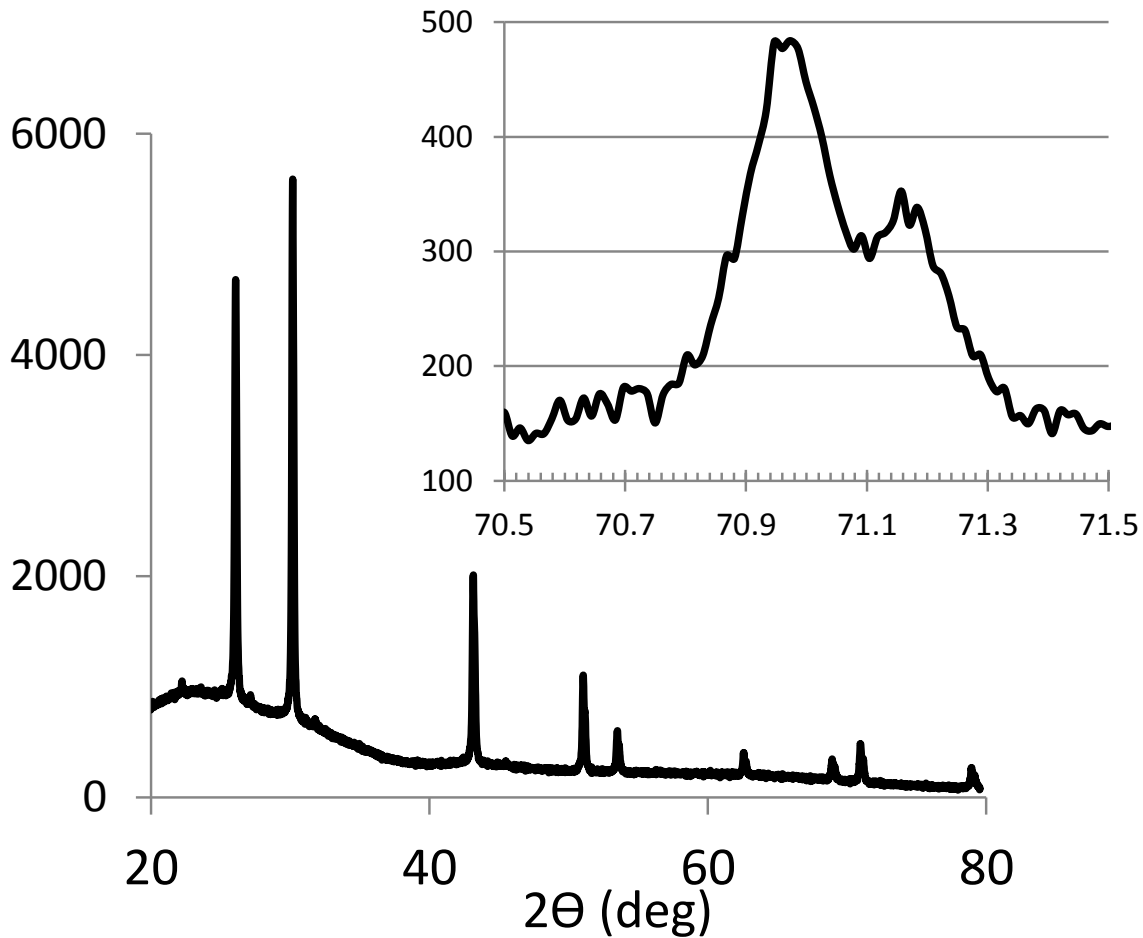


Figure 74. Highly resolved p-XRD pattern. The lattice constant a value can be measured using the average Cu $K\alpha$ value of 1.54184 \AA for all values of 2θ less than $ca 60^\circ$. Inset: average XRD patterns for all depositions, with of course little or no difference in peak position.

The lattice parameters are remarkably consistent and summarized in Table 22. The lattice constant determined for our samples from all peaks below 63° gave consistent values for the lattice constant from each deposition (Table 23) and an overall average of $5.930(5) \text{ \AA}$ consistent with the literature. An average plot of all samples is shown in Figure 74, a small non-indexed peak appearing at $2\theta = 22.71^\circ$ is seen for the films deposited at 400°C . At the higher angle diffraction close to 71° is weak and somewhat noisy and the average of all peak is shown (inset Figure 74). However the two component peaks for the Cu $K\alpha$ components can be seen and beautifully corresponding values for the a value of 5.934 \AA and 5.935 \AA are seen from the (420) reflection. These results show that the thin films are well crystallized.

Table 23. The values of the lattice parameter calculated twice for each temperature from the ca 71° (420) peak.

Sample	2θ	2θ	λ = 1.5405 Å	λ = 1.54434 Å
C(1) 350 °C	70.940	71.180	5.936	5.934
C(1) 400 °C	70.990	71.180	5.933	5.934
C(1) 450 °C	70.960	71.170	5.935	5.934
C(2) 350 °C	70.950	71.160	5.936	5.935
C(2) 400 °C	70.970	71.160	5.934	5.935
C(2) 450 °C	70.960	71.160	5.935	5.935
		Av	5.935(1)	5.934(1)

The relative orientations are summarized in Figure 75 and slightly rod like SEM images were seen in the image. The coverage area is largely close to 100% at the substrate temperature at several temperatures (Figure 90 and always >80–90). Various particle sizes and morphologies were obtained and the average particle size was estimated using the intercept technique where a random straight line is drawn through the micrograph, the number of grain boundaries intersecting the line are counted. The average grain size is found by dividing the number of intersections by the actual line length.

$$\text{Average grain size} = 1 / (\text{number of intersections} / \text{actual length of the line})$$

At 350 °C when Pb-morphu complex was used, cubic-shaped PbS particles were formed with an average size of 85 nm (Figure 75a). A rise in temperature to 400 °C resulted in the formation of a mixture of spherical and cubic shaped particles with an average size of 84 nm (Figure 75b). At higher deposition temperature of 450 °C, predominantly rod-shaped PbS particles were obtained with an average size of 83 nm (Figure 75c). A slight decrease in the particle grain size with an increase of temperature was observed. When Pb-pyrtru complex was used as precursor, a remarkable difference in grain sizes and uniformity was observed as the temperature was varied from 350 to 450 °C. At 350 °C, spherical particles aggregates were formed with an average size of 71 nm (Figure 75d). As the temperature was increased to 400 °C, the shape of crystallites changed from spherical to cubic particles with an average size of 90 nm (Figure 75e) and the

deposition at 450 °C resulted in the growth of large cube-shaped PbS particles with an average size of 105 nm (Figure 75f). An increase in the particle size with an increase of temperature was observed. EDX analysis results showed that the films are sulfur deficient (Table 24). This could be due to the large atomic size of lead as compared to sulfur.

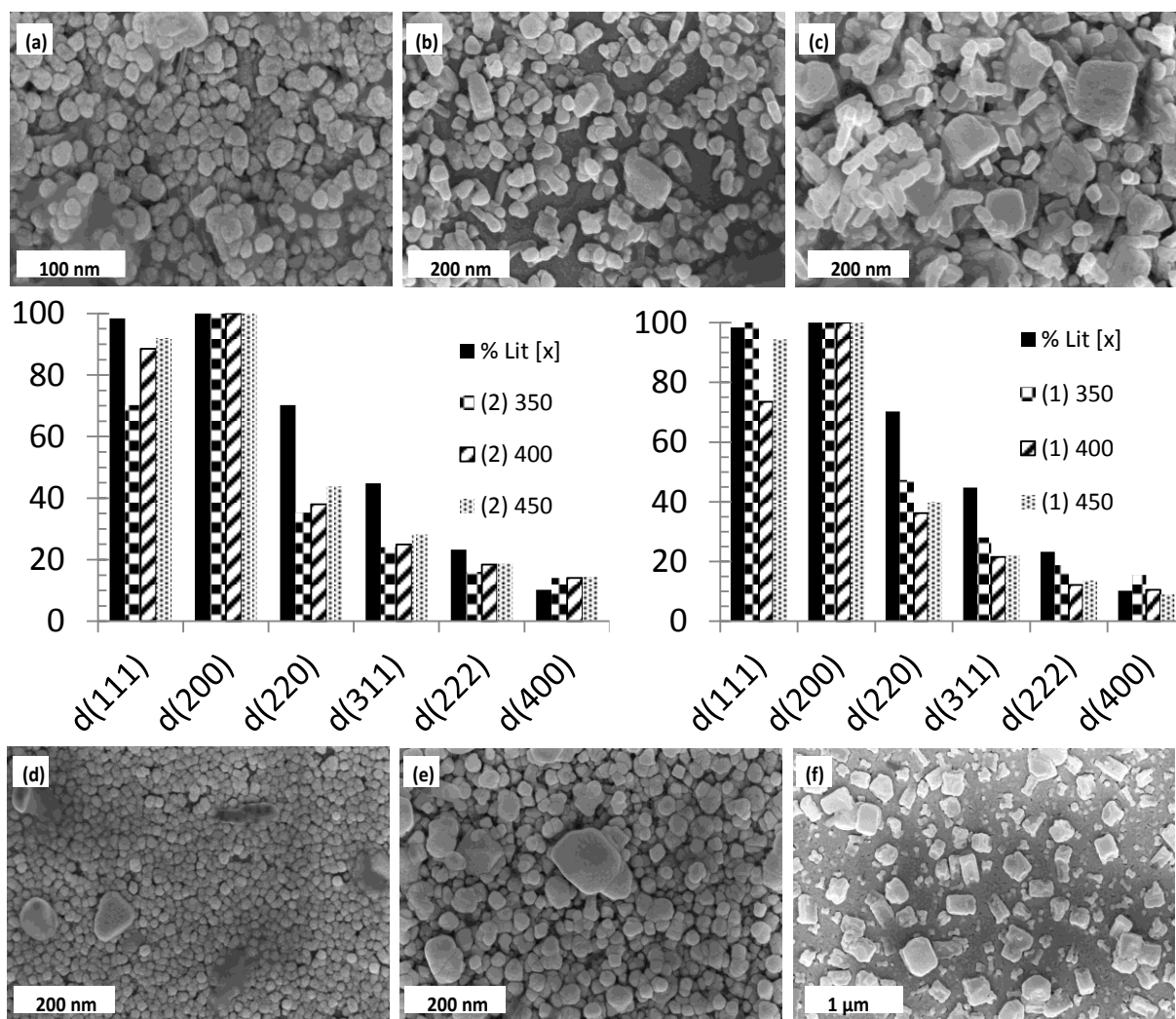


Figure 75. SEM images of PbS films deposited from Pb-morpho complex onto glass substrates at (a) 350, (b) 400 and 450 °C and from Pb-pyrro complex at (d) 350, (e) 400 and (f) 450 °C. The orientations of the powder patterns for both depositions are shown in the middle compared to the literature pattern of PbS. There is a small tendency for films to extend along one axis as seen in SEM and by XRD.

Table 24. Elemental composition found by EDX spectroscopy of Pb and S in the thin films deposited using both complexes Pb-morphtu (1) and Pb-pyrirtu (2).

Complex	Temp (°C)	Pb	S	Pb : S
(1)	350	60	40	1 : 0.667
	400	60	40	1 : 0.672
	450	54	46	1 : 0.840
(2)	350	54	46	1 : 0.869
	400	56	44	1 : 0.776
	450	61	39	1 : 0.639

The room temperature UV–Vis absorption spectra of the PbS films recorded in the wavelength range of 250 –1000 nm, uncoated glass substrate as a reference are shown in the Figures 76 and 77. The energy band gap (E_g) was determined from the Tauc plot equation²⁵⁹ using their transmission and reflectance curves as well as the following formula:

$$(\alpha h\nu)^2 = A(h\nu - E_g)$$

$h\nu$ is the energy of the incident light, E_g the band gap of the sample and α is the absorption coefficient.

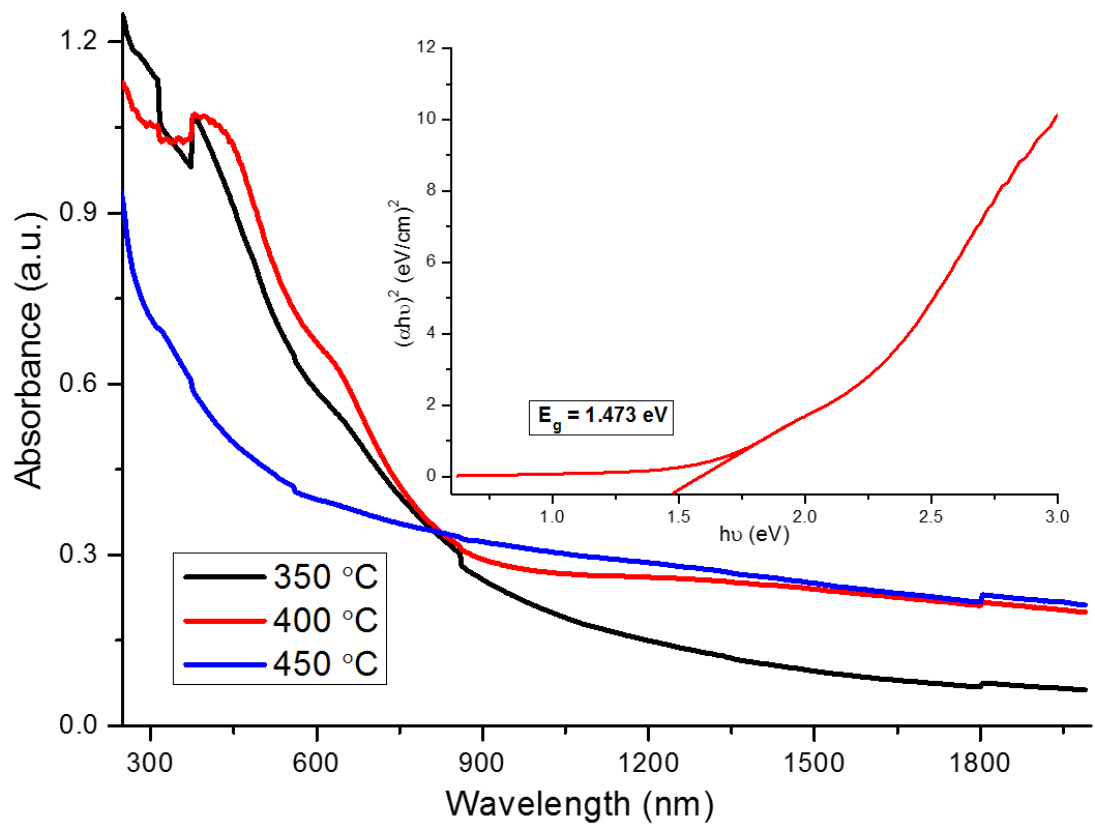


Figure 76. UV–Vis absorption spectra of PbS films deposited on glass substrate using complex (1) at 350, 400 and 450 °C (Inset: Representative Tauc plots for the PbS obtained at 400 °C).

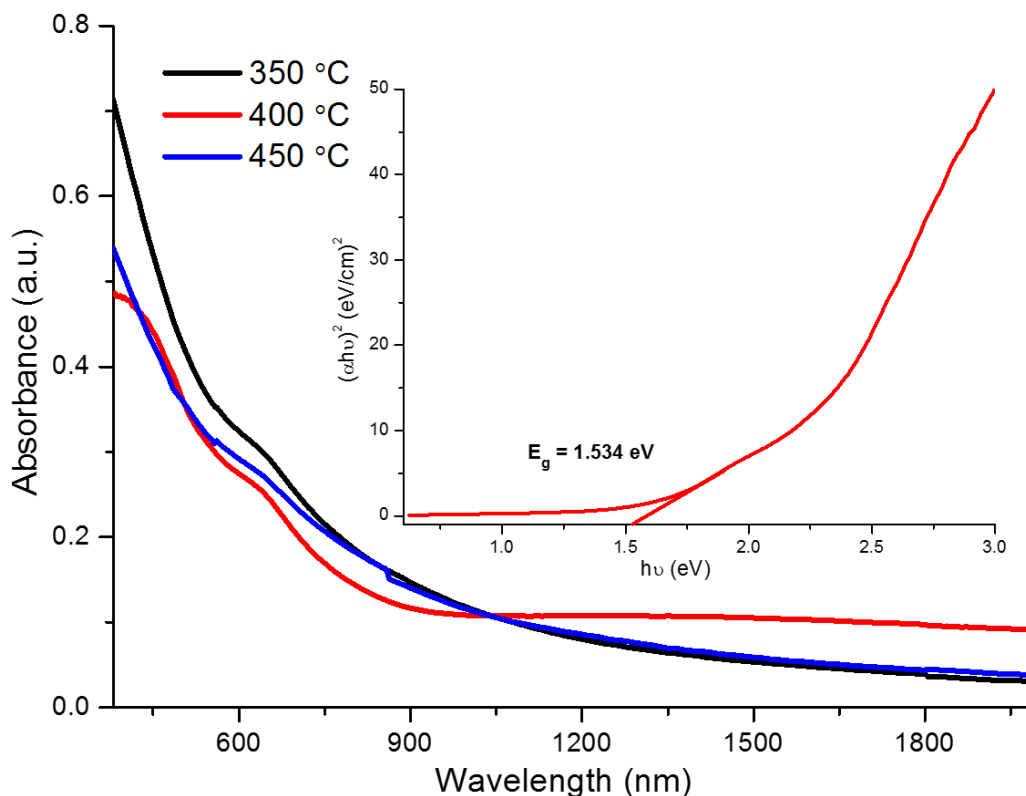


Figure 77. UV–Vis absorption spectra of PbS films deposited on glass substrate using complex (2) at 350, 400 and 450 °C (Inset: Representative Tauc plots for the PbS obtained at 400 °C).

A strong blue shift as compared to the bulk PbS was observed in the absorption band edges of all the PbS films deposited at the different temperatures. The observation is in line with the literature where the reported PbS band gap varying in a wide range up to 2.3 eV from the bulk value of 0.41 eV^{260–263}. This work reports PbS thin films with band gap in the range of 1.46 – 1.55 eV. These band gap values are larger than expected for particles with sizes in the range of 70 – 105 nm, greater than PbS Bohr exciton radii (18 nm)^{260,264}. The results further reveal that the band gap of the as-deposited PbS films gradually decreases (from 1.49 eV to 1.46 eV – Pb-morphu complex and 1.55 eV to 1.46 eV – Pb-pyrriu complex) as temperatures were increased from 350 °C to 450 °C, respectively.²⁶¹

3.6.2. Syntheses and characterization of copper sulfide thin films

In this section, we report the deposition of copper sulfide thin films by AACVD from of N-morpholine-N'-benzoylthioureatocopper(II) and N-pyrrolidine-N'-benzoylthioureatocopper(II) complexes used as molecular precursors. These copper complexes and thin films were characterized as reported in section 2.6 and 2.7.

The P-XRD results of the deposited copper sulfide thin films at temperatures between 350 and 450 °C are presented in Figures 78a and 79a. The diffraction peaks are matched in general, to a mixture of hexagonal Cu₂S (ICDD: 046-1195) and cubic CuS₂ phase (ICDD: 033-0492) in all films deposited at various temperatures from both complexes¹³¹. The P-XRD patterns of the as deposited films at 350 and 400 °C from Cu-morphthtu complex showed two reflection peaks (200)[#], (210)^{*} indexed to the cubic and hexagonal phase respectively while at 450 °C two new reflection peaks (111)[#] and (101)^{*} detected are indexed to the cubic and hexagonal phase respectively. On the other hand, when complex (4) was used, one prominent reflection peak (200)[#] was observed at 350 °C while at 400 and 450 °C two new reflection peaks (210)^{*} and (101)^{*} appeared. Furthermore, intensity of (200)[#] peak in p-XRD pattern of copper sulfide films showed to increase as a result of temperature increase. No specific peak of any other phase of copper sulfide or impurities was detected. The SEM images of the copper thin films deposited are shown in Figures 78 and 79. The morphology of thin films prepared at 350 °C from complex (3) is mainly composed of small snowy particles forming large cubic clusters (Figure 78b), with an average size ca. 420 nm. Uniform coverage was observed, without the presence of any fissures in the film. EDX analysis (Table 25) showed the deposition of slightly sulfur deficient films Cu:S (50.9:49.1). Films deposited at 400 °C revealed non uniform spherical block like crystallites (Figure 78c) with sizes ca. 460 nm. The size of the crystallites increases considerably and the morphology obtained at this temperature is closely related to the previously reported copper sulfide thin films using the copper thiobiuret complex¹³¹. A copper to sulfur ratio of 51.6:48.4 was observed for these thin films by EDX analysis. Deposition of films at a higher temperature of 450 °C shows in the formation of uniform cubic shaped structures with sizes greater than 590 nm (Figure 78d). The EDX results also showed sulfur deficient thin films with a copper to sulfur ratio of 54.7:45.3. The shape of thin films were observed to be highly reliant on the growth temperature.

Table 25. Elemental composition found by EDX spectroscopy of Cu and S in the thin films deposited using both complexes Cu-morphu (3) and Cu-pyrrtu (4).

Complex	Temp (°C)	Cu	S	Cu : S
(3)	350	50.9	49.1	1 : 0.959
	400	54.7	45.3	1 : 0.778
	450	51.6	48.4	1 : 0.916
(4)	350	54.1	45.9	1 : 0.826
	400	51.4	48.6	1 : 0.959
	450	51.9	48.1	1 : 0.916

Table 26. Phases and morphologies of copper sulfide thin films obtained.

Deposited thin films by AACVD				
Complex	Deposition temp (°C)	Phase (formula)	Morphology	Average crystallite size (nm)
(3)	350	Mixture of	large cubic clusters	420
	400	hexagonal (Cu ₂ S) and	spherical to cubic	460
	450	cubic(CuS ₂)	cubic	590
(4)	350	Mixture of	Snowy flake-like	310
	400	hexagonal (Cu ₂ S) and	Spherical crystallites	470
	450	cubic(CuS ₂)	Spherical crystallites	580

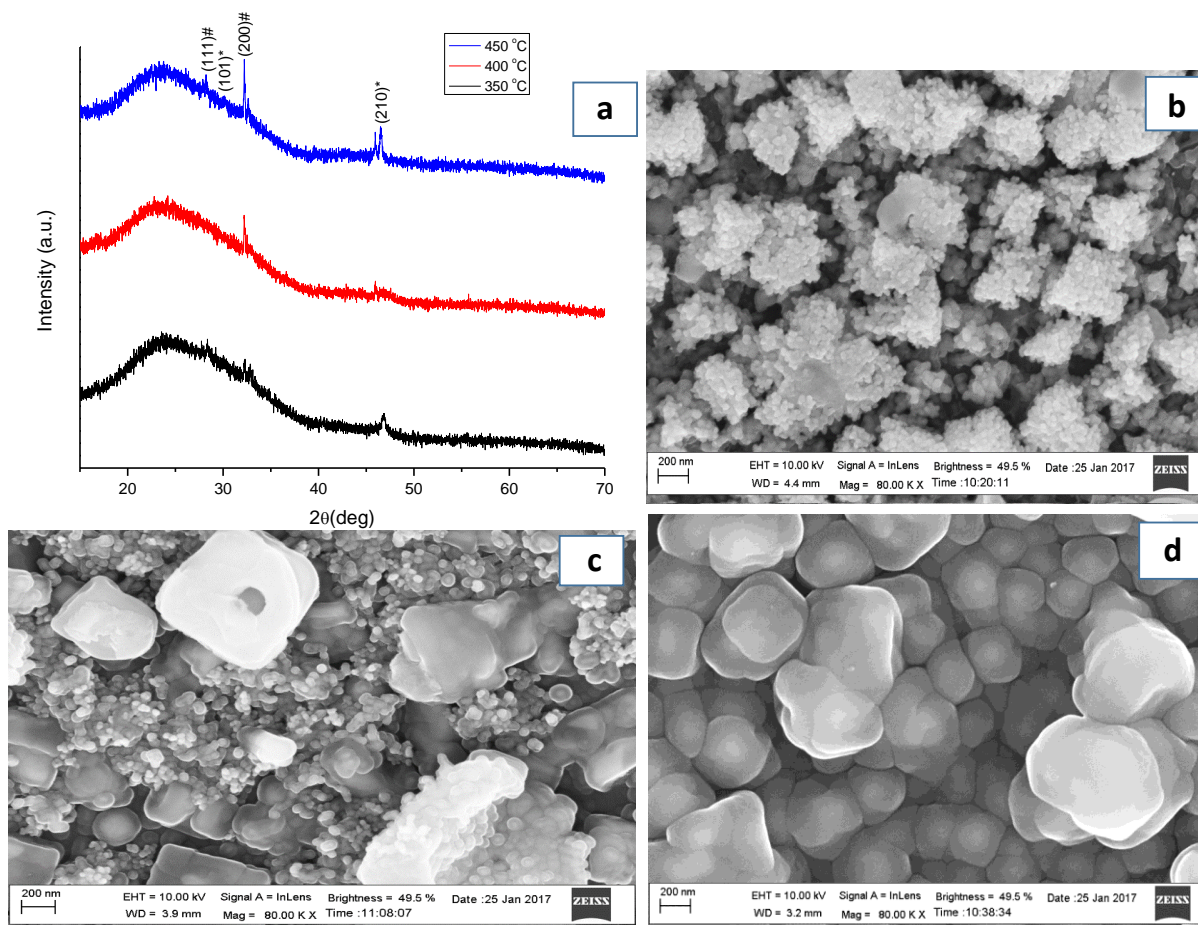


Figure 78. a) P-XRD pattern of CuS deposited on glass substrate by AACVD from Cu-morphu complex (* hexagonal Cu_2S , # cubic CuS_2) and SEM images of CuS films deposited at deposition temperatures (b) 350 °C, (c) 400 °C and (d) 450 °C.

The same trend was observed when Cu-pyrrtu complex was used (Figure 79), deposition at 350 °C gave films with uniform morphology based on snowy flakes with sizes in the range of 280-320 nm (Figure 79b). The morphology changed forming large cubic clusters with some irregular spherical particles at 400 °C (Figure 79c). Although the films deposited at 450 °C showed large, irregular spherical particles (Figure 79d). EDX analysis revealed sulfur deficient thin films at all temperatures. A uniform distribution of copper and sulfur was indicated by EDX analysis, as almost same percentages of copper to sulfur were observed at different regions of the thin films. The increase in crystallite size is due to inter-particle aggregation, as a function of temperature. The decomposition of the precursor and thermal diffusion of the particles at the substrate surface is directly related to the temperature. The higher incident flux can cause a shadowing effect during

growth process. The particles will tend to form aggregates by combining with particles, present near the impact point. Similarly, the adatom layer may behave as a template for incoming molecular flux at higher temperature and results in the accelerating of the growth of crystallites to larger particles. However, the specific growth mechanism by CVD method is fairly complex and may embrace some other factors²⁶⁵. The summary of phases, morphology and average crystallite sizes of copper sulfide films are presented in Table 26.

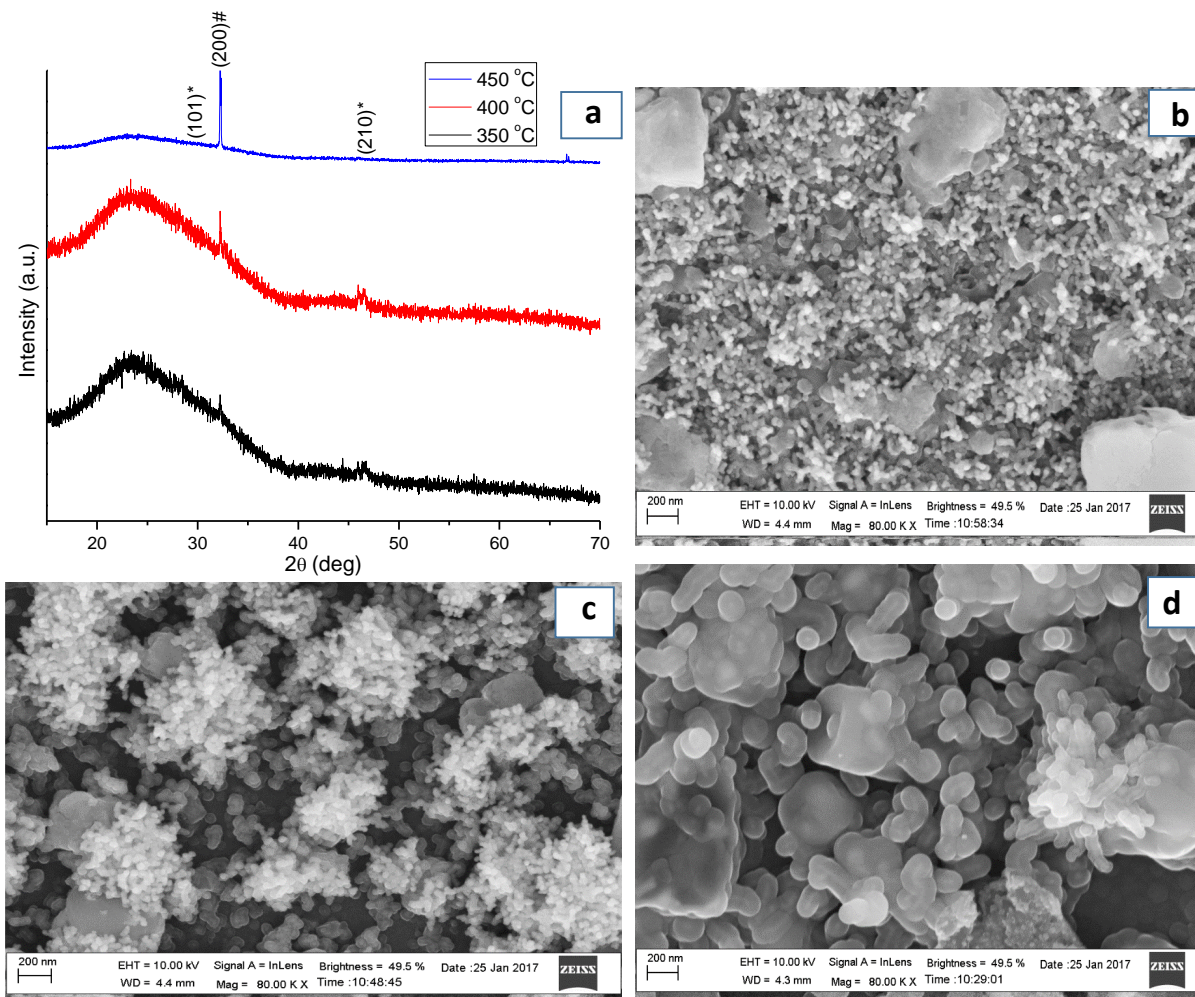


Figure 79. a) P-XRD pattern of CuS deposited on glass substrate by AACVD from Cu-pyrrtu complex (* hexagonal Cu_2S , # cubic CuS_2) and SEM images of CuS films deposited at deposition temperatures (b) 350 °C, (c) 400 °C and (d) 450 °C.

3.6.3. Syntheses and characterization of cadmium sulfide thin films

In this section, we report the deposition of hexagonal CdS thin films of various morphologies by AACVD method on glass substrate at different temperatures in THF and chloroform, using cadmium(II) dihexyl (a), diethyl (b), piperidinyl (c) dithiocarbamates and ethyl xanthate (d) complexes as single source precursors. The effect of the alkyl chain of the precursor, the temperature as well as the solvent used on the optical properties and morphology of the CdS films is also investigated.

Clean yellowish and uniform CdS films were obtained when CdS thin films were deposited on a glass substrate. The room temperature UV–Vis absorption spectra of the CdS thin films were recorded in the range of 400–800 nm, using the glass substrate as a reference are shown in Figures 80i, 81i and 82i. The energy band gaps (E_g) were estimated using the Tauc plots²⁵⁹ as shown in Figures 80ii, 81ii and 82ii. The deposited CdS thin films showed variation in the energy band gap with temperature and precursor type. When dihexyl dithiocarbamate complex (C_6 carbon chain compound) was dissolved in THF and deposited at 400 °C, an absorption band edge at 510 nm was observed (Figure 80ia), showing a slight blue shift of 5 nm compared to the bulk CdS (515 nm). When the ethyl dithiocarbamate complex (carbon chain of the dithiocarbamate precursor was reduced from C_6 to C_2), a shift to higher wavelength was observed in the absorption band edge (Figure 80ib). When the heterocyclic piperidinyl dithiocarbamate complex (cyclic C_5 carbon chain) was used, a red shift of 8 nm was observed (Figure 80ic) with the absorption band edge at 523 nm. When the starting material was then changed to the ethyl xanthate complex, an absorption band edge at 508 nm (Figure 80id) was observed.

When the deposition temperature was increased from 400 °C to 450 °C (Figure 81, Table 27), all the absorption spectra were red shifted except for the films obtained from the ethyl xanthate complex. The decrease in the energy band gap of the films, could be due to the increase of particle size at this temperature.

The effect of solvent on the optical properties of the CdS films was investigated at 450 °C by dissolving the precursors in the solvent mixture (THF + chloroform) (Figure 82i). It was observed that the CdS films obtained absorbed at higher wavelengths compared to the films which were synthesized in THF alone. This could be attributed to the fact that chloroform is a weaker coordinating solvent compared to THF (Figure 82, Table 27).

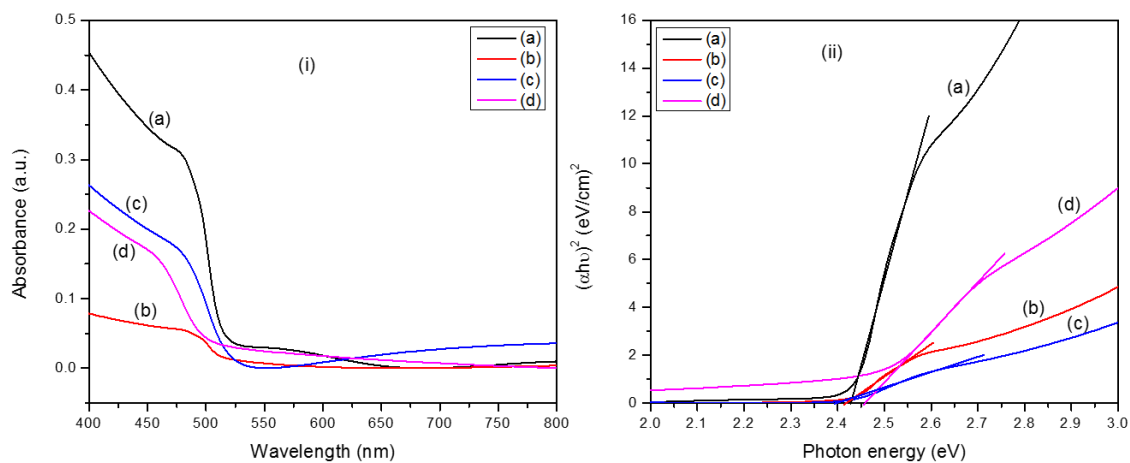


Figure 80. (Left UV-Vis absorption spectra of CdS films deposited on glass substrate using complexes (a), (b), (c) and (d) at temperature of 400°C; Right Tauc plot showing the estimated optical band gap).

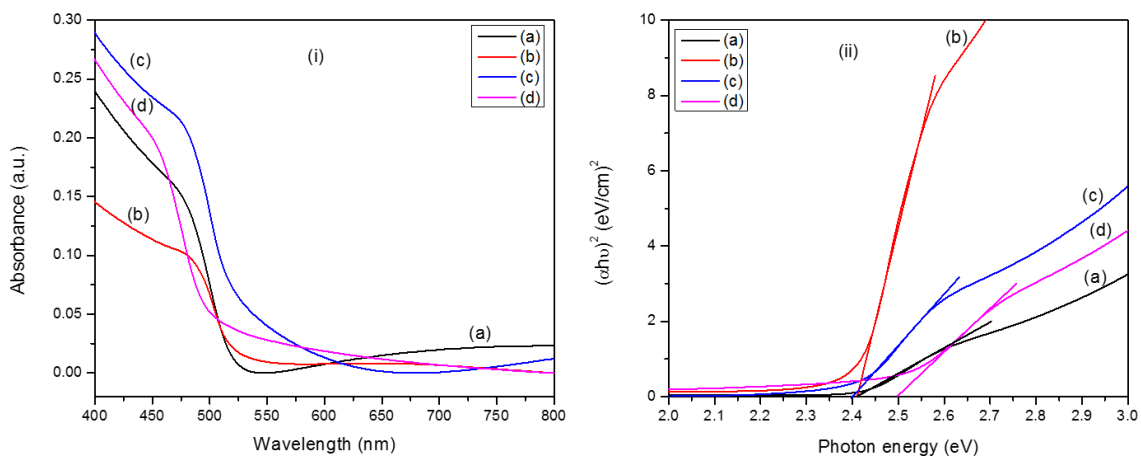


Figure 81. (Left UV-Vis absorption spectra of CdS films deposited on glass substrate using complexes (a), (b), (c) and (d) in THF solvent at temperature of 450°C; Right Tauc plot showing the estimated optical band gap).

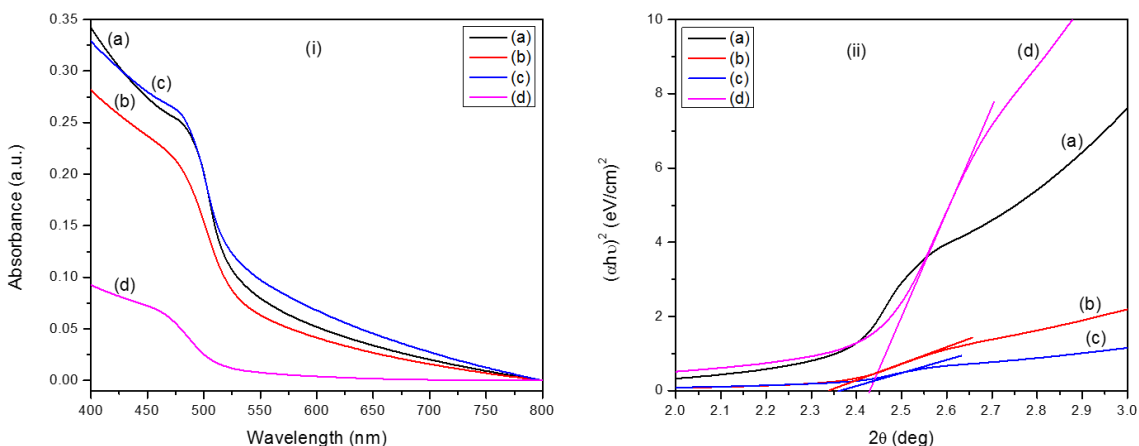


Figure 82. (Left UV-Vis absorption spectra of CdS films deposited on glass substrate using mixed solvents (THF+chloroform) using complexes (a), (b), (c) and (d) at temperatures of 450°C; Right Tauc plot showing the estimated optical band gap).

The photoluminescence (PL) properties of the deposited CdS thin films using the cadmium complexes were investigated by exciting the films at 300 nm excitation wavelength. The emission spectra are shown in Figures 83, 84 and 85. The deposited CdS films at 400 °C showed broad peaks in the 515-560 nm and 520-545 nm regions when dihexyl dithiocarbamate (**a**) (Figure 83a) and diethyl dithiocarbamate (**b**) (Figure 83b) complexes respectively were used. A low emission peak at 485 nm blue shifted to the absorption band edge was however observed when the piperidinyl dithiocarbamate complex (**c**) (Figure 83c) was used. When the ethyl xanthate complex (**d**) (Figure 83d) was used, a broad peak in the 530-545 nm region was observed. The broad peaks observed between 520 and 570 nm are probably due to electron–hole traps (surface defect emission from sulfur vacancies)²⁶⁶. It could also be related to microstructure imperfection and lattice defects of the CdS thin films²⁶⁷, leading to the red emission. The same observation was made when the temperature was increased to 450 °C and using the mixed solvents (THF + chloroform), (Figures 99 and 100). The optical properties of the deposited CdS thin films are summarized in Table 27.

Table 27. Optical properties of the deposited CdS thin films.

Cd(II) complex	Temp (°C)	Solvent	Band edge (nm)	Band gap (eV)	PL max. (nm)
(a)	400	THF	510	2.43	515-560
(b)			515	2.41	520-545
(c)			523	2.37	485
(d)			508	2.44	530-545
(a)	450	THF	515	2.41	489
(b)			520	2.42	490
(c)			518	2.40	486
(d)			498	2.49	520-550
(a)	450	THF + chloroform	523	2.37	500-545
(b)			527	2.35	487
(c)			508	2.44	485
(d)			525	2.36	520-540

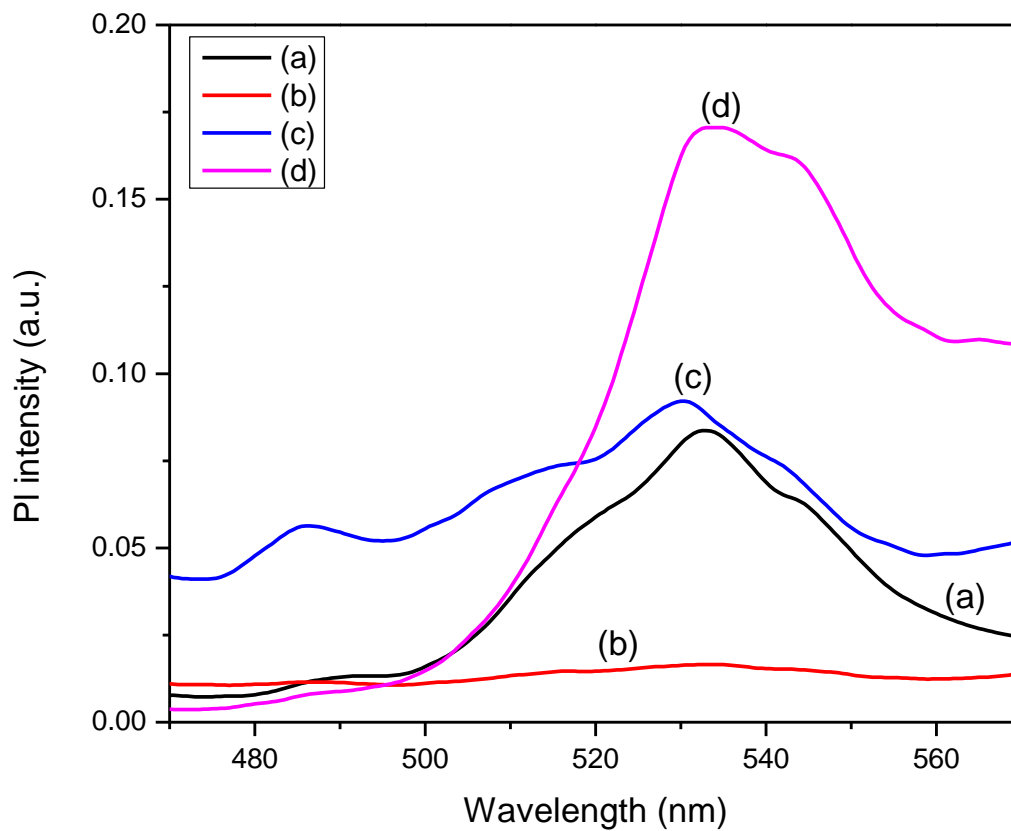


Figure 83. Photoluminescence emission spectra of CdS thin films deposited at 400 °C using complexes (a), (b), (c) and (d) ($\lambda_{\text{exc}} = 300 \text{ nm}$).

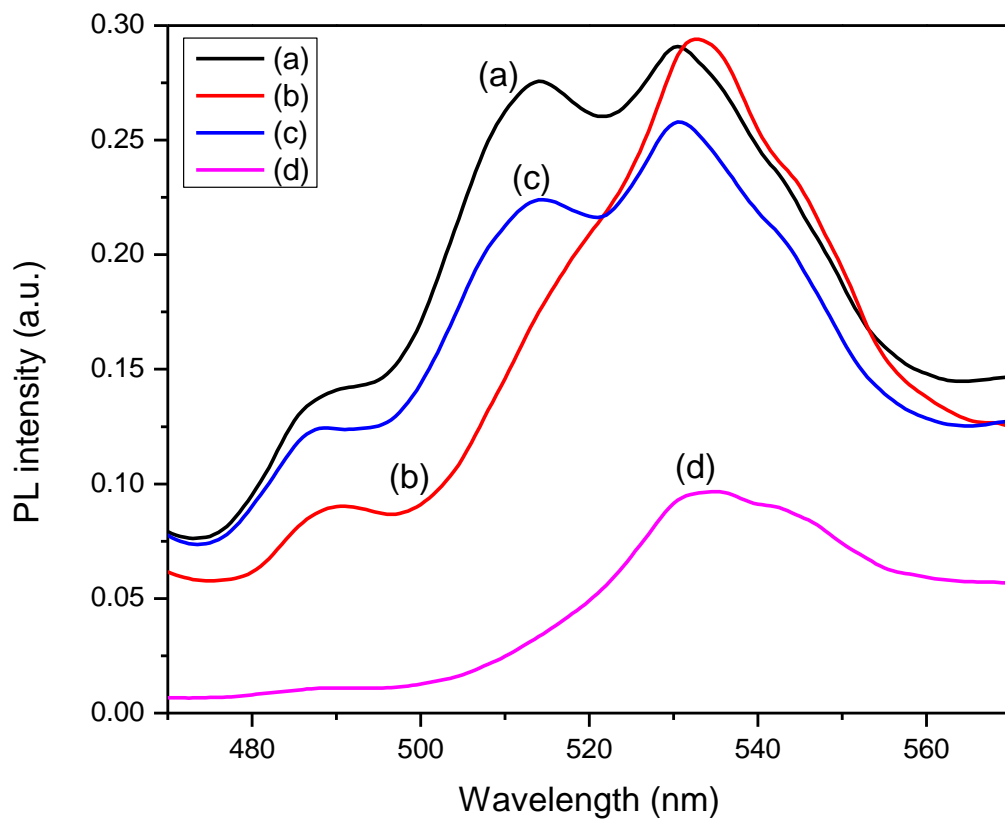


Figure 84. Photoluminescence emission spectra of CdS thin films deposited at 450 °C using complexes (a), (b), (c) and (d) ($\lambda_{exc} = 300$ nm).

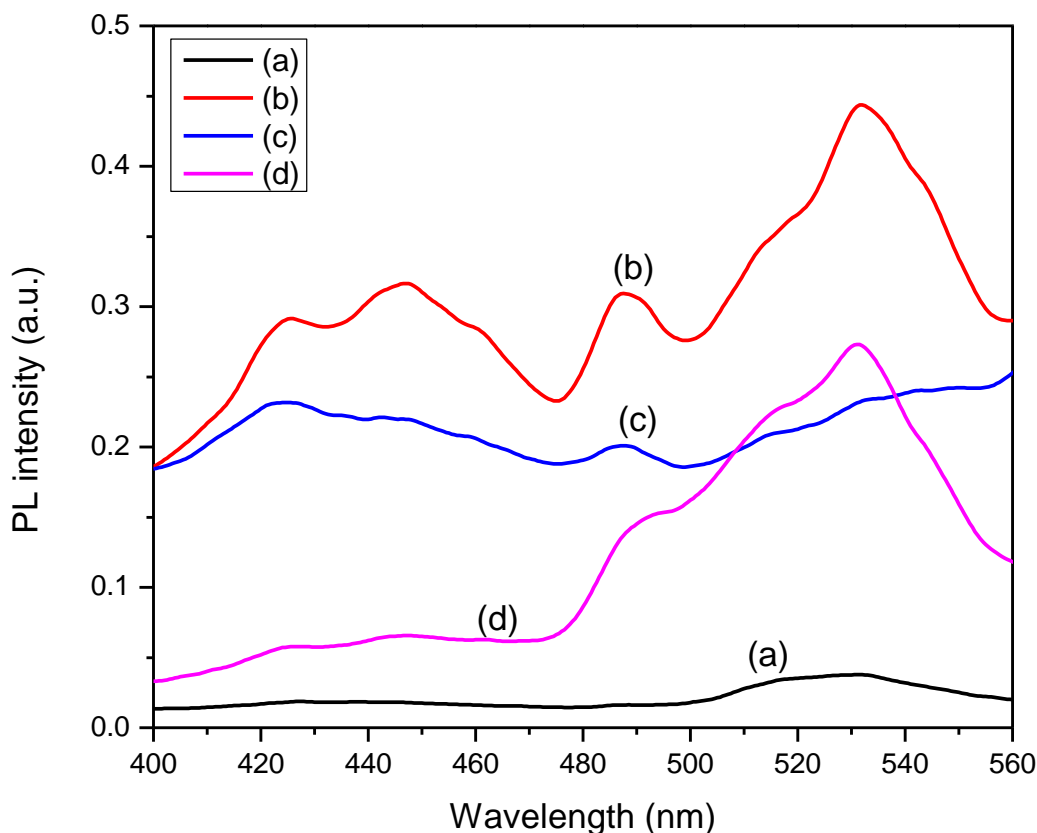


Figure 85. Photoluminescence emission spectra of CdS thin films deposited using mixed solvents (THF + chloroform) at 450 °C using complexes (a), (b), (c) and (d) ($\lambda_{exc} = 300$ nm).

P-XRD patterns (Figures 101, 102 and 103) showed deposition of hexagonal phase CdS thin films. The three dominant peaks in the diffraction patterns of the films deposited at 400 °C and 450 °C (Figures 86 and 87) can be assigned to (100), (002), (101) reflections of the pure hexagonal phase and the values matched to those in the ICDD values (card # 01-077-2306). Also, the high intensity of the (002) peak in the p-XRD pattern of CdS thin films is an indication that the particles were preferably elongated along the c-axis²²⁸. When the mixed solvent (THF + chloroform) was used at 450 °C (Figure 88), extra peaks were visible and indexed to the hexagonal phase. The presence of the un-indexed peaks in the XRD patterns obtained from complexes (a) and (c) could be attributed to some impurities from the alkyl and heterocyclic carbon chain of the materials. Also, a reduction in the intensity of the (002) peak in p-XRD patterns of all the synthesized samples was observed.

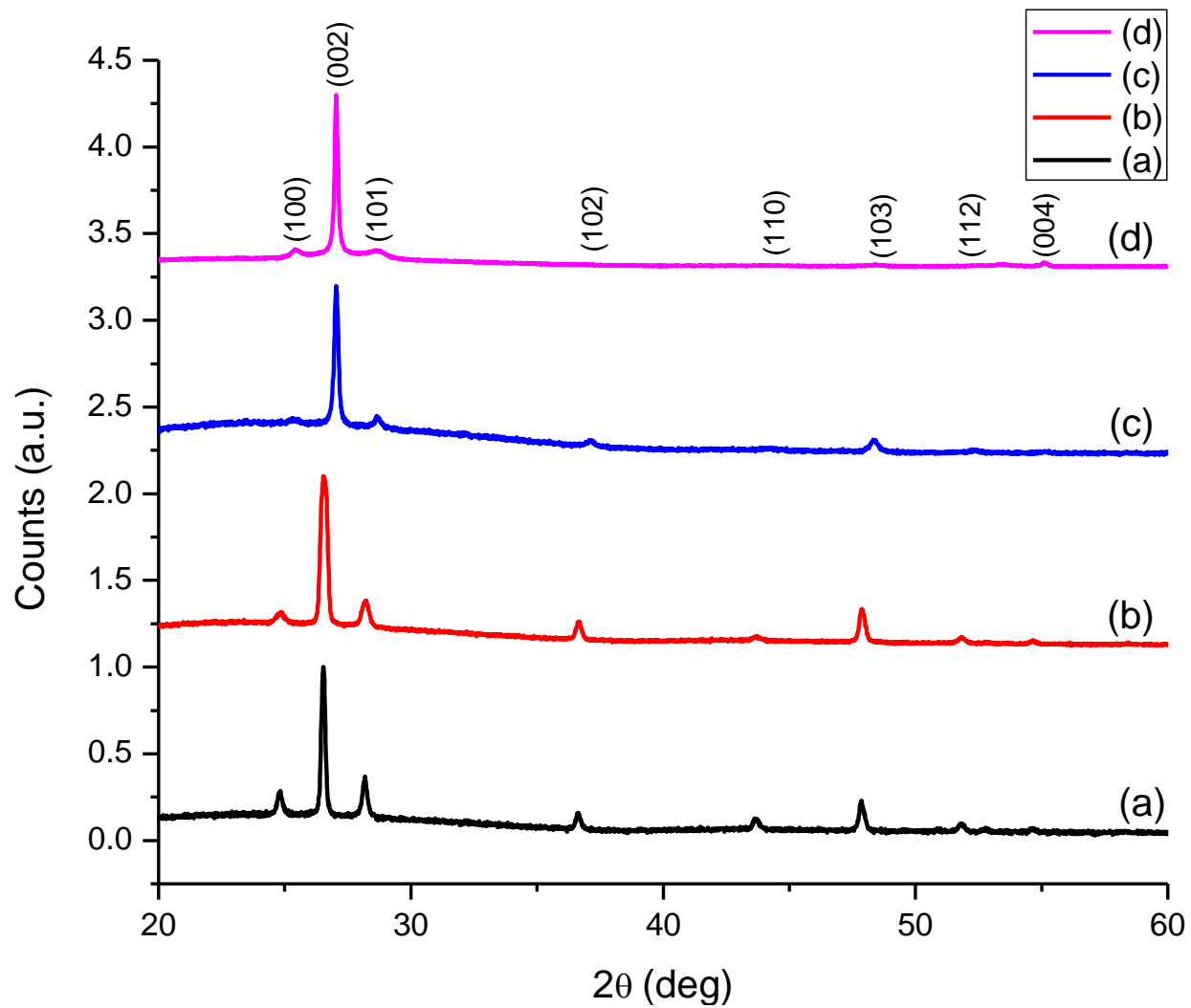


Figure 86. Powder X-ray patterns of CdS films deposited at 400 °C using complexes (a), (b), (c) and (d).

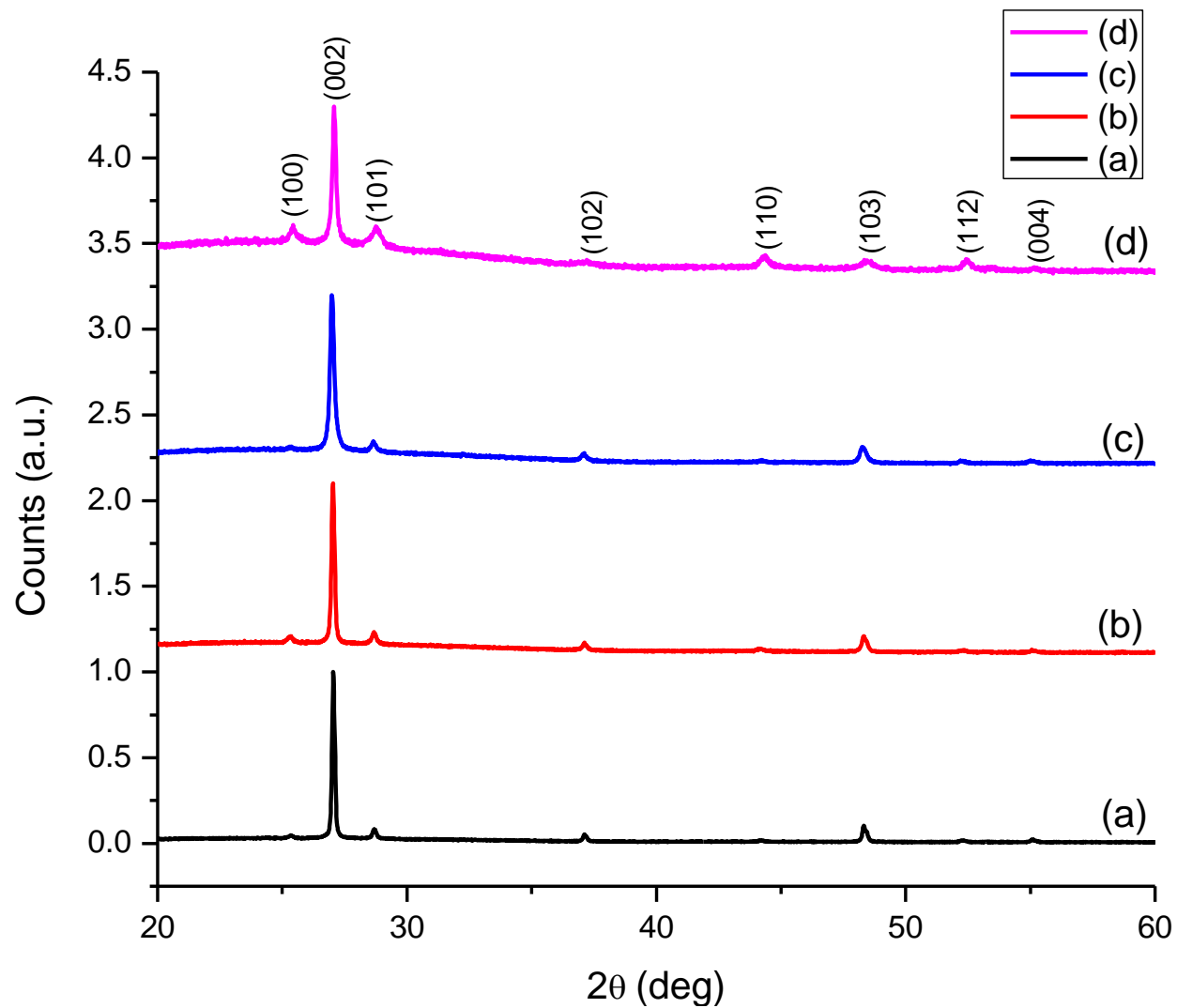


Figure 87. Powder X-ray patterns of CdS films deposited at 450 °C using complexes (a), (b), (c) and (d).

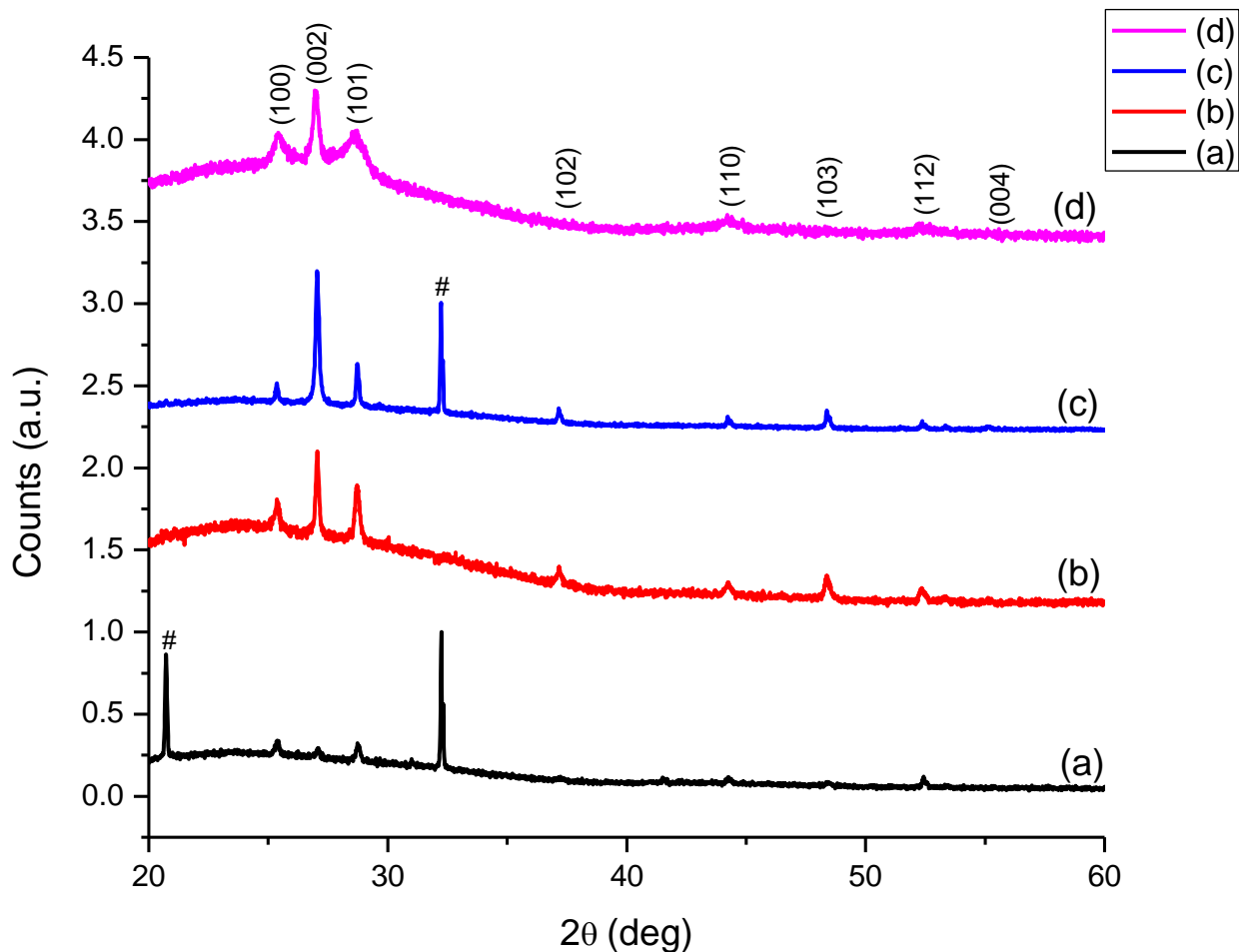


Figure 88. Powder X-ray patterns of CdS films deposited using mixed solvents (THF+chloroform) at 450 °C using complexes (a), (b), (c) and (d).

The scanning electron microscopy (SEM) micrographs of the deposited CdS films are shown in Figures 89, 90 and 91. The films deposited revealed variability in morphologies when the precursor was varied from Cd(II) dithiocarbamates to ethyl xanthate at 400 and 450 °C. The surface morphology of CdS films deposited at 400 °C is presented in Figure 89. When complex (a) (C₆ carbon chain) was used, densely packed granular crystallites were formed with particle sizes ranging from 60 – 120 nm (Figure 89a). Complex (b) (C₂ carbon chain), produced loose and well packed with uniform and regular patterns of roughly cubic to spherical shaped particles. A decrease in the particle size (20 - 32 nm) was observed (Figure 89b). When complex (c) was used (heterocyclic carbon chain), very compact and hexagonal-like shaped CdS films were deposited with average size of 22-35 nm (Figure 89c). Ethyl xanthate precursor (d) (C₂ carbon chain) interestingly resulted in the formation of star shaped CdS films (Figure 89d), with lengths of 33-

63 nm and diameters of 12 - 23 nm. As the deposition temperature was raised to 450 °C (Figure 90), morphology and coverage of films significantly changed. All films showed increased coverage of approximately 100 %. Complex (a) showed spherical shaped and aggregated grains with *ca.* 90 nm in size (Figure 90a). When complex (b) was used (Figure 90b), formation of larger hexagonal granule-shaped crystallites was observed, whereas complex (c) produced irregular flake-like shaped particles with sizes in the range of 104 - 186 nm (Figure 90c). Changing the precursor from dithiocarbamate to xanthate (d), formation of spike-like shaped particles with sizes ranging from 200 - 245 nm (Figure 90d) was observed.

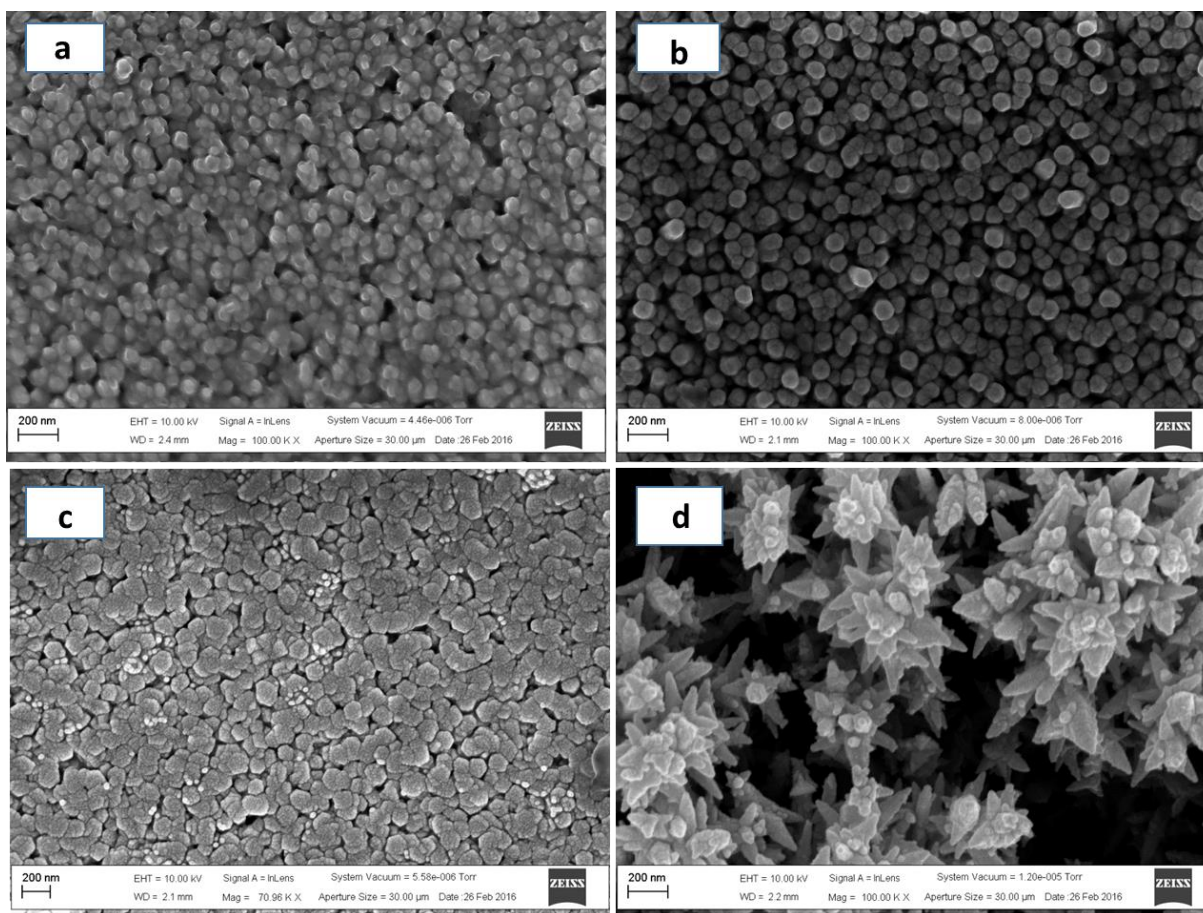


Figure 89. SEM images of CdS films deposited on glass substrate at 400 °C using complexes (a), (b), (c) and (d).

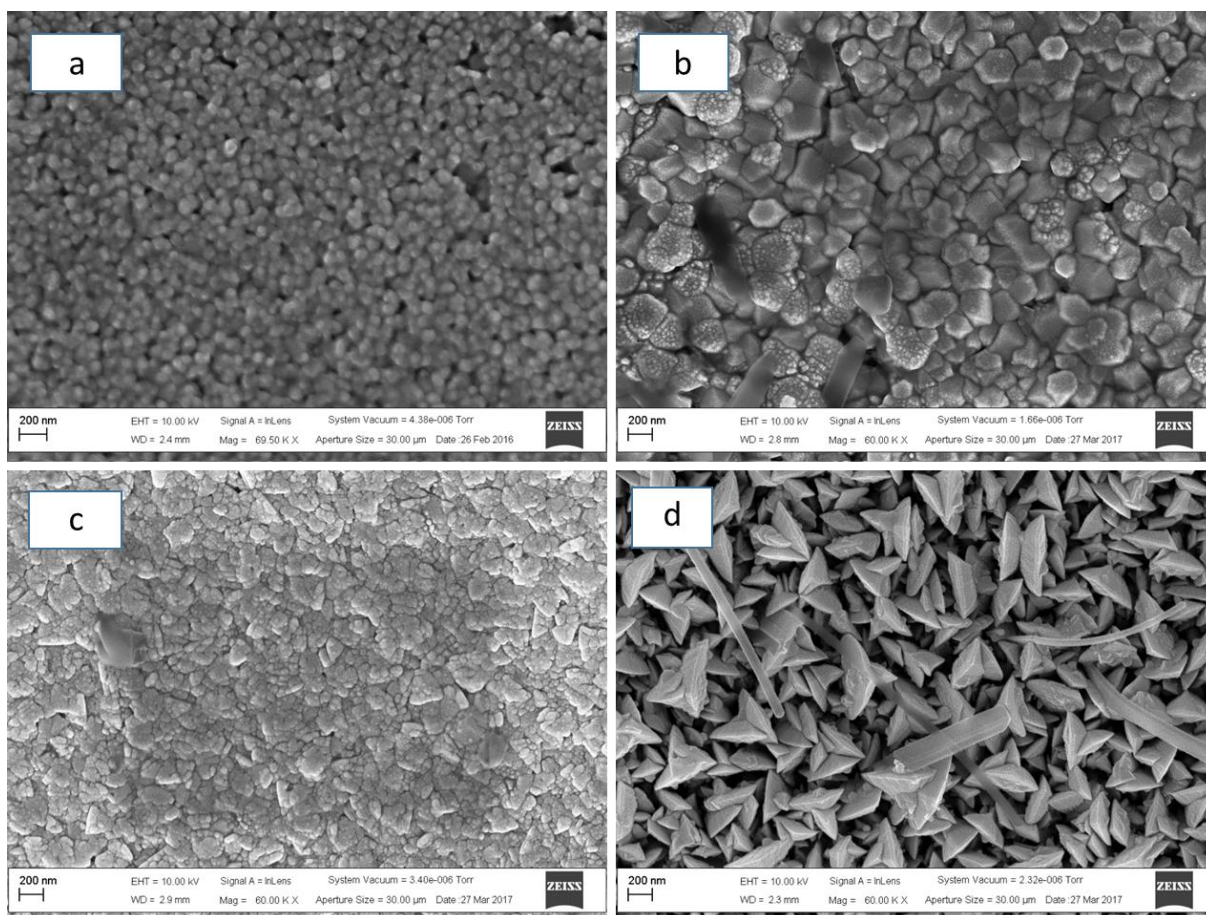


Figure 90. SEM images of CdS films deposited on glass substrate at 450 °C using complexes (a), (b), (c) and (d).

The effect of solvent on the microstructure of CdS films was also investigated using solvent mixture (THF + chloroform) and representative results obtained at 450 °C are shown in Figure 91. The CdS thin films deposited using complex (a) showed regular hexagonal-like structures with particle sizes ranging from 140-205 nm (Figure 91a). With complex (b), relatively small, regular spherical shaped with an average particle size of 57-60 nm were obtained (Figure 91b). Predominantly regular flake-like shaped in the size range of 150-205 nm were formed when complex (c) was used (Figure 91c). Also, regular rose flower shaped with average particle sizes ranging from 230-300 nm were deposited when the xanthate complex (d) was used (Figure 91d).

Variation in the morphology of the films formed at different temperatures suggests that both the solvent (THF) and temperature (400 and 450 °C) have an effect on the properties of the resulting

microstructures. However, the change in the morphology of the films deposited using mixed solvents (THF + chloroform) at 450 °C indicates that chloroform plays a role in shape directing of the film grown at the surface. It has been reported that at moderate temperature (400 °C), the heterogeneous process is dominant, rendering the precursor molecule to absorb on the substrate surface, and subsequent evaporation, vaporization and decomposition tend to produce high quality films with good adhesive strengths²⁶⁸ (Figures 89b and 89c). With the increase in temperature to 450 °C, the aerosol absorbs more heat in the delivery tube causing solvent evaporation, while vaporization of the precursor molecules starts before absorbing on the substrate surface resulting in the deposition of films with distorted structure (Figures 90b and 90c).

The role of solvent in the processing of thin film deposition can be discussed on the basis of the heat of combustion and the coordination ability of the solvent used. THF has moderate heat of combustion (2501.2 KJ.mol⁻¹) and a good coordinating ability, favoring heterogeneous nucleation mode at 400 °C. While chloroform with much lower heat of combustion (473.21 KJ.mol⁻¹) and very poor coordinating ability compared to THF, evaporates faster causing homogeneous nucleation^{268,269} (growth of porous thin films with irregular texture and poor adhesion to the substrate as seen in Figures 91a, 106c and 106d. The EDX measurements at 20 kV confirmed the stoichiometry of CdS thin films (ratio 1:1) deposited at different temperatures in all the samples. Table 28 shows the atomic percentage of CdS films using each precursor at different deposition temperatures with their average particle sizes.

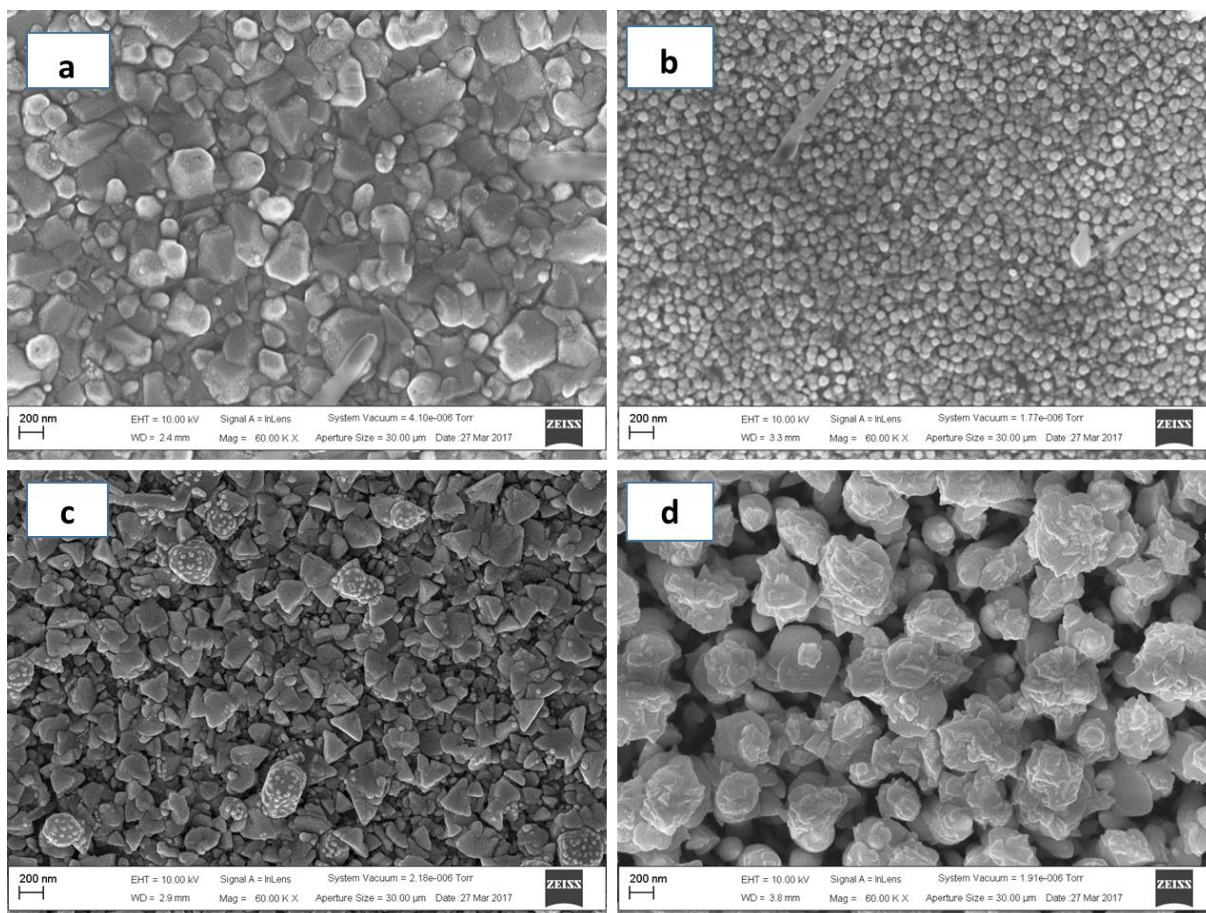


Figure 91. SEM images of CdS films deposited on glass substrate at 450 °C using mixed solvents (THF + chloroform) using complexes (a), (b), (c) and (d).

Table 28. Elemental analyses by EDX (atomic %) of CdS thin films using each precursor at different deposition temperatures with their average particle sizes.

Cd(II) complex	Temp. (°C)	Solvent	Cd %	S %	Cd/S ratio	Particle size (nm)	Shape
(a)	400	THF	50.4	49.6	1.02	60-120	Granular crystallites
(b)			50.3	49.7	1.01	20-32	Regular spherical granules
(c)			50.6	47.4	1.02	22-35	Hexagonal-like
(d)			50	50	1.00	Length = 33-63 Diameter = 12-23	star
(a)	450	THF	50.1	49.9	1.00	<i>ca.</i> 90	Spherical
(b)			50.8	49.2	1.03	190-230	Larger hexagonal granule
(c)			53.8	46.2	1.16	104-186	Irregular flake-like
(d)			50.6	49.4	1.02	200-245	Spike-like
(a)	450	THF + chloroform	50.5	49.5	1.02	140-205	Regular hexagonal-like
(b)			51.0	49.0	1.04	<i>ca.</i> 60	Regular spherical
(c)			50.5	49.5	1.02	150-205	Regular flake-like
(d)			51.6	48.4	1.07	230-300	Rose flower

In conclusion, the heterocyclic benzoylthioureas Pb(II) and Cu(II) complexes, dihexyl, diethyl, piperidine dithiocarbamates and ethyl xanthate Cd(II) complexes have shown to be efficient single source precursors for the deposition of PbS, Cu_xS_y and CdS thin films on glass substrate. The deposition temperature has an influence on the morphology, size and the monodispersivity of the deposited thin films.

GENERAL CONCLUSION AND PERSPECTIVES

Some of the main findings from this research include:

- ❖ The as-synthesized heterocyclic ligands bonded in bidentate mode using both S-donors for bonding in the case dithiocarbamate and xanthate ligands and S-donor and O-donor for bonding in the case of thiourea ligands. This information was obtained from infrared studies of the ligands.
- ❖ When the complexes were used as single source precursors to synthesize PbS, Cu_xS_y , CdS, In-doped CdS and Ga-doped CdS nanoparticles, it was found that PbS and CdS nanoparticles revealed quantum confinement in their absorption band edges.
- ❖ The variation of capping agents [hexadecylamine (HDA), oleylamine (OLA), dodecanethiol (DT) and castor oil (CO)] slightly affected the shape at lower temperatures (150 °C, 190 °C, 200 °C) but considerably at higher temperatures (>200 °C).
- ❖ A change in the capping agent from HDA to OLA resulted in an increase in the band gap energy (shift to lower wavelength) for the CdS nanoparticles.
- ❖ A variation in the reaction temperature from 150 °C to 250 °C (150 °C, 190 °C, 200 °C, 230 °C, 250 °C) had a significant effect on the shapes and sizes of the PbS, Cu_xS_y and CdS nanoparticles produced – metal sulfides with different shapes were produced. The PbS nanoparticles had shapes ranging from oval, rod-like to predominantly cubic. The Cu_xS_y nanoparticles were cubic, spherical, hexagonal nanorods and rod-like in shape. CdS nanoparticles formed spherical, cubic and rod-like shapes.
- ❖ The shapes of CdS nanoparticles changed with In and Ga doping.
- ❖ The surface morphologies and sizes of the thin films produced with the three different metals (Pb, Cu and Cd) depended on the precursor used, the deposition temperature and the solvent used.
- ❖ The optical properties of the PbS thin films produced gave band gaps which suggested a strong blue shift when compared to the bulk PbS. CdS thin films also showed an overall blue shift in their absorption bands when compared to the bulk CdS.

In perspective, we plan to

- further study the mechanism of the interaction of the precursor on the morphology evolution of the metal sulfide nanomaterials,
- investigate the use of PbS, Cu_xS_y and CdS nanoparticles and thin films for solar cells and gas sensors applications.

REFERENCES

- 1 J. Reedijk and K. Poeppelmeier, Comprehensive Inorganic Chemistry II (Second Edition): From Elements to Applications, *Theory Methods*, 2013, 1–7196.
- 2 K. P. Jayadevan and T. Y. Tseng, One-dimensional semiconductor nanostructures as absorber layers in solar cells, *J. Nanosci. Nanotechnol.*, 2005, **5**, 1768–1784.
- 3 L. Brus, Quantum crystallites and nonlinear optics, *Appl. Phys. A*, 1991, **53**, 465–474.
- 4 G. Perna, V. Capozzi, M. Ambrico, V. Augelli, T. Ligonzo, A. Minafra, L. Schiavulli and M. Pallara, Structural and optical characterization of undoped and indium-doped CdS films grown by pulsed laser deposition, *Thin Solid Films*, 2004, **453**, 187–194.
- 5 J. Barman, K. C. Sarma, M. Sarma and K. Sarma, Structural and optical studies of chemically prepared CdS nanocrystalline thin films, *IJPAP Vol465 May 2008*.
- 6 G. Giribabu, G. Murali, D. A. Reddy, C. Liu and R. P. Vijayalakshmi, Structural, optical and magnetic properties of Co doped CdS nanoparticles, *J. Alloys Compd.*, 2013, **581**, 363–368.
- 7 L. D. Nyamen, V. S. R. Pullabhotla, A. A. Nejo, P. Ndifon and N. Revaprasadu, Heterocyclic dithiocarbamates: precursors for shape controlled growth of CdS nanoparticles, *New J. Chem.*, 2011, **35**, 1133–1139.
- 8 N. L. Pickett and P. O'Brien, Syntheses of semiconductor nanoparticles using single-molecular precursors, *Chem. Rec.*, 2001, **1**, 467–479.
- 9 D. Fan, M. Afzaal, M. A. Mallik, C. Q. Nguyen, P. O'Brien and P. J. Thomas, Using coordination chemistry to develop new routes to semiconductor and other materials, *Coord. Chem. Rev.*, 2007, **251**, 1878–1888.
- 10 S. Decker and K. J. Klabunde, Enhancing effect of Fe₂O₃ on the ability of nanocrystalline calcium oxide to adsorb SO₂, *J. Am. Chem. Soc.*, 1996, **118**, 12465–12466.
- 11 R. A. Sperling, T. Pellegrino, J. K. Li, W. H. Chang and W. J. Parak, Electrophoretic Separation of Nanoparticles with a Discrete Number of Functional Groups, *Adv. Funct. Mater.*, 2006, **16**, 943–948.
- 12 H. Weller, Quantized Semiconductor Particles: A novel state of matter for materials science, *Adv. Mater.*, 1993, **5**, 88–95.
- 13 M. G. Bawendi, M. L. Steigerwald and L. E. Brus, The Quantum Mechanics of Larger Semiconductor Clusters ('Quantum Dots'), *Annu. Rev. Phys. Chem.*, 1990, **41**, 477–496.

- 14 L. Li, J. Hu, W. Yang and A. P. Alivisatos, Band Gap Variation of Size- and Shape-Controlled Colloidal CdSe Quantum Rods, *Nano Lett.*, 2001, **1**, 349–351.
- 15 P. V. Kamat, Quantum Dot Solar Cells. Semiconductor Nanocrystals as Light Harvesters, *J. Phys. Chem. C*, 2008, **112**, 18737–18753.
- 16 W. O. Winer, Molybdenum disulfide as a lubricant: A review of the fundamental knowledge, *Wear*, 1967, **10**, 422–452.
- 17 Y. Wang and N. Herron, Nanometer-sized semiconductor clusters: materials synthesis, quantum size effects, and photophysical properties, *J. Phys. Chem.*, 1991, **95**, 525–532.
- 18 A. Hagfeldt and M. Graetzel, Light-Induced Redox Reactions in Nanocrystalline Systems, *Chem. Rev.*, 1995, **95**, 49–68.
- 19 J. H. Fendler and F. C. Meldrum, The Colloid Chemical Approach to Nanostructured Materials, *Adv. Mater.*, 1995, **7**, 607–632.
- 20 M. A. Malik and P. O’Brien, in Precursor Chemistry of Advanced Materials, ed. R. A. Fischer, Springer Berlin Heidelberg, 2005, 73–204.
- 21 T. Trindade, P. O’Brien and N. L. Pickett, Nanocrystalline Semiconductors: Synthesis, Properties, and Perspectives, *Chem. Mater.*, 2001, **13**, 3843–3858.
- 22 C. B. Murray, D. J. Norris and M. G. Bawendi, Synthesis and characterization of nearly monodisperse CdE (E = sulfur, selenium, tellurium) semiconductor nanocrystallites, *J. Am. Chem. Soc.*, 1993, **115**, 8706–8715.
- 23 N. Revaprasadu, M. A. Malik, P. O’Brien and G. Wakefield, A simple route to synthesise nanodimensional CdSe–CdS core–shell structures from single molecule precursors, *Chem. Commun.*, 1999, **0**, 1573–1574.
- 24 L. Zhu, B. J. Richardson and Q. Yu, Controlled colloidal synthesis of iron pyrite FeS₂ nanorods and quasi-cubic nanocrystal agglomerates, *Nanoscale*, 2013, **6**, 1029–1037.
- 25 P. V. Vanitha and P. O’Brien, Phase Control in the Synthesis of Magnetic Iron Sulfide Nanocrystals From a Cubane-Type Fe–S Cluster, 2008, **130(5)**, 17256–17257.
- 26 S. G. Kwon and T. Hyeon, Formation Mechanisms of Uniform Nanocrystals via Hot-Injection and Heat-Up Methods, *Small*, 2011, **7**, 2685–2702.
- 27 G. B. Shombe, E. B. Mubofu, S. Mlowe and N. Revaprasadu, Synthesis and characterization of castor oil and ricinoleic acid capped CdS nanoparticles using single source precursors, *Mater. Sci. Semicond. Process.*, 2016, **43**, 230–237.

- 28 J. Akhtar, M. Banski, M. A. Malik, N. Revaprasadu, A. Podhorodecki and J. Misiewicz, Facile synthesis of phosphine free ultra-small PbSe nanocrystals and their light harvesting studies in ETA solar cells, *Dalton Trans.*, 2014, **43**, 16424–16430.
- 29 J. Akhtar, M. A. Malik, P. O'Brien, K. G. U. Wijayantha, R. Dharmadasa, S. J. O. Hardman, D. M. Graham, B. F. Spencer, S. K. Stubbs, W. R. Flavell, D. J. Binks, F. Sirotti, M. E. Kazzi and M. Silly, A greener route to photoelectrochemically active PbS nanoparticles, *J. Mater. Chem.*, 2010, **20**, 2336–2344.
- 30 G. B. Shombe, E. B. Mubofu, S. Mlowe and N. Revaprasadu, Synthesis of hierarchical PbS nanostructures capped with castor oil, *Mater. Lett.*, 2016, **185**, 17–20.
- 31 L. D. Nyamen, N. Revaprasadu and P. T. Ndifon, Low temperature synthesis of PbS and CdS nanoparticles in olive oil, *Mater. Sci. Semicond. Process.*, 2014, **27**, 191–196.
- 32 S. J. A. Moniz, C. S. Blackman, C. J. Carmalt and G. Hyett, MOCVD of crystalline Bi₂O₃ thin films using a single-source bismuth alkoxide precursor and their use in photodegradation of water, *J. Mater. Chem.*, 2010, **20**, 7881–7886.
- 33 C. S. Blackman, C. J. Carmalt, I. P. Parkin, L. Apostolico, K. C. Molloy, A. J. P. White and D. J. Williams, Single-source CVD routes to titanium phosphide, *J. Chem. Soc. Dalton Trans.*, 2002, **0**, 2702–2709.
- 34 X. Hou and K.-L. Choy, Processing and Applications of Aerosol-Assisted Chemical Vapor Deposition, *Chem. Vap. Depos.*, 2006, **12**, 583–596.
- 35 E. Lewis, S. Haigh and P. O'Brien, The synthesis of metallic and semiconducting nanoparticles from reactive melts of precursors, *J. Mater. Chem. A*, 2014, **2**, 570–580.
- 36 A. K. Bakly, B. F. Spencer and P. O'Brien, The deposition of thin films of cadmium zinc sulfide Cd_{1-x}Zn_xS at 250 °C from spin-coated xanthato complexes: a potential route to window layers for photovoltaic cells, *J. Mater. Sci.*, 2018, **53**, 4360–4370.
- 37 T. Trindade and P. O'Brien, Synthesis of CdS and CdSe nanoparticles by thermolysis of diethyldithio-or diethyldiseleno-carbamates of cadmium, *J. Mater. Chem.*, 1996, **6**, 343–347.
- 38 T. Trindade, P. O'Brien and X. Zhang, Synthesis of CdS and CdSe Nanocrystallites Using a Novel Single-Molecule Precursors Approach, *Chem. Mater.*, 1997, **9**, 523–530.
- 39 Y. Li, X. Li, C. Yang and Y. Li, Controlled synthesis of CdS nanorods and hexagonal nanocrystals, *J. Mater. Chem.*, 2003, **13**, 2641–2648.

- 40 S. S. Garje, D. J. Eisler, J. S. Ritch, M. Afzaal, P. O'Brien and T. Chivers, A New Route to Antimony Telluride Nanoplates from a Single-Source Precursor, *J. Am. Chem. Soc.*, 2006, **128**, 3120–3121.
- 41 M. Afzaal, D. Crouch, M. A. Malik, M. Motevalli, P. O'Brien, J.-H. Park and J. D. Woollins, Deposition of II-VI Thin Films by LP-MOCVD Using Novel Single-Source Precursors, *Eur. J. Inorg. Chem.*, 2004, **2004**, 171–177.
- 42 C. Q. Nguyen, A. Adeogun, M. Afzaal, M. A. Malik and P. O'Brien, Facile and reproducible syntheses of bis(dialkylselenophosphenyl)-selenides and -diselenides: X-ray structures of (iPr₂PSe)₂Se, (iPr₂PSe)₂Se₂ and (Ph₂PSe)₂Se, *Chem. Commun.*, 2006, **0**, 2179–2181.
- 43 C. Q. Nguyen, A. Adeogun, M. Afzaal, M. A. Malik and P. O'Brien, Metal complexes of selenophosphinates from reactions with (R₂PSe)₂Se: [M(R₂PSe₂)_n] (M = Zn(II), Cd(II), Pb(II), In(III), Ga(III), Cu(I), Bi(III), Ni(II); R = iPr, Ph) and [MoV₂O₂Se₂(Se₂PiPr₂)₂], *Chem. Commun.*, 2006, **0**, 2182–2184.
- 44 S. N. Mlondo, N. Revaprasadu, P. Christian and P. O'Brien, Cadmium and Lead Thiosemicarbazide Complexes: Precursors for the Synthesis of CdS Nanorods and PbS nanoparticles, *Mater. Res. Soc. Symp. Proc.*, 2005, **879E**, Z7.6.
- 45 P. S. Nair, T. Radhakrishnan, N. Revaprasadu, G. A. Kolawole and P. O'Brien, A single-source route to CdS nanorods, *Chem. Commun.*, 2002, **0**, 564–565.
- 46 P. S. Nair, T. Radhakrishnan, N. Revaprasadu, G. Kolawole and P. O'Brien, Cadmium ethylxanthate: A novel single-source precursor for the preparation of CdS nanoparticles, *J. Mater. Chem.*, 2002, **12**, 2722–2725.
- 47 N. Pradhan, B. Katz and S. Efrima, Synthesis of High-Quality Metal Sulfide Nanoparticles from Alkyl Xanthate Single Precursors in Alkylamine Solvents, *J. Phys. Chem. B*, 2003, **107**, 13843–13854.
- 48 J. Cusack, M. G. B. Drew and T. R. Spalding, Syntheses and spectroscopy of diamine complexes of Zn(II) and Cd(II) ethylxanthates and the molecular structures of [M(S₂COEt)₂TMEDA]: formation of CdS nanoparticles from [Cd(S₂COEt)₂] and [Cd(S₂COEt)₂TMEDA], *Polyhedron*, 2004, **23**, 2315–2321.
- 49 T. Trindade, P. O'Brien, X. Zhang and M. Motevalli, Synthesis of PbS nanocrystallites using a novel single moleculeprecursors approach: X-ray single-crystal structure of Pb(S₂CNEtPri)₂, *J. Mater. Chem.*, 1997, **7**, 1011–1016.

- 50 A. A. Memon, M. Afzaal, M. A. Malik, C. Q. Nguyen, P. O'Brien and J. Raftery, The N-alkyldithiocarbamate complexes $[M(S_2CNHR)_2]$ ($M = Cd(II) Zn(II)$; $R = C_2H_5, C_4H_9, C_6H_{13}, C_{12}H_{25}$); their synthesis, thermal decomposition and use to prepare of nanoparticles and nanorods of CdS, *Dalton Trans.*, 2006, **0**, 4499–4505.
- 51 P. A. Ajibade, D. C. Onwudiwe and M. J. Moloto, Synthesis of hexadecylamine capped nanoparticles using group 12 complexes of N-alkyl-N-phenyl dithiocarbamate as single-source precursors, *Polyhedron*, 2011, **30**, 246–252.
- 52 P. Sreekumari Nair, T. Radhakrishnan, N. Revaprasadu, G. A. Kolawole and P. O'Brien, $Cd(NH_2CSNHNHCSNH_2)Cl_2$: a new single-source precursor for the preparation of CdS nanoparticles, *Polyhedron*, 2003, **22**, 3129–3135.
- 53 M. J. Moloto, M. A. Malik, P. O'Brien, M. Motevalli and G. A. Kolawole, Synthesis and characterisation of some N-alkyl/aryl and N,N'-dialkyl/aryl thiourea cadmium(II) complexes: the single crystal X-ray structures of $[CdCl_2(CS(NH_2)NHCH_3)_2]_n$ and $[CdCl_2(CS(NH_2)NHCH_2CH_3)_2]$, *Polyhedron*, 2003, **22**, 595–603.
- 54 J. C. Bruce, N. Revaprasadu and K. R. Koch, Cadmium(II) complexes of N,N-diethyl-N'-benzoylthio(seleno)urea as single-source precursors for the preparation of CdS and CdSe nanoparticles, *New J. Chem.*, 2007, **31**, 1647–1653.
- 55 N. Moloto, N. Revaprasadu, M. J. Moloto, P. O'Brien and M. Helliwell, N,N'-Diisopropyl- and N,N'-dicyclohexylthiourea cadmium(II) complexes as precursors for the synthesis of CdS nanoparticles, *Polyhedron*, 2007, **26**, 3947–3955.
- 56 L. D. Nyamen, N. Revaprasadu, R. V. S. R. Pullabhotla, A. A. Nejo, P. T. Ndifon, M. A. Malik and P. O'Brien, Synthesis of multi-podal CdS nanostructures using heterocyclic dithiocarbamate complexes as precursors, *Polyhedron*, 2013, **56**, 62–70.
- 57 W. N. Kun, S. Mlowe, L. D. Nyamen, P. T. Ndifon, M. A. Malik, O. Q. Munro and N. Revaprasadu, Heterocyclic Bismuth(III) Dithiocarbamate Complexes as Single-Source Precursors for the Synthesis of Anisotropic Bi_2S_3 Nanoparticles, *Chem. Eur. J.*, 2016, **22**, 13127–13135.
- 58 S. A. Arain, C. Wilkins and H. Badaruddin, in Advanced Materials Research, *Trans Tech Publ*, 2014, **875**, 228–231.

- 59 J. Akhtar, M. A. Malik, P. O'Brien and M. Helliwell, Controlled synthesis of PbS nanoparticles and the deposition of thin films by Aerosol-Assisted Chemical Vapour Deposition (AACVD), *J. Mater. Chem.*, 2010, **20**, 6116–6124.
- 60 D. Barreca, A. Gasparotto, C. Maragno, R. Seraglia, E. Tondello, A. Venzo, V. Krishnan and H. Bertagnolli, Cadmium O-alkylxanthates as CVD precursors of CdS: a chemical characterization, *Appl. Organomet. Chem.*, 2005, **19**, 59–67.
- 61 M. Al-Shakban, P. D. Matthews, G. Deogratias, P. D. McNaughter, J. Raftery, I. Vitorica-Yrezabal, E. B. Mubofu and P. O'Brien, Novel Xanthate Complexes for the Size-Controlled Synthesis of Copper Sulfide Nanorods, *Inorg. Chem.*, 2017, **56**, 9247–9254.
- 62 M. J. Moloto, N. Revaprasadu, P. O'Brien and M. A. Malik, N-alkylthioureacadmium (II) complexes as novel precursors for the synthesis of CdS nanoparticles, *J. Mater. Sci. Mater. Electron.*, 2004, **15**, 313–316.
- 63 K. Ramasamy, M. A. Malik, P. O'Brien and J. Raftery, Metal complexes of thiobiurets and dithiobiurets: Novel single source precursors for metal sulfide thin film nanostructures, *Dalton Trans.*, 2010, **39**, 1460–1463.
- 64 M. D. Khan, J. Akhtar, M. A. Malik and N. Revaprasadu, Tuning the Phase and Shape of Copper Sulfide Nanostructures Using Mixed Solvent Systems, *ChemistrySelect*, 2016, **1**, 5982–5989.
- 65 S. C. Masikane, S. Mlowe, C. Gervas, N. Revaprasadu, A. S. Pawar and S. S. Garje, Lead(II) halide cinnamaldehyde thiosemicarbazone complexes as single source precursors for oleylamine-capped lead sulfide nanoparticles, *J. Mater. Sci. Mater. Electron.*, 2018, **29**, 1479–1488.
- 66 C. Gervas, S. Mlowe, M. P. Akerman, I. Ezekiel, T. Moyo and N. Revaprasadu, Synthesis of rare pure phase Ni₃S₄ and Ni₃S₂ nanoparticles in different primary amine coordinating solvents, *Polyhedron*, 2017, **122**, 16–24.
- 67 C. Gervas, M. D. Khan, C. Zhang, C. Zhao, R. K. Gupta, E. Carleschi, B. P. Doyle and N. Revaprasadu, Effect of cationic disorder on the energy generation and energy storage applications of Ni_xCo_{3-x}S₄ thiospinel, *RSC Adv.*, 2018, **8**, 24049–24058.
- 68 R. P. Feynman, R. B. Leighton and M. Sands, The feynman lectures on physics, *Am. J. Phys.*, 1965, **33**, 750–752.

- 69 A. Braun, E. Braun and S. MacDonald, Revolution in miniature: The history and impact of semiconductor electronics, *Cambridge University Press*, 1982.
- 70 W. Shockley, Electrons and holes in semiconductors: with applications to transistor electronics, *van Nostrand New York*, 1950.
- 71 D. A. Neamen, Semiconductor physics and devices, *McGraw-Hill New York*, 1997, **3**.
- 72 R. Narayanan and M. A. El-Sayed, Shape-Dependent Catalytic Activity of Platinum Nanoparticles in Colloidal Solution, *Nano Lett.*, 2004, **4**, 1343–1348.
- 73 Y. Li and M. A. El-Sayed, The Effect of Stabilizers on the Catalytic Activity and Stability of Pd Colloidal Nanoparticles in the Suzuki Reactions in Aqueous Solution, *J. Phys. Chem. B*, 2001, **105**, 8938–8943.
- 74 P. Sharma, S. Brown, G. Walter, S. Santra and B. Moudgil, Nanoparticles for bioimaging, *Adv. Colloid Interface Sci.*, 2006, **123–126**, 471–485.
- 75 N. Revaprasadu and S. N. Mlondo, Use of metal complexes to synthesize semiconductor nanoparticles, *Pure Appl. Chem.*, 2006, **78**, 1691–1702.
- 76 B. O. Dabbousi, J. Rodriguez-Viejo, F. V. Mikulec, J. R. Heine, H. Mattoussi, R. Ober, K. F. Jensen and M. G. Bawendi, (CdSe)ZnS Core–Shell Quantum Dots: Synthesis and Characterization of a Size Series of Highly Luminescent Nanocrystallites, *J. Phys. Chem. B*, 1997, **101**, 9463–9475.
- 77 M.-C. Daniel and D. Astruc, Gold Nanoparticles: Assembly, Supramolecular Chemistry, Quantum-Size-Related Properties, and Applications toward Biology, Catalysis, and Nanotechnology, *Chem. Rev.*, 2004, **104**, 293–346.
- 78 C. Kittel, Introduction to solid state, *John Wiley & Sons New Jersey*, 1966, **162**.
- 79 T. Vossmeier, L. Katsikas, M. Giersig, I. G. Popovic, K. Diesner, A. Chemseddine, A. Eychmueller and H. Weller, CdS Nanoclusters: Synthesis, Characterization, Size Dependent Oscillator Strength, Temperature Shift of the Excitonic Transition Energy, and Reversible Absorbance Shift, *J. Phys. Chem.*, 1994, **98**, 7665–7673.
- 80 A. P. Alivisatos, Semiconductor Clusters, Nanocrystals, and Quantum Dots, *Science*, 1996, **271**, 933–937.
- 81 J. J. Ramsden and M. Grätzel, Photoluminescence of small cadmium sulphide particles, *J. Chem. Soc. Faraday Trans. 1 Phys. Chem. Condens. Phases*, 1984, **80**, 919–933.

- 82 S. Jeong, M. Achermann, J. Nanda, S. Ivanov, V. I. Klimov and J. A. Hollingsworth, Effect of the Thiol–Thiolate Equilibrium on the Photophysical Properties of Aqueous CdSe/ZnS Nanocrystal Quantum Dots, *J. Am. Chem. Soc.*, 2005, **127**, 10126–10127.
- 83 S. Sun, C. B. Murray, D. Weller, L. Folks and A. Moser, Monodisperse FePt Nanoparticles and Ferromagnetic FePt Nanocrystal Superlattices, *Science*, 2000, **287**, 1989–1992.
- 84 A.-H. Lu, E. L. Salabas and F. Schüth, Magnetic Nanoparticles: Synthesis, Protection, Functionalization, and Application, *Angew. Chem. Int. Ed.*, 2007, **46**, 1222–1244.
- 85 N. K. Devaraj, B. H. Ong and M. Matsumoto, Yield Control of Chemically-Synthesized Magnetite Nanoparticles, *Synth. React. Inorg. Met.-Org. Nano-Met. Chem.*, 2008, **38**, 208–211.
- 86 W. D. C. Jr and D. G. Rethwisch, Fundamentals of Materials Science and Engineering: An Integrated Approach, *John Wiley & Sons*, 2012.
- 87 D.-R. Jung, J. Kim, C. Nahm, H. Choi, S. Nam and B. Park, Review paper: Semiconductor nanoparticles with surface passivation and surface plasmon, *Electron. Mater. Lett.*, 2011, **7**, 185.
- 88 R. Rossetti, J. L. Ellison, J. M. Gibson and L. E. Brus, Size effects in the excited electronic states of small colloidal CdS crystallites, *J. Chem. Phys.*, 1984, **80**, 4464–4469.
- 89 A. R. Kortan, R. Hull, R. L. Opila, M. G. Bawendi, M. L. Steigerwald, P. J. Carroll and L. E. Brus, Nucleation and Growth of CdSe on ZnS Quantum Crystallite Seeds, and Vice Versa, in Inverse Micelle Media, *J. Am. Chem. Soc.*, 1990, **112**, 1327–1332.
- 90 J. Gao and B. Xu, Applications of nanomaterials inside cells, *Nano Today*, 2009, **4**, 37–51.
- 91 S. Chen and W. Liu, Oleic acid capped PbS nanoparticles: Synthesis, characterization and tribological properties, *Mater. Chem. Phys.*, 2006, **98**, 183–189.
- 92 V. K. LaMer and R. H. Dinegar, Theory, Production and Mechanism of Formation of Monodispersed Hydrosols, *J. Am. Chem. Soc.*, 1950, **72**, 4847–4854.
- 93 Y. Jun, J. Choi and J. Cheon, Shape Control of Semiconductor and Metal Oxide Nanocrystals through Nonhydrolytic Colloidal Routes, *Angew. Chem. Int. Ed.*, 2006, **45**, 3414–3439.
- 94 K. N. Thakkar, S. S. Mhatre and R. Y. Parikh, Biological synthesis of metallic nanoparticles, *Nanomedicine Nanotechnol. Biol. Med.*, 2010, **6**, 257–262.
- 95 T. Trindade and P. O. Brien, Lead(II) dithiocarbamate complexes as precursors for the LP-MOCVD of lead sulfide, *Chem. Vap. Depos.*, 1997, **3**, 75–77.

- 96 S. Mlowe, L. D. Nyamen, P. T. Ndifon, M. A. Malik, J. Raftery, P. O'Brien and N. Revaprasadu, Aerosol assisted chemical vapor deposition (AACVD) of CdS thin films from heterocyclic cadmium(II) complexes, *Inorganica Chim. Acta*, 2015, **434**, 181–187.
- 97 M. Afzaal, D. Crouch, M. A. Malik, M. Motevalli, P. O'Brien, J.-H. Park and J. D. Woollins, Deposition of II-VI Thin Films by LP-MOCVD Using Novel Single-Source Precursors, *Eur. J. Inorg. Chem.*, 2004, **2004**, 171–177.
- 98 P. O'Brien and J. Waters, Deposition of Ni and Pd Sulfide Thin Films via Aerosol-Assisted CVD, *Chem. Vap. Depos.*, 2006, **12**, 620–626.
- 99 H. Weller, Colloidal Semiconductor Q-Particles: Chemistry in the Transition Region Between Solid State and Molecules, *Angew. Chem. Int. Ed. Engl.*, 1993, **32**, 41–53.
- 100A. Henglein, Catalysis of photochemical reactions by colloidal semiconductors, *Pure Appl. Chem.*, 1984, **56**, 1215–1224.
- 101C. B. Murray, C. R. Kagan and M. G. Bawendi, Synthesis and Characterization of Monodisperse Nanocrystals and Close-Packed Nanocrystal Assemblies, *Annu. Rev. Mater. Sci.*, 2000, **30**, 545–610.
- 102M. Kuno, J. K. Lee, B. O. Dabbousi, F. V. Mikulec and M. G. Bawendi, The band edge luminescence of surface modified CdSe nanocrystallites: Probing the luminescing state, *J. Chem. Phys.*, 1997, **106**, 9869–9882.
- 103J. E. B. Katari, V. L. Colvin and A. P. Alivisatos, X-ray Photoelectron Spectroscopy of CdSe Nanocrystals with Applications to Studies of the Nanocrystal Surface, *J. Phys. Chem.*, 1994, **98**, 4109–4117.
- 104 M. A. Malik, p. O'Brien and N. Revaprasadu, Semiconductor nanoparticles: their properties, synthesis and potential for application, *South Afr. J. Sci.*, 2000, **96**, 55–60.
- 105S. D. Bunge, K. M. Krueger, T. J. Boyle, M. A. Rodriguez, T. J. Headley and V. L. Colvin, Growth and morphology of cadmium chalcogenides: the synthesis of nanorods, tetrapods, and spheres from CdO and Cd(O₂CCH₃)₂, *J. Mater. Chem.*, 2003, **13**, 1705–1709.
- 106S. C. Masikane and N. Revaprasadu, Castor oil and olive oil-capped In₂S₃ and CuInS₂ nanoparticles from xanthate complexes, *Mater. Sci. Semicond. Process.*, 2018, **76**, 73–79.
- 107B. Ludolph and M. A. Malik, Novel single molecule precursor routes for the direct synthesis of highly monodispersed quantum dots of cadmium or zinc sulfide or selenide, *Chem. Commun.*, 1998, **0**, 1849–1850.

- 108L. D. Nyamen, V. S. R. Pullabhotla, A. A. Nejo, P. Ndifon and N. Revaprasadu, Heterocyclic dithiocarbamates: precursors for shape controlled growth of CdS nanoparticles, *New J. Chem.*, 2011, **35**, 1133–1139.
- 109E. Davidovich, D. J. Aframian, J. Shapira and B. Peretz, A comparison of the sialochemistry, oral pH, and oral health status of down syndrome children to healthy children, *Int. J. Paediatr. Dent.*, 2010, **20**, 235–241.
- 110S. Sun and H. Zeng, Size-Controlled Synthesis of Magnetite Nanoparticles, *J. Am. Chem. Soc.*, 2002, **124**, 8204–8205.
- 111T. Hyeon, S. S. Lee, J. Park, Y. Chung and H. B. Na, Synthesis of Highly Crystalline and Monodisperse Maghemite Nanocrystallites without a Size-Selection Process, *J. Am. Chem. Soc.*, 2001, **123**, 12798–12801.
- 112J. Park, K. An, Y. Hwang, J.-G. Park, H.-J. Noh, J.-Y. Kim, J.-H. Park, N.-M. Hwang and T. Hyeon, Ultra-large-scale syntheses of monodisperse nanocrystals, *Nat. Mater.*, 2004, **3**, 891.
- 113D. A. H. Hanaor, G. Triani and C. C. Sorrell, Morphology and photocatalytic activity of highly oriented mixed phase titanium dioxide thin films, *Surf. Coat. Technol.*, 2011, **205**, 3658–3664.
- 114W. Knoll and R. C. Advincula, Functional Polymer Films, *John Wiley & Sons*, 2013.
- 115P. Marchand, I. A. Hassan, I. P. Parkin and C. J. Carmalt, Aerosol-assisted delivery of precursors for chemical vapour deposition: expanding the scope of CVD for materials fabrication, *Dalton Trans.*, 2013, **42**, 9406–9422.
- 116M. A. Malik, M. Afzaal and P. O'Brien, Precursor Chemistry for Main Group Elements in Semiconducting Materials, *Chem. Rev.*, 2010, **110**, 4417–4446.
- 117J. Akhtar, M. Afzaal, M. A. Vincent, N. A. Burton, J. Raftery, I. H. Hillier and P. O'Brien, Understanding the Decomposition Pathways of Mixed Sulfur/Selenium Lead Phosphinato Complexes Explaining the Formation of Lead Selenide, *J. Phys. Chem. C*, 2011, **115**, 16904–16909.
- 118P. O'Brien, M. A. Malik and N. Revaprasadu, Precursor Routes to Semiconductor Quantum Dots, *Phosphorus Sulfur Silicon Relat. Elem.*, 2005, **180**, 689–712.
- 119Y. C. Zhang, T. Qiao, X. Y. Hu, G. Y. Wang and X. Wu, Shape-controlled synthesis of PbS microcrystallites by mild solvothermal decomposition of a single-source molecular precursor, *J. Cryst. Growth*, 2005, **277**, 518–523.

- 120J. Akhtar, M. Afzaal, M. A. Vincent, N. A. Burton, I. H. Hillier and P. O'Brien, Low temperature CVD growth of PbS films on plastic substrates, *Chem. Commun.*, 2011, **47**, 1991–1993.
- 121J. M. Clark, G. Kociok-Köhn, N. J. Harnett, M. S. Hill, R. Hill, K. C. Molloy, H. Saponia, D. Stanton and A. Sudlow, Formation of PbS materials from lead xanthate precursors, *Dalton Trans.*, 2011, **40**, 6893–6900.
- 122K. Abe, T. Hanada, Y. Yoshida, N. Tanigaki, H. Takiguchi, H. Nagasawa, M. Nakamoto, T. Yamaguchi and K. Yase, Two-dimensional array of silver nanoparticles, *Thin Solid Films*, 1998, **327–329**, 524–527.
- 123T. H. Larsen, M. Sigman, A. Ghezelbash, R. C. Doty and B. A. Korgel, Solventless Synthesis of Copper Sulfide Nanorods by Thermolysis of a Single Source Thiolate-Derived Precursor, *J. Am. Chem. Soc.*, 2003, **125**, 5638–5639.
- 124J. Chen, L. Chen and L.-M. Wu, The Solventless Syntheses of Unique PbS Nanowires of X-Shaped Cross Sections and the Cooperative Effects of Ethylenediamine and a Second Salt, *Inorg. Chem.*, 2007, **46**, 8038–8043.
- 125Y.-B. Chen, L. Chen and L.-M. Wu, Structure-Controlled Solventless Thermolytic Synthesis of Uniform Silver Nanodisks, *Inorg. Chem.*, 2005, **44**, 9817–9822.
- 126N. O. Boadi, M. A. Malik, P. O'Brien and J. A. M. Awudza, Single source molecular precursor routes to lead chalcogenides, *Dalton Trans.*, 2012, **41**, 10497–10506.
- 127D. V. Talapin, S. Haubold, A. L. Rogach, A. Kornowski, M. Haase and H. Weller, A Novel Organometallic Synthesis of Highly Luminescent CdTe Nanocrystals, *J. Phys. Chem. B*, 2001, **105**, 2260–2263.
- 128X. Peng, M. C. Schlamp, A. V. Kadavanich and A. P. Alivisatos, Epitaxial Growth of Highly Luminescent CdSe/CdS Core/Shell Nanocrystals with Photostability and Electronic Accessibility, *J. Am. Chem. Soc.*, 1997, **119**, 7019–7029.
- 129I. B. Douglass and F. B. Dains, Some Derivatives of Benzoyl and Furoyl Isothiocyanates and their Use in Synthesizing Heterocyclic Compounds¹, *J. Am. Chem. Soc.*, 1934, **56**, 719–721.
- 130P. S. Nair, M. M. Chili, T. Radhakrishnan, N. Revaprasadu, P. Christian and P. O'Brien, Some effects of the nature of the ligands and temperature of decomposition on the formation of CdS nanoparticles from cadmium complexes of alkyl-substituted thioureas : NRF / Royal Society programme, *South Afr. J. Sci.*, 2005, **101**, 466–470.

- 131 A. L. Abdelhady, K. Ramasamy, M. A. Malik, P. O'Brien, S. J. Haigh and J. Raftery, New routes to copper sulfide nanostructures and thin films, *J. Mater. Chem.*, 2011, **21**, 17888–17895.
- 132 M. J. Moloto, N. Revaprasadu, G. A. Kolawole, P. O'Brien and M. A. Malik, The synthesis and characterization of Cu_xS_y , and PbS nanoparticles from alkylthiourea lead and copper complexes : NRF / Royal Society programme, *South Afr. J. Sci.*, 2005, **101**, 463–465.
- 133 A. Singhal, D. P. Dutta, A. K. Tyagi, S. M. Mobin, P. Mathur and I. Lieberwirth, Palladium(II)/allylpalladium(II) complexes with xanthate ligands: Single-source precursors for the generation of palladium sulfide nanocrystals, *J. Organomet. Chem.*, 2007, **692**, 5285–5294.
- 134 E. A. Lewis, P. D. McNaughter, Z. Yin, Y. Chen, J. R. Brent, S. A. Saah, J. Raftery, J. A. M. Awudza, M. A. Malik, P. O'Brien and S. J. Haigh, In Situ Synthesis of PbS Nanocrystals in Polymer Thin Films from Lead(II) Xanthate and Dithiocarbamate Complexes: Evidence for Size and Morphology Control, *Chem. Mater.*, 2015, **27**, 2127–2136.
- 135 P. D. McNaughter, S. A. Saah, M. Akhtar, K. Abdulwahab, M. A. Malik, J. Raftery, J. A. M. Awudza and P. O'Brien, The effect of alkyl chain length on the structure of lead(II) xanthates and their decomposition to PbS in melt reactions, *Dalton Trans.*, 2016, **45**, 16345–16353.
- 136 M. D. Khan, M. A. Malik, J. Akhtar, S. Mlowe and N. Revaprasadu, Phase pure deposition of flower-like thin films by aerosol assisted chemical vapor deposition and solvent mediated structural transformation in copper sulfide nanostructures, *Thin Solid Films*, 2017, **638**, 338–344.
- 137 A. A. Memon, M. Dilshad, N. Revaprasadu, M. A. Malik, J. Raftery and J. Akhtar, Deposition of cadmium sulfide and zinc sulfide thin films by aerosol-assisted chemical vapors from molecular precursors, *Turk. J. Chem.*, 2015, **39**, 169–178.
- 138 T. F. Tadros, Applied Surfactants: Principles and Applications, *John Wiley & Sons*, 2006.
- 139 X. Wang, H. Fu, A. Peng, T. Zhai, Y. Ma, F. Yuan and J. Yao, One-Pot Solution Synthesis of Cubic Cobalt Nanoskeletons, *Adv. Mater.*, 2009, **21**, 1636–1640.
- 140 H. Goesmann and C. Feldmann, Nanoparticulate Functional Materials, *Angew. Chem. Int. Ed.*, 2010, **49**, 1362–1395.
- 141 Y. Song, J. Hormes and C. S. S. R. Kumar, Microfluidic Synthesis of Nanomaterials, *Small*, 2008, **4**, 698–711.

- 142J.-H. Park, M. Afzaal, M. Kemmler, P. O'Brien, D. J. Otway, J. Raftery and J. Waters, The deposition of thin films of CuME₂ by CVD techniques (M = In, Ga and E = S, Se), *J. Mater. Chem.*, 2003, **13**, 1942–1949.
- 143S. Dowland, T. Lutz, A. Ward, S. P. King, A. Sudlow, M. S. Hill, K. C. Molloy and S. A. Haque, Direct Growth of Metal Sulfide Nanoparticle Networks in Solid-State Polymer Films for Hybrid Inorganic–Organic Solar Cells, *Adv. Mater.*, 2011, **23**, 2739–2744.
- 144P.-L. Ong, I. Levitsky, P.-L. Ong and I. A. Levitsky, Organic / IV, III-V Semiconductor Hybrid Solar Cells, *Energies*, 2010, **3**, 313–334.
- 145C. S. S. R. Kumar, *Nanomaterials for Biosensors*, John Wiley & Sons, 2007.
- 146R. H. Griffin, O. Mozenon, M. A. Beking, M. C. DeRosa, G. Lopinski and N. G. Tarr, Quantitative Radio-Labeled Biomolecule Detection Using a Functionalized CMOS Sensor, *IEEE Trans. Nucl. Sci.*, 2014, **61**, 1112–1117.
- 147Y.-S. Chang, S. Savitha, S. Sadhasivam, C.-K. Hsu and F.-H. Lin, Fabrication, characterization, and application of greigite nanoparticles for cancer hyperthermia, *J. Colloid Interface Sci.*, 2011, **363**, 314–319.
- 148R. S. Chaugule, S. Purushotham and R. V. Ramanujan, Magnetic Nanoparticles as Contrast Agents for Magnetic Resonance Imaging, *Proc. Natl. Acad. Sci. India Sect. Phys. Sci.*, 2012, **82**, 257–268.
- 149S. A. El-Safty, A. Shahat and M. Rabiul Awual, Efficient adsorbents of nanoporous aluminosilicate monoliths for organic dyes from aqueous solution, *J. Colloid Interface Sci.*, 2011, **359**, 9–18.
- 150I. Udom, P. D. Myers, M. K. Ram, A. F. Hepp, E. Archibong, E. K. Stefanakos and D. Y. Goswami, Optimization of photocatalytic degradation of phenol using simple photocatalytic reactor, *Am. J. Anal. Chem.*, 2014, **5**, 743.
- 151A. Fujishima, T. N. Rao and D. A. Tryk, Titanium dioxide photocatalysis, *J. Photochem. Photobiol. C Photochem. Rev.*, 2000, **1**, 1–21.
- 152R. Ghosh Chaudhuri and S. Paria, Core/shell nanoparticles: classes, properties, synthesis mechanisms, characterization, and applications, *Chem. Rev.*, 2011, **112**, 2373–2433.
- 153Bruker APEX2, SAINT and SADABS, 2012, Bruker AXS Inc., Madison, Wisconsin, USA., .
- 154G. M. Sheldrick, Crystal structure refinement with SHELXL, *Acta Crystallogr. Sect. C Struct. Chem.*, 2015, **71**, 3–8.

- 155L. J. Farrugia, WinGX and ORTEP for Windows: an update, *J. Appl. Crystallogr.*, 2012, **45**, 849–854.
- 156D. J. Gardiner, in *Practical Raman Spectroscopy*, Springer, 1989, 1–12.
- 157C. G. Pope, X-Ray Diffraction and the Bragg Equation, *J. Chem. Educ.*, 1997, **74**, 129.
- 158M. Mikami, I. Nakagawa and T. Shimanouchi, Far infra-red spectra and metal—ligand force constants of acetylacetonates of transition metals, *Spectrochim. Acta Part Mol. Spectrosc.*, 1967, **23**, 1037–1053.
- 159H. Arslan, N. Külçü and U. Flörke, Synthesis and characterization of copper (II), nickel (II) and cobalt (II) complexes with novel thiourea derivatives, *Transit. Met. Chem.*, 2003, **28**, 816–819.
- 160M. Merdivan, F. Karipcin, N. Kulcu and R. S. Aygun, Study of the Thermal Decompositions on N,N-Dialkyl-N'-Benzoylthiourea Complexes of Cu(II), Ni(II), Pd(II), Pt(II), Cd(II), Ru(III) and Fe(III), *J. Therm. Anal. Calorim.*, 1999, **58**, 551–557.
- 161L. Beyer, M. Pulst, H. R. Paul and E. Hoyer, Nickelchelate von β -Mercaptozimtaldehyden und deren Azomethinen, *Adv. Synth. Catal.*, 1975, **317**, 265–272.
- 162O. V. Dolomanov, L. J. Bourhis, R. J. Gildea, J. a. K. Howard and H. Puschmann, OLEX2: a complete structure solution, refinement and analysis program, *J. Appl. Crystallogr.*, 2009, **42**, 339–341.
- 163S. I. Sadovnikov and A. I. Gusev, Structure and properties of PbS films, *J. Alloys Compd.*, 2013, **573**, 65–75.
- 164D. Saikia and P. Phukan, Fabrication and evaluation of CdS/PbS thin film solar cell by chemical bath deposition technique, *Thin Solid Films*, 2014, **562**, 239–243.
- 165N. Bahlawane, E. Fischer Rivera, K. Kohse-Höinghaus, A. Brechling and U. Kleineberg, Characterization and tests of planar Co₃O₄ model catalysts prepared by chemical vapor deposition, *Appl. Catal. B Environ.*, 2004, **53**, 245–255.
- 166F. Caruso, M.-L. Chan and M. Rossi, A Short Pb···Pb Separation in the Polymeric Compound Bis(pyrrolidinecarbodithioato)lead(II) and a Conformational Pathway Interconversion for the “Pb_{II}S₄” Framework, *Inorg. Chem.*, 1997, **36**, 3609–3615.
- 167R. O. Diffraction, CrysAlisPro Software system, Version 1.171. 37.31, Rigaku Corporation, Oxford, UK, 2014.

- 168O. V. Dolomanov, L. J. Bourhis, R. J. Gildea, J. A. Howard and H. Puschmann, OLEX2: a complete structure solution, refinement and analysis program, *J. Appl. Crystallogr.*, 2009, **42**, 339–341.
- 169J.-P. Joly, M. Beley, K. Selmeczi and E. Wenger, A new C₂-symmetric diaza-crown ether–CuII mononuclear complex containing 1,2,3-triazole ligands, *Inorg. Chem. Commun.*, 2009, **12**, 382–384.
- 170S. Garcia-Fontan, P. Rodriguez-Seoane, J. S. Casas, J. Sordo and M. M. Jones, Spectroscopic study of cadmium(II) complexes with heterocyclic dithiocarbamate ligands, *Inorganica Chim. Acta*, 1993, **211**, 211–215.
- 171R. D. Bereman, M. R. Churchill and D. Nalewajek, Coordination chemistry of new sulfur-containing ligands. 16. Crystal and molecular structure of tris(pyrrole-*n*-carbodithioato)iron(III)-hemikis(dichloromethane), Fe(S₂CNC₄H₄)_{3.0.5}CH₂Cl₂, a low-spin dithiocarbamate complex of iron(III), *Inorg. Chem.*, 1979, **18**, 3112–3117.
- 172C. P. Sharma, N. Kumar, M. C. Khandpal, S. Chandra and V. G. Bhide, Studies on the preparation and characterization of bis-dithiocarbamate derivatives of di-*n*-butyl- and di-*n*-hexyl Sn(IV), *J. Inorg. Nucl. Chem.*, 1981, **43**, 923–930.
- 173L. D. Nyamen, V. S. R. R. Pullabhotla, A. A. Nejo, P. T. Ndifon, J. H. Warner and N. Revaprasadu, Synthesis of anisotropic PbS nanoparticles using heterocyclic dithiocarbamate complexes, *Dalton Trans.*, 2012, **41**, 8297–8302.
- 174H. Karami, M. Ghasemi and S. Matini, Synthesis, characterization and application of lead sulfide nanostructures as ammonia gas sensing agent, *Int J Electrochem Sci*, 2013, **8**, 11661–11679.
- 175S. Günes, K. P. Fritz, H. Neugebauer, N. S. Sariciftci, S. Kumar and G. D. Scholes, Hybrid solar cells using PbS nanoparticles, *Sol. Energy Mater. Sol. Cells*, 2007, **91**, 420–423.
- 176F. C. J. M. van Veggel, Near-Infrared Quantum Dots and Their Delicate Synthesis, Challenging Characterization, and Exciting Potential Applications, *Chem. Mater.*, 2014, **26**, 111–122.
- 177J. D. Patel, F. Mighri, A. Ajji and S. Elkoun, Room temperature synthesis of aminocaproic acid-capped lead sulphide nanoparticles, *Mater. Sci. Appl.*, 2012, **3**, 125.

- 178M. Asad, M. Fathipour, M. H. Sheikhi and M. Pourfath, High-performance infrared photo-transistor based on SWCNT decorated with PbS nanoparticles, *Sens. Actuators Phys.*, 2014, **220**, 213–220.
- 179L. Sun, J. J. Choi, D. Stachnik, A. C. Bartnik, B.-R. Hyun, G. G. Malliaras, T. Hanrath and F. W. Wise, Bright infrared quantum-dot light-emitting diodes through inter-dot spacing control, *Nat. Nanotechnol.*, 2012, **7**, 369–373.
- 180I. Jen-La Plante, T. W. Zeid, P. Yang and T. Mokari, Synthesis of metal sulfide nanomaterials via thermal decomposition of single-source precursors, *J. Mater. Chem.*, 2010, **20**, 6612–6617.
- 181A. O. Nejo, A. A. Nejo, R. V. S. R. Pullabhotla and N. Revaprasadu, Facile synthesis of organically capped PbS nanoparticles, *J. Alloys Compd.*, 2012, **537**, 19–23.
- 182P. O'Brien and R. Nomura, Single-molecule precursor chemistry for the deposition of chalcogenide (S or Se)-containing compound semiconductors by MOCVD and related methods, *J. Mater. Chem.*, 1995, **5**, 1761–1773.
- 183J. Joo, H. B. Na, T. Yu, J. H. Yu, Y. W. Kim, F. Wu, J. Z. Zhang and T. Hyeon, Generalized and Facile Synthesis of Semiconducting Metal Sulfide Nanocrystals, *J. Am. Chem. Soc.*, 2003, **125**, 11100–11105.
- 184A. Saeed, U. Flörke and M. F. Erben, A review on the chemistry, coordination, structure and biological properties of 1-(acyl/aroyl)-3-(substituted) thioureas, *J. Sulfur Chem.*, 2014, **35**, 318–355.
- 185H. Arslan, N. Duran, G. Borekci, C. Koray Ozer, C. Akbay, H. Arslan, N. Duran, G. Borekci, C. Koray Ozer and C. Akbay, Antimicrobial Activity of Some Thiourea Derivatives and Their Nickel and Copper Complexes, *Molecules*, 2009, **14**, 519–527.
- 186M. Merdivan, R. S. Aygün and N. Külcü, Thermal behaviour of some metal complexes of N,N-diethyl-N'-benzoyl thiourea, *J. Therm. Anal. Calorim.*, 1997, **48**, 1423–1429.
- 187S. Axnanda, M. Scheele, E. Crumlin, B. Mao, R. Chang, S. Rani, M. Faiz, S. Wang, A. P. Alivisatos and Z. Liu, Direct Work Function Measurement by Gas Phase Photoelectron Spectroscopy and Its Application on PbS Nanoparticles, *Nano Lett.*, 2013, **13**, 6176–6182.
- 188M. R. Karim, M. D. Aktaruzzaman, M. Ashrafuzzaman and M. D. B. Zaman, A conventional synthesis approach to prepare lead sulfide (PbS) nanoparticles via solvothermal method, *Chalcogenide Lett.*, 2014, **11**, 531–539.

- 189 Y. Ji, D. R. Yang, H. Zhang, X. Y. Ma, J. Xu and D. L. Que, Morphology Control of PbS Nanocrystals by a Novel Hydrothermal Process, <https://www.scientific.net/SSP.99-100.197>, (accessed 14 November 2018).
- 190 N. Wang, X. Cao, L. Guo, S. Yang and Z. Wu, Facile Synthesis of PbS Truncated Octahedron Crystals with High Symmetry and Their Large-Scale Assembly into Regular Patterns by a Simple Solution Route, *ACS Nano*, 2008, **2**, 184–190.
- 191 Y. Cao, P. Hu and D. Jia, Solvothermal synthesis, growth mechanism, and photoluminescence property of sub-micrometer PbS anisotropic structures, *Nanoscale Res. Lett.*, 2012, **7**, 668.
- 192 Y. Yin and A. P. Alivisatos, Colloidal nanocrystal synthesis and the organic–inorganic interface, *Nature*, 2004, **437**, 664–670.
- 193 M. Green, The nature of quantum dot capping ligands, *J. Mater. Chem.*, 2010, **20**, 5797–5809.
- 194 J. H. Warner and H. Cao, Shape control of PbS nanocrystals using multiple surfactants, *Nanotechnology*, 2008, **19**, 305605.
- 195 W. W. Scanlon, Recent advances in the optical and electronic properties of PbS, PbSe, PbTe and their alloys, *J. Phys. Chem. Solids*, 1959, **8**, 423–428.
- 196 H. Li, D. Chen, L. Li, F. Tang, L. Zhang and J. Ren, Size- and shape-controlled synthesis of PbSe and PbS nanocrystals via a facile method, *Cryst. Eng. Comm.*, 2010, **12**, 1127–1133.
- 197 P. S. Nair and G. D. Scholes, Thermal decomposition of single source precursors and the shape evolution of CdS and CdSe nanocrystals, *J. Mater. Chem.*, 2006, **16**, 467–473.
- 198 B. Srinivas, B. G. Kumar and K. Muralidharan, Stabilizer free copper sulphide nanostructures for rapid photocatalytic decomposition of rhodamine B, *J. Mol. Catal. Chem.*, 2015, **410**, 8–18.
- 199 H. Lei, P. Qin, W. Ke, Y. Guo, X. Dai, Z. Chen, H. Wang, B. Li, Q. Zheng and G. Fang, Performance enhancement of polymer solar cells with high work function CuS modified ITO as anodes, *Org. Electron.*, 2015, **22**, 173–179.
- 200 M. Zhou, N. Peng, Z. Liu, Y. Xi, H. He, Y. Xia, Z. Liu and S. Okada, Synthesis of sub-10 nm copper sulphide rods as high-performance anode for long-cycle life Li-ion batteries, *J. Power Sources*, 2016, **306**, 408–412.
- 201 B. J. Mulder, Optical properties of crystals of cuprous sulphides (chalcocite, djurleite, $\text{Cu}_{1.9}\text{S}$, and digenite), *Phys. Status Solidi A*, 1972, **13**, 79–88.

- 202 Y. Wu, C. Wadia, W. Ma, B. Sadtler and A. P. Alivisatos, Synthesis and photovoltaic application of copper(I) sulfide nanocrystals, *Nano Lett.*, 2008, **8**, 2551–2555.
- 203 Q. Tian, F. Jiang, R. Zou, Q. Liu, Z. Chen, M. Zhu, S. Yang, J. Wang, J. Wang and J. Hu, Hydrophilic Cu₉S₅ nanocrystals: a photothermal agent with a 25.7% heat conversion efficiency for photothermal ablation of cancer cells in vivo, *ACS Nano*, 2011, **5**, 9761–9771.
- 204 G. Song, L. Han, W. Zou, Z. Xiao, X. Huang, Z. Qin, R. Zou and J. Hu, A Novel Photothermal Nanocrystals of Cu₇S₄ Hollow Structure for Efficient Ablation of Cancer Cells, *Nano-Micro Lett.*, 2014, **6**, 169–177.
- 205 S. Li, H. Wang, W. Xu, H. Si, X. Tao, S. Lou, Z. Du and L. S. Li, Synthesis and assembly of monodisperse spherical Cu₂S nanocrystals, *J. Colloid Interface Sci.*, 2009, **330**, 483–487.
- 206 A. Tang, S. Qu, K. Li, Y. Hou, F. Teng, J. Cao, Y. Wang and Z. Wang, One-pot synthesis and self-assembly of colloidal copper (I) sulfide nanocrystals, *Nanotechnology*, 2010, **21**, 285602.
- 207 L. Chen, Y.-B. Chen and L.-M. Wu, Synthesis of Uniform Cu₂S Nanowires from Copper-Thiolate Polymer Precursors by a Solventless Thermolytic Method, *J. Am. Chem. Soc.*, 2004, **126**, 16334–16335.
- 208 M. Al-Shakban, P. D. Matthews, G. Deogratias, P. D. McNaughten, J. Raftery, I. Vitorica-Yrezabal, E. B. Mubofu and P. O'Brien, Novel xanthate complexes for the size-controlled synthesis of copper sulfide nanorods, *Inorg. Chem.*, 2017, **56**, 9247–9254.
- 209 H.-T. Zhang, G. Wu and X.-H. Chen, Large-scale synthesis and self-assembly of monodisperse hexagon Cu₂S nanoplates, *Langmuir*, 2005, **21**, 4281–4282.
- 210 H. T. Zhang, G. Wu and X. H. Chen, Controlled synthesis and characterization of covellite (CuS) nanoflakes, *Mater. Chem. Phys.*, 2006, **98**, 298–303.
- 211 A. Ghezelbash and B. A. Korgel, Nickel sulfide and copper sulfide nanocrystal synthesis and polymorphism, *Langmuir*, 2005, **21**, 9451–9456.
- 212 H. Zhang, Y. Zhang, J. Yu and D. Yang, Phase-selective synthesis and self-assembly of monodisperse copper sulfide nanocrystals, *J. Phys. Chem. C*, 2008, **112**, 13390–13394.
- 213 N. Mntungwa, M. D. Khan, S. Mlowe and N. Revaprasadu, A simple route to alkylamine capped antimony nanoparticles, *Mater. Lett.*, 2015, **145**, 239–242.
- 214 M. D. Khan, J. Akhtar, M. A. Malik, M. Akhtar and N. Revaprasadu, Phase-pure fabrication and shape evolution studies of SnS nanosheets, *New J. Chem.*, 2015, **39**, 9569–9574.

- 215 M. D. Khan, M. A. Malik, J. Akhtar, S. Mlowe and N. Revaprasadu, Phase pure deposition of flower-like thin films by aerosol assisted chemical vapor deposition and solvent mediated structural transformation in copper sulfide nanostructures, *Thin Solid Films*, 2017, **638**, 338–344.
- 216 F. Cao, H. Wang, Z. Xia, X. Dai, S. Cong, C. Dong, B. Sun, Y. Lou, Y. Sun, J. Zhao and G. Zou, An alternative route towards monodisperse CdS quantum dots for hybrid solar cells, *Mater. Chem. Phys.*, 2015, **149–150**, 124–128.
- 217 E. V. Kolobkova, D. S. Kukushkin, N. V. Nikonorov, A. I. Sidorov and T. A. Shakhverdov, Luminescent properties of molecular clusters (CdS)_n fluorophosphate glass, *Glass Phys. Chem.*, 2015, **41**, 104–107.
- 218 L. Maserati, I. Moreels, M. Prato, R. Krahne, L. Manna and Y. Zhang, Oxygen Sensitivity of Atomically Passivated CdS Nanocrystal Films, *ACS Appl. Mater. Interfaces*, 2014, **6**, 9517–9523.
- 219 J. Xiong, W. Wu, Y. Liu, L. Shen and L. Wu, Fabrication of hierarchical CdS nanosphere via one-pot process for photocatalytic water splitting, *J. Nanoparticle Res.*, 2015, **17**, 55.
- 220 Z. A. Peng and X. Peng, Nearly Monodisperse and Shape-Controlled CdSe Nanocrystals via Alternative Routes: Nucleation and Growth, *J. Am. Chem. Soc.*, 2002, **124**, 3343–3353.
- 221 S. Mlowe, D. J. Lewis, M. A. Malik, J. Raftery, E. B. Mubofu, P. O'Brien and N. Revaprasadu, Bis(piperidinedithiocarbamate)pyridinecadmium(II) as a single-source precursor for the synthesis of CdS nanoparticles and aerosol-assisted chemical vapour deposition (AACVD) of CdS thin films, *New J. Chem.*, 2014, **38**, 6073–6080.
- 222 L. Stroea, A. K. Bansal, I. D. W. Samuel, S. Kowalski, S. Allard, U. Scherf, L. Ortolani, S. Cavallini, S. Toffanin and F. Antolini, Growth of Photoluminescent Cadmium Sulphide Quantum Dots from Soluble Single Source Precursors in Solution and in Film, *Sci., Adv., Mater.*, 2015, **7(1)**, 1-14.
- 223 J. D. Patel, F. Mighri, A. Ajji and T. K. Chaudhuri, Development of CdS Nanostructures by Thermal Decomposition of Aminocaproic Acid-Mixed Cd-Thiourea Complex Precursor, *J. Nanosci. Nanotechnology*, 2015, **15(4)**, 2733-2741.
- 224 M. Green, The nature of quantum dot capping ligands, *J. Mater. Chem.*, 2010, **20**, 5797–5809.
- 225 Y. Yin and A. P. Alivisatos, Colloidal nanocrystal synthesis and the organic–inorganic interface, *Nature*, 2004, **437**, 664–670.

- 226X. Peng, L. Manna, W. Yang, J. Wickham, E. Scher, A. Kadavanich and A. P. Alivisatos, Shape control of CdSe nanocrystals, *Nature*, 2000, **404**, 59.
- 227H. P. Klug and L. E. Alexander, X-ray diffraction procedures: for polycrystalline and amorphous materials, *X-Ray Diffr. Proced. Polycryst. Amorph. Mater. 2nd Ed. Harold P Klug Leroy E Alexander*, 1974, 992.
- 228P. Yan, Y. Xie, Y. Qian and X. Liu, A cluster growth route to quantum-confined CdS nanowires, *Chem. Commun.*, 1999, 1293–1294.
- 229N. Moloto, N. Revaprasadu, P. L. Musetha and M. J. Moloto, The effect of precursor concentration, temperature and capping group on the morphology of CdS nanoparticles, *J. Nanosci. Nanotechnol.*, 2009, **9**, 4760–4766.
- 230W. W. Yu, Y. A. Wang and X. Peng, Formation and stability of size-, shape-, and structure-controlled CdTe nanocrystals: ligand effects on monomers and nanocrystals, *Chem. Mater.*, 2003, **15**, 4300–4308.
- 231L. Spanhel, M. Haase, H. Weller and A. Henglein, Photochemistry of colloidal semiconductors. 20. Surface modification and stability of strong luminescing CdS particles, *J. Am. Chem. Soc.*, 1987, **109**, 5649–5655.
- 232M. O’neil, J. Marohn and G. McLendon, Dynamics of electron-hole pair recombination in semiconductor clusters, *J. Phys. Chem.*, 1990, **94**, 4356–4363.
- 233A. Mukherjee, P. Ghosh, A. A. Aboud and P. Mitra, Influence of copper incorporation in CdS: Structural and morphological studies, *Mater. Chem. Phys.*, 2016, **184**, 101–109.
- 234A. Tang, L. Yi, W. Han, F. Teng, Y. Wang, Y. Hou and M. Gao, Synthesis, optical properties, and superlattice structure of Cu (I)-doped CdS nanocrystals, *Appl. Phys. Lett.*, 2010, **97**, 033112.
- 235H. Khallaf, G. Chai, O. Lupan, L. Chow, S. Park and A. Schulte, Characterization of gallium-doped CdS thin films grown by chemical bath deposition, *Appl. Surf. Sci.*, 2009, **255**, 4129–4134.
- 236S. Yılmaz, S. B. Törelı, İ. Polat, M. A. Olgar, M. Tomakin and E. Bacaksız, Enhancement in the optical and electrical properties of CdS thin films through Ga and K co-doping, *Mater. Sci. Semicond. Process.*, 2017, **60**, 45–52.
- 237Y.-N. Xu and W. Y. Ching, Electronic, optical, and structural properties of some wurtzite crystals, *Phys. Rev. B*, 1993, **48**, 4335.

- 238 K. Ravichandran and V. Senthamilselvi, Effect of indium doping level on certain physical properties of CdS films deposited using an improved SILAR technique, *Appl. Surf. Sci.*, 2013, **270**, 439–444.
- 239 A. Pan, R. Liu, Q. Yang, Y. Zhu, G. Yang, B. Zou and K. Chen, Stimulated Emissions in Aligned CdS Nanowires at Room Temperature, *J. Phys. Chem. B*, 2005, **109**, 24268–24272.
- 240 V. Singh, P. K. Sharma and P. Chauhan, Surfactant mediated phase transformation of CdS nanoparticles, *Mater. Chem. Phys.*, 2010, **121**, 202–207.
- 241 J. E. Spanier, R. D. Robinson, F. Zhang, S.-W. Chan and I. P. Herman, Size-dependent properties of CeO_{2-y} nanoparticles as studied by Raman scattering, *Phys. Rev. B*, 2001, **64**, 245407.
- 242 G. Perna, V. Capozzi, M. Ambrico, V. Augelli, T. Ligonzo, A. Minafra, L. Schiavulli and M. Pallara, Structural and optical characterization of undoped and indium-doped CdS films grown by pulsed laser deposition, *Thin Solid Films*, 2004, **453**, 187–194.
- 243 S. Yılmaz, İ. Polat, M. A. Olgar, M. Tomakin, S. B. Törelı and E. Bacaksız, Physical properties of CdS:Ga thin films synthesized by spray pyrolysis technique, *J. Mater. Sci. Mater. Electron.*, 2017, **28**, 3191–3199.
- 244 B. Srinivas, B. G. Kumar and K. Muralidharan, Stabilizer free copper sulphide nanostructures for rapid photocatalytic decomposition of rhodamine B, *J. Mol. Catal. Chem.*, 2015, **410**, 8–18.
- 245 T. Fu, Research on gas-sensing properties of lead sulfide-based sensor for detection of NO₂ and NH₃ at room temperature, *Sens. Actuators B Chem.*, 2009, **140**, 116–121.
- 246 W. Wu, Y. He, Y. Wu and T. Wu, Self-template synthesis of PbS nanodendrites and its photocatalytic performance, *J. Alloys Compd.*, 2011, **509**, 9356–9362.
- 247 M. Nyman, K. Jenkins, M. J. Hampden-Smith, T. T. Kodas, E. N. Duesler, A. L. Rheingold and M. L. Liable-Sands, Feed-Rate-Limited Aerosol-Assisted Chemical Vapor Deposition of Cd_xZn_{1-x}S and ZnS: Mn with Composition Control, *Chem. Mater.*, 1998, **10**, 914–921.
- 248 H. H. Afifi, S. A. Mahmoud and A. Ashour, Structural study of ZnS thin films prepared by spray pyrolysis, *Thin Solid Films*, 1995, **263**, 248–251.
- 249 S. M. Salim and O. Hamid, Growth and characterization of lead sulfide films deposited on glass substrates, *Renew. Energy*, 2001, **24**, 575–580.

- 250 T. Kannianen, S. Lindroos, J. Ihanus and M. Leskelä, Growth of lead selenide thin films by the successive ionic layer adsorption and reaction (SILAR) technique, *J. Mater. Chem.*, 1996, **6**, 983–986.
- 251 D. M. Frigo, O. F. Khan and P. O'Brien, Growth of epitaxial and highly oriented thin films of cadmium and cadmium zinc sulfide by low-pressure metalorganic chemical vapour deposition using diethyldithiocarbamates, *J. Cryst. Growth*, 1989, **96**, 989–992.
- 252 D. Barreca, A. Gasparotto, C. Maragno, E. Tondello and C. Sada, CVD of Nanophasic (Zn, Cd)S Thin Films: From Multi-Layers to Solid Solutions, *Chem. Vap. Depos.*, 2004, **10**, 229–236.
- 253 S.-M. Lee, Y. Jun, S.-N. Cho and J. Cheon, Single-crystalline star-shaped nanocrystals and their evolution: programming the geometry of nano-building blocks, *J. Am. Chem. Soc.*, 2002, **124**, 11244–11245.
- 254 T. Mandal, G. Piburn, V. Stavila, I. Rusakova, T. Ould-Ely, A. C. Colson and K. H. Whitmire, New mixed ligand single-source precursors for PbS nanoparticles and their solvothermal decomposition to anisotropic nano- and microstructures, *Chem. Mater.*, 2011, **23**, 4158–4169.
- 255 T. Duan, W. Lou, X. Wang and Q. Xue, Size-controlled synthesis of orderly organized cube-shaped lead sulfide nanocrystals via a solvothermal single-source precursor method, *Colloids Surf. Physicochem. Eng. Asp.*, 2007, **310**, 86–93.
- 256 L. S. Ramsdell, The crystal structure of some metallic sulfides, *Am. Mineral. J. Earth Planet. Mater.*, 1925, **10**, 281–304.
- 257 R. W. G. Wyckoff, Fluorite structure, *Cryst. Struct.*, 1963, **1**, 239–444.
- 258 Y. Noda, K. Masumoto, S. Ohba, Y. Saito, K. Toriumi, Y. Iwata and I. Shibuya, Temperature dependence of atomic thermal parameters of lead chalcogenides, PbS, PbSe and PbTe, *Acta Crystallogr. Sect. C*, 1987, **43**, 1443–1445.
- 259 A. E. Rakhshani, Study of Urbach tail, bandgap energy and grain-boundary characteristics in CdS by modulated photocurrent spectroscopy, *J. Phys. Condens. Matter*, 2000, **12**, 4391.
- 260 C. Rajashree, A. R. Balu and V. S. Nagarethinam, Substrate temperature effect on the Physical properties of Spray deposited Lead sulfide thin films suitable for solar control coatings, *Int. J. Chem. Tech. Res.*, 2014, **6**, 347–360.

- 261 M. M. Abbas, A. A.-M. Shehab, N. A. Hassan and A. K. Al-Samuraee, Effect of temperature and deposition time on the optical properties of chemically deposited nanostructure PbS thin films, *Thin Solid Films*, 2011, **519**, 4917–4922.
- 262 J. N. Zemel, J. D. Jensen and R. B. Schoolar, Electrical and optical properties of epitaxial films of PbS, PbSe, PbTe, and SnTe, *Phys. Rev.*, 1965, **140**, A330.
- 263 B. Thangaraju and P. Kaliannan, Spray pyrolytically deposited PbS thin films, *Semicond. Sci. Technol.*, 2000, **15**, 849.
- 264 I. Kang and F. W. Wise, Electronic structure and optical properties of PbS and PbSe quantum dots, *JOSA B*, 1997, **14**, 1632–1646.
- 265 M. D. Khan, M. A. Malik, J. Akhtar, S. Mlowe and N. Revaprasadu, Phase pure deposition of flower-like thin films by aerosol assisted chemical vapor deposition and solvent mediated structural transformation in copper sulfide nanostructures, *Thin Solid Films*, 2017, **638**, 338–344.
- 266 J. Dilag, H. Kobus and A. V. Ellis, Cadmium sulfide quantum dot/chitosan nanocomposites for latent fingerprint detection, *Forensic. Sci. Int.*, 2009, **187**, 97–102.
- 267 J. X. Yang, Z. G. Jin, Y. T. Chai, H. Y. Du, T. J. Liu and T. Wang, Growth and characterization of CuInSe₂ thin films prepared by successive ionic layer adsorption and reaction method with different deposition temperatures, *Thin Solid Films*, 2009, **517**, 6617–6622.
- 268 M. A. Ehsan, H. N. Ming, M. Misran, Z. Arifin, E. R. Tiekink, A. P. Safwan, M. Ebadi, W. J. Basirun and M. Mazhar, Effect of AACVD Processing Parameters on the Growth of Greenockite (CdS) Thin Films using a Single-Source Cadmium Precursor, *Chem. Vap. Depos.*, 2012, **18**, 191–200.
- 269 R. Díaz-Torres and S. Alvarez, Coordinating ability of anions and solvents towards transition metals and lanthanides, *Dalton Trans.*, 2011, **40**, 10742–10750.

ANNEX 1. Publications

- 1) **Kevin I. Y. Ketchemen**, Sixberth Mlowe, Linda D. Nyamen, Ahmed A. Aboud, Matthew P. Akerman, Peter T. Ndifon, Paul O'Brien, Neerish Revaprasadu, Heterocyclic lead(II) thioureato complexes as single-source precursors for the aerosol assisted chemical vapour deposition of PbS thin films, *Inorg. Chim. Acta*, 2018, **479**, 42-48.
- 2) **Kevin I. Y. Ketchemen**, Sixberth Mlowe, Linda D. Nyamen, Peter T. Ndifon, Neerish Revaprasadu, Paul O'Brien, CdS thin films deposition by AACVD: effect of precursor type, decomposition temperature and solvent, *J. Mater Sci: Mater. Electron.* 2018, **29**, 14462-14470.
- 3) **Kevin I. Y. Ketchemen**, Malik D. Khan, Sixberth Mlowe, Linda D. Nyamen, Peter T. Ndifon, Paul O'Brien, Neerish Revaprasadu, Tailoring shape and crystallographic phase of copper sulfide nanostructures using novel thiourea complexes as single source precursors, *J. Inorg. Organomet. Polym.* 2019, 1-11.
- 4) **Kevin I. Y. Ketchemen**, Sixberth Mlowe, Paul D. McNaughter, Matthew P. Akerman, Inigo Vitorica-Yrezabal, George Whitehead, Linda D. Nyamen, Peter T. Ndifon, Neerish Revaprasadu and Paul O'Brien, Synthesis, characterization and crystal structures of Fe(III), Co(II), Ni(II), Cu(II), Zn(II) and In(III) N-morpholine-N'-benzoylthiourea complexes (**Manuscript being finalised for publication**).
- 5) **Kevin I. Y. Ketchemen**, Siphamandla C. Masikane, Suliman Alderhami, Paul D. McNaughter, Ghulam Murtaza, Linda D. Nyamen, Paul O'Brien, Peter T. Ndifon and Neerish Revaprasadu, Indium and gallium-doped CdS nanoparticles from melts of ethyl xanthate complexes (**Manuscript being finalised for publication**).
- 6) **Kevin I. Y. Ketchemen**, Sixberth Mlowe, Linda D. Nyamen, Peter T. Ndifon, Neerish Revaprasadu, Comparative study on effect of precursors on the morphology and electronic properties of CdS nanoparticles (**Manuscript in preparation**).

- 7) Maurice Kuate, Mariam Conde Asseng, Awawou G. Paboudam, Evans Mainsah Ngandung, Francis Merlin Tchieno, **Kevin I. Y. Ketchemen**, Tonle Kenfack Ignas, Peter T. Ndifon, Synthesis, cyclic voltammetry and biological studies of Co(II), Ni(II) and Cu(II) complexes of a tridentate Schiff bases derived from 2-aminothiophenol and 2-Hydroxynaphtaldehyde (**Manuscript being finalised for publication**).



Heterocyclic lead(II) thioureato complexes as single-source precursors for the aerosol assisted chemical vapour deposition of PbS thin films

Kevin I.Y. Ketchemen^{a,b}, Sixberth Mlowe^a, Linda D. Nyamen^b, Ahmed A. About^{a,c}, Matthew P. Akerman^d, Peter T. Ndifon^{b,*}, Paul O'Brien^{e,*}, Neerish Revaprasadu^{a,*}

^a Department of Chemistry, University of Zululand, Private Bag X1001, KwaDangezwa 3880, South Africa

^b Department of Inorganic Chemistry, University of Yaoundé I, P.O. Box 812, Yaoundé, Cameroon

^c Department of Physics, Faculty of Science, Beni-Suef University, Beni-Suef 62514, Egypt

^d School of Chemistry and Physics, University of KwaZulu-Natal, Private Bag X01, Scottsville, Pietermaritzburg 3209, South Africa

^e The School of Chemistry and The School of Materials, The University of Manchester Oxford Road, Manchester M13 9PL, UK

ARTICLE INFO

Article history:

Received 23 January 2018

Received in revised form 3 April 2018

Accepted 14 April 2018

Available online 21 April 2018

Keywords:

Single source precursors

Lead sulfide

AACVD

Thin films

Optical properties

ABSTRACT

The lead *N*-benzoylthioureato complexes of *N*-morpholine (**1**) and *N*-pyrrolidine (**2**) were synthesized and characterized by elemental analysis, Fourier Transform Infra-Red (FT-IR) spectroscopy, proton nuclear magnetic resonance (¹H nmr) and thermogravimetric analyses (TGA). The X-ray single crystal structure of complex (**1**) was determined. The compounds were both used as single source precursors to deposit PbS films on glass substrates at 350, 400 and 450 °C using aerosol assisted chemical vapour deposition (AACVD). The surface morphology of PbS films were determined by scanning electron microscopy (SEM), the crystalline phases established by powder X-ray diffraction (p-XRD) analyses and composition by energy dispersive X-ray spectroscopy (EDX). The particle sizes were found to range between 82 and 85 nm from complex (**1**) and 70–105 nm for (**2**). The PbS films were studied by Near Infra-red (NIR) UV-Vis spectroscopy, band gap ranging from 1.46 to 1.55 eV were observed.

© 2018 Elsevier B.V. All rights reserved.

1. Introduction

There is considerable interest in thin films of semiconductors for their novel and potentially useful optoelectronic properties [1–4]. Amongst such semiconductors, PbS has been extensively studied because of its cheapness and potential usefulness in solar cells [5–7]. Lead sulfide (PbS) is a IV–VI semiconductor with a large Bohr exciton radius of 18 nm and a small band gap of 0.41 eV (3100 nm) which is tunable with particle size [8–10]. Furthermore, PbS has been found useful in several other applications such as thermoelectric, sensors and photocatalysts [11–15]. The methods used to prepare or deposit this material can profoundly affect phase composition, thermal stability, crystallite size and morphology, which in turn can influence the functional behavior of the material. Many methods including single source route [16–21], spray pyrolysis, chemical bath deposition [22], successive ionic layer absorption [23] and chemical vapour deposition (CVD) [24–27], have been used.

Different single source precursors have been used in CVD for deposition of metal chalcogenide thin films [28–31], and have

the advantage of avoiding toxic precursors and eliminating undesired effects of the anions of the metal salt [32]. Dithiocarbamates [33,34], thiosemicarbazides [35], xanthate [25,36], imidodiphosphinates, *N*-alkyl thiourea [37], dichalcogenophosphinates and dichalcogenophosphates [38] lead complexes have been investigated for the preparation of PbS

Herein we report the synthesis of *N*-morpholine (**1**) and *N*-pyrrolidine (**2**) lead (II) *N*-benzoylthioureato complexes. The X-ray single crystal structure of bis(*N*-morpholine-*N*'-benzoylthioureato)lead(II) complex (**1**) is also elucidated. These complexes have been used as single source precursors for the deposition of cubic, spherical and rod-shaped PbS crystallites in thin films on glass substrate at various temperatures by AACVD.

2. Experimental

2.1. Chemicals

Benzoyl chloride 99%, morpholine 99%, pyrrolidine 99%, potassium thiocyanate 98.5% (Sigma–Aldrich). Lead nitrate 99%, ethanol 99.5%, dichloromethane, chloroform and acetone (Merck) were used as purchased without any further purification.

* Corresponding authors.

E-mail address: RevaprasaduN@unizulu.ac.za (N. Revaprasadu).

2.2. Instrumentation

Microanalysis was performed on a Perkin-Elmer automated model 2400 series II CHNS/O analyzer. The ^1H NMR spectra of both ligands were obtained using a Bruker advance III 400 MHz spectrophotometer. Infrared spectra were recorded on a Perkin-Elmer Spectrum Two UATR FT-IR spectrophotometer directly on small samples of the compounds in the 500–4250 cm^{-1} range. Thermogravimetric analysis was carried out at 20 $^\circ\text{C min}^{-1}$ heating rate using a Perkin Elmer Pyris 6 TGA up to 600 $^\circ\text{C}$ in a closed perforated aluminium pan under N_2 gas flow. Optical absorption measurements were carried out using a Lambda 1050 Perkin-Elmer spectrophotometer. Measurements were done at room temperature. The surface morphology and structure of the film was determined using a Zeiss Sigma VP-03-67 field emission gun scanning electron microscopy (FESEM), equipped with an Oxford instrument X-max 50 EDX detector. Powder X-ray diffraction (pXRD) patterns of the nanoparticles were recorded at room temperature in the angle 2 θ range (20–80 $^\circ$) using an Advanced Bruker AXS D8 diffractometer, equipped with nickel-filtered $\text{Cu K}\alpha$ radiation ($\lambda = 1.542 \text{ \AA}$) at 40 kV and 40 mA.

2.3. X-ray crystallographic analysis

Thin colourless, plate-like crystals of (1) were grown from a 1:1 mixture of dichloromethane and ethanol. X-ray data was recorded on a Bruker Apex Duo equipped with an Oxford Instruments Cryojet operating at 100(2) K and an Incoatec microsource operating at 30 W power. The data were collected with $\text{Mo K}\alpha$ ($\lambda = 0.71073 \text{ \AA}$) radiation at a crystal-to-detector distance of 50 mm. Data were collected using omega and phi scans with exposures taken at 30 W X-ray power and 0.50 $^\circ$ frame widths using APEX2 [39]. The data were reduced with the programme SAINT [39] using outlier rejection, scan speed scaling, as well as standard Lorentz and polarization correction factors. A SADABS semi-empirical multi-scan absorption correction [39] was applied to the data. Direct methods, SHELX-2016 [40] and WinGX [41], were used to solve the structure. All non-hydrogen atoms were located in the difference density map and refined anisotropically with SHELX-2016 [40]. All hydrogen atoms were included as idealized contributors in the least squares process. Their positions were calculated using a standard riding model of SHELX with C-H_{aromatic} distances of 0.93 \AA and $U_{\text{iso}} = 1.2 \text{ Ueq}$ and C-H_{methylene} distances of 0.99 \AA and $U_{\text{iso}} = 1.2 \text{ Ueq}$.

2.4. Preparation of the ligands

The ligands were prepared using a procedure similar to that reported in the literature [42,43]. Benzoyl chloride (2.0 mL; 17 mmol) was dissolved in 50 mL of acetone and added dropwise to a suspension of potassium thiocyanate (1.67 g; 17 mmol) in 30 mL of acetone. The reaction mixture was heated under reflux for 30 min, then cooled to room temperature. A solution of the corresponding amine (1.5 mL; 17 mmol) in 10 mL of acetone was added and the resulting mixture stirred for 2 h. Hydrochloric acid (300 mL, 0.1 M) was added to the resultant solution and the solid product filtered off, washed with water and purified by recrystallization in ethanol: dichloromethane (1:1) mixture.

N-morpholine-*N*'-benzoylthiourea HL¹: White. Yield: 75%, m.p. 144–146 $^\circ\text{C}$. Anal. Calcd for $\text{C}_{12}\text{H}_{14}\text{N}_2\text{O}_2\text{S}$ (%): C, 57.58; H, 5.64; N, 11.19. Found: C, 57.98; H, 5.62; N, 11.07. IR (cm^{-1}): $\nu(\text{N}-\text{H})$ 3239 (br), $\nu(\text{C}=\text{O})$ 1663 (s), $\nu(\text{C}=\text{S})$ 1000 (s). ^1H NMR: δ , 8.1 (s, 1H, NH), 7.80 (m, 2H, C_6H_5), 7.60 (d, 1H, C_6H_5), 7.54 (m, 2H, C_6H_5), 3.78 (s, 4H, CH_2), 3.0 (s, 4H, CH_2).

N-pyrrolidine-*N*'-benzoylthiourea HL²: Yellow. Yield: 73%, m.p. 130–132.8 $^\circ\text{C}$. Anal. Calcd for $\text{C}_{12}\text{H}_{14}\text{N}_2\text{O}_2\text{S}$ (%): C, 61.51; H, 6.02; N, 11.96. Found: C, 61.92; H, 5.89; N, 11.08. IR (cm^{-1}): $\nu(\text{N}-\text{H})$

3148 (br), $\nu(\text{C}=\text{O})$ 1643 (s), $\nu(\text{C}=\text{S})$ 978.57 (s). ^1H NMR: δ 8.0 (s, 1H, NH), 7.80 (m, 2H, C_6H_5), 7.60 (d, 1H, C_6H_5), 7.50 (m, 2H, C_6H_5), 3.0 (s, 4H, CH_2), 2.0 (s, 4H, CH_2).

2.5. Preparation of the lead complexes

Lead nitrate (0.72 g; 2 mmol) was dissolved in 20 mL of water and added dropwise to a solution of the corresponding ligand (4 mmol) in 50 mL of ethanol at room temperature. The resulting mixture was stirred for 30 min and the product obtained was filtered off and recrystallized in ethanol: dichloromethane (1:1).

Bis(*N*-morpholine-*N*'-benzoylthiourea)lead(II) (1). White. Yield: 91%, m.p. 167–169 $^\circ\text{C}$. Anal. Calcd for $\text{C}_{24}\text{H}_{26}\text{N}_4\text{O}_4\text{PbS}_2$ (%): C, 40.84; H, 3.71; N, 7.94. Found: C, 39.85; H, 3.69; N, 7.93. IR (cm^{-1}): $\nu(\text{C}=\text{N})$ 1587 (s), $\nu(\text{C}=\text{O})$ 1473 (s).

Bis(*N*-pyrrolidine-*N*'-benzoylthiourea)lead(II) (2). Yellow. Yield: 74%, m.p. 154–157 $^\circ\text{C}$. Anal. Calcd for $\text{C}_{24}\text{H}_{26}\text{N}_4\text{O}_4\text{PbS}_2$ (%): C, 42.78; H, 3.89; N, 8.31. Found: C, 41.14; H, 3.51; N, 7.43. IR (cm^{-1}): $\nu(\text{C}=\text{N})$ 1586 (s), $\nu(\text{C}=\text{O})$ 1487 (s).

2.6. Deposition of films by AACVD

In a typical deposition, 0.2 g (0.3 mmol) of the precursor was dissolved in 25 mL of chloroform in a two-necked 100 mL round-bottom flask with a gas inlet that allowed the carrier gas (argon) to pass into the solution to assist the transport of the aerosol. This flask was connected to the reactor tube by a piece of reinforced tubing. The argon flow rate was controlled by a Platon flow gauge. Seven glass substrates (approx. 1 \times 2 cm) were placed inside the reactor tube in a Carbolite furnace. The precursor solution in a round-bottom flask was kept in a water bath above the piezoelectric modulator of a Pifco ultrasonic humidifier (Model No. 1077). Aerosol droplets of the precursor were transferred into the hot wall zone of the reactor by carrier gas. Both the solvent and the precursor were evaporated and the precursor vapor reached the heated substrate surface where thermally induced reactions and film deposition took place. The reaction temperatures were varied between 350 and 450 $^\circ\text{C}$.

3. Results and discussion

3.1. Characterization of the ligands and the complexes

The *N*-morpholine-*N*'-benzoylthiourea ligand and its corresponding Pb(II) complex (1) were obtained as white powders

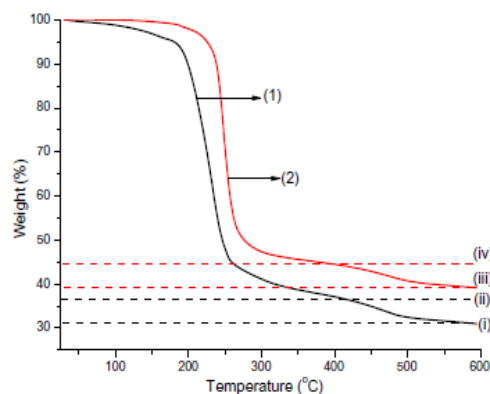


Fig. 1. Thermogravimetric analysis (TGA) plots of complexes (1) and (2) at a heating rate of 10 $^\circ\text{C min}^{-1}$ under nitrogen atmosphere.

whilst the *N*-pyrrolidine-*N'*-benzoylthiourea ligand and its Pb(II) complex (**2**) were yellow. The compounds were obtained in good yields based on the expected formulas as confirmed by microanalysis. IR results revealed that the medium peak appearing at 3239 cm^{-1} for HL¹ and 3148 cm^{-1} for HL² is attributed to the stretching of the N–H group adjacent to the carbonyl group. This N–H bond is replaced by the C=N bond upon complexation of the ligand to the metal ion by action of a base. The appearance of two new peaks in the IR spectra of the complexes is observed at 1587 cm^{-1} and

1586 cm^{-1} respectively for complexes (**1**) and (**2**) and attributed to the C=N bond. The strong band at 1663 cm^{-1} for HL¹ and 1643 cm^{-1} for HL² is attributed to the vibration of the C=O of carbonyl groups which shifts to lower wavenumbers upon complexation. Deprotonation involved delocalization of C=O stretching vibration which is in agreement with the literature [26,44] thus confirming the coordination to the central metal ion through oxygen atom from the carbonyl. The same observation was made in complex (**2**). The proposed structure of bis-(*N*-pyrrolidine-*N'*-(benzoyl)thioureato)lead (II) complex (**2**) is presented in ESI Fig. S1.

The TGA profiles of both complexes showed a two-step decomposition pattern while the DTA curves of both complexes exhibited a single endothermic peak centred at 230.61 °C and 249.37 °C for complexes (**1**) and (**2**) respectively (ESI Fig. S2) which correspond to the decomposition process. The first steps gave a loss of 58% (54.19%, 2 MB = 2morpholinylbenzamide) (**1**) (Fig. 1; step ii) and 52% (52.01%, 2 PB = 2pyrrolidinylbenzamide) (**2**) (Fig. 1; step iv) at 282 and 293 °C, respectively corresponding to the loss of the organic moiety. Second decomposition steps at 485 and 493 °C with mass losses of a further 10% (calcd: 7.38%; 2CN, step i) (**1**) and 9% (7.73%; 2CN; step iii) (**2**) occurred, respectively [45]. The final residues of 33% (calc. 33.90%) (**1**) and 39% (calc. 35.51%) (**2**) closely correspond to the theoretical values of PbS, respectively. The higher experimental residues for (**2**) can be attributed to carbonaceous contamination from aryl and heterocyclic groups.

Table 1
Crystal data and structure refinement details for (**1**).

Crystal Data	Complex (1)
Chemical formula	C ₂₄ H ₂₈ N ₄ O ₄ PbS ₂
Molar mass (g mol ⁻¹)	705.80
Crystal system, space group	Monoclinic, P2 ₁ /n
Temperature (K)	100(2)
a, b, c (Å)	13.430(2), 8.0145(13), 23.392(4)
α, β, γ (°)	90, 92.456(5), 90
V (Å ³)	2515.6(7)
Z	4
Radiation type	Mo Kα
μ (mm ⁻¹)	6.91
Crystal size (mm)	0.6 × 0.05 × 0.02
Data Collection	
Diffractometer	Bruker APEXII CCD diffractometer
Absorption correction	Multi-scan, SADABS
T _{min} , T _{max}	0.645, 0.746
No. of measured, independent and observed [I > 2σ(I)] reflections	23490, 6186, 5398
R _{int}	0.035
Refinement	
R[F ² > 2σ(F ²)], wR(F ²), S	0.024, 0.052, 1.05
No. of reflections	6186
No. of parameters	316
H-atom treatment	H-atom parameters constrained
Δρ _{max} , Δρ _{min} (e Å ⁻³)	1.00, -0.64

3.2. Single crystal X-ray structure of *N*-morpholine-*N'*-benzoylthioureato lead(II) (**1**)

The Pb(II) metal centre of complex (**1**) is four-coordinate with the coordination sphere comprising two bidentate *N*-morpholine-derived benzoylthioureato ligands. The ligands are coordinated through the carbonyl oxygen atom and a deprotonated thiol group yielding a monoanionic ligand and neutral lead(II) chelate. The coordination geometry of the lead(II) complex can be described as hemidirected i.e. the bonds between the ligand and metal

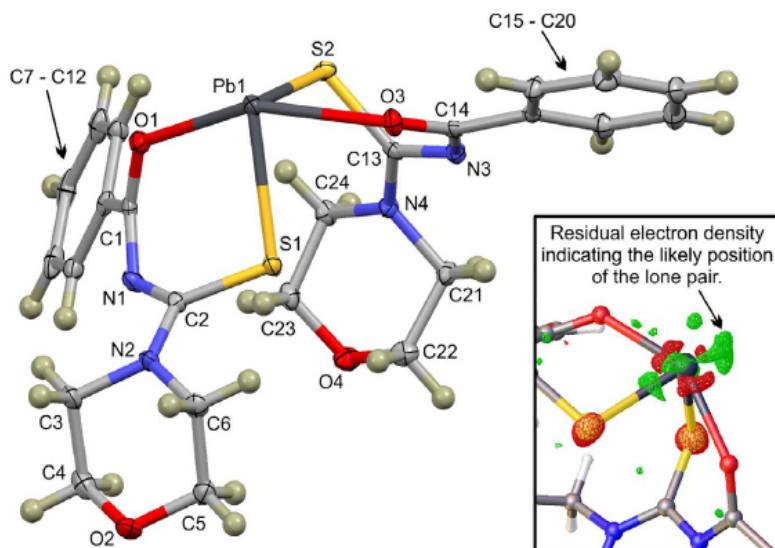


Fig. 2. Displacement ellipsoid plot (50% probability) of (**1**) showing the distorted trigonal bipyramidal geometry as well as the void in the coordination sphere, as conventionally attributed to the electron density. Hydrogen atoms are rendered as spheres of arbitrary radius. [Inset] Difference Fourier map showing the probable location of the electron density residing on the lead (II) ion. The contour has $\rho = -1.8$ e, the red and green grids indicate electron density maxima and minima, respectively. The plot was rendered using OLEX2 [46].

occupy only part of the encompassing globe of the metal ion, The compound crystallised in the monoclinic space group $P2_1/n$ with a single molecule in the asymmetric unit ($Z = 4$). Crystal and structure refinement data are given in Table 1. The contents of the asymmetric unit and the Difference Fourier map of (1) are shown in Fig. 2, the latter illustrates the likely position of the lone pair of electrons on the lead(II) ion.

The data in Table 2 illustrate the bond parameters associated with the metal ion coordination sphere, thus making it difficult to formally categorize the coordination geometry. The bond

parameters are comparable to those of related four-coordinate hemi-directed lead(II) chelates with pseudo trigonal bipyramidal geometry [47–49]. The carbonyl groups have a mean C=O bond length of 1.268(6) Å, highlighting their double bond character. The O3–C14–C15 bond angle which measures 117.1(3)° further highlights the sp^2 hybridised nature of C14.

The structure packs as inversion dimers (Fig. 3) supported by complementary Pb–S interactions between the lead ion and sulfur atom of an adjacent molecule with an interaction distance of 3.6157(9) Å. This motif leads to the formation of a four-membered ring. Interactions of this type are common, but not ubiquitous in comparable O_2S_2 lead(II) complexes [47,48]. And also seen in many related cadmium complexes. The dimeric structures are linked into a one-dimensional supramolecular structure (Fig. 3) through C–H...O interactions with a C...O interaction distance of 3.399(4) Å. This structure propagates collinear to the *b*-axis. Bond length cannot be definitively linked to bond strength due to various packing constraints in the crystal lattice. However, both the Pb...S and C–H...O interactions are significantly shorter than the sum of the van der Waals radii of the interacting atoms, 0.304 and 0.204 Å, respectively. This short bond length suggests a genuine and indeed moderately strong interaction. In the case of the C–H...O interaction, this statement is further supported by the

Table 2
Selected geometric parameters describing complex (1).

Bond	Length (Å)	Bond	Angle (°)
Pb1–O1	2.448(2)	O1–Pb1–S1	79.63(5)
Pb1–O3	2.455(2)	S1–Pb1–O3	76.81(6)
Pb1–S1	2.687(1)	O3–Pb1–S2	76.24(5)
Pb1–S2	2.689(1)	S2–Pb1–O1	85.11(5)
C1–O1	1.262(4)	S1–Pb1–S2	96.07(2)
C14–O3	1.275(4)	O1–Pb1–O3	147.99(7)
		O1–C1–C7	118.3(3)
		O3–C14–C15	117.1(3)

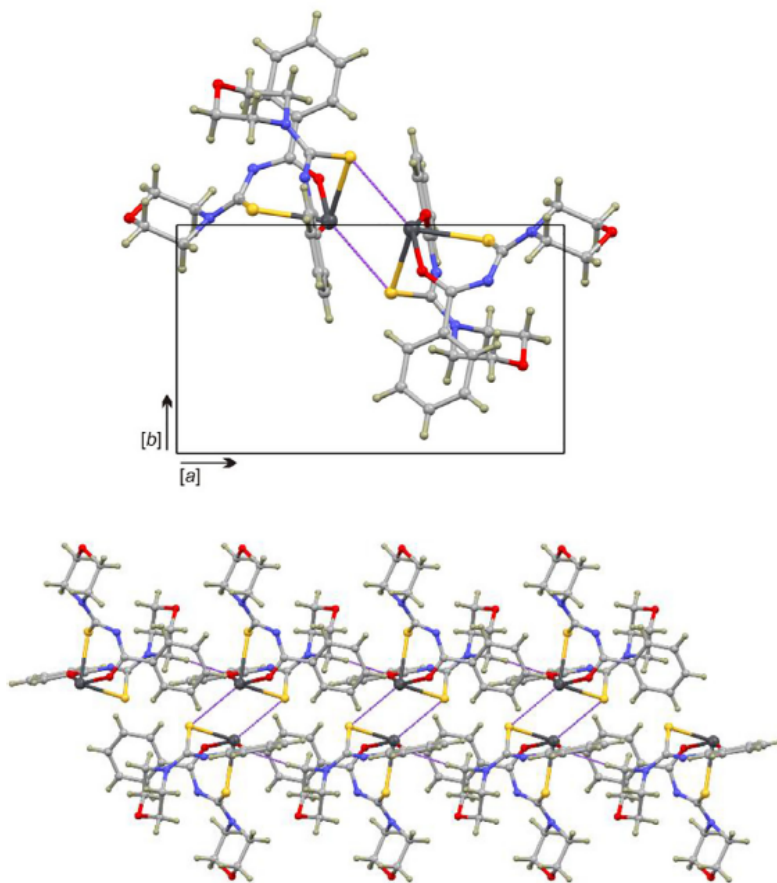


Fig. 3. [Top] Dimeric structure of (1) stabilised by Pb...S and weak Pb...Pb interactions.

fact that the bond angle (171.4°) does not deviate significantly from the ideal angle of 180° .

The dimeric structure indicates weak stabilizing Pb...Pb interactions. The separation of the metal ions comprising the dimer measures $3.9777(7)$ Å. In the literature there is debate as to whether Pb–Pb bonds exist or would be better described as van der Waals interactions [50]. The van der Waals parameter for a bond of this nature is 4.04 Å, thus the distance noted in the present compound is only modestly shorter and may indicate weak stabilizing van der Waals interactions between the metal ions. If the Pb...Pb contact and lone pair are considered part of the coordination sphere then the chelate could be loosely categorized as a distorted octahedron.

[Bottom] One dimensional polymer of (1) comprising dimeric molecules cross-linked by short, $3.399(4)$ Å, C, C–H...O interactions. Respective symmetry codes: $1-x, -y, 2-z$ and $x, -1+y, z$. Interactions are shown as dashed purple tubes, all atoms are rendered as spheres of arbitrary radius.

Table 3
Calculated Lattice Parameter/Å (Calculated for all peaks below $2\theta = 60^\circ$).

Temp./°C	Complex (1)	Complex (2)
350	5.930(5)	5.933(4)
400	5.931(6)	5.932(4)
450	5.923(6)	5.932(4)
Average	5.928(4)	5.932(5)

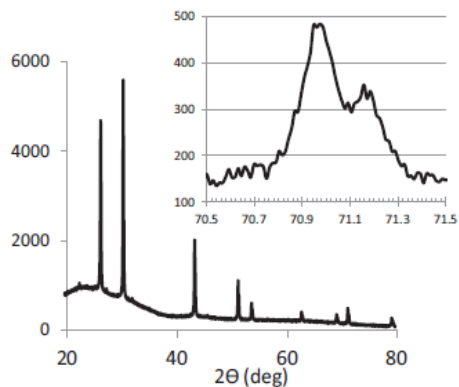


Fig. 4. Highly resolved p-XRD pattern. The lattice constant a value can be measured using the average Cu K α value of 1.54184 Å for all values of 2θ less than ca 60° . The lattice parameters are remarkable consistent and summarized in Table 3. At higher 2θ angles the peaks for both the 1.5405 Å and 1.54434 Å of Cu K alpha wavelengths are seen, and values for lattice constants can be measured for all 6 samples twice, again accurate and consistent values are obtained summarized in Table 4. Histograms of spectra are quite consistent for all samples with some evidence for slight rod like orientation (Fig. 5). Inset: average XRD patterns for all depositions, with of course little or no difference in peak position.

Table 4
The values of the lattice parameter calculated twice for each temperature from the ca 71° ($4\ 2\ 0$) peak.

Sample	2θ	2θ	$\lambda = 1.5405$ Å	$\lambda = 1.54434$ Å
C(1) 350 °C	70.940	71.180	5.936	5.934
C(1) 400 °C	70.990	71.180	5.933	5.934
C(1) 450 °C	70.960	71.170	5.935	5.934
C(2) 350 °C	70.950	71.160	5.936	5.935
C(2) 400 °C	70.970	71.160	5.934	5.935
C(2) 450 °C	70.960	71.160	5.935	5.935
		Av	5.935(1)	5.934(1)

3.3. Physical and morphological studies of PbS thin films

The films deposited by AACVD were investigated by powder X-ray diffraction. The recorded patterns for films obtained using complexes (1) and (2) are summarized in the ESI (Figs. S3 and S4). The films deposited are all of well-defined galena PbS with the halite structure (ICDD 05-0592). The deposited films all gave very sharp peaks in the p-XRD and indeed at values greater than ca 60° of the 2θ the peaks for 1.5405 Å and 1.54434 Å of Cu K alpha radiation are seen. These results indicate good crystallinity. There are many literature studies of PbS: the original mineralogical study in 1925 [51] gave 5.3 Å lattice parameter, whilst Wyckoff in 1963 gives 5.9363 Å [52] and one at 298 K by Noda 1987 [53] gives 5.9315 Å.

The lattice constant determined for our samples from all peaks below 63° gave consistent values for the lattice constant from each deposition (Table 3) and an overall average of $5.930(5)$ Å consistent with the literature. An average plot of all samples is shown in Fig. 4, a small non-indexed peak appearing at $2\theta = 22.71^\circ$ is seen for the films deposited at 400 °C. At the higher angle diffraction close to 71° is weak and somewhat noisy and the average of all peak is shown (inset Fig. 4). However the two component peaks for the Cu K α components can be seen and beautifully corresponding values for the a value of 5.934 Å and 5.935 Å are seen from the ($4\ 2\ 0$) reflection. These results show that the thin films are well crystallised.

The relative orientations are summarized in Fig. 5 and slightly rod like SEM images were observed. The coverage area is largely close to 100% at the substrate temperature at several temperatures (Fig. 5 and always $> 80-90$). Various particle sizes and morphologies were obtained and the average particle size was estimated using the intercept technique where a random straight line is drawn through the micrograph, the number of grain boundaries intersecting the line are counted. The average grain size is found by dividing the number of intersections by the actual line length.

$$\text{Average grain size} = 1/(\text{number of intersections/actual length of the line})$$

At 350 °C when complex (1) was used, cubic-shaped PbS particles were formed with an average size of 85 nm (Fig. 5a). A rise in temperature to 400 °C resulted in the formation of a mixture of spherical and cubic shaped particles with an average size of 84 nm (Fig. 5b). At higher deposition temperature of 450 °C, predominantly rod-shaped PbS particles were obtained with an average size of 83 nm (Fig. 5c). A slight decrease in the particle grain size with an increase of temperature was observed. When complex (2) was used as precursor, a remarkable difference in grain sizes and uniformity was observed as the temperature was varied from 350 to 450 °C. At 350 °C, spherical particles aggregates were formed with an average size of 71 nm (Fig. 5d). As the temperature was increased to 400 °C, the shape of crystallites changed from spherical to cubic particles with an average size of 90 nm (Fig. 5e) and the deposition at 450 °C resulted in the growth of large cube-shaped PbS particles with a average size of 105 nm (Fig. 5f). An increase in the particle size with an increase of temper-

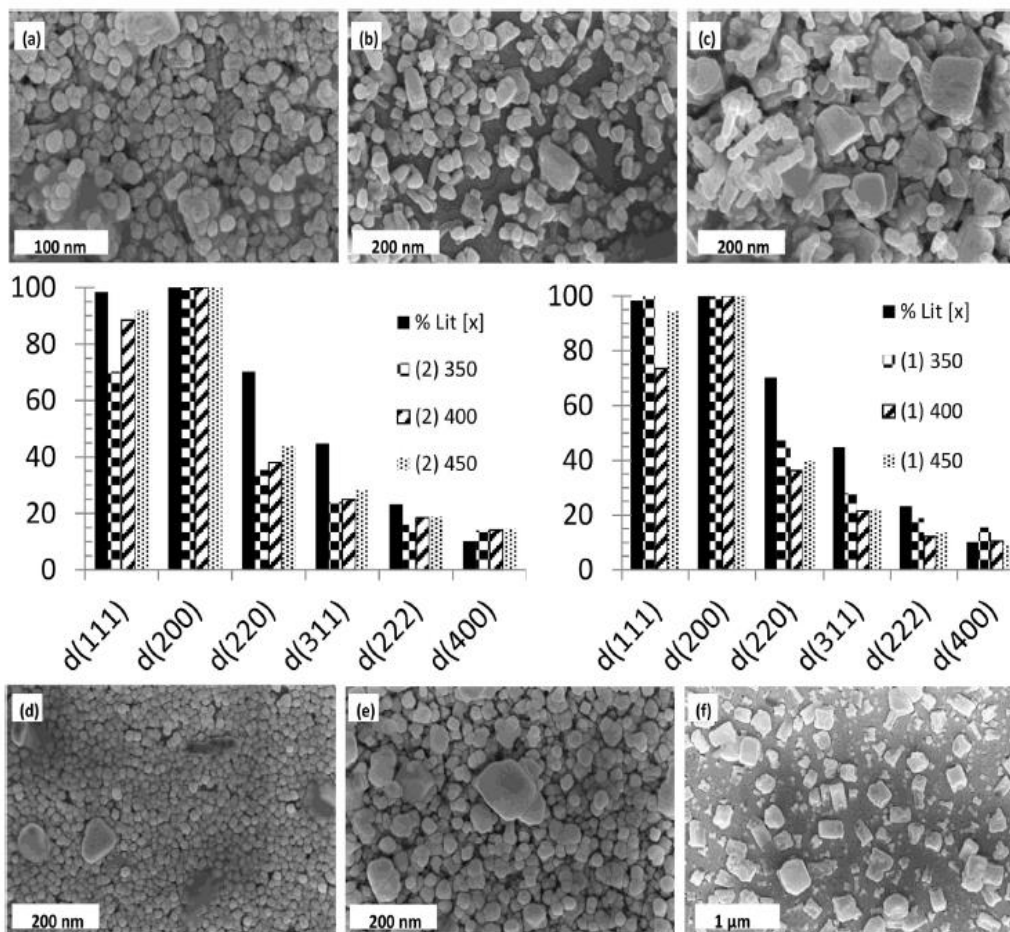


Fig. 5. SEM images of PbS films deposited from complex (1) onto glass substrates at (a) 350, (b) 400 and 450 °C and from complex (2) at (d) 350, (e) 400 and (f) 450 °C. The orientations of the powder patterns for both depositions are shown in the middle compared to the literature pattern of PbS. There is a small tendency for films to extend along one axis as seen in SEM and by XRD.

ature was observed. EDX analysis results showed that the films are sulfur deficient (ESI Table S1). This could be due to the large atomic size of lead as compared to sulfur.

3.4. Optical properties of PbS thin films

The room temperature UV-Vis absorption spectra of the PbS samples recorded in the wavelength range of 250–2000 nm, uncoated glass substrate as a reference are shown in the ESI Figs. S5 and S6. The energy band gap (E_g) was determined from the Tauc plot equation [54] using their transmission and reflectance curves as well as the following formula:

$$(\alpha h\nu)^2 = A(h\nu - E_g)$$

$h\nu$ is the energy of the incident light, E_g the band gap of the sample and α is the absorption coefficient.

A strong blue shift as compared to the bulk PbS was observed in the absorption band edges of all the PbS films deposited at the different temperatures. The observation is in line with the literature where the reported PbS band gap varying in a wide range up to

2.3 eV from the bulk value of 0.41 eV [55–58]. This work reports PbS thin films with band gap in the range of 1.46–1.55 eV. These band gap values are larger than expected for particles with sizes in the range of 70–105 nm, greater than PbS Bohr exciton radii (18 nm) [2,58]. The results further reveal that the band gap of the as-deposited PbS films gradually decreases (from 1.49 eV to 1.46 eV – complex (1) and 1.55 eV to 1.46 eV – complex (2)) as temperatures were increased from 350 °C to 450 °C, respectively [56].

4. Conclusion

N-morpholine (1) and *N*-pyrrolidine (2) lead(II) *N'*-benzoylthiourea complexes have been synthesized, characterized and the single crystal X-ray structure of *N*-morpholine-*N'*-benzoylthiourea-Pb(II) complex (1) elucidated. The lead(II) complexes were successfully used to deposit PbS thin films by AACVD at various temperatures. The films showed blue shift in their absorption band edge as compared to bulk PbS and the particle size was tunable with the deposition temperature. Analyses confirmed the forma-

tion of crystalline PbS in the galena form (halite structure) of excellent crystallinity compatible with PbS. There may be some sulfur deficiency in the PbS films may make the PbS thin films and study their potential application as gas sensors.

Acknowledgements

The authors thank the Royal Society/Department For International Development (RS-DFID) Africa Capacity Building Initiative and the National Research Foundation (NRF) South Africa through the South African Research Chair Initiative (SARChI) for their financial support.

Appendix A. Supplementary data

Supplementary data associated with this article can be found, in the online version, at <https://doi.org/10.1016/j.ica.2018.04.023>.

References

- [1] M.A. Malik, M. Afzaal, P. O'Brien, *Chem. Rev.* 110 (2010) 4417.
- [2] I. Kang, F.W. Wise, *J. Opt. Soc. Am. B* 14 (1997) 1632.
- [3] N.O. Boadi, M.A. Malik, P. O'Brien, J.A. Awudza, *Dalton Trans.* 41 (2012) 10497.
- [4] J.M. Skelton, S.C. Parker, A. Togo, I. Tanaka, A. Walsh, *Phys. Rev. B* 89 (2014) 205203.
- [5] X. Yao, S. Liu, Y. Chang, G. Li, L. Mi, X. Wang, Y. Jiang, *ACS Appl. Mater. Interfaces* 7 (2015) 23117.
- [6] C. E. Pérez-García, R. Ramírez-Bon, V. Vorobiev, *MATEC Web of Conferences: EDP Sciences* (2015).
- [7] J. Akhtar, M. Sher, M. Dilshad, W. Khalid, N. Revaprasadu, M.A. Malik, *Mater. Sci. Semicond. Process.* 36 (2015) 20.
- [8] W. Scanlon, *J. Phys. Chem. Solids* 8 (1959) 423.
- [9] F.W. Wise, *Acc. Chem. Res.* 33 (2000) 773.
- [10] J. Tang, E.H. Sargent, *Adv. Mater.* 23 (2011) 12.
- [11] L.-D. Zhao, S.-H. Lo, J. He, H. Li, K. Biswas, J. Androulakis, C.-I. Wu, T.P. Hogan, D.-Y. Chung, V. P. Dravid and M. G. Kanatzidis, *J. Am. Chem. Soc.* 133 (2011) 20476.
- [12] S. Johnsen, J. He, J. Androulakis, V.P. Dravid, I. Todorov, D.Y. Chung, M.G. Kanatzidis, *J. Am. Chem. Soc.* 133 (2011) 3460.
- [13] H. Karami, M. Ghasemi, S. Matini, *Int. J. Electrochem. Sci.* 8 (2013) 11661.
- [14] T. Fu, *Sens. Actuators B Chem.* 140 (2009) 116.
- [15] W. Wu, Y. He, Y. Wu, T. Wu, *J. Alloys Compd.* 509 (2011) 9356.
- [16] Z. Tshemese, M.D. Khan, S. Mlowe, N. Revaprasadu, *Mater. Sci. Eng. B* 227 (2018) 116.
- [17] L.D. Nyamen, V.R. Pullabhotla, A.A. Nejo, P.T. Ndifon, J.H. Warner, N. Revaprasadu, *Dalton Trans.* 41 (2012) 8297.
- [18] P.S. Nair, T. Radhakrishnan, N. Revaprasadu, G. Kolawole, A. Luyt, V. Djoković, *Appl. Phys. A* 81 (2005) 835.
- [19] S.C. Masikane, S. Mlowe, C. Gervas, N. Revaprasadu, A.S. Pawar, S.S. Garje, *J. Mater. Sci. Mater. Electron.* 29 (2018) 1479.
- [20] K.P. Mubiyi, N. Revaprasadu, S.S. Garje, M.J. Moloto, *J. Saudi Chem. Soc.* 21 (2017) 593.
- [21] G.B. Shombe, E.B. Mubofu, S. Mlowe, N. Revaprasadu, *Mater. Lett.* 185 (2016) 17.
- [22] S. Salim, O. Hamid, *Renew. Energ.* 24 (2001) 575.
- [23] T. Kannianen, S. Lindroos, J. Ihanus, M. Leskelä, *J. Mater. Chem.* 6 (1996) 983.
- [24] N. Fainer, M. Kosinova, Y.M. Rumyantsev, E. Salman, F. Kuznetsov, *Thin Solid Films* 280 (1996) 16.
- [25] M.D. Khan, S. Hameed, N. Haider, A. Afzal, M.C. Sportelli, N. Cioffi, M.A. Malik, J. Akhtar, *Mater. Sci. Semicond. Process.* 46 (2016) 39.
- [26] H. Arslan, N. Külcü, U. Flörke, *Transition Met. Chem.* 28 (2003) 816.
- [27] M. Afzaal, K. Ellwood, N.L. Pickett, P. O'Brien, J. Raftery, J. Waters, *J. Mater. Chem.* 14 (2004) 1310.
- [28] M. Khan, M. Malik, J. Akhtar, S. Mlowe, N. Revaprasadu, *Thin Solid Films* 638 (2017) 338.
- [29] R.A. Hussain, A. Badshah, N. Haider, M.D. Khan, B. Lal, *J. Chem. Sci.* 127 (2015) 499.
- [30] R.A. Hussain, A. Badshah, F. Yasmin, M.D. Khan, M.N. Tahir, *Aust. J. Chem.* 68 (2015) 298.
- [31] A.A. Memon, M. Dilshad, N. Revaprasadu, M.A. Malik, J. Raftery, *J. Akhtar Turk. J. Chem.* 39 (2015) 169.
- [32] D. Barreca, A. Gasparotto, C. Maragno, R. Seraglia, E. Tondello, A. Venzo, V. Krishnan, H. Bertagnolli, *Appl. Organomet. Chem.* 19 (2005) 59.
- [33] S.-M. Lee, Y.-W. Jun, S.-N. Cho, J. Cheon, *J. Am. Chem. Soc.* 124 (2002) 11244.
- [34] T. Trindade, P. O'Brien, X.-M. Zhang, M. Motevalli, *J. Mater. Chem.* 7 (1997) 1011.
- [35] T. Mandal, G. Piburn, V. Stavila, I. Rusakova, T. Ould-Ely, A.C. Colson, K.H. Whitmire, *Chem. Mater.* 23 (2011) 4158.
- [36] N. Pradhan, B. Katz, S. Efrima, *J. Phys. Chem. B* 107 (2003) 13843.
- [37] M. Moloto, N. Revaprasadu, G. Kolawole, P. O'Brien, M. Malik, *S. Afr. J. Sci.* 101 (2005) 463.
- [38] T. Duan, W. Lou, X. Wang, Q. Xue, *Colloids Surf. A: Physicochem. Eng. Asp.* 310 (2007) 86.
- [39] Bruker APEX2, SAINT and SADABS, Bruker AXS Inc., Madison, Wisconsin, USA (2012).
- [40] G.M. Sheldrick, *Acta Crystallogr. C* 71 (2015) 3.
- [41] L.J. Farrugia, *J. Appl. Crystallogr.* 45 (2012) 849.
- [42] I.B. Douglass, F. Dains, *J. Am. Chem. Soc.* 56 (1934) 719.
- [43] L. Beyer, M. Pulst, H. Paul, E. Hoyer, *J. Prakt. Chem.* 317 (1975) 265.
- [44] M. Mikami, I. Nakagawa, T. Shimanouchi, *Spectrochim Acta Part A Mol. Spectrosc.* 23 (1967) 1037.
- [45] M. Merdivan, F. Karipcin, N. Kulcu, R. Aygun, *J. Therm. Anal. Calorim.* 58 (1999) 551.
- [46] O.V. Dolomanov, L.J. Bourhis, R.J. Gildea, A.K. Howard, H. Puschmann, *J. Appl. Crystallogr.* 42 (2009) 339.
- [47] S. Sadovnikov, A. Gusev, *J. Alloys Compd.* 573 (2013) 65.
- [48] D. Saikia, P. Phukan, *Thin Solid Films* 562 (2014) 239.
- [49] N. Bahlawane, E.F. Rivera, K. Kohse-Höinghaus, A. Brechlin, U. Kleineberg, *Appl. Catal. B Environ.* 53 (2004) 245.
- [50] M.-L. Chan, M. Rossi, *Inorg. Chem.* 36 (1997) 3609.
- [51] L.S. Ramsdell, *U-M* (1925).
- [52] R.G. Wyckoff, *Cryst. Struct. Interci. Publ.* 1 (1963) 239.
- [53] Noda, K. Masumoto, S. Ohba, Y. Saito, K. Toriumi, Y. Iwata, I. Shibuya, *Acta Crystallogr. Sect. C Cryst. Struct. Commun.* 43 (1987) 1443.
- [54] A. Rakhshani, *J. Phys. Condens. Matter* 12 (2000) 4391.
- [55] J.N. Zemel, J.D. Jensen, R.B. Schoolar, *Phys. Rev.* 140 (1965) A330.
- [56] M. Abbas, A.A.-M. Shehab, N. Hassan, A. Al-Samurrae, *Thin Solid Films* 519 (2011) 4917.
- [57] B. Thangaraju, P. Kaliannan, Spray pyrolytically deposited PbS thin films, *Semiconductor Sci. Tech.* 15 (2000) 849.
- [58] C. Rajashree, A. Balu, V. Nagarethinam, *Int J. Chem. Tech. Res.* 6 (2014) 347.



CdS thin films deposition by AACVD: effect of precursor type, decomposition temperature and solvent

Kevin I. Y. Ketchemen^{1,2} · Sixberth Mlowe² · Linda D. Nyamen¹ · Peter T. Ndifon¹ · Neerish Revaprasadu² · Paul O'Brien^{3,4}

Received: 28 May 2018 / Accepted: 28 June 2018
© Springer Science+Business Media, LLC, part of Springer Nature 2018

Abstract

Hexagonal cadmium sulfide (CdS) thin films were deposited on glass substrates by aerosol assisted chemical vapour deposition (AACVD) using cadmium(II) dithiocarbamate and xanthate complexes in tetrahydrofuran (THF) and mixed solvents (THF + chloroform) at 400 and 450 °C. The surface morphology and size of the CdS films determined using scanning electron microscopy, showed the formation of films of various morphologies depending on the precursor, the deposition temperature and solvent used. An increase in temperature resulted in an increase in particle size and a change in morphology with the formation of CdS films with distorted structures. The CdS films showed an overall blue shift in their absorption band edge (2.35–2.49 eV) compared to bulk CdS. In dithiocarbamates, a slight blue shift was observed with a shift to higher wavelengths with the reduction of the carbon chain of the dithiocarbamate and an increase in temperature. Films from xanthate complexes showed a strong blue shift at both deposition temperatures. The use of mixed THF + chloroform solvent at 450 °C showed the formation of films with irregular structures compared to those deposited using THF solvent alone, indicating the role of the solvent in shape direction of the films formation. The elemental composition determined by energy dispersive X-ray spectroscopy measurements revealed a 1:1 (Cd:S) ratio in all the samples confirming the stoichiometry of the CdS films.

1 Introduction

Cadmium sulfide (CdS) is one of the most studied semiconductor with a direct band gap energy of 2.42 eV [1, 2]. CdS thin films have been used for a wide variety of technological applications including photovoltaic cells, electro-optic modulators, sensors, electroluminescent and photo luminescent devices and antireflection coatings [3–5]. Deposition

techniques such as spray pyrolysis [6], chemical bath deposition [7], sol–gel [8], and metal–organic chemical vapor deposition (MOCVD) [9–12], have been used to deposit CdS films. Other deposition techniques have also been employed to deposit CdS thin films, these include spin coating deposition [13], pulsed laser deposition [14] and interface diffusion deposition [15]. The AACVD technique involves the deposition of high quality thin films under soft processing conditions in which the volatility of the precursor is no longer crucial compared to the conventional CVD technique [16]. Furthermore, AACVD has received much attention because of the superior quality of films produced, low cost, ease of composition control and homogeneity of uniform films.

The use of single-source precursors (SSPs) has proven to be advantageous when compared to other techniques due to the existence of pre-formed bonds which can lead to a material with less defects and better stoichiometry [17]. A wide range of SSPs including dithiocarbamates [10, 11, 18, 19], xanthates [9, 20], *N*-alkyl thioureas [21], and dithioimidodiphosphinates [22, 23], have been used for the preparation of CdS thin films. The dithiocarbamate and xanthate ligands were used in this study because of their ease of preparation, stability and reactivity with metal salts.

Electronic supplementary material The online version of this article (<https://doi.org/10.1007/s10854-018-9579-x>) contains supplementary material, which is available to authorized users.

✉ Neerish Revaprasadu
RevaprasaduN@unizulu.ac.za

¹ Department of Inorganic Chemistry, University of Yaoundé I, P.O. Box 812, Yaoundé, Cameroon

² Department of Chemistry, University of Zululand, Private Bag X1001, KwaDlangezwa 3880, South Africa

³ School of Chemistry, The University of Manchester, Oxford Road, Manchester M13 9PL, UK

⁴ School of Materials, The University of Manchester, Oxford Road, Manchester M13 9PL, UK

The nature of thin films deposited by AACVD depends on gas-phase nucleation of homogeneous and heterogeneous reactions, and is influenced by the deposition conditions such as the physical properties of the solvent (boiling point, heat of combustion and coordination ability), as well as the growth temperature and nature of the substrate. By tuning these parameters, CdS thin films with a variety of morphologies and particle sizes can be obtained. Ehsan et al. [24] reported the synthesis of greenockite CdS thin films in solvents such as pyridine, toluene and THF solutions at temperatures varying from 350 to 450 °C. At 350 °C, using the same precursor, regular-shaped hexagons were formed in pyridine, while irregular-shaped materials were formed in toluene and needle-like objects formed in THF. The role of solvent in the morphology formation was explained by the heat of combustion and coordinating ability of the solvents used. Upon increase of the deposition temperature, a deterioration to small-sized particles was observed. O'Brien and co-workers have reported a number of dithiocarbamate cadmium(II) complexes as single source precursors for CdS thin films using the low pressure metal-organic chemical vapour deposition (LP-MOCVD) technique [11, 25]. Mlowe et al. [26, 27] used piperidinyl and tetrahydroquinoline cadmium dithiocarbamate complexes to deposit CdS thin films at various temperatures. These studies showed that the growth of CdS films was influenced by the deposition temperature where the morphologies of CdS films obtained become increasingly dense with increase in temperature.

In this work, we report the deposition of hexagonal CdS thin films of various morphologies by AACVD method on glass substrates at different temperatures in THF and chloroform, using cadmium(II) dihexyl (a), diethyl (b), piperidinyl (c) dithiocarbamates and ethyl xanthate (d) complexes as single source precursors. The effect of the alkyl chain of the precursor, the reaction temperature and the solvent used on the optical properties and morphology of the CdS films was also investigated.

2 Experimental

2.1 Chemicals

Sodium diethyl dithiocarbamate trihydrate 97% (Sigma-Aldrich), dihexylamine 97% (Sigma-Aldrich), potassium ethyl xanthogenate 96% (Sigma-Aldrich), piperidine 99% (Sigma-Aldrich), carbon disulfide 99.5% (Sigma-Aldrich), ethanol 99.5%, chloroform, petroleum ether, tetrahydrofuran (THF) (Merck), sodium hydroxide 98% (Merck), cadmium chloride monohydrate 99% (Merck) and acetone (Merck) were used as purchased without any further purification.

2.2 Instrumentation

Microanalysis was performed on a Perkin-Elmer automated model 2400 series II CHNS/O analyser. Infrared spectra were recorded on a Bruker FT-IR tensor 27 spectrophotometer directly on small samples of the compounds in the range 200–4000 cm^{-1} . Thermogravimetric analysis was carried out at a heating rate of 20 °C min^{-1} using a Perkin Elmer Pyris 6 TGA up to 600 °C in a closed perforated aluminium pan under N_2 gas flow. Optical absorption measurements were carried out using a Lambda 1050 Perkin-Elmer spectrophotometer. A Perkin-Elmer LS 55 spectrofluorimeter was used to measure the photoluminescence of the CdS thin films. Both measurements were done at room temperature. Scanning electron microscopy (SEM) and EDX measurements were carried out on carbon coated films using Edward's E306A coating system. SEM analysis was performed using a Philips XL 30FEG and EDX was carried out using a DX4 instrument. Powder X-ray Diffraction patterns (p-XRD) were recorded in the high angle 2θ range of 20°–60° using a Bruker AXS D8 Advance X-ray diffractometer, equipped with nickel filtered $\text{Cu K}\alpha$ radiation ($\lambda = 1.5406 \text{ \AA}$) at 40 kV, 40 mA and at room temperature.

2.3 Preparation of the piperidinyl dithiocarbamate ligand

Carbon disulfide (6.0 mL, 100 mmol) was added in small portions to an equimolar mixture of sodium hydroxide (4.0 g, 100 mmol) and the corresponding piperidinyl (9.9 mL, 100 mmol) cooled in an ice bath at 0 °C. After 30 min, the solidified mass was then dried in air and recrystallized in a mixture of acetone/petroleum ether. The product was collected and washed with chloroform and suction dried.

$\text{Na}(\text{pip-dtc})$, (pip = piperidinyl, dtc = dithiocarbamate), yield: 88%, IR (cm^{-1} ; ATR) 967, ν (C=S); 1468, ν (C=N); 3367, ν (O-H). Microanalysis, calc. for $\text{C}_8\text{H}_{14}\text{NS}_2\text{O}_2\text{Na}$: C, 32.87, H, 6.44; N, 6.39; found: C, 32.57; H, 6.29; N, 5.96.

2.4 Preparation of the cadmium(II) complexes

2.4.1 Synthesis of cadmium(II) dihexyl dithiocarbamate complex

Carbon disulfide (1.2 mL, 20 mmol) was added in small portions to an equimolar mixture of sodium hydroxide (0.8 g, 20 mmol) and dihexylamine (4.7 mL, 20 mmol) cooled in an ice bath at 0 °C. After 15 min, cadmium chloride (2.0 g, 10.0 mmol) dissolved in distilled water (30.0 mL) was added dropwise to the corresponding solution of the

dithiocarbamate ligand while stirring. The reaction mixture was stirred for 1 h and the precipitate formed was filtered, washed with excess distilled water and dried overnight at room temperature.

[Cd(dihex-dtc)₂], (a) (dihex = dihexyl and dtc = dithiocarbamate), yield: 88%, IR (cm⁻¹; ATR) 980, ν (C=S); 1490, ν (C=N); 390, ν (Cd-S). Microanalysis, calc. for C₂₆H₅₂CdN₂S₄: C, 49.30, H, 8.27; N, 4.42; found: C, 48.56; H, 8.43; N, 4.34.

2.4.2 Synthesis of cadmium(II) diethyl dithiocarbamate, piperidinyl dithiocarbamate and ethyl xanthate complexes

Cadmium chloride (1.0 g, 5.0 mmol) was dissolved in distilled water (25.0 mL) and added dropwise to a solution of the dithiocarbamate or xanthate ligands (10.0 mmol). The reaction mixture was stirred for 1 h, and the precipitate formed was filtered, washed with excess distilled water and dried overnight at room temperature.

[Cd(dieth-dtc)₂], (b) (dieth = diethyl and dtc = dithiocarbamate), yield: 94%, IR (cm⁻¹; ATR) 970, ν (C=S); 1495, ν (C=N); 380, ν (Cd-S). Microanalysis, calc. for C₁₀H₂₀CdN₂S₄: C, 29.37, H, 4.93; N, 6.85; found: C, 29.19; H, 4.77; N, 6.73.

[Cd(pip-dtc)₂], (c) (pip = piperidinyl and dtc = dithiocarbamate), yield: 83%, IR (cm⁻¹; ATR) 3324, ν (O-H); 1480, ν (C=N); 970, ν (C=S); 388, ν (Cd-S). Microanalysis, calc. for C₁₂H₂₀CdN₂S₄: C, 45.40, H, 3.81; N, 5.29; found: C, 45.57; H, 3.61, N, 5.73.

[Cd(eth-xan)₂], (d) (eth = ethyl and xan = xanthato), yield: 96%, IR (cm⁻¹; ATR) 1200, ν (C-O); 1035, ν (C-S); 350, ν (Cd-S). Microanalysis, calc. for C₆H₁₀CdO₂S₄: C, 20.31, H, 2.84; found: C, 20.32; H, 2.67.

2.5 Deposition of CdS thin films by AACVD

In a typical deposition, 0.2 g (0.4 mmol) of the precursor was dissolved in 25 mL of THF in a two-necked 100 mL round-bottom flask with a gas inlet that allowed the carrier gas (argon) to pass into the solution to aid the transport of the aerosol. This flask was connected to the reactor tube by a piece of reinforced tubing. The argon flow rate was controlled by a Platon flow gauge. Seven glass substrates (approx. 1 × 2 cm) were placed inside the reactor tube, in a Carbolite furnace. The precursor solution in a round-bottom flask was kept in a water bath above the piezoelectric modulator of a Pifco ultrasonic humidifier (Model No. 1077). Aerosol droplets of the precursor were transferred into the hot wall zone of the reactor by carrier gas. Both the solvent and the precursor were evaporated and the precursor vapor reached the heated substrate surface where thermally induced reactions and film deposition took place. The

reaction temperature was varied between 400 and 450 °C and the solvent mixture (chloroform/THF) was also used at 450 °C.

3 Results and discussion

3.1 Characterization of piperidinyl dithiocarbamate ligand and the cadmium(II) complexes

The piperidinyl dithiocarbamate ligand, its corresponding cadmium(II) complex and the Cd(II) complexes synthesized from dihexyl/diethyl dithiocarbamates and ethyl xanthate were obtained in good yields. These synthesized products (Fig. 1) were confirmed by IR, microanalysis and TGA. The piperidinyl dithiocarbamate ligand and its complex and the diethyl dithiocarbamate complex were white powders while dihexyl dithiocarbamate and ethyl xanthate complexes were yellow precipitates. The complexes are air and moisture stable at room temperature.

The TGA plots of the complexes are presented in Fig. S1. All the complexes showed a single step decomposition at 320, 334, 340 and 186 °C, displaying a weight loss of 76.2, 62.1, 63.2 and 57.6% (calc: 77.2, 64.7, 66.6 and 59.3%) corresponding to the loss of the organic moiety for dihexyl dithiocarbamate (a), diethyl dithiocarbamate (b), piperidinyl dithiocarbamate (c) and ethyl xanthate (d) complexes, respectively. The final residues of 23.8, 37.9, 36.8 and 42.4% were close to the calculated values of 22.8, 35.3, 33.4 and 40.7% for CdS respectively. Piperidinyl dithiocarbamate cadmium(II) complex was more stable than diethyl dithiocarbamate and dihexyl dithiocarbamate cadmium(II) complexes respectively. The ethyl xanthate cadmium(II) complex was less stable due to the resonance effect resulting from the oxygen being more electronegative than nitrogen.

3.2 Optical properties of CdS thin films

3.2.1 UV-Visible studies of CdS thin films

Clean yellowish and uniform CdS films were obtained when CdS thin films were deposited on a glass substrate. The room temperature UV-Vis absorption spectra of the CdS thin films were recorded in the range of 400–800 nm, using the glass substrate as a reference are shown in Figs. 2i, S2i and S3i. The energy band gaps (E_g) were estimated using the Tauc plots [28] as shown in Figs. 2ii, S2ii and S3ii. The deposited CdS thin films showed variation in the energy band gap with temperature and precursor type. When the dihexyl dithiocarbamate complex (C₆ carbon chain compound) was dissolved in THF and deposited at 400 °C, an absorption band edge at 510 nm was observed (Fig. 2ia), showing a slight blue shift of 5 nm compared to the bulk

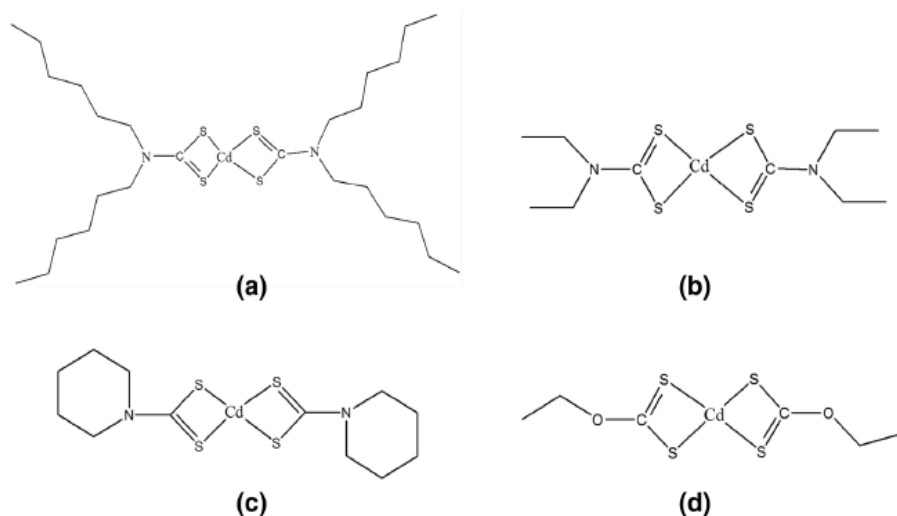


Fig. 1 Proposed structures of complexes **a** cadmium dihexyl dtc, **b** cadmium diethyl dtc, **c** cadmium piperidine dtc and **d** cadmium ethyl xanthate (where *dtc* dithiocarbamate)

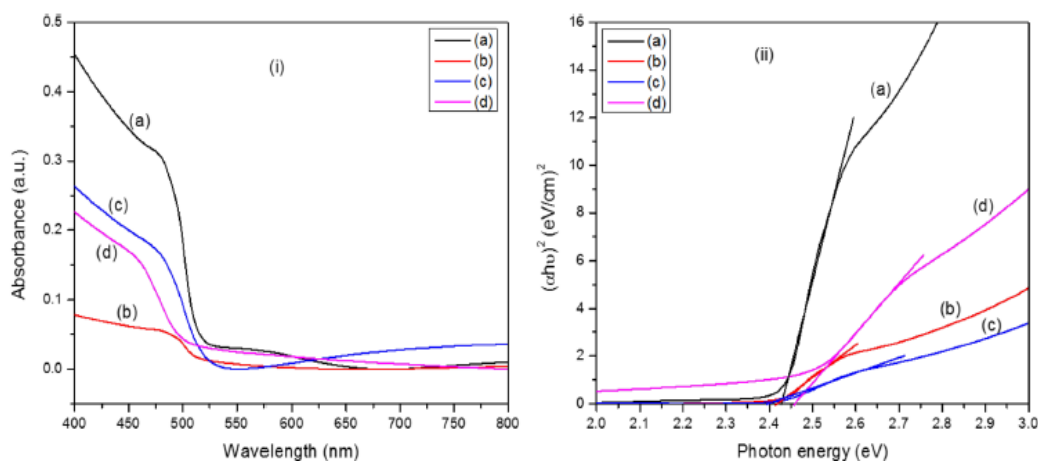


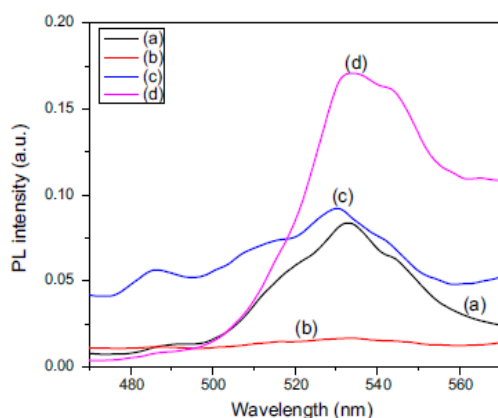
Fig. 2 (Left UV-Vis absorption spectra of CdS films deposited on glass substrate using complexes (a–d) at temperature of 400 °C; right Tauc plot showing the estimated optical band gap)

CdS (515 nm). When the ethyl dithiocarbamate complex (carbon chain of the dithiocarbamate precursor was reduced from C₆ to C₂), a shift to higher wavelength was observed in the absorption band edge (Fig. 2ib). When the heterocyclic piperidiny dithiocarbamate complex (cyclic C₅ carbon chain) was used, a red shift of 8 nm was observed (Fig. 2ic) with the absorption band edge at 523 nm. When the starting material was then changed to the ethyl xanthate complex, an absorption band edge at 508 nm (Fig. 2id) was observed.

When the deposition temperature was increased from 400 to 450 °C (Fig. S2, Table 1), all the absorption spectra were red shifted except for the films obtained from the ethyl xanthate complex. The decrease in the energy band gap (2.41, 2.42, 2.40 and 2.49 eV) of the films, respectively, could be due to the increase of particle size at this temperature [29, 30]. The effect of solvent on the optical properties of the CdS films was investigated at 450 °C by dissolving the precursors in the solvent mixture (THF + chloroform) (ESI Fig.

Table 1 Optical properties of the deposited CdS thin films

Cd(II) complex	Temp (°C)	Solvent	Band edge (nm)	Band gap (eV)	PL max. (nm)
(a)	400	THF	510	2.43	515–560
(b)			515	2.41	520–545
(c)			523	2.37	485
(d)			508	2.44	530–545
(a)	450	THF	515	2.41	489
(b)			520	2.42	490
(c)			518	2.40	486
(d)			498	2.49	520–550
(a)	450	THF + chloroform	523	2.37	500–545
(b)			527	2.35	487
(c)			508	2.44	485
(d)			525	2.36	520–540

**Fig. 3** Photoluminescence emission spectra of CdS thin films deposited at 400 °C using complexes (a–d) ($\lambda_{exc} = 300$ nm)

S3i). It was observed that the CdS films obtained absorbed at higher wavelengths compared to the films which were synthesized in THF alone. This could be attributed to the fact that chloroform is a weaker coordinating solvent compared to THF (Fig. 3; Table 1).

3.2.2 Photoluminescence studies of CdS thin films

The photoluminescence (PL) properties of the deposited CdS thin films using the cadmium complexes were investigated by exciting the films at 300 nm excitation wavelength. The emission spectra are shown in Fig. 3 and ESI Figs. S4 and S5. The deposited CdS films at 400 °C showed broad peaks in the 515–560 nm and 520–545 nm regions when dihexyl dithiocarbamate (a) (Fig. 3a) and diethyl dithiocarbamate (b) (Fig. 3b) complexes respectively were used. A low emission peak at 485 nm blue shifted to the absorption

band edge was however observed when the piperidiny dithiocarbamate complex (c) (Fig. 3c) was used. When the ethyl xanthate complex (d) (Fig. 3d) was used, a broad peak in the 530–545 nm region was observed.

The broad peaks observed between 520 and 570 nm is probably due to electron–hole traps (surface defect emission from sulfur vacancies) [31]. It could also be related to microstructure imperfection and lattice defects of the CdS thin films [32], leading to the red emission. The same observation was made when the temperature was increased to 450 °C, using the mixed solvents (THF + chloroform), (ESI Figs. S4 and S5). The optical properties of the deposited CdS thin films are summarized in Table 1.

3.3 Physical properties of the CdS thin films

3.3.1 XRD studies

p-XRD patterns (Fig. 4 and ESI Figs. S6 and S7) showed deposition of hexagonal phase CdS thin films. The three dominant peaks in the diffraction patterns of the films deposited at 400 and 450 °C (Figs. 4 and S6) can be assigned to the (100), (002), (101) reflections of the pure hexagonal phase and the values matched to those in the ICDD values (card # 01-077-2306). Also, the high intensity of the (002) peak in the p-XRD pattern of CdS thin films is an indication that the particles were preferably elongated along the c-axis [33]. When the mixed solvent (THF + chloroform) was used at 450 °C (Fig. S7), extra peaks were visible and indexed to the hexagonal phase. The presence of the un-indexed peaks in the XRD patterns obtained from complexes (a) and (c) could be attributed to some impurities from the alkyl and heterocyclic carbon chain of the materials. Also, a reduction in the intensity of the (002) peak in p-XRD patterns of all the synthesized samples was observed.

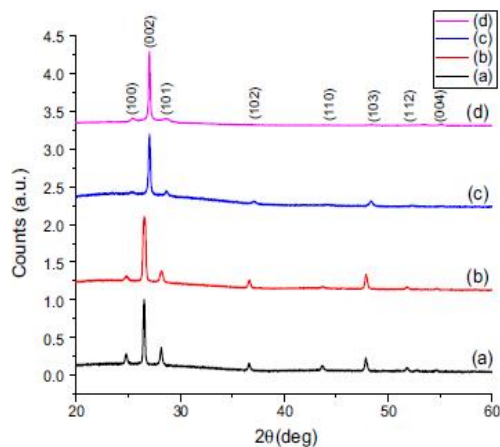


Fig. 4 Powder X-ray patterns of CdS films deposited at 400 °C using complexes (a–d)

3.3.2 Scanning electron microscopy (SEM) studies

The SEM micrographs of the deposited CdS films are shown in Figs. 5, 6 and ESI Fig. S8. The films deposited revealed variability in morphologies when the precursor was varied

from Cd(II) dithiocarbamates to ethyl xanthate at 400 and 450 °C. The surface morphology of CdS films deposited at 400 °C is presented in Fig. 5. When complex (a) (C6 carbon chain) was used, densely packed granular crystallites were formed with particle sizes ranging from 60 to 120 nm (Fig. 5a). Complex (b) (C2 carbon chain), produced loose and well packed with uniform and regular patterns of roughly cubic to spherical shaped particles. A decrease in the particle size (20–32 nm) was observed (Fig. 5b). When complex (c) was used (heterocyclic carbon chain), very compact and hexagonal-like shaped CdS films were deposited with average size of 22–35 nm (Fig. 5c). The ethyl xanthate precursor (d) (C₂ carbon chain) interestingly resulted in the formation of star shaped CdS films (Fig. 5d), with lengths of 33–63 nm and diameters of 12–23 nm. Therefore, the mechanism of the morphology changes can be explained with the increase of alkyl chain length leading to the decrease of the nanomaterial size. This phenomenon was also observed by McNaughton and co-workers [34], where on decomposing lead(II) xanthates with longer alkyl chains, smaller cubic particles were formed in a melt reaction. As the deposition temperature was raised to 450 °C (ESI Fig. S8), morphology and coverage of films significantly changed. All films showed increased coverage of approximately 100%. Complex (a) showed spherical shaped and aggregated grains with ca. 90 nm in size (ESI Fig. S8a). When complex (b) was

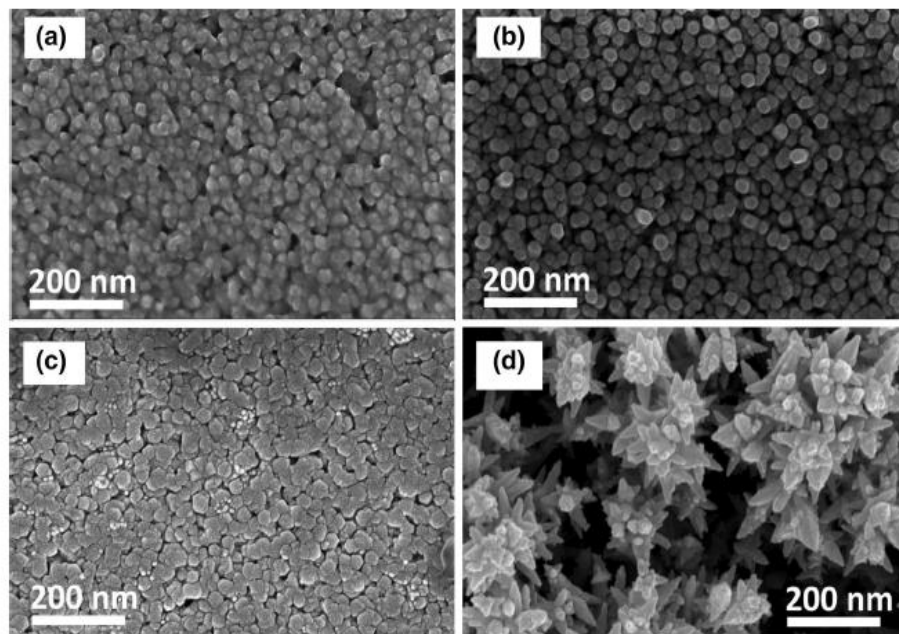


Fig. 5 SEM images of CdS films deposited on glass substrate at 400 °C using complexes (a–d)

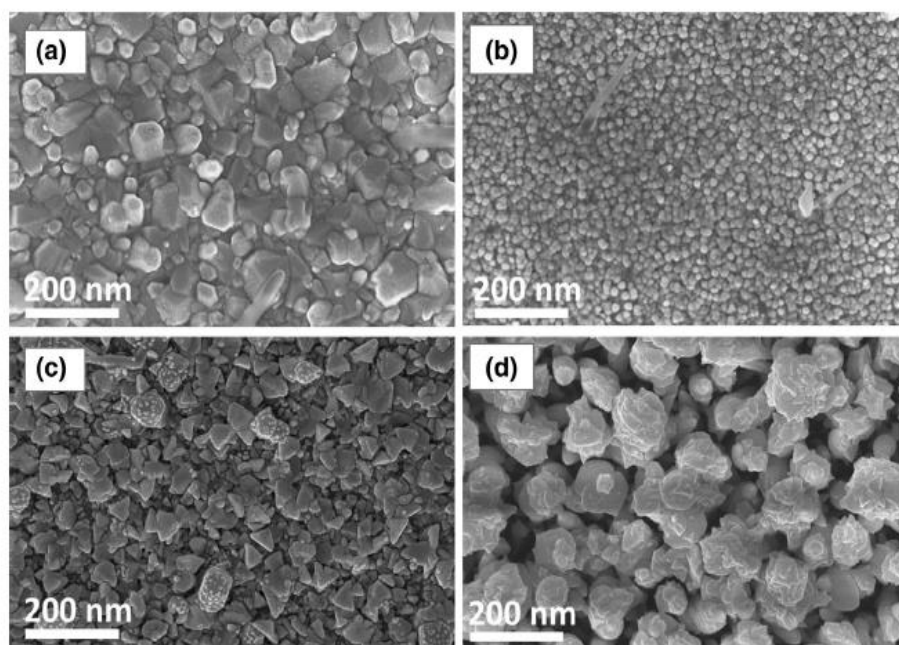


Fig. 6 SEM images of CdS films deposited on glass substrate at 450 °C using mixed solvents (THF + chloroform) using complexes (a–d)

used (ESI Fig. S8b), formation of larger hexagonal granule-shaped crystallites was observed, whereas complex (c) produced irregular flake-like shaped particles with sizes in the range of 104–186 nm (ESI Fig. S8c). A change in precursor from dithiocarbamate to xanthate (d), showed the formation of spike-like shaped particles with sizes ranging from 200 to 245 nm (ESI Fig. S8d).

The effect of solvent on the microstructure of CdS films was also investigated using solvent mixture (THF + chloroform) and representative results obtained at 450 °C are shown in Fig. 6. The CdS thin films deposited using complex (a) showed regular hexagonal-like structures with particle sizes ranging from 140 to 205 nm (Fig. 6a). With complex (b), relatively small, regular spherical shaped with an average particle size of 57–60 nm were obtained (Fig. 6b). Predominantly regular flake-like shaped in the size range of 150–205 nm were formed when complex (c) was used (Fig. 6c). Also, regular rose flower shaped with average particle sizes ranging from 230 to 300 nm were deposited when the xanthate complex (d) was used (Fig. 6d).

Variation in the morphology of the films formed at different temperatures suggests that both the solvent (THF) and temperature (400 and 450 °C) have an effect on the properties of the resulting microstructures. However, the change in the morphology of the films deposited using mixed solvents (THF + chloroform) at 450 °C indicates that chloroform

plays a role in shape directing of the film grown at the surface. It has been reported that at moderate temperature (400 °C), the heterogeneous process is dominant, rendering the precursor molecule to absorb on the substrate surface, and subsequent evaporation, vaporization and decomposition tend to produce high quality films with good adhesive strengths [24] (Fig. 5b, c). With the increase in temperature to 450 °C, the aerosol absorbs more heat in the delivery tube causing solvent evaporation, while vaporization of the precursor molecules starts before absorption on the substrate surface resulting in the deposition of films with distorted structure (ESI Fig. S8b, c).

The role of solvent in the processing of thin film deposition can be discussed on the basis of the heat of combustion and the coordination ability of the solvent used. THF has moderate heat of combustion ($2501.2 \text{ kJ mol}^{-1}$) and a good coordinating ability, favoring heterogeneous nucleation mode at 400 °C while chloroform with much lower heat of combustion ($473.21 \text{ kJ mol}^{-1}$) and very poor coordinating ability compared to THF, evaporates faster causing homogeneous nucleation [24, 35] (growth of porous thin films with irregular texture and poor adhesion to the substrate as seen in Fig. 6a, c, d). The EDX measurements at 20 kV confirmed the stoichiometry of CdS thin films (ratio 1:1) deposited at different temperatures in all the samples. Table 2 shows the atomic percentage of CdS films using each precursor at

Table 2 Elemental analysis by EDX (atomic %) of CdS thin films using each precursor at different deposition temperatures with their average particle size

Cd(II) complex	Temp. (°C)	Solvent	Cd %	S %	Cd/S ratio	Particle size (nm)	Shape
(a)	400	THF	50.4	49.6	1.02	60–120	Granular crystallites
(b)			50.3	49.7	1.01	20–32	Regular spherical granules
(c)			50.6	47.4	1.02	22–35	Hexagonal-like
(d)			50	50	1.00	Length = 33–63 Diameter = 12–23	Star
(a)	450	THF	50.1	49.9	1.00	ca. 90	Spherical
(b)			50.8	49.2	1.03	190–230	Larger hexagonal granule
(c)			53.8	46.2	1.16	104–186	Irregular flake-like
(d)			50.6	49.4	1.02	200–245	Spike-like
(a)	450	THF + chloroform	50.5	49.5	1.02	140–205	Regular hexagonal-like
(b)			51.0	49.0	1.04	ca. 60	Regular spherical
(c)			50.5	49.5	1.02	150–205	Regular flake-like
(d)			51.6	48.4	1.07	230–300	Rose flower

different deposition temperatures with their average particle sizes.

4 Conclusion

CdS thin films have been successfully synthesized by AACVD of cadmium(II) dihexyl dithiocarbamate, diethyl dithiocarbamate, piperidinyl dithiocarbamate and ethyl xanthate as single-source precursors. The optical properties of the deposited CdS films as well as their size and shape were influenced by the nature of the precursor, the temperature of decomposition and the solvent used. The p-XRD and SEM/EDX analyses confirmed the formation of hexagonal CdS thin films, with various well-defined morphologies and precise elemental ratios of CdS films. The deposition temperature, length of the alkyl chain of the precursor and solvent used also affected the morphology of the resulting films.

Acknowledgements The authors thank the Royal Society—Department For International Development (RS–DFID) capacity building initiative and the National Research Foundation (NRF) South Africa through the South African Research Chair Initiative (SARChI) for their financial support. The authors also acknowledge the University of KwaZulu Natal for TEM analyses.

Funding The study was funded by South African Agency for Science and Technology Advancement, DFID.

References

1. Y. Li, X. Li, C. Yang, Y. Li, *J. Mater. Chem.* **13**, 2641 (2003)
2. L.D. Nyamen, N. Revaprasadu, R.V. Pullabhotla, A.A. Nejo, P.T. Ndifon, M.A. Malik, P. O'Brien, *Polyhedron* **56**, 62 (2013)

3. Y. Nicolau, M. Dupuy, M. Brunel, *J. Electrochem. Soc.* **137**, 2915 (1990)
4. M. Nyman, K. Jenkins, M. Hampden-Smith, T. Kodas, E. Duesler, A. Rheingold, M.L. Liable-Sands, *Chem. Mater.* **10**, 914 (1998)
5. M. Wei, K.L. Choy, *Chem. Vap. Depos.* **8**, 15 (2002)
6. H. Afifi, S. Mahmoud, A. Ashour, *Thin Solid Films* **263**, 248 (1995)
7. P. Němec, I. Němec, P. Nahalkova, Y. Němcová, F. Trojaneck, P. Malý, *Thin Solid Films* **403**, 9 (2002)
8. Z. Zang, X. Zeng, J. Du, M. Wang, X. Tang, *Opt. Lett.* **41**, 3463 (2016)
9. D. Barreca, A. Gasparotto, C. Maragno, E. Tondello, C. Sada, *Chem. Vap. Depos.* **10**, 229 (2004)
10. M.B. Hursthouse, M.A. Malik, M. Motevalli, P. O'Brien, *Polyhedron* **11**, 45 (1992)
11. D.M. Frigo, O.F. Khan, P. O'Brien, *J. Cryst. Growth* **96**, 989 (1989)
12. K. Ramasamy, M.A. Malik, P. O'Brien, *J. Raftery, Dalton Trans.* **39**, 1460 (2010)
13. J. Patel, F. Mighri, A. Aji, D. Tiwari, T.K. Chaudhuri, *Appl. Phys. A* **117**, 1791 (2014)
14. O. Vigil-Galán, J. Vidal-Larramendi, A. Escamilla-Esquivel, G. Contreras-Puente, F. Cruz-Gandarilla, G. Arriaga-Mejía, M. Chavarría-Castañeda, M. Tufiño-Velázquez, *Phys. Status Solidi A* **203**, 2018 (2006)
15. E. Albrasi, P.J. Thomas, P. O'Brien, *J. Mater. Chem. C* **1**, 671 (2013)
16. M.A. Malik, M. Afzaal, P. O'Brien, *Chem. Rev.* **110**, 4417 (2010)
17. D. Barreca, A. Gasparotto, C. Maragno, R. Seraglia, E. Tondello, A. Venzo, V. Krishnan, H. Bertagnolli, *Appl. Organomet. Chem.* **19**, 59 (2005)
18. C. Byrom, M. Malik, P. O'Brien, P.A. White, D. Williams, *Polyhedron* **19**, 211 (2000)
19. M.A. Malik, M. Motevalli, T. Saeed, P. O'Brien, *Adv. Mater.* **5**, 653 (1993)
20. D. Barreca, A. Gasparotto, C. Maragno, E. Tondello, *J. Electrochem. Soc.* **151**, 428 (2004)
21. M. Moloto, N. Revaprasadu, P. O'Brien, M. Malik, *J. Mater. Sci. Mater. Electron.* **15**, 313 (2004)
22. C.Q. Nguyen, A. Adeogun, M. Afzaal, M.A. Malik, P. O'Brien, *Chem. Commun.* **20**, 2182 (2006)

23. D. Oyetunde, M. Afzaal, M.A. Vincent, I.H. Hillier, P. O'Brien, *Inorg. Chem.* **50**, 2052 (2011)
24. M.A. Ehsan, H.N. Ming, M. Misran, Z. Arifin, E.R. Tiekink, A.P. Safwan, M. Ebadi, W.J. Basirun, M. Mazhar, *Chem. Vap. Depos.* **18**, 191 (2012)
25. M. Chungaze, M.A. Malik, P. O'Brien, *Adv. Funct. Mater.* **7**, 311 (1997)
26. S. Mlowe, L.D. Nyamen, P.T. Ndifon, M.A. Malik, J. Raftery, P. O'Brien, N. Revaprasadu, *Inorg. Chim. Acta* **434**, 181 (2015)
27. S. Mlowe, D.J. Lewis, M.A. Malik, J. Raftery, E.B. Mubofu, P. O'Brien, N. Revaprasadu, *New J. Chem.* **38**, 6073 (2014)
28. A. Rakhshani, *J. Phys.* **12**, 4391 (2000)
29. L.D. Nyamen, V.S.R. Pullabhotla, A.A. Nejo, P. Ndifon, N. Revaprasadu, *New J. Chem.* **35**, 1133 (2011)
30. G.B. Shombe, E.B. Mubofu, S. Mlowe, N. Revaprasadu, *Mater. Sci. Semicond. Process.* **43**, 230 (2016)
31. J. Dilag, H. Kobus, A.V. Ellis, *Forensic Sci. Int.* **187**, 97 (2009)
32. N. Chestnoy, T.D. Harris, R. Hull, L.E. Brus, *J. Phys. Chem.* **90**, 3393 (1986)
33. P. Yan, Y. Xie, Y. Qian, X. Liu, *Chem. Commun.* **14**, 1293 (1999)
34. P.D. McNaughter, S.A. Saah, M. Akhtar, K. Abdulwahab, M.A. Malik, J. Raftery, J.A.M. Awudza, P. O'Brien, *Dalton Trans.* **45**, 16345 (2016)
35. R. Díaz-Torres, S. Alvarez, *Dalton Trans.* **40**, 10742 (2011)



Tailoring Shape and Crystallographic Phase of Copper Sulfide Nanostructures Using Novel Thiourea Complexes as Single Source Precursors

Kevin I. Y. Ketchemen^{1,2,3} · Malik D. Khan¹ · Sixberth Mlowe¹ · Linda D. Nyamen² · Peter T. Ndifon² · Paul O'Brien^{3,4} · Neerish Revaprasadu¹

Received: 24 September 2018 / Accepted: 20 December 2018
© Springer Science+Business Media, LLC, part of Springer Nature 2019

Abstract

Copper sulfide thin films and nanoparticles have been prepared via aerosol assisted chemical vapour deposition and solvothermal hot injection routes, respectively. Both routes employed heterocyclic amine based benzoylthiourea-copper(II) complexes as single source precursors. Copper sulfide thin films of diverse morphologies ranging from cubic to snowy or irregular crystallites depending on the deposition temperature were observed. Powder X-ray diffraction studies of the as deposited thin films have indicated the formation of hexagonal and cubic phases of copper sulfide. In the case of the nanoparticles, Roxbyite ($\text{Cu}_{1.75}\text{S}$) phase was obtained in dodecanethiol at temperatures of 150, 190 and 230 °C. However, a preferred growth of nanoparticles was observed in the presence of oleylamine whereas the roxbyite phase was obtained at temperatures of 150, 200 and 250 °C. Also transmission electron microscopy showed the formation of close to spherical, hexagonal nano-disk and rod shaped nanoparticles.

Keywords Heterocyclic thiourea · Aerosol assisted chemical vapour deposition · Thermolysis · Copper sulfide · Nanoparticles · Thin films

1 Introduction

Considerable attention has been given to the synthesis of semiconductor nanomaterials due to their unique size dependent, optical and electronic properties. Copper sulfide

is a p-type semiconductor which has found applications in diverse fields such as, photo catalysis [1], solar cells [2], sensors [3], lithium ion batteries [4] and supercapacitors [5]. It has an indirect band gap of ~1.2 eV (for chalcocite) and 1.5 eV (for digenite) [6]. It is found in many stoichiometric compositions ranging from the copper rich phase of chalcocite Cu_2S [7], djurleite $\text{Cu}_{1.96}\text{S}$ [8], digenite $\text{Cu}_{1.8}\text{S}$ [9], anilite $\text{Cu}_{1.75}\text{S}$ [10] to copper poor phase of covellite CuS and villamaninite CuS_2 [11].

Complexes of alkylxanthates [12], thiobiurets [13], thiobenzoates [14], dithiocarbamates [15] and dithiolates [16] have been used to synthesize copper sulfide nanostructures resulting in the formation of spheres [17], triangular nanoplates [18], nanorods [19], nanodiscs [20] and nanowires [21]. Khan and co-workers have prepared copper sulfide nanoparticles with various shapes and super-lattices using the *bis*(O-isobutyldithiocarbonato)copper(II) complex via the hot injection route [22]. Al-Shakban and co-workers, reported the preparation of monodisperse copper sulfide nanorods via the hot injection of novel xanthate copper complexes. They showed that the width of the obtained rods is dependent on the length of the xanthate chain [23].

Electronic supplementary material The online version of this article (<https://doi.org/10.1007/s10904-018-01066-z>) contains supplementary material, which is available to authorized users.

✉ Peter T. Ndifon
pndifon@yahoo.com

✉ Neerish Revaprasadu
RevaprasaduN@unizulu.ac.za

¹ Department of Chemistry, University of Zululand, Private Bag X1001, Kwadlangezwa 3880, South Africa

² Department of Inorganic Chemistry, University of Yaoundé I, P.O. Box 812, Yaoundé, Cameroon

³ School of Chemistry, University of Manchester, Oxford Road, Manchester M13 9PL, UK

⁴ School of Materials, University of Manchester, Oxford Road, Manchester M13 9PL, UK

Similarly, Chen et al. synthesized nanoplates of Cu₂S [24] and nanoflakes of CuS [25] following the thermal decomposition of [Cu(acac)₂] (acac = acetylacetonate) with elemental sulfur in oleylamine. They also synthesized Cu₂S nanoparticles using cysteine as the sulfur source [26]. As a result, thermal decomposition of precursors including [Cu(acac)₂] or CuCl₂ and elemental sulfur or dodecanethiol, revealed hexagonal nanodisks of CuS [27], Cu₇S₄ [20] and Cu₂S [28].

Despite the exhaustive work conducted thus far on the synthesis of copper sulfide nanoparticles, the effect of capping agents on their morphology and phase remains ambiguous and challenging. Similarly, copper sulfide thin films have been synthesized by various methods such as spray pyrolysis [29], successive ionic layer adsorption and reaction [30], chemical bath deposition [31] and chemical vapour deposition [12]. In our earlier studies, we reported the use of metal complexes of dithiocarbamates [32–35], dithiocarbamatoimido diphosphinates [36], dithiocarbamato phosphinates [37] and xanthates [38, 39] as effective starting materials for the deposition of variety of metal chalcogenide thin films or nanomaterials. However, only a few reports have investigated the shape and phase formation of copper sulfide nanostructures using copper(II) thiourea complexes. Following the interest on these class of compounds, our research group has recently reported the use of lead heterocyclic thiourea complexes as single-source precursors for the deposition of PbS thin films [40]. Both bis(*N*-morpholine-*N'*-benzoylthioureato)Pb(II) [C₂₄H₂₆N₄O₄PbS₂] and bis(*N*-pyrrolidine-*N'*-benzoylthioureato)Pb(II) [C₂₄H₂₆N₄O₂PbS₂] complexes were used as precursors to deposit PbS thin films.

In this work, we report the synthesis of *N*-morpholine-*N'*-benzoylthioureatocopper(II) and *N*-pyrrolidine-*N'*-benzoylthioureatocopper(II) complexes and their use in the synthesis of copper sulfide nanoparticles and thin films. The effect of temperature and coordinating solvents, such as, oleylamine and 1-dodecanethiol, on the shape and crystal phase of the as synthesized copper sulfide nanoparticles were examined. The copper sulfide thin films were also deposited using the same precursors by aerosol assisted chemical vapour deposition (AACVD).

2 Experimental Section

2.1 Chemicals

Benzoyl chloride 99%, morpholine 99%, pyrrolidine 99%, potassium thiocyanate 98.5%, copper(II) chloride 97%, dodecanethiol (DT) 98.5%, oleylamine (OLA) 98%, (Sigma-Aldrich), acetone, chloroform, dichloromethane, ethanol and methanol (Merck) were purchased and used without any further purification.

2.2 Instrumentation

Microanalysis was made on a Perkin–Elmer automated analyser, model 2400 series II CHNS/O. The ¹H NMR spectra of the ligands were obtained using a Bruker Advance III 400 MHz spectrophotometer and the spectra are presented in ESI Figs. S1 and S2. Infrared spectra were recorded on a Perkin–Elmer Spectrum Two UATR FT-IR spectrophotometer directly on small samples of the compounds in the 500–4250 cm⁻¹ range. Thermogravimetric analysis was performed at 10 °C min⁻¹ heating rate, using a Perkin Elmer Pyris 6 TGA up to 600 °C in a closed perforated aluminium pan under N₂ gas flow. TEM and HRTEM experiments were done using a JEOL 1400 TEM and JEOL 2100 HRTEM, respectively. The samples were prepared by placing a drop of a dilute solution of nanoparticles on Formvar-coated grids (150 mesh) for TEM, and holey carbon grids for HRTEM. The samples were allowed to dry completely at room temperature and viewed at an accelerating voltage of 100 kV (TEM) and 200 kV (HRTEM), and images captured digitally using a Megaview III camera. The acquired images were further processed using Soft Imaging Systems iTEM software (TEM), and Gatan camera with Gatan software (HRTEM). The surface morphology and structure of the film was determined using a Zeiss Sigma VP-03-67 field emission gun scanning electron microscopy (FEG–SEM), equipped with an Oxford instrument X-max 50 EDX detector. Powder X-ray diffraction (P-XRD) patterns of the nanostructures were recorded at room temperature in the 2θ range (15°–70°) using an Advanced Bruker AXS D8 diffractometer, equipped with nickel-filtered Cu Kα radiation (λ = 1.542 Å) at 40 kV and 40 mA.

2.3 Preparation of the Ligands and Copper Complexes

The ligands were synthesized and characterized following the method reported elsewhere [40]. Copper(II) chloride (0.27 g; 2.0 mmol) was dissolved in 10.0 mL of water and added dropwise to a solution of the corresponding ligand (4.0 mmol) in 50.0 mL of ethanol at room temperature. The resulting mixture was stirred for 30 min and the solid product obtained was filtered off and recrystallized in ethanol:dichloromethane (1:1) mixture.

Bis(*N*-morpholine-*N'*-benzoylthioureato)copper(II) (**1**). Green. Yield: 90%, Anal. Calcd for C₂₄H₂₆N₄O₄CuS₂ (%): C, 51.28; H, 4.66; N, 9.97. Found: C, 51.04; H, 4.64; N, 9.74. IR (cm⁻¹): √(C = N) 1588 (s), √(C = O) 1472 (s).

Bis(*N*-pyrrolidine-*N'*-benzoylthioureato)copper(II) (**2**). Green. Yield: 84%, Anal. Calcd for C₂₄H₂₆N₄O₂CuS₂ (%):

C, 54.37; H, 4.94; N, 10.57. Found: C, 53.89; H, 4.78; N, 10.09. IR (cm^{-1}): $\nu(\text{C}=\text{N})$ 1574 (s), $\nu(\text{C}=\text{O})$ 1473 (s).

2.4 Deposition of Films by AACVD

The films were deposited using a procedure reported previously [41], with slight modifications. Briefly, 0.35 mmol of the precursor [complex (1) or (2)] was dissolved in 25.0 mL of chloroform in a two-necked 100 mL round-bottom flask. A gas inlet was connected to one neck to allow the carrier gas (nitrogen) to pass into the solution to assist the transport of the aerosol. Seven glass substrates (approx. 1×2 cm) were placed inside the reactor tube in a Carbolite furnace, and the reactor tube was connected to the round bottom flask by a piece of reinforced tubing. The nitrogen flow rate was controlled by a Platon flow gauge. The precursor solution in a round-bottom flask was kept in a water bath above the piezoelectric modulator of a Pifco ultrasonic humidifier (Model No. 1077) for generation of the aerosol droplets of the precursor, which were transferred into the hot wall zone of the reactor by the carrier gas. Both the solvent and the precursor were evaporated when the precursor vapour reached the heated substrate surface where thermally induced reactions and film deposition take place. The reaction temperatures were varied between 350 and 450 °C.

2.5 Synthesis of Nanoparticles

2.5.1 Synthesis of OLA Capped Cu_xS_y Nanoparticles

Copper sulfide nanoparticles were synthesized by the thermolysis method, using either OLA or DT as capping agents. Briefly, 5.0 mL of the capping agent (OLA or DT) was placed in a three-necked flask and purged with N_2 , after applying vacuum for few minutes at room temperature, using a Schlenk line to evacuate any air. The capping agent was slowly heated to the desired temperature (150, 200 or 250 °C) and the temperature was maintained for 10 min. A specified amount (0.35 mmol) of the precursors [complex (1) or complex (2)] was dispersed in 3.0 mL of the dispersion solvent (OLA and/or DT) and injected into the pre-heated capping agent. Upon injection, the colourless solution turned brownish, and a drop in temperature of 15–20 °C was observed, the temperature was quickly maintained to desired temperature (i.e. 150, 200 or 250 °C). After a reaction time of 30 min, 30.0 mL of methanol was added, this resulted to the formation of a flocculent precipitate. The precipitate was separated by centrifugation and then dispersed in toluene to obtain dark brownish OLA- or DT-capped Cu_xS_y nanoparticles.

3 Results and Discussion

3.1 Characterization of the Ligands and the Complexes

The prepared compounds (ESI Fig. S3) were obtained as greenish powders. The products were obtained in good yields, and the purity was confirmed by microanalysis. IR studies revealed that the medium peak appearing at 3239 cm^{-1} for HL^1 and 3148 cm^{-1} for HL^2 is attributed to the stretching of the N–H bond adjacent to the carbonyl group. This N–H bond is replaced by a C=N bond upon complexation of the ligand to the metal ion by action of a base. The appearance of one new peak a C=N for each complex in the IR spectra of the complexes is observed at 1588 cm^{-1} and 1574 cm^{-1} respectively for complexes (1) and (2) and attributed to the C=N vibration of the bond. The intense band at 1663 cm^{-1} for HL^1 and 1643 cm^{-1} for HL^2 is attributed to the vibration of the C=O of carbonyl which shifts to lower wavenumbers upon complexation. Deprotonation involves delocalization of C=O stretching vibration which is in agreement with the literature [42, 43], confirming the coordination to the central metal ion through the oxygen atom from the carbonyl.

The TGA plot of complex (1) showed a two-step decomposition pattern, while complex (2) undergoes a single step decomposition (ESI Fig. S4). The first step gave a loss of 72.24% (68.03%, $2\text{MB} = 2\text{morpholinylbenzamide}$) (1) (ESI Fig. S4; step ii) and 70.13% (75.92%, $2\text{PB} + 2\text{CN}$ where $2\text{PB} = 2\text{pyrrolidinylbenzamide}$) (2) (ESI Fig. S4; step iii) at 315 and 327 °C, respectively matching to the loss of the organic moiety. The second decomposition step at 386 °C with mass loss of 9.43% (calc: 9.26%; 2CN , step i) (1) occurred [44]. The final residues of 16.90% (calc. 17.00%) (1) and 20.45% (calc. 18.03%) (2), corresponds closely to the theoretical values of CuS , respectively. The higher experimental residues for (2) can be attributed to the carbon contamination from aryl and heterocyclic groups.

3.2 Copper Sulfide Thin Films

The P-XRD results of the deposited copper sulfide thin films at temperatures between 350 and 450 °C are presented in Figs. 1a and 2a. The diffraction peaks are matched in general, to a mixture of hexagonal Cu_2S (ICDD: 046-1195) and cubic CuS_2 phase (ICDD: 033-0492) in all films deposited at various temperatures from both complexes [13]. The P-XRD patterns of the as deposited films at 350 and 400 °C from complex (1) showed two reflection peaks $(200)^\#$, $(210)^*$ indexed to the cubic and

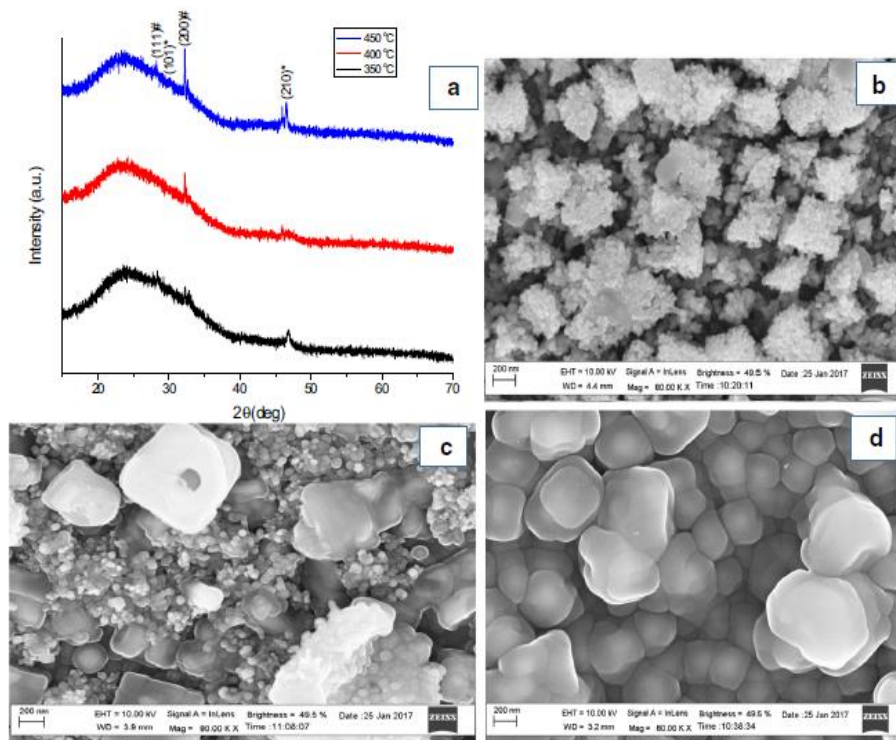


Fig. 1 **a** P-XRD pattern of CuS deposited on glass substrate by AACVD from complex **(1)** (*hexagonal Cu_2S , #cubic CuS) and SEM images of CuS films deposited at deposition temperatures **b** 350 °C, **c** 400 °C and **d** 450 °C

hexagonal phase respectively while at 450 °C two new reflection peaks (111)[#] and (101)^{*} detected are indexed to the cubic and hexagonal phase respectively. On the other hand, when complex **(2)** was used, one prominent reflection peak (200)[#] was observed at 350 °C while at 400 and 450 °C two new reflection peaks (210)^{*} and (101)^{*} appeared. Furthermore, intensity of (200)[#] peak in P-XRD pattern of copper sulfide films showed to increase as a result of temperature increase. No specific peak of any other phase of copper sulfide or impurities was detected. The SEM images of the copper thin films deposited are shown in Figs. 1 and 2. The morphology of thin films prepared at 350 °C from complex **(1)** is mainly composed of small snowy particles forming large cubic clusters (Fig. 1b), with an average size *ca.* 420 nm. Uniform coverage was observed, without the presence of any fissures in the film. EDX analysis (ESI Table S1) showed the deposition of slightly sulfur deficient films Cu:S (50.9:49.1). Films deposited at 400 °C revealed non uniform spherical block like crystallites (Fig. 1c) with sizes *ca.* 460 nm. The size of the crystallites increases considerably and the morphology obtained at this temperature is closely related to

the previously reported copper sulfide thin films using the copper thiobiurete complex [13]. A copper to sulfur ratio of 51.6:48.4 was observed for these thin films by EDX analysis. Deposition of films at a higher temperature of 450 °C shows in the formation of uniform cubic shaped structures with sizes greater than 590 nm (Fig. 1d). The EDX results also showed sulfur deficient thin films with a copper to sulfur ratio of 54.7:45.3. The shape of thin films were observed to be highly reliant on the growth temperature.

The same trend was observed when complex **(2)** was used (Fig. 2), deposition at 350 °C gave films with uniform morphology based on snowy flakes with sizes in the range of 280–320 nm (Fig. 2b). The morphology changed forming large cubic clusters with some irregular spherical particles at 400 °C (Fig. 2c). Although the films deposited at 450 °C showed large, irregular spherical particles (Fig. 2d). EDX analysis revealed sulfur deficient thin films at all temperatures. A uniform distribution of copper and sulfur was indicated by EDX analysis, as almost same percentages of copper to sulfur were observed at different regions of the thin films. The increase in crystallite size

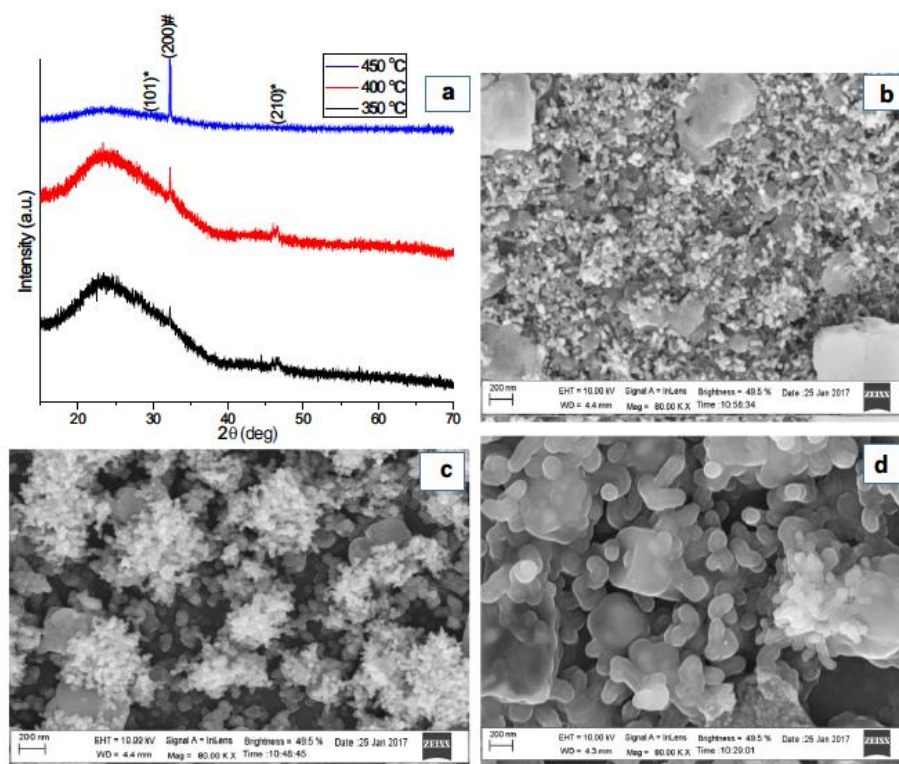


Fig. 2 a P-XRD pattern of CuS deposited on glass substrate by AACVD from complex (2) (*hexagonal Cu_2S , #cubic CuS_2) and SEM images of CuS films deposited at deposition temperatures b 350 °C, c 400 °C and d 450 °C

is due to inter-particle aggregation, as a function of temperature. The decomposition of the precursor and thermal diffusion of the particles at the substrate surface is directly related to the temperature. The higher incident flux can cause a shadowing effect during growth process. The particles will tend to form aggregates by combining with particles, present near the impact point. Similarly, the adatom

layer may behave as a template for incoming molecular flux at higher temperature and results in the accelerating of the growth of crystallites to larger particles. However, the specific growth mechanism by CVD method is fairly complex and may embrace some other factors [12]. The summary of phases, morphology and average crystallite sizes of copper sulfide films are presented in Table 1.

Table 1 Phases and morphology of copper sulfide thin films obtained

Deposited thin films by AACVD				
Complex	Deposition temp (°C)	Phase (formula)	Morphology	Average crystallite size (nm)
(1)	350	Mixture of hexagonal (Cu_2S) and cubic(CuS_2)	Large cubic clusters	420
	400		Spherical to cubic	460
	450		Cubic	590
(2)	350	Mixture of hexagonal (Cu_2S) and cubic(CuS_2)	Snowy flake-like	310
	400		Spherical crystallites	470
	450		Spherical crystallites	580

3.3 Copper Sulfide Nanoparticles

3.3.1 OLA as Dispersion Solvent in OLA

Oleylamine (OLA) has a dual role in being an effective coordinating solvent, and also is known to help in the decomposition of the variety of molecular complexes [45–48]. When the complex was dispersed in OLA, the color of the

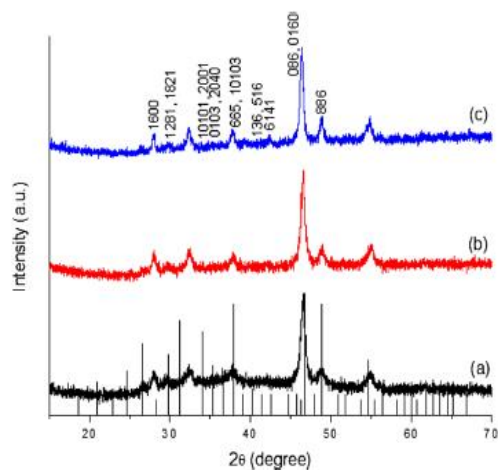


Fig. 3 P-XRD of nanoparticles prepared from complex (1) in OLA at (a) 150 °C, (b) 200 °C and (c) 250 °C when OLA is used both as dispersion solvent and capping agent

complex starts changing from green to greenish brown, which may indicate the interaction of OLA with complexes and its decomposition. The diffraction peaks of the nanoparticles prepared from complex (1) (Fig. 3) are indexed to the Roxbyite phase (ICDD #00-023-0958) with no presence of any other phase as an impurity. As such the peak width broadness is in accordance with the small size of the nanospheres. The intensity of the peaks increases slightly with increasing temperature. However, the peak present at the 2θ value of 46.5° was the most intense at all temperatures, which may indicate a preferred orientation along that plane. The same phase was observed when complex (2) was used and the P-XRD results show that at low temperatures (150 and 200 °C), intense peaks were observed (ESI Fig. S5a, b), whereas at 250 °C a decrease in the intensity of the peaks was observed (ESI Fig. S5c).

TEM images shown in Fig. 4 revealed that the as-synthesized nanoparticles from complex (1) at 150 °C (Fig. 4a) have seemingly spherical morphology. When the temperature was raised to 200 °C, an increase of the average size of the particles and agglomeration (Fig. 4b) occurred. When the reaction was carried out at 250 °C the size further increased with a broader size distribution, some elongated particles also start to appear (Fig. 4c) due to interparticle aggregation. The diffraction rings in the selected area electron diffraction (SAED) patterns from complexes (1) and (2) at 250 °C (Fig. 4d, h) confirms the formation of crystalline copper sulfide nanoparticles composed of polycrystalline copper sulfide nanoparticles. Similarly, the same trend was also observed when complex (2) was used. At 150 °C

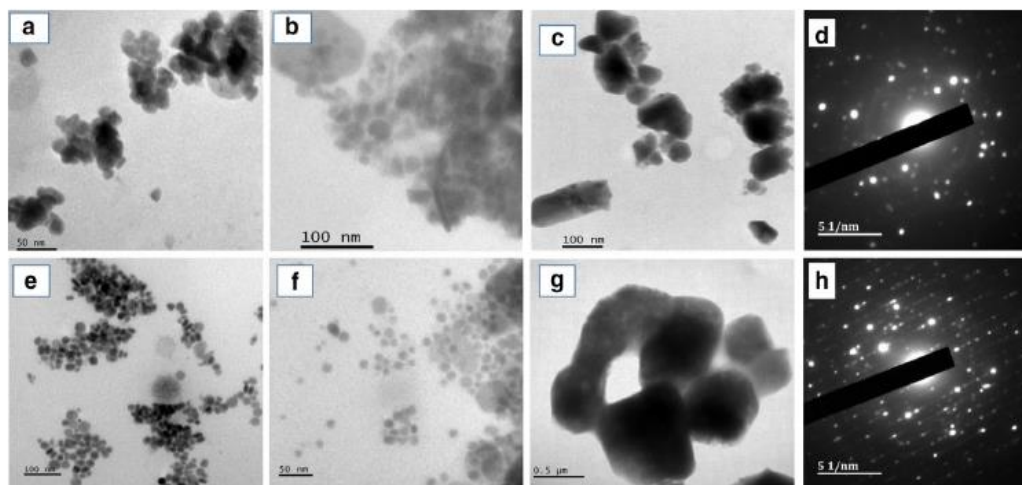


Fig. 4 TEM images of copper sulfide nanoparticles prepared at a, e 150 °C, b, f 200 °C and c, g 250 °C, from complexes (1) and (2) respectively when OLA is used both as dispersion solvent and cap-

ping agent; d and h showing the SAED patterns of nanoparticles prepared at 250 °C from complexes (1) and (2) respectively

(Fig. 4e) agglomerated spherically shaped nanoparticles were obtained. While at 200 °C (Fig. 4f) uniform spherical nanoparticles were observed and when the temperature was raised to 250 °C (Fig. 4g) non uniform cubic shaped nanoparticles were formed. As a result, the morphology of the particles obtained at a comparatively lower temperature is somewhat more uniform compared to the morphology of particles at higher temperature. Therefore, the rate of the reaction is significantly affected with increase in temperature and higher rate of precursor decomposition provides higher monomer concentration. The increase in monomer

concentration leads to enhanced nucleation and growth of the nanoparticles [12].

3.3.2 OLA as Dispersion Solvent in DT

In an attempt to investigate the effect of capping agent, we replaced OLA by a comparatively weak coordinating solvent (DT). The solution was then directly injected into DT at the wanted growth temperatures (150–230 °C). The diffraction pattern of the nanocrystallites synthesized from complex (1) is presented in Fig. 5. Since copper sulfide has various possible crystallographic phases having almost the same stoichiometry, it is difficult to assign the peaks. However, the P-XRD results revealed that the most prominent reflection peaks match well with the pure $\text{Cu}_{1.75}\text{S}$ Roxbyite phase (ICDD #00-023-0958), although some few minor intensity peaks confirm the presence of the Anilite phase as an impurity. The intensity of the peaks increases slightly with increasing temperature. A similar trend is observed for complex (2) (ESI Fig. S6a, b). At low temperatures (150 and 190 °C) the XRD patterns are broad but at 250 °C the Roxbyite phase is more pronounced. Nevertheless, a negligible impurity of the Anilite phase also appears at higher temperature (ESI Fig. S6c).

Nearly uniform monodispersed spherical CuS nanoparticles were obtained from complex (1) synthesized at reaction 150 and 190 °C (Fig. 6a, b). As the temperature was elevated to 190 °C, an increase in the size of the particles was observed considerably, but the morphology remained spherical (Fig. 6b). Mixed morphology was obtained at higher temperature of 230 °C, and some rod-like particles were also formed along with the spherical particles (Fig. 6c, d). The change in growth kinetics of the different planes can lead to the formation of elongated or rod-like particles. The OLA may acts as a strong base to deprotonate the

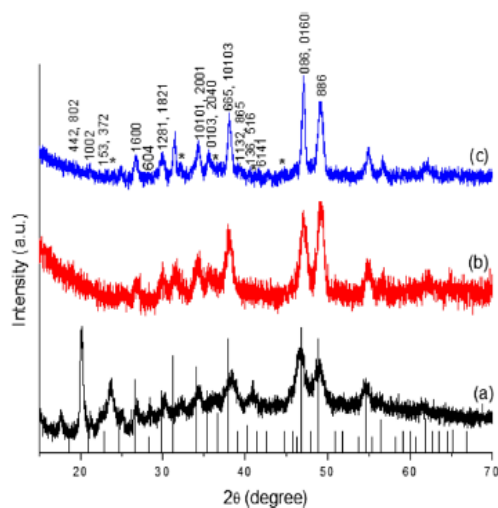


Fig. 5 P-XRD of nanoparticles obtained from complex (1) at (a) 150 °C, (b) 190 °C and (c) 230 °C when OLA is used as dispersion solvent in DT. The (*) represents the presence of Anilite phase (ICDD: 00-033-0489)

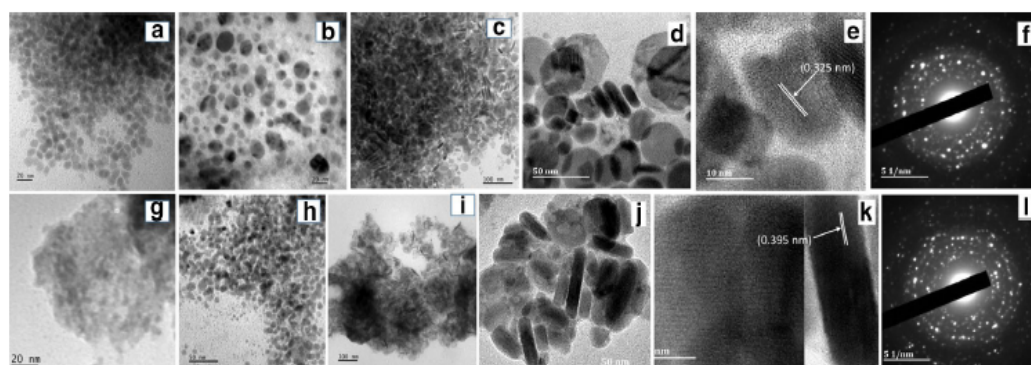


Fig. 6 TEM images of nanoparticles prepared at **a, g** 150 °C, **b, h** 190 °C and **c, d, i, j** 230 °C, from complexes (1) and (2) respectively when OLA is used as dispersion solvent in DT. HRTEM images **e,**

k at 230 °C from complexes (1) and (2); **f, l** showing the SAED patterns of nanoparticles prepared at 230 °C from complexes (1) and (2) respectively

thiol, creating an ionic environment, which probably caused limited growth of some of the planes and eventually leads to the formation of nanorods. Likewise a similar finding was observed when complex (2) was used as the precursor (Fig. 6g–j). The HRTEM images of the samples prepared at 230 °C are shown in (Fig. 6e, k) from precursors (1) and (2) respectively. The lattice fringes indicate the highly crystalline nature of the nanoparticles. The d-spacings measured from the lattice fringes of the different crystallites correspond approximately to the roxbyite $\text{Cu}_{1.75}\text{S}$ phase. For example d-spacing of 3.25 Å from complex (1) (Fig. 6e) can be indexed to (1600) plane whereas d-spacing of 3.95 Å from complex (2) (Fig. 6k) can be indexed to (1002) plane of roxbyite phase. The SAED patterns (Fig. 6f, l) contain information from a large number of nanoparticles and the polycrystalline diffraction rings can be indexed to the Roxbyite $\text{Cu}_{1.75}\text{S}$ phase within measurement errors.

3.3.3 DT as Dispersion Solvent in DT

The effect of DT was observed by using DT alone as a capping agent and dispersion medium, while keeping all the other parameters constant. The P-XRD patterns showed that, nanoparticles with the Roxbyite ($\text{Cu}_{1.75}\text{S}$) phase (ICDD #00-023-0958) were obtained, when both precursors were decomposed at different temperatures (150, 190 and 230 °C). It was also noticed that, the intensity of the peaks increases significantly with the increase of the temperature for both complexes. However, the Roxbyite phase is more prominent for nanoparticles prepared from complex (1) (Fig. 7) than from complex (2) (ESI Fig. S7).

TEM images (Fig. 8) showed that the synthesized nanoparticles from complex (1) at 150 °C are fairly mono-dispersed with uniform spherical morphology (Fig. 8a). The size of the particles increased faintly with change in temperature to 190 °C (Fig. 8b). When the reaction was carried out at 230 °C the size was further increased, leading to the formation of poly-dispersed spherical particles (Fig. 8c). When complex (2) was used, the same trend was observed except at 190 °C, where the spherical nanoparticles became faceted in six equivalent directions resulting in hexagonal nano-disks (Fig. 8e). The HRTEM image (Fig. 8f) for the sample prepared from complex (2) at 190 °C shows plane or standing hexagonal nanodisks. The fine determined lattice fringes indicate the highly crystalline nature of the nanocrystals. The d-spacing determined from the lattice fringes of the different crystallites match to the roxbyite $\text{Cu}_{1.75}\text{S}$ phase. For instance, spacing of 3.75 Å (Fig. 8f) can be indexed to (153, 372) plane of roxbyite phase. The SAED pattern (Fig. 8g) contains information from a large number of nanoparticles and the polycrystalline diffraction rings can be matched to the roxbyite $\text{Cu}_{1.75}\text{S}$ phase within measurement errors. Better capping

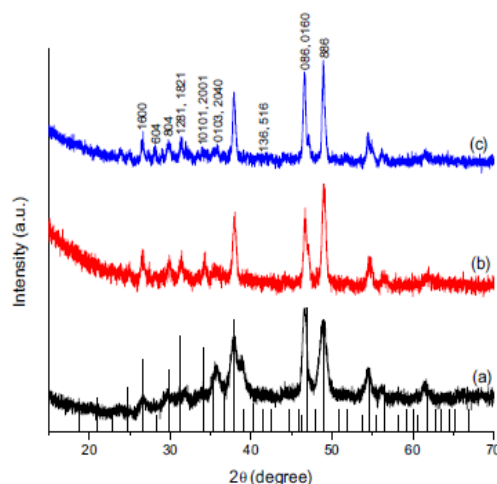


Fig. 7 P-XRD pattern of $\text{Cu}_{1.75}\text{S}$ nanoparticles obtained from complex (1) at (a) 150 °C (b) 190 °C and (c) 230 °C when DT is used both as dispersion solvent and capping agent

of the nanoparticles can be achieved at lower temperature, as the higher temperature decreases the tendency of ligands for effective capping. The summary of the phases, morphology and average size of copper sulfide nanoparticles are presented in Table 2.

4 Conclusion

Copper sulfide thin films have been deposited on glass substrates from *N*-morpholine and *N*-pyrrolidine-*N'*-benzoylthiourea-copper(II) complexes following the AACVD method. The morphology of the films significantly depends on deposition temperature. Nanoparticles of copper sulfide were synthesized by hot injection method using mixed solvent systems i.e. OLA, OLA/DT mixture and DT. The morphology and the specific orientation of the nanoparticles were highly influenced by the solvent system and temperature of the reaction. It was further noticed that the solvent used as capping agent can change the kinetics of decomposition of the complexes leading to different orientation and/or morphology of the nanoparticles. Likewise, the phase of copper sulfide also depends on the method used to prepare it while using the same precursor, i.e. mixed cubic and hexagonal phases was obtained by AACVD whereas roxbyite was obtained by colloidal thermolysis. We intend to investigate the physical properties of these nanomaterials with diverse morphologies in order to explore the influence on electrical and optical properties.

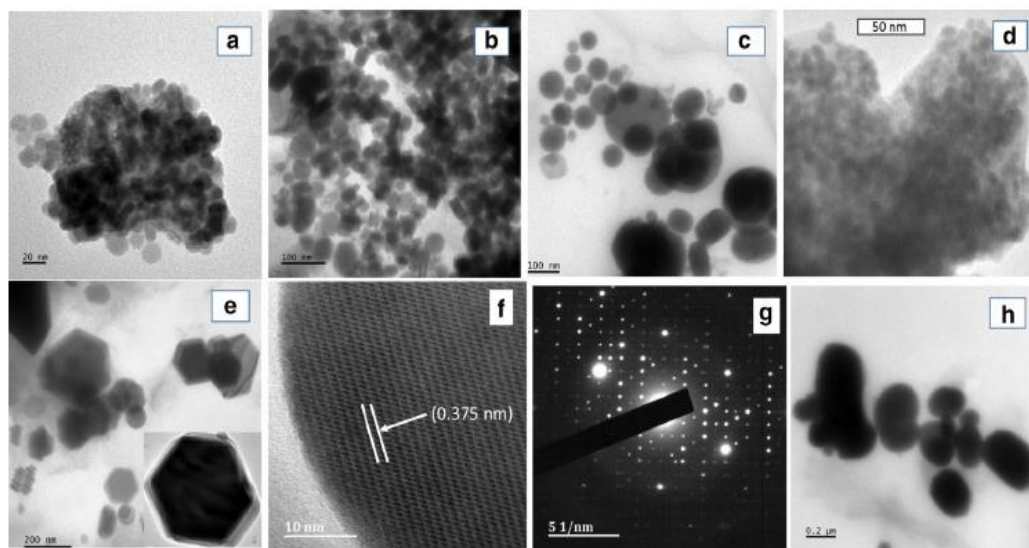


Fig. 8 TEM images of nanoparticles prepared at **a, d** 150 °C, **b, e** 190 °C and **c, h** 230 °C, from complexes (1) and (2) respectively when DT is used both as dispersion solvent and capping agent.

HRTEM image (inset **f**) at 190 °C from complex (2). Inset **g** showing the SAED pattern of nanoparticles prepared at 190 °C from complex (2)

Table 2 Phases and morphology of copper sulfide nanoparticles

Nanoparticles prepared by the hot injection method						
Complex	Dispersion medium	Capping agent	Reaction temp (°C)	Phase (formula)	Morphology	Average size (nm)
(1)	OLA	OLA	150	Roxbyite (Cu _{1.75} S)	Spherical	13
			200		Spherical	16
			250		spherical	50
	OLA	DT	150	Roxbyite (Cu _{1.75} S)	Spherical	7
			190		Spherical	12
			230		Nanorods	Length: 30, width: 7
DT	DT	150	Roxbyite (Cu _{1.75} S)	Spherical	12	
		190		Spherical	31	
		230		spherical	53	
(2)	OLA	OLA	150	Roxbyite (Cu _{1.75} S)	Nanorods	Length: 14, width: 7
			200		Spherical	15
			250		Spherical	62
	OLA	DT	150	Roxbyite (Cu _{1.75} S)	Spherical	3
			190		Spherical	8
			230		Nanorods	Length: 51, width: 9
	DT	DT	150	Roxbyite (Cu _{1.75} S)	Spherical	6
			190		Nanodisks	86
			230		Spherical	189

Acknowledgements The authors thank the Royal Society/Department for International Development (RS-DFID) Africa Capacity Building Initiative programme and the National Research Foundation (NRF) South Africa through the South African Research Chair Initiative (SARChI) for their financial support. The authors also acknowledge the University of Kwa-Zulu Natal for TEM analyses.

References

1. B. Srinivas, B.G. Kumar, K. Muralidharan, Stabilizer free copper sulphide nanostructures for rapid photocatalytic decomposition of rhodamine B. *J. Mol. Catal. Chem.* **410**, 8–18 (2015)

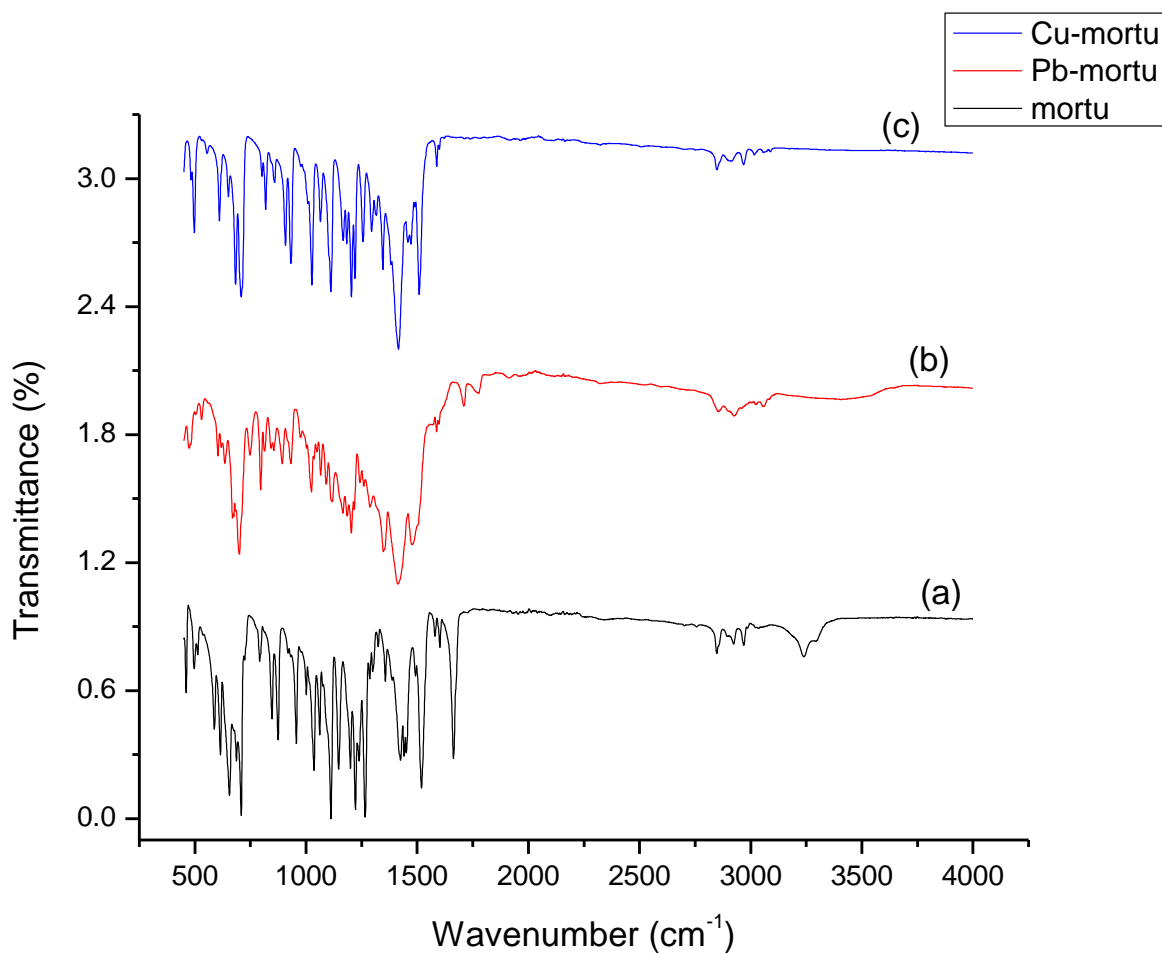
2. H. Lei, P. Qin, W. Ke, Y. Guo, X. Dai, Z. Chen et al., Performance enhancement of polymer solar cells with high work function CuS modified ITO as anodes. *Org. Electron.* **22**, 173–179 (2015)
3. A.A. Sagade, R. Sharma, Copper sulphide (Cu₂S) as an ammonia gas sensor working at room temperature. *Sens. Actuators B* **133**, 135–143 (2008)
4. M. Zhou, N. Peng, Z. Liu, Y. Xi, H. He, Y. Xia, Z. Liu, S. Okada, Synthesis of sub-10 nm copper sulfide rods as high-performance anode for long-cycle life Li-ion batteries. *J. Power Sources* **306**, 408–412 (2016)
5. Y.-K. Hsu, Y.-C. Chen, Y.-G. Lin, Synthesis of copper sulfide nanowire arrays for high-performance supercapacitors. *Electrochim. Acta* **139**, 401–407 (2014)
6. B. Mulder, Optical properties of crystals of cuprous sulphides (chalcocite, djurleite, Cu₁₁9S, and digenite. *Phys. Status Solidi A* **13**, 79–88 (1972)
7. Y. Wu, C. Wadia, W. Ma, B. Sadler, A.P. Alivisatos, Synthesis and photovoltaic application of copper(I) sulfide nanocrystals. *Nano Lett.* **8**, 2551–2555 (2008)
8. M. Lotfi-pour, T. Machani, D.P. Rossi, K.E. Plass, α -Chalcocite nanoparticle synthesis and stability. *Chem. Mater.* **23**, 3032–3038 (2011)
9. Q. Tian, F. Jiang, R. Zou, Q. Liu, Z. Chen, M. Zhu et al., Hydrophilic Cu₂S nanocrystals: a photothermal agent with a 25.7% heat conversion efficiency for photothermal ablation of cancer cells in vivo. *ACS Nano* **5**, 9761–9771 (2011)
10. G. Song, L. Han, W. Zou, Z. Xiao, X. Huang, Z. Qin et al., A novel photothermal nanocrystals of Cu₂S₄ hollow structure for efficient ablation of cancer cells. *Nano-Micro Lett.* **6**, 169–177 (2014)
11. Y. Takano, N. Uchiyama, S. Ogawa, N. Mōri, Y. Kimishima, S. Arisawa et al., Superconducting properties of CuS_{2-x}Se_x under high pressure. *Physica C* **341**, 739–740 (2000)
12. M.D. Khan, M.A. Malik, J. Akhtar, S. Mlowe, N. Revaprasadu, Phase pure deposition of flower-like thin films by aerosol assisted chemical vapor deposition and solvent mediated structural transformation in copper sulfide nanostructures. *Thin Solid Films* **638**, 338–344 (2017)
13. A.L. Abdelhady, K. Ramasamy, M.A. Malik, P. O'Brien, S.J. Haigh, J. Raftery, New routes to copper sulfide nanostructures and thin films. *J. Mater. Chem.* **21**, 17888–17895 (2011)
14. W.P. Lim, C.T. Wong, S.L. Ang, H.Y. Low, W.S. Chin, Phase-selective synthesis of copper sulfide nanocrystals. *Chem. Mater.* **18**, 6170–6177 (2006)
15. M.D. Khan, M. Akhtar, M.A. Malik, N. Revaprasadu, P. O'Brien, New examples of phase control in the preparation of copper sulfide nanoparticles and deposition of thin films by AACVD from bis (piperidinedithiocarbamate) copper(II) complex. *ChemistrySelect* **3**, 2943–2950 (2018)
16. X.-S. Du, Z.-Z. Yu, A. Dasari, J. Ma, Y.-Z. Meng, Y.-W. Mai, Facile synthesis and assembly of Cu₂S nanodisks to corncoblike nanostructures. *Chem. Mater.* **18**, 5156–5158 (2006)
17. S. Li, H. Wang, W. Xu, H. Si, X. Tao, S. Lou et al., Synthesis and assembly of monodisperse spherical Cu₂S nanocrystals. *J. Colloid Interface Sci.* **330**, 483–487 (2009)
18. W. Lou, M. Chen, X. Wang, W. Liu, Size control of monodisperse copper sulfide faceted nanocrystals and triangular nanoplates. *J. Phys. Chem. C* **111**, 9658–9663 (2007)
19. J.M. Luther, H. Zheng, B. Sadler, A.P. Alivisatos, Synthesis of PbS nanorods and other ionic nanocrystals of complex morphology by sequential cation exchange reactions. *J. Am. Chem. Soc.* **131**, 16851–16857 (2009)
20. Y. Wang, Y. Hu, Q. Zhang, J. Ge, Z. Lu, Y. Hou et al., One-pot synthesis and optical property of copper(I) sulfide nanodisks. *Inorg. Chem.* **49**, 6601–6608 (2010)
21. L. Chen, Y.-B. Chen, L.-M. Wu, Synthesis of uniform Cu₂S nanowires from copper – thiolate polymer precursors by a solventless thermolytic method. *J. Am. Chem. Soc.* **126**, 16334–16335 (2004)
22. M.D. Khan, J. Akhtar, M.A. Malik, N. Revaprasadu, Tuning the phase and shape of copper sulfide nanostructures using mixed solvent systems. *ChemistrySelect* **1**, 5982–5989 (2016)
23. M. Al-Shakban, P.D. Matthews, G. Deogratias, P.D. McNaughten, J. Raftery, I. Vitorica-Yrezabal et al., Novel xanthate complexes for the size-controlled synthesis of copper sulfide nanorods. *Inorg. Chem.* **56**, 9247–9254 (2017)
24. H.-T. Zhang, G. Wu, X.-H. Chen, Large-scale synthesis and self-assembly of monodisperse hexagon Cu₂S nanoplates. *Langmuir* **21**, 4281–4282 (2005)
25. H. Zhang, G. Wu, X. Chen, Controlled synthesis and characterization of covellite (CuS) nanoflakes. *Mater. Chem. Phys.* **98**, 298–303 (2006)
26. I. Jen-La Plante, T.W. Zeid, P. Yang, T. Mokari, Synthesis of metal sulfide nanomaterials via thermal decomposition of single-source precursors. *J. Mater. Chem.* **20**, 6612–6617 (2010)
27. A. Ghezelbash, B.A. Korgel, Nickel sulfide and copper sulfide nanocrystal synthesis and polymorphism. *Langmuir* **21**, 9451–9456 (2005)
28. A. Tang, S. Qu, K. Li, Y. Hou, F. Teng, J. Cao et al., One-pot synthesis and self-assembly of colloidal copper(I) sulfide nanocrystals. *Nanotechnology* **21**, 285602 (2010)
29. S.-Y. Wang, W. Wang, Z.-H. Lu, Asynchronous-pulse ultrasonic spray pyrolysis deposition of Cu_xS (x = 1, 2) thin films. *Mater. Sci. Eng. B* **103**, 184–188 (2003)
30. S. Sartale, C. Lokhande, Growth of copper sulphide thin films by successive ionic layer adsorption and reaction (SILAR) method. *Mater. Chem. Phys.* **65**, 63–67 (2000)
31. H. Hu, P. Nair, Electrical and optical properties of poly (methyl methacrylate) sheets coated with chemically deposited CuS thin films. *Surf. Coat. Technol.* **81**, 183–189 (1996)
32. A.A. Memon, M. Dilshad, N. Revaprasadu, M.A. Malik, J. Raftery, J. Akhtar, Deposition of cadmium sulfide and zinc sulfide thin films by aerosol-assisted chemical vapors from molecular precursors. *Turk. J. Chem.* **39**, 169–178 (2015)
33. T. Trindade, P. O'Brien, Synthesis of CdS and CdSe nanoparticles by thermolysis of diethyldithio- or diethyldiseleno-carbamates of cadmium. *J. Mater. Chem.* **6**, 343–347 (1996)
34. N. Moloto, N. Revaprasadu, M. Moloto, P. O'Brien, M. Helliwell, N. N'-Diisopropyl- and N, N'-dicyclohexylthiourea cadmium(II) complexes as precursors for the synthesis of CdS nanoparticles. *Polyhedron* **26**, 3947–3955 (2007)
35. M. Lazell, S.J. Nørager, P. O'Brien, N. Revaprasadu, The use of dithio- and diselenocarbamates as precursors to nanoscale materials. *Mater. Sci. Eng. C* **16**, 129–133 (2001)
36. M. Afzaal, D. Crouch, M.A. Malik, M. Motevalli, P. O'Brien, J.H. Park et al., Deposition of II-VI thin films by LP-MOCVD using novel single-source precursors. *Eur. J. Inorg. Chem.* **2004**, 171–177 (2004)
37. C.Q. Nguyen, A. Adeogun, M. Afzaal, M.A. Malik, P. O'Brien, Facile and reproducible syntheses of bis (dialkylselenophosphanyl)-selenides and diselenides: X-ray structures of (i Pr₂PSe)₂Se, (i Pr₂PSe)₂Se₂ and (Ph₂PSe)₂Se. *Chem. Commun.* **20**, 2179–2181 (2006)
38. T. Alqahtani, M.D. Khan, D.J. Kelly, S.J. Haigh, D.J. Lewis, P. O'Brien, Synthesis of Bi_{1-2x}Sb_{2x}S₃ (0 ≤ x ≤ 1) solid solutions from solventless thermolysis of metal xanthate precursors. *J. Mater. Chem. C* **6**, 12652–12659 (2018)
39. M.D. Khan, G. Murtaza, N. Revaprasadu, P. O'Brien, Synthesis of chalcopyrite-type and thiospinel minerals/materials by low temperature melts of xanthates. *Dalton Trans.* **47**, 8870–8873 (2018)
40. K.I. Ketchemen, S. Mlowe, L.D. Nyamen, A.A. Aboud, M.P. Akerman, P.T. Ndifon et al., Heterocyclic lead(II) thioureato complexes as single-source precursors for the aerosol assisted

- chemical vapour deposition of PbS thin films. *Inorg. Chim. Acta* **479**, 42–48 (2018)
41. M.D. Khan, S. Hameed, N. Haider, A. Afzal, M.C. Sportelli, N. Cioffi et al., Deposition of morphology-tailored PbS thin films by surfactant-enhanced aerosol assisted chemical vapor deposition. *Mater. Sci. Semicond. Process.* **46**, 39–45 (2016)
 42. H. Arslan, N. Külcü, U. Flörke, Synthesis and characterization of copper(II), nickel(II) and cobalt(II) complexes with novel thiourea derivatives. *Transit. Met. Chem.* **28**, 816–819 (2003)
 43. M. Mikami, I. Nakagawa, T. Shimanouchi, Far infra-red spectra and metal—ligand force constants of acetylacetonates of transition metals. *Spectrochim. Acta A* **23**, 1037–1053 (1967)
 44. M. Merdivan, F. Karipcin, N. Kulcu, R. Aygun, Study of the thermal decompositions on *N, N*-dialkyl-*N'*-benzoylthiourea complexes of Cu(II), Ni(II), Pd(II), Pt(II), Cd(II), Ru(III) and Fe(III). *J. Ther. Anal. Calorim.* **58**, 551–557 (1999)
 45. N. Mntungwa, M. Khan, S. Mlowe, N. Revaprasadu, A simple route to alkylamine capped antimony nanoparticles. *Mater. Lett.* **145**, 239–242 (2015)
 46. M.D. Khan, J. Akhtar, M.A. Malik, M. Akhtar, N. Revaprasadu, Phase-pure fabrication and shape evolution studies of SnS nanosheets. *New J. Chem.* **39**, 9569–9574 (2015)
 47. M.D. Khan, M. Aamir, M. Sohail, M. Sher, J. Akhtar, M.A. Malik et al., Novel single source precursor for synthesis of Sb₂Se₃ nanorods and deposition of thin films by AACVD: photo-electrochemical study for water reduction catalysis. *Sol. Energy* **169**, 526–534 (2018)
 48. M.D. Khan, M. Aamir, G. Murtaza, M.A. Malik, N. Revaprasadu, Structural investigations of SnS_{1-x}Se_x solid solution synthesized from chalcogeno-carboxylate complexes of organo-tin by colloidal and solvent-less routes. *Dalton Trans.* **47**, 10025–10034 (2018)

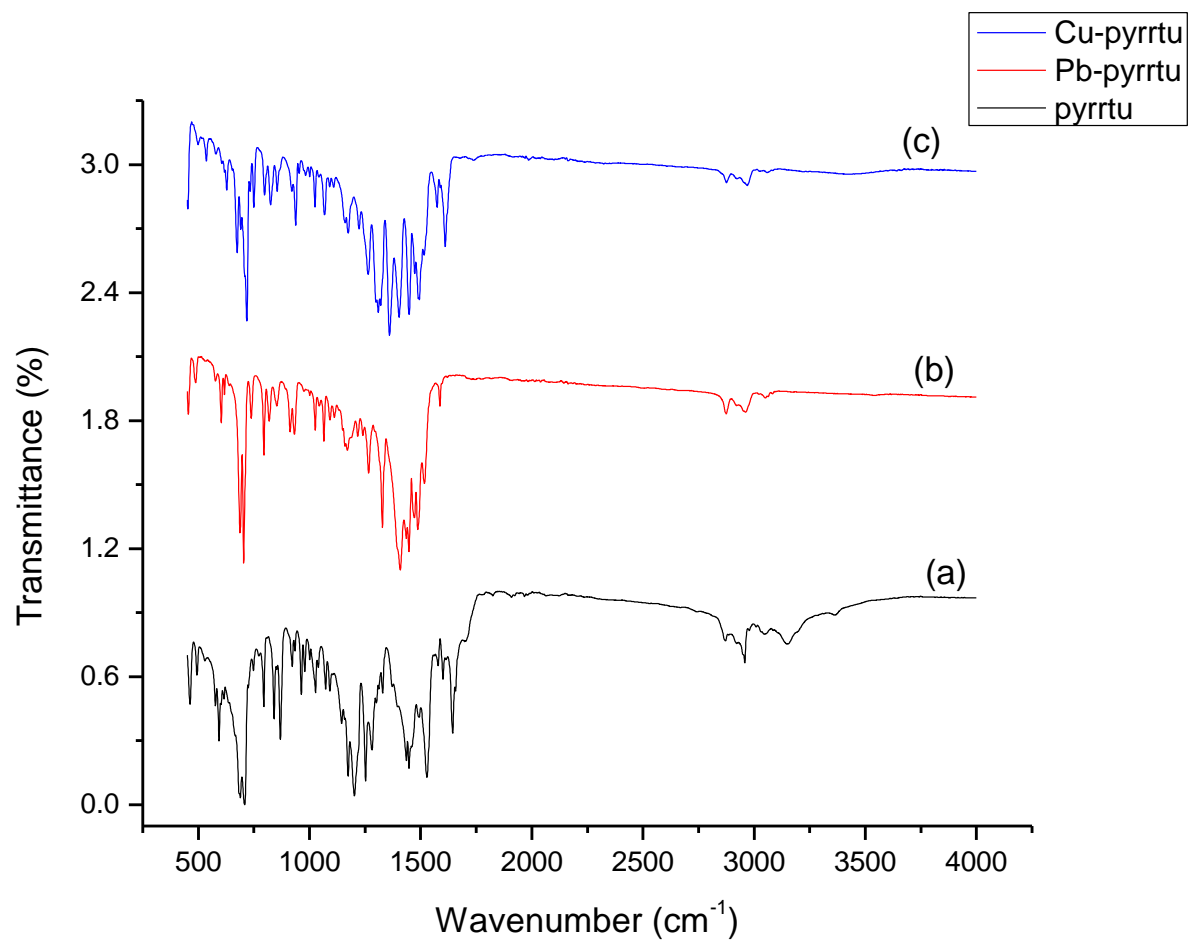
Publisher's Note Springer Nature remains neutral with regard to jurisdictional claims in published maps and institutional affiliations.

ANNEX 2. Spectroscopic infrared and ^1H NMR spectra of the ligands and metal complexes.

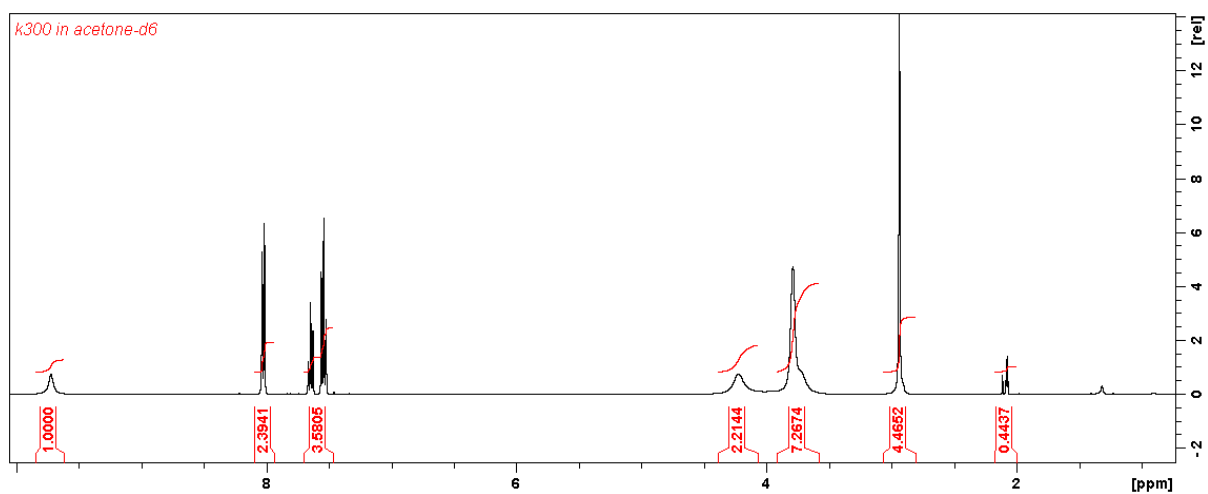
ANNEX 2.1. Infra-red spectra of the (a): N-morpholine-N'-benzoylthiourea ligand the corresponding (b): Pb(II) and (c) Cu(II) metal complexes.



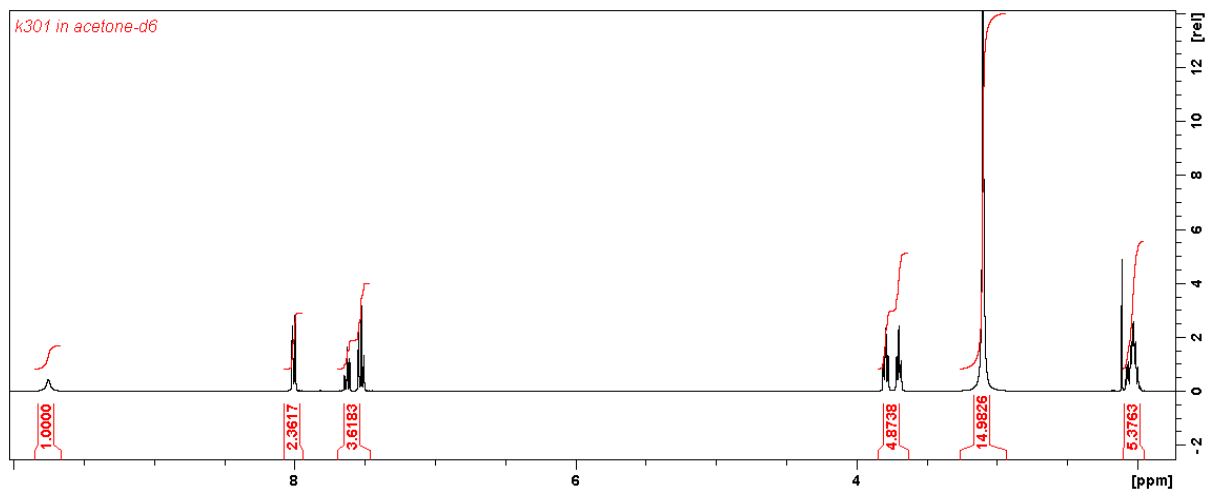
ANNEX 2.2. Infra-red spectra of the (a): N-pyrrolidine-N'-benzoylthiourea ligand the corresponding (b): Pb(II) and (c) Cu(II) metal complexes.



ANNEX 2.3. ^1H NMR spectrum of the N-morpholine-N'-benzoylthiourea ligand.



ANNEX 2.4. ^1H NMR spectrum of the N-pyrrolidine-N'-benzoylthiourea ligand.



ANNEX 3. Crystallographic data of the Pb(II) and Cu(II) crystal structures.

Table 1. Bond lengths [Å] and angles [deg] for C₂₄H₂₆N₄O₄PbS₂.

Bonds lengths [Å]	Angles [deg]
Pb1 - O1	2.448(2)
Pb1 - O3	2.455(2)
Pb1 - S1	2.6870(9)
Pb1 - S2	2.6890(9)
S1 - C2	1.753(3)
S2 - C13	1.756(3)
O1 - C1	1.262(4)
O2 - C5	1.430(4)
O2 - C4	1.432(4)
O3 - C14	1.275(4)
O4 - C22	1.428(4)
O4 - C23	1.433(4)
N1 - C1	1.333(4)
N1 - C2	1.342(4)
N2 - C2	1.342(4)
N2 - C6	1.466(4)
N2 - C3	1.473(4)
N3 - C14	1.338(4)
N3 - C13	1.346(4)
N4 - C13	1.337(4)
N4 - C21	1.479(4)
N4 - C24	1.483(4)
C1 - C7	1.504(4)
C3 - C4	1.521(5)
C3 - H7	0.9900
C3 - H8	0.9900
C4 - H5	0.9900

C4 - H6	0.9900
C5 - C6	1.519(4)
C5 - H3	0.9900
C5 - H4	0.9900
C6 - H2	0.9900
C6 - H1	0.9900
C7 - C12	1.394(5)
C7 - C8	1.405(4)
C8 - C9	1.394(5)
C8 - H13	0.9500
C9 - C10	1.382(5)
C9 - H12	0.9500
C10 - C11	1.389(5)
C10 - H11	0.9500
C11 - C12	1.395(5)
C11 - H9	0.9500
C12 - H10	0.9500
C14 - C15	1.494(4)
C15 - C16	1.400(5)
C15 - C20	1.405(4)
C16 - C17	1.395(4)
C16 - H18	0.9500
C17 - C18	1.386(5)
C17 - H17	0.9500
C18 - C19	1.394(5)
C18 - H16	0.9500
C19 - C20	1.389(5)
C19 - H15	0.9500
C20 - H14	0.9500
C21 - C22	1.514(4)
C21 - H26	0.9900

C21 - H25	0.9900
C22 - H24	0.9900
C22 - H23	0.9900
C23 - C24	1.523(4)
C23 - H21	0.9900
C23 - H22	0.9900
C24 - H19	0.9900
C24 - H20	0.9900

O1 - Pb1 - O3	147.99(7)
O1 - Pb1 - S1	79.63(5)
O3 - Pb1 - S1	76.81(6)
O1 - Pb1 - S2	85.10(6)
O3 - Pb1 - S2	76.23(6)
S1 - Pb1 - S2	96.07(2)
C2 - S1 - Pb1	103.65(10)
C13 - S2 - Pb1	98.34(10)
C1 - O1 - Pb1	127.27(18)
C5 - O2 - C4	111.0(2)
C14 - O3 - Pb1	132.9(2)
C22 - O4 - C23	109.3(2)
C1 - N1 - C2	125.0(3)
C2 - N2 - C6	125.3(3)
C2 - N2 - C3	121.4(3)
C6 - N2 - C3	112.2(2)
C14 - N3 - C13	124.2(3)
C13 - N4 - C21	122.7(3)
C13 - N4 - C24	125.3(3)
C21 - N4 - C24	112.0(2)

O1 - C1 - N1	126.3(3)
O1 - C1 - C7	118.3(3)
N1 - C1 - C7	115.3(3)
N2 - C2 - N1	117.7(3)
N2 - C2 - S1	118.3(2)
N1 - C2 - S1	123.5(2)
N2 - C3 - C4	108.6(3)
N2 - C3 - H7	110.0
C4 - C3 - H7	110.0
N2 - C3 - H8	110.0
C4 - C3 - H8	110.0
H7 - C3 - H8	108.4
O2 - C4 - C3	110.9(3)
O2 - C4 - H5	109.5
C3 - C4 - H5	109.5
O2 - C4 - H6	109.5
C3 - C4 - H6	109.5
H5 - C4 - H6	108.0
O2 - C5 - C6	111.1(3)
O2 - C5 - H3	109.4
C6 - C5 - H3	109.4
O2 - C5 - H4	109.4
C6 - C5 - H4	109.4
H3 - C5 - H4	108.0
N2 - C6 - C5	108.5(3)
N2 - C6 - H2	110.0
C5 - C6 - H2	110.0
N2 - C6 - H1	110.0
C5 - C6 - H1	110.0
H2 - C6 - H1	108.4
C12 - C7 - C8	119.2(3)

C12 - C7 - C1	122.6(3)
C8 - C7 - C1	118.2(3)
C9 - C8 - C7	119.7(3)
C9 - C8 - H13	120.1
C7 - C8 - H13	120.1
C10 - C9 - C8	121.0(3)
C10 - C9 - H12	119.5
C8 - C9 - H12	119.5
C9 - C10 - C11	119.4(3)
C9 - C10 - H11	120.3
C11 - C10 - H11	120.3
C10 - C11 - C12	120.5(3)
C10 - C11 - H9	119.7
C12 - C11 - H9	119.7
C7 - C12 - C11	120.2(3)
C7 - C12 - H10	119.9
C11 - C12 - H10	119.9
N4 - C13 - N3	117.3(3)
N4 - C13 - S2	119.6(2)
N3 - C13 - S2	122.7(2)
O3 - C14 - N3	126.5(3)
O3 - C14 - C15	117.1(3)
N3 - C14 - C15	116.4(3)
C16 - C15 - C20	119.2(3)
C16 - C15 - C14	119.7(3)
C20 - C15 - C14	121.1(3)
C17 - C16 - C15	120.3(3)
C17 - C16 - H18	119.9
C15 - C16 - H18	119.9
C18 - C17 - C16	120.2(3)
C18 - C17 - H17	119.9

C16 - C17 - H17	119.9
C17 - C18 - C19	119.8(3)
C17 - C18 - H16	120.1
C19 - C18 - H16	120.1
C20 - C19 - C18	120.5(3)
C20 - C19 - H15	119.8
C18 - C19 - H15	119.8
C19 - C20 - C15	120.0(3)
C19 - C20 - H14	120.0
C15 - C20 - H14	120.0
N4 - C21 - C22	109.7(2)
N4 - C21 - H26	109.7
C22 - C21 - H26	109.7
N4 - C21 - H25	109.7
C22 - C21 - H25	109.7
H26 - C21 - H25	108.2
O4 - C22 - C21	111.8(3)
O4 - C22 - H24	109.3
C21 - C22 - H24	109.3
O4 - C22 - H23	109.3
C21 - C22 - H23	109.3
H24 - C22 - H23	107.9
O4 - C23 - C24	111.6(2)
O4 - C23 - H21	109.3
C24 - C23 - H21	109.3
O4 - C23 - H22	109.3
C24 - C23 - H22	109.3
H21 - C23 - H22	108.0
N4 - C24 - C23	108.8(3)
N4 - C24 - H19	109.9
C23 - C24 - H19	109.9

N4 - C24 - H20	109.9
C23 - C24 - H20	109.9
H19 - C24 - H20	108.3

Table 2. Anisotropic displacement parameters for C₂₄H₂₆N₄O₄PbS₂.

	U11	U22	U33	U23	U13	U12
Pb1	0.01362(6)	0.01192(6)	0.01115(6)	-0.00057(5)	0.00273(4)	-0.00130(5)
S1	0.0137(3)	0.0179(4)	0.0111(3)	0.0027(3)	0.0024(3)	0.0021(4)
S2	0.0111(3)	0.0132(4)	0.0159(4)	-0.0008(3)	0.0003(3)	0.0015(3)
O1	0.0161(10)	0.0169(12)	0.0130(10)	0.0025(10)	0.0005(8)	-0.0024(10)
O2	0.0126(10)	0.0397(16)	0.0205(12)	-0.0035(12)	0.0039(9)	0.0002(12)
O3	0.0218(11)	0.0170(11)	0.0112(10)	0.0016(10)	0.0022(8)	0.0025(11)
O4	0.0175(11)	0.0169(12)	0.0222(12)	0.0032(11)	0.0008(9)	-0.0034(11)
N1	0.0144(12)	0.0170(14)	0.0162(13)	0.0060(12)	0.0058(10)	0.0026(13)
N2	0.0120(12)	0.0217(15)	0.0132(12)	0.0032(12)	0.0036(9)	0.0041(13)
N3	0.0158(13)	0.0148(14)	0.0111(12)	0.0024(11)	0.0007(10)	-0.0010(12)
N4	0.0138(12)	0.0121(13)	0.0127(12)	0.0019(11)	0.0005(10)	-0.0020(12)
C1	0.0160(14)	0.0156(16)	0.0063(13)	0.0013(13)	0.0006(11)	0.0001(14)
C2	0.0131(14)	0.0122(15)	0.0126(14)	0.0020(13)	0.0005(11)	-0.0012(14)
C3	0.0175(15)	0.0291(19)	0.0126(15)	0.0028(15)	0.0050(12)	0.0041(16)
C4	0.0277(18)	0.0226(18)	0.0180(16)	0.0000(15)	0.0080(14)	-0.0017(17)
C5	0.0175(15)	0.0257(19)	0.0157(15)	-0.0033(15)	-0.0013(12)	0.0034(16)
C6	0.0171(15)	0.0194(17)	0.0171(15)	0.0007(15)	0.0019(12)	0.0060(16)
C7	0.0176(14)	0.0142(15)	0.0090(13)	-0.0016(13)	-0.0028(11)	0.0015(15)
C8	0.0190(15)	0.0196(17)	0.0123(14)	-0.0015(14)	0.0002(12)	0.0037(15)
C9	0.0333(19)	0.0199(18)	0.0131(15)	-0.0047(15)	-0.0023(14)	0.0095(18)
C10	0.053(2)	0.0120(16)	0.0130(16)	-0.0041(14)	-0.0100(16)	0.0036(19)
C11	0.035(2)	0.0187(17)	0.0134(15)	0.0040(15)	-0.0056(14)	-0.0094(18)
C12	0.0211(16)	0.0215(17)	0.0120(14)	0.0013(14)	-0.0016(12)	-0.0015(16)
C13	0.0118(14)	0.0121(15)	0.0121(14)	-0.0025(13)	0.0048(11)	0.0000(14)

C14	0.0083(13)	0.0172(16)	0.0121(14)	0.0032(13)	0.0012(10)	0.0025(14)
C15	0.0083(12)	0.0171(16)	0.0125(14)	0.0037(13)	0.0011(10)	-0.0001(14)
C16	0.0191(16)	0.0194(17)	0.0141(15)	0.0032(14)	-0.0022(12)	-0.0036(16)
C17	0.0228(17)	0.0183(17)	0.0249(17)	0.0073(15)	-0.0030(14)	-0.0073(16)
C18	0.0202(16)	0.030(2)	0.0164(16)	0.0096(16)	0.0002(13)	-0.0018(17)
C19	0.0267(17)	0.0265(19)	0.0149(15)	0.0023(16)	0.0005(13)	0.0043(18)
C20	0.0179(15)	0.0161(16)	0.0157(15)	-0.0003(14)	0.0014(12)	0.0021(15)
C21	0.0172(15)	0.0160(16)	0.0143(14)	-0.0009(14)	-0.0019(12)	-0.0028(15)
C22	0.0169(15)	0.0155(16)	0.0239(17)	-0.0002(15)	0.0000(13)	0.0001(16)
C23	0.0218(16)	0.0146(16)	0.0145(15)	0.0013(14)	0.0033(12)	-0.0009(16)
C24	0.0183(15)	0.0118(15)	0.0154(15)	0.0023(13)	0.0014(12)	0.0012(15)

Table 3. Torsion angles [deg] for C₂₄H₂₆N₄O₄PbS₂.

Pb1 - O1 - C1 - N1	52.5(4)
Pb1 - O1 - C1 - C7	-131.3(2)
C2 - N1 - C1 - O1	-26.9(5)
C2 - N1 - C1 - C7	156.9(3)
C6 - N2 - C2 - N1	162.6(3)
C3 - N2 - C2 - N1	-4.3(4)
C6 - N2 - C2 - S1	-9.8(4)
C3 - N2 - C2 - S1	-176.7(2)
C1 - N1 - C2 - N2	147.5(3)
C1 - N1 - C2 - S1	-40.6(4)
Pb1 - S1 - C2 - N2	-128.7(2)
Pb1 - S1 - C2 - N1	59.5(3)
C2 - N2 - C3 - C4	111.9(3)
C6 - N2 - C3 - C4	-56.6(4)
C5 - O2 - C4 - C3	-59.3(3)
N2 - C3 - C4 - O2	56.7(4)

C4 - O2 - C5 - C6	59.6(4)
C2 - N2 - C6 - C5	-111.2(3)
C3 - N2 - C6 - C5	56.7(3)
O2 - C5 - C6 - N2	-57.3(3)
O1 - C1 - C7 - C12	-163.0(3)
N1 - C1 - C7 - C12	13.6(4)
O1 - C1 - C7 - C8	18.5(4)
N1 - C1 - C7 - C8	-165.0(3)
C12 - C7 - C8 - C9	-0.8(4)
C1 - C7 - C8 - C9	177.8(3)
C7 - C8 - C9 - C10	1.4(5)
C8 - C9 - C10 - C11	-0.7(5)
C9 - C10 - C11 - C12	-0.5(5)
C8 - C7 - C12 - C11	-0.4(4)
C1 - C7 - C12 - C11	-179.0(3)
C10 - C11 - C12 - C7	1.1(5)
C21 - N4 - C13 - N3	3.7(4)
C24 - N4 - C13 - N3	-177.4(3)
C21 - N4 - C13 - S2	176.8(2)
C24 - N4 - C13 - S2	-4.3(4)
C14 - N3 - C13 - N4	-147.3(3)
C14 - N3 - C13 - S2	39.8(4)
Pb1 - S2 - C13 - N4	115.0(2)
Pb1 - S2 - C13 - N3	-72.3(3)
Pb1 - O3 - C14 - N3	-21.3(5)
Pb1 - O3 - C14 - C15	161.58(19)
C13 - N3 - C14 - O3	19.6(5)
C13 - N3 - C14 - C15	-163.3(3)
O3 - C14 - C15 - C16	-2.8(4)
N3 - C14 - C15 - C16	179.8(3)
O3 - C14 - C15 - C20	174.9(3)

N3 - C14 - C15 - C20	-2.5(4)
C20 - C15 - C16 - C17	-0.9(5)
C14 - C15 - C16 - C17	176.8(3)
C15 - C16 - C17 - C18	0.9(5)
C16 - C17 - C18 - C19	-0.4(5)
C17 - C18 - C19 - C20	-0.1(5)
C18 - C19 - C20 - C15	0.1(5)
C16 - C15 - C20 - C19	0.4(5)
C14 - C15 - C20 - C19	-177.3(3)
C13 - N4 - C21 - C22	125.6(3)
C24 - N4 - C21 - C22	-53.4(3)
C23 - O4 - C22 - C21	-60.6(3)
N4 - C21 - C22 - O4	56.6(3)
C22 - O4 - C23 - C24	61.4(3)
C13 - N4 - C24 - C23	-125.3(3)
C21 - N4 - C24 - C23	53.7(3)
O4 - C23 - C24 - N4	-57.7(3)

Table 1. Bond lengths [Å], angles [deg] and torsion angles [deg] for C₂₄H₂₆N₄O₄CuS₂.

Bond lengths [Å]	Angles [deg]
Cu1 - O1	1.9061(15)
Cu1 - O1	1.9061(15)
Cu1 - S1	2.2812(5)
Cu1 - S1	2.2812(5)
Cu2 - O3	1.9091(15)
Cu2 - O3	1.9091(15)
Cu2 - S2	2.2790(5)
Cu2 - S2	2.2790(5)
S1 - C1	1.730(2)
S2 - C15	1.728(2)
O1 - C2	1.261(3)
O2 - C12	1.429(2)
O2 - C11	1.430(3)
O3 - C14	1.265(3)
O4 - C18	1.429(2)
O4 - C17	1.429(3)
N1 - C2	1.333(3)
N1 - C1	1.340(3)
N2 - C14	1.330(3)
N2 - C15	1.340(3)
N3 - C15	1.354(3)
N3 - C16	1.469(2)
N3 - C19	1.472(3)
C1 - N5	1.354(3)
C2 - C3	1.495(3)
C3 - C8	1.392(3)
C3 - C4	1.395(3)
C4 - C5	1.385(3)
C4 - H5	0.9500

C5 - C6	1.381(4)
C5 - H4	0.9500
C6 - C7	1.387(3)
C6 - H3	0.9500
C7 - C8	1.386(3)
C7 - H2	0.9500
C8 - H1	0.9500
N5 - C13	1.469(3)
N5 - C10	1.472(3)
C10 - C11	1.519(3)
C10 - H12	0.9900
C10 - H13	0.9900
C11 - H11	0.9900
C11 - H10	0.9900
C12 - C13	1.513(3)
C12 - H9	0.9900
C12 - H6	0.9900
C13 - H8	0.9900
C13 - H7	0.9900
C14 - C20	1.500(3)
C16 - C17	1.520(3)
C16 - H21	0.9900
C16 - H22	0.9900
C17 - H16	0.9900
C17 - H15	0.9900
C18 - C19	1.514(3)
C18 - H19	0.9900
C18 - H20	0.9900
C19 - H18	0.9900
C19 - H17	0.9900
C20 - C25	1.388(3)

C20 - C21	1.399(3)
C21 - C22	1.383(3)
C21 - H27	0.9500
C22 - C23	1.387(4)
C22 - H23	0.9500
C23 - C24	1.390(3)
C23 - H26	0.9500
C24 - C25	1.387(3)
C24 - H25	0.9500
C25 - H24	0.9500
O1 - Cu1 - O1	180.0
O1 - Cu1 - S1	86.23(5)
O1 - Cu1 - S1	93.77(5)
O1 - Cu1 - S1	93.77(5)
O1 - Cu1 - S1	86.23(5)
S1 - Cu1 - S1	180.0
O3 - Cu2 - O3	180.0
O3 - Cu2 - S2	93.51(5)
O3 - Cu2 - S2	86.49(5)
O3 - Cu2 - S2	86.49(5)
O3 - Cu2 - S2	93.51(5)
S2 - Cu2 - S2	180.00(3)
C1 - S1 - Cu1	106.83(7)
C15 - S2 - Cu2	107.23(7)
C2 - O1 - Cu1	131.33(14)
C12 - O2 - C11	108.74(15)
C14 - O3 - Cu2	131.97(14)
C18 - O4 - C17	108.94(15)
C2 - N1 - C1	125.27(18)

C14 - N2 - C15	125.24(18)
C15 - N3 - C16	123.78(17)
C15 - N3 - C19	121.48(16)
C16 - N3 - C19	112.33(16)
N1 - C1 - N5	114.76(18)
N1 - C1 - S1	128.19(16)
N5 - C1 - S1	117.00(15)
O1 - C2 - N1	129.5(2)
O1 - C2 - C3	115.51(18)
N1 - C2 - C3	114.98(18)
C8 - C3 - C4	119.0(2)
C8 - C3 - C2	122.00(19)
C4 - C3 - C2	119.0(2)
C5 - C4 - C3	120.3(2)
C5 - C4 - H5	119.8
C3 - C4 - H5	119.8
C6 - C5 - C4	120.4(2)
C6 - C5 - H4	119.8
C4 - C5 - H4	119.8
C5 - C6 - C7	119.7(2)
C5 - C6 - H3	120.2
C7 - C6 - H3	120.2
C8 - C7 - C6	120.2(2)
C8 - C7 - H2	119.9
C6 - C7 - H2	119.9
C7 - C8 - C3	120.4(2)
C7 - C8 - H1	119.8
C3 - C8 - H1	119.8
C1 - N5 - C13	121.18(17)
C1 - N5 - C10	124.10(17)
C13 - N5 - C10	112.85(16)

N5 - C10 - C11	110.68(17)
N5 - C10 - H12	109.5
C11 - C10 - H12	109.5
N5 - C10 - H13	109.5
C11 - C10 - H13	109.5
H12 - C10 - H13	108.1
O2 - C11 - C10	112.40(17)
O2 - C11 - H11	109.1
C10 - C11 - H11	109.1
O2 - C11 - H10	109.1
C10 - C11 - H10	109.1
H11 - C11 - H10	107.9
O2 - C12 - C13	111.79(17)
O2 - C12 - H9	109.3
C13 - C12 - H9	109.3
O2 - C12 - H6	109.3
C13 - C12 - H6	109.3
H9 - C12 - H6	107.9
N5 - C13 - C12	109.42(17)
N5 - C13 - H8	109.8
C12 - C13 - H8	109.8
N5 - C13 - H7	109.8
C12 - C13 - H7	109.8
H8 - C13 - H7	108.2
O3 - C14 - N2	130.0(2)
O3 - C14 - C20	115.68(18)
N2 - C14 - C20	114.26(18)
N2 - C15 - N3	114.25(17)
N2 - C15 - S2	128.23(15)
N3 - C15 - S2	117.49(15)
N3 - C16 - C17	110.22(16)

N3 - C16 - H21	109.6
C17 - C16 - H21	109.6
N3 - C16 - H22	109.6
C17 - C16 - H22	109.6
H21 - C16 - H22	108.1
O4 - C17 - C16	111.51(17)
O4 - C17 - H16	109.3
C16 - C17 - H16	109.3
O4 - C17 - H15	109.3
C16 - C17 - H15	109.3
H16 - C17 - H15	108.0
O4 - C18 - C19	112.00(17)
O4 - C18 - H19	109.2
C19 - C18 - H19	109.2
O4 - C18 - H20	109.2
C19 - C18 - H20	109.2
H19 - C18 - H20	107.9
N3 - C19 - C18	110.45(17)
N3 - C19 - H18	109.6
C18 - C19 - H18	109.6
N3 - C19 - H17	109.6
C18 - C19 - H17	109.6
H18 - C19 - H17	108.1
C25 - C20 - C21	119.2(2)
C25 - C20 - C14	121.81(19)
C21 - C20 - C14	119.0(2)
C22 - C21 - C20	120.2(2)
C22 - C21 - H27	119.9
C20 - C21 - H27	119.9
C21 - C22 - C23	120.1(2)
C21 - C22 - H23	119.9

C23 - C22 - H23	119.9
C22 - C23 - C24	120.2(2)
C22 - C23 - H26	119.9
C24 - C23 - H26	119.9
C25 - C24 - C23	119.5(2)
C25 - C24 - H25	120.3
C23 - C24 - H25	120.3
C24 - C25 - C20	120.8(2)
C24 - C25 - H24	119.6
C20 - C25 - H24	119.6

Table 2. Anisotropic displacement parameters for $C_{24}H_{26}N_4O_4CuS_2$.

	U11	U22	U33	U23	U13	U12
Cu1	0.0142(2)	0.01366(18)	0.01502(18)	-0.00583(14)	-0.00177(14)	0.00235(14)
Cu2	0.0162(2)	0.01585(18)	0.01006(17)	-0.00299(13)	-0.00468(14)	0.00297(14)
S1	0.0169(3)	0.0133(2)	0.0138(2)	-0.00361(19)	-0.0004(2)	0.0012(2)
S2	0.0180(3)	0.0138(2)	0.0108(2)	-0.00194(18)	-0.0043(2)	0.0017(2)
O1	0.0180(8)	0.0191(8)	0.0165(7)	-0.0044(6)	-0.0024(6)	0.0052(6)
O2	0.0156(8)	0.0117(7)	0.0174(7)	0.0001(6)	-0.0009(6)	0.0029(6)
O3	0.0230(9)	0.0164(7)	0.0146(7)	-0.0045(6)	-0.0084(6)	0.0046(6)
O4	0.0183(8)	0.0130(7)	0.0140(7)	0.0012(6)	-0.0055(6)	0.0020(6)
N1	0.0149(9)	0.0109(8)	0.0155(8)	-0.0021(7)	-0.0002(7)	-0.0007(7)
N2	0.0146(9)	0.0115(8)	0.0115(8)	0.0010(6)	-0.0017(7)	-0.0008(7)
N3	0.0154(9)	0.0094(8)	0.0109(8)	0.0002(6)	-0.0025(7)	0.0010(7)
C1	0.0102(10)	0.0128(9)	0.0160(10)	-0.0032(8)	-0.0007(8)	-0.0050(8)
C2	0.0132(11)	0.0131(10)	0.0173(10)	-0.0058(8)	-0.0036(8)	-0.0029(8)
C3	0.0135(11)	0.0116(10)	0.0196(10)	-0.0026(8)	-0.0056(8)	-0.0017(8)
C4	0.0202(12)	0.0146(10)	0.0259(12)	-0.0042(9)	-0.0014(9)	0.0018(9)
C5	0.0233(13)	0.0108(10)	0.0326(13)	-0.0001(9)	-0.0074(10)	0.0027(9)

C6	0.0210(13)	0.0166(11)	0.0233(11)	0.0063(9)	-0.0081(9)	-0.0020(9)
C7	0.0220(13)	0.0215(11)	0.0205(11)	-0.0002(9)	0.0014(9)	0.0016(10)
C8	0.0188(12)	0.0119(10)	0.0220(11)	-0.0012(8)	-0.0029(9)	0.0031(9)
N5	0.0159(10)	0.0115(8)	0.0113(8)	-0.0013(6)	-0.0012(7)	0.0004(7)
C10	0.0168(11)	0.0141(10)	0.0118(9)	0.0003(8)	-0.0035(8)	0.0004(8)
C11	0.0160(11)	0.0139(10)	0.0171(10)	0.0004(8)	-0.0011(8)	-0.0007(8)
C12	0.0129(11)	0.0141(10)	0.0148(10)	-0.0016(8)	-0.0026(8)	0.0018(8)
C13	0.0156(11)	0.0125(10)	0.0128(10)	-0.0006(8)	0.0005(8)	-0.0005(8)
C14	0.0122(11)	0.0165(10)	0.0093(9)	-0.0009(8)	0.0020(8)	0.0003(8)
C15	0.0080(10)	0.0148(10)	0.0117(9)	-0.0017(7)	0.0002(7)	-0.0025(8)
C16	0.0166(11)	0.0112(10)	0.0138(10)	-0.0002(8)	-0.0026(8)	0.0018(8)
C17	0.0176(11)	0.0112(9)	0.0149(10)	0.0014(8)	-0.0031(8)	-0.0004(8)
C18	0.0173(11)	0.0137(10)	0.0116(9)	-0.0005(8)	-0.0031(8)	0.0020(8)
C19	0.0176(11)	0.0103(9)	0.0127(10)	-0.0002(7)	-0.0046(8)	-0.0011(8)
C20	0.0139(11)	0.0146(10)	0.0111(9)	0.0020(8)	0.0020(8)	0.0006(8)
C21	0.0219(12)	0.0200(11)	0.0127(10)	0.0013(8)	-0.0037(9)	0.0011(9)
C22	0.0240(13)	0.0188(11)	0.0193(11)	0.0078(9)	0.0001(9)	0.0036(9)
C23	0.0231(13)	0.0123(10)	0.0259(12)	0.0031(9)	0.0059(10)	0.0007(9)
C24	0.0238(13)	0.0180(11)	0.0206(11)	-0.0025(9)	-0.0025(9)	-0.0023(9)
C25	0.0168(11)	0.0159(10)	0.0145(10)	0.0028(8)	-0.0019(8)	0.0001(9)

Table 3. Torsion angles [deg] for C₂₄H₂₆N₄O₄CuS₂.

C2 - N1 - C1 - N5	172.4(2)
C2 - N1 - C1 - S1	-10.5(3)
Cu1 - S1 - C1 - N1	17.2(2)
Cu1 - S1 - C1 - N5	-165.64(15)
Cu1 - O1 - C2 - N1	27.9(4)
Cu1 - O1 - C2 - C3	-153.06(15)
C1 - N1 - C2 - O1	-14.9(4)

C1 - N1 - C2 - C3	165.99(19)
O1 - C2 - C3 - C8	-171.3(2)
N1 - C2 - C3 - C8	8.0(3)
O1 - C2 - C3 - C4	9.4(3)
N1 - C2 - C3 - C4	-171.4(2)
C8 - C3 - C4 - C5	-1.0(3)
C2 - C3 - C4 - C5	178.3(2)
C3 - C4 - C5 - C6	0.5(4)
C4 - C5 - C6 - C7	0.4(4)
C5 - C6 - C7 - C8	-0.9(4)
C6 - C7 - C8 - C3	0.4(4)
C4 - C3 - C8 - C7	0.5(3)
C2 - C3 - C8 - C7	-178.8(2)
N1 - C1 - N5 - C13	5.8(3)
S1 - C1 - N5 - C13	-171.70(16)
N1 - C1 - N5 - C10	169.12(19)
S1 - C1 - N5 - C10	-8.4(3)
C1 - N5 - C10 - C11	145.5(2)
C13 - N5 - C10 - C11	-49.9(2)
C12 - O2 - C11 - C10	-59.4(2)
N5 - C10 - C11 - O2	53.7(2)
C11 - O2 - C12 - C13	61.9(2)
C1 - N5 - C13 - C12	-143.0(2)
C10 - N5 - C13 - C12	51.9(2)
O2 - C12 - C13 - N5	-58.3(2)
Cu2 - O3 - C14 - N2	-22.2(4)
Cu2 - O3 - C14 - C20	160.42(15)
C15 - N2 - C14 - O3	12.4(4)
C15 - N2 - C14 - C20	-170.16(19)
C14 - N2 - C15 - N3	-172.4(2)
C14 - N2 - C15 - S2	9.9(3)

C16 - N3 - C15 - N2	-168.42(18)
C19 - N3 - C15 - N2	-7.4(3)
C16 - N3 - C15 - S2	9.5(3)
C19 - N3 - C15 - S2	170.50(15)
C15 - N3 - C16 - C17	-146.1(2)
C19 - N3 - C16 - C17	51.4(2)
C18 - O4 - C17 - C16	61.0(2)
N3 - C16 - C17 - O4	-56.7(2)
C17 - O4 - C18 - C19	-60.7(2)
C15 - N3 - C19 - C18	146.08(19)
C16 - N3 - C19 - C18	-50.9(2)
O4 - C18 - C19 - N3	55.8(2)
O3 - C14 - C20 - C25	176.0(2)
N2 - C14 - C20 - C25	-1.8(3)
O3 - C14 - C20 - C21	-4.3(3)
N2 - C14 - C20 - C21	177.9(2)
C25 - C20 - C21 - C22	-0.4(3)
C14 - C20 - C21 - C22	179.9(2)
C20 - C21 - C22 - C23	-0.1(4)
C21 - C22 - C23 - C24	0.1(4)
C22 - C23 - C24 - C25	0.3(4)
C23 - C24 - C25 - C20	-0.8(4)
C21 - C20 - C25 - C24	0.8(3)
C14 - C20 - C25 - C24	-179.4(2)